MEASUREMENT OF THE RATE OF MUON CAPTURE IN HYDROGEN GAS AND DETERMINATION OF THE PROTON'S PSEUDOSCALAR COUPLING

BY

STEVEN MICHAEL CLAYTON

B.S., University of Minnesota, 1997
M.S., University of Illinois at Urbana-Champaign, 1999

DISSERTATION

Submitted in partial fulfillment of the requirements
for the degree of Doctor of Philosophy in Physics
in the Graduate College of the
University of Illinois at Urbana-Champaign, 2007

Urbana, Illinois

Abstract

A measurement is presented of the rate Λ_S of ordinary muon capture on the proton from the singlet μp atomic state. Negative muons were stopped in a time projection chamber operating on ultrapure, deuterium-depleted hydrogen gas at 10 bar and room temperature. Under these conditions molecular formation amounts to a small correction, and ambiguity in the interpretation due to a poorly-known molecular transition rate is avoided. The disappearance rate of the negative muons was determined from the time spectrum of their decay electrons. After some small corrections, the difference of this rate from the world average positive muon (inverse) lifetime is attributed to Λ_S. The result is $\Lambda_S = 725.0 \pm 13.7_{\mathrm{stat}} \pm 10.7_{\mathrm{syst}}\ \mathrm{s}^{-1}$, which determines the proton's pseudoscalar coupling to be $g_P(q^2 = -0.88 m_\mu^2) = 7.3 \pm 1.1$, consistent with theoretical predictions based on chiral perturbation theory. This is the final result of the analysis of data accumulated by the MuCap collaboration in their 2004 experimental running period.

The MuCap experiment, the data analysis leading to the result for Λ_S, and contextual information are described in this dissertation. In the first chapter, a brief historical review of previous measurements of muon capture on the proton introduces many of the experimental challenges. The next chapter covers the standard-model phenomenological calculation of Λ_S and knowledge of the proton's weak form factors, and results of modern calculations using chiral perturbation theory are quoted. The subject of muon atomic and molecular kinetics in hydrogen, important for understanding many of the key features the experiment, is discussed in Chapter 3. The MuCap experimental design and apparatus are presented with selected details in Chapter 4. The next two chapters cover data analysis, evaluations of systematic corrections and uncertainties, and demonstrations of internal consistency of the Λ_S result with variations of analysis parameters. The dissertation concludes with a results chapter, in which the the method used to determine g_P from the experimental result for Λ_S is shown.

Acknowledgements

Many people contributed to the design, construction, execution, and subsequent data analysis of the MuCap experiment. The international collaboration included V.A. Andreev, T.I. Banks, T.A. Case, D.B. Chitwood, K.M. Crowe, J. Deutsch, J. Egger, S.J. Freedman, V.A. Ganzha, T. Gorringe, F.E. Gray, D.W. Hertzog, M. Hildebrandt, P. Kammel, B. Kiburg, S. Knaack, P.A. Kravtsov, A.G. Krivshich, B. Lauss, K.L. Lynch, E.M. Maev, O.E. Maev, F. Mulhauser, C.S. Özben, C. Petitjean, G.E. Petrov, R. Prieels, G.N. Schapkin, G.G. Semenchuk, M.A. Soroka, V. Tishchenko, A.A. Vasilyev, A.A. Vorobyov, M.E. Vznuzdaev, and P. Winter. I personally benefitted from scientific as well as cultural exchanges with members of the collaboration, especially during meetings at the Petersburg Nuclear Physics Institute (Russia), the University of California Berkeley, and the University of Illinois at Urbana-Champaign, and during several experimental running periods at the Paul Scherrer Institute (Switzerland).

Thanks are due to the members of the Precision Muon Group at UIUC during the course of the MuCap experiment: Dan Chitwood, Jason Crnkovic, Paul Debevec, Andrea Esler, Fred Gray, Scott Headley, David Hertzog, Peter Kammel, Brendan Kiburg, Tim Klein, Sara Knaack, Josh Kunkle, Ron McNabb, Gerco Onderwater, Cenap Özben, Nidhi Patel, Chris Polly, David Webber, and Peter Winter. I enjoyed the frequent lunchtime physics discussions, which usually involved two or three coffehouse tables pushed together and a plot of current research presented by one of us for consideration. I am grateful to my advisors, Peter Kammel and David Hertzog, for their guidance and support.

Funding for the Illinois group was provided by the National Science Foundation under contracts NSF-PHY-00-72044, NSF-PHY-02-44889, NSF-PHY-06-01067. Computing resources for the UIUC data analysis described in this dissertation were provided by the National Center for Supercomputing Applications (NCSA) at the University of Illinois at Urbana-Champaign.

Contents

Chapter 1

Introduction

1.1 Context

The basic process of ordinary muon capture on the proton,

$$\mu^- + p \rightarrow n + \nu_\mu, \tag{1.1}$$

provides a theoretically clean, electroweak probe of the nucleon. Like neutron beta decay, ordinary muon capture is sensitive to the low-energy electroweak form factors of the nucleon, the vector and axial-vector couplings g_V and g_A. Because of the higher momentum transfer in muon capture, the process is additionally sensitive to recoil-order terms, in particular the pseudoscalar coupling g_P. Although there is a standard-model prediction based on symmetries of quantum chromodynamics, no precise, unambiguous measurement of the rate of ordinary muon capture on the proton was achieved until this year, when the MuCap collaboration released their first result from the experiment that is the topic of this dissertation.

Muon capture proceeds from the ground state of a μp atom, which is similar to a hydrogen atom with the electron replaced by a muon. Due to the larger mass of the muon compared to the electron, $m_\mu \approx 200 m_e$, the Bohr radius of the μp atom is approximately 200 times smaller than that of the hydrogen atom. The large mass of the muon also makes the capture process kinematically possible, unlike electron capture on an isolated proton. The muon in a μp atom disappears predominantly through decay into an electron and two neutrinos,

$$\mu^- \rightarrow e^- + \overline{\nu}_e + \nu_\mu, \tag{1.2}$$

at the same rate (aside from a small bound-state correction) as positive muon decay, $\lambda_\mu^+ \approx 455000\ \text{s}^{-1}$. Process 1.1, for a μp in the state with total spin $F = 0$, occurs at the predicted rate $\Lambda_S \approx 700\ \text{s}^{-1}$, about 0.15% of the of the muon decay rate.

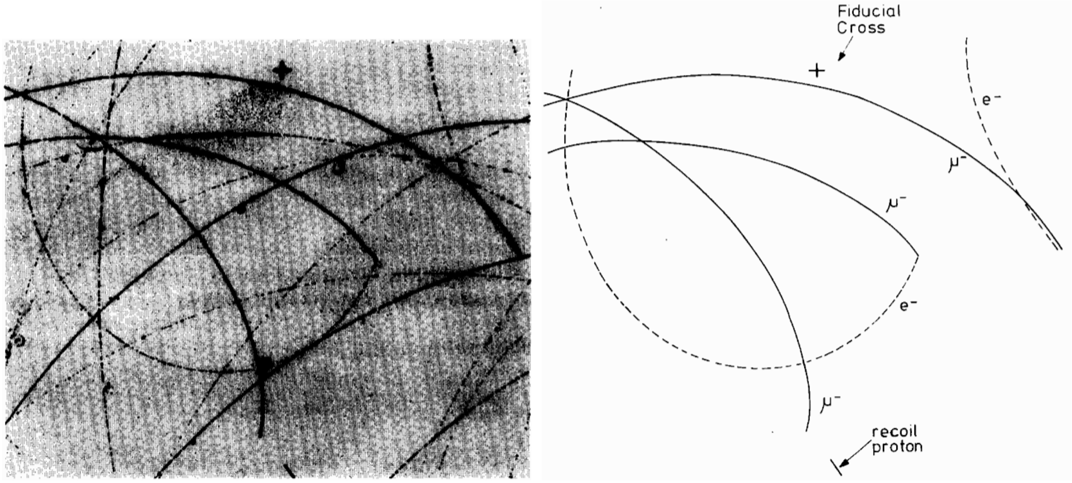

(a) Photograph. (b) Sketch.

Figure 1.1: (from Ref. [1]) Example photograph and accompanying sketch of muon stops in a liquid hydrogen bubble chamber. Three muons, identified as such by their curvature and range, entered from the upper left edge of the fiducial region shown in the image. Two of the muons decayed into electrons, while the third (stopped in the lower part of the region) did not have a decay electron track. The short line segment some distance from the stop was interpreted, based on its range and angle, as a proton recoil induced by the 5.2-MeV neutron from muon capture on the proton.

Experiments to measure the capture rate on the proton involve stopping muons in a hydrogen target to prepare the muon–proton bound state. Compared to muons on any other nucleus including other isotopes of hydrogen, the binding energy of the μp is the smallest. Muon transfer rates away from the proton to isotopic or elemental impurities in the hydrogen target are high, setting strict purity requirements. The all-neutral final state of capture on the proton makes direct detection difficult. A survey of previous measurements will help explain important experimental challenges.

1.2 Previous Measurements of Muon Capture in Hydrogen

1.2.1 Early Observations

The first direct observation of muon capture in hydrogen, reported by Hildebrand in 1962 [2], was based on stopping negative muons in a liquid hydrogen bubble chamber. An incident muon was identified by its range in hydrogen and the curvature of its track in the 20 kG applied field. Muon capture on the proton was identified by two characteristics: 1) the absence of a decay-electron track, and 2) the appearance of a short track, some distance from the muon stop position and consistent with a recoil proton from $n+p$ scattering, where n is the 5.2-MeV neutron originating from the muon stop position. The example bubble-chamber event in Fig. 1.1 is copied from the review by Mukhopadhyay [1], who credits Hildebrand for the photograph. Hildebrand notes [2] that the cut on neutron energy, effected through kinematic requirements (range and angle) on the recoil proton, were important to reduce a large contribution from low-energy background neutrons. Many photographs were analyzed: out of $N_{\text{stop}} = 2.35 \times 10^3$ muon stops, $N_{\text{rec}} = 26 \pm 7.2$ were identified as resulting in muon capture on the proton. The efficiency ϵ to detect a recoil proton from the 5.2-MeV neutron was reported to be $\epsilon = 0.120$. The rate of muon capture on the proton was thus determined:

$$\Lambda_c = \frac{N_{\text{rec}}}{\epsilon N_{\text{stop}}} = 420 \pm 120 \text{ s}^{-1}. \tag{1.3}$$

This result, Hildebrand explains, first of all confirms that muon capture does occur in liquid hydrogen, and second, the rate is consistent with the $V-A$ theory while ruling out the $V+A$ version. The target conditions of this early measurement were not ideal due to relatively high concentrations of deuterium ($c_d = 22 \pm 2$ ppm) and $Z > 1$ impurities (c_Z up to 1 ppm); however, improvements were anticipated.

A series of measurements in liquid hydrogen followed, employing targets of higher purity (both isotopically and elementally), and some recording higher statistics via external neutron counters. In these experiments the predominant initial state in the capture process was the $p\mu p$ molecule, which formed quickly at the high density of liquid hydrogen. Interpretation of the capture rate in terms of basic physical parameters is hampered in particular by uncertainty in the transition rate λ_{op} from the ortho $p\mu p$ molecular state, which is the one initally formed, to the lower-energy para $p\mu p$ molecular state, in which the capture rate is approximately three times lower than in the ortho state. Dependence on knowledge of λ_{op} can be avoided by reducing the hydrogen density, such that the molecular formation rate is low and most captures occur from the μp atomic state.

1.2.2 Ordinary Muon Capture in Hydrogen Gas

The first measurement of muon capture on the proton designed to eliminate molecular formation employed a pressure vessel filled with deuterium-depleted hydrogen (protium) at

8 atm pressure and room temperature. The experiment is summarized here following the description by Alberigi Quaranta *et al.* in their Physical Review article published in 1969 [3].

The number N_n of detected neutrons from the capture process was measured, and the singlet capture rate was determined from [3]

$$\Lambda_S^{\text{expt}} = \lambda_0 \frac{N_n}{N_\mu \epsilon_n} l \left(1 + \frac{N_n l}{N_\mu \epsilon_n} \right), \tag{1.4}$$

where N_μ is the number of muons stopped in the gas, λ_0 is the muon decay rate in the absence of capture, $l = 1.01$ is a correction factor for the small amount of molecular formation, and ϵ_n is the overall neutron detection efficiency. The experiment had to cope with backgrounds from several sources. Experimental challenges, and the ways they were overcome, include the following:

1. Captures on impurities in the gas. The transfer rate of the muon from μp to any impurity atom is high, and the capture rate is much higher on $Z > 1$ nuclei than on the proton. The target gas was cycled through a Pd filter on a daily basis to maintain impurities at a level of less than 1 ppm.

2. Bremsstrahlung γ-rays from decay electrons. The muon is $\sim 10^3$ times more likely to decay into an electron than capture on the proton in a μp atom, and γ's produced by the decay electrons have the same time distribution as neutrons from the μp capture process. Pulse-shape discrimination was used to distinguish neutrons from photons, and the authors note this selection "turned out to be essential."

3. External sources (flat background). The flat background was measured and subtracted from the data.

4. Captures from muons that stop in wall material. The spatial distribution of muon stops in the target is very broad due to the low density of the hydrogen gas. It is unavoidable that some stop in wall material of a practically-sized pressure vessel containing the hydrogen. The solution was to delay neutron counting by 0.8 μs, by which time muons that stopped directly in the stainless-steel walls had disappeared through capture.

5. Diffusion of the μp, by as much as ~ 3 mm, into wall material and subsequent capture. Delaying the start-time of neutron counting does not help, since diffusion into walls by μp atoms formed nearby takes place over an extended time. Studies indicated

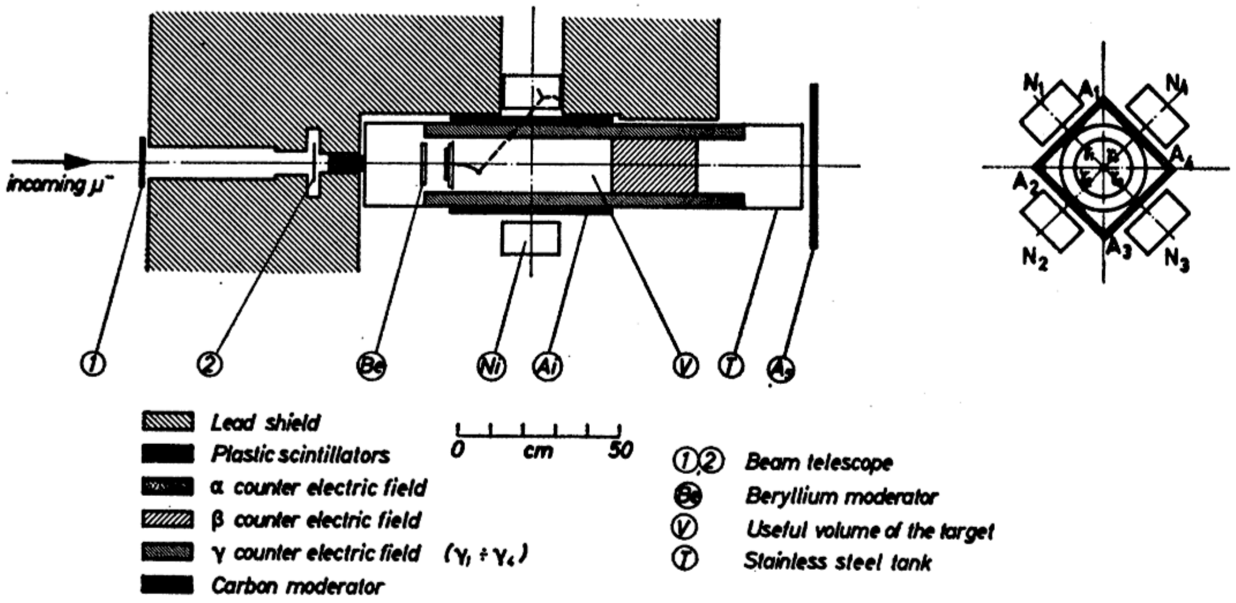

Figure 1.2: (from Ref. [3], legend rearranged) "Simplified scheme of the experimental arrangement used to measure the nuclear capture rate of negative muons by free protons in a gaseous target."

> that as many as 2% of all muon stops within the volume could diffuse into the walls, which would completely swamp the desired measurement. The solution was a series of proportional counters, covering the interior surface of the pressure vessel and operating on the protium gas itself, to veto muons that stop within 4.4 cm from the walls.

A diagram (from Ref. [3]) of the experimental apparatus is shown in Fig. 1.2. The key challenge was to count only the events in which muons stopped within the pressure vessel and well-away from any $Z > 1$ material. The proportional counters (PC's) designed for this purpose are named α, β, and γ, and their active regions are indicated in the diagram. PCα, inside the vessel at the upstream end, detected incident muons. PCβ was at the downstream end to detect muons that stopped too far downstream. The wires of PCγ ran parallel to the beam axis and were evenly spaced at a constant diameter from the centerline. This defined an active region between the inner pressure vessel wall and a coaxial cylinder composed of stainless-steel ground wires positioned $\approx$ 4 cm within the vessel wall. The fiducial volume V was specified in the logic by $\alpha\bar{\beta}\bar{\gamma}$; it comprised a cylinder of hydrogen gas 491 mm long and 172 mm in diameter, separated from the vessel wall by 4.4 cm. Since wires of the proportional counters defined the surface of V, it was possible for muons to stop directly in or diffuse into these wires without being detected. By the time counting started, 0.9 μs after the muon

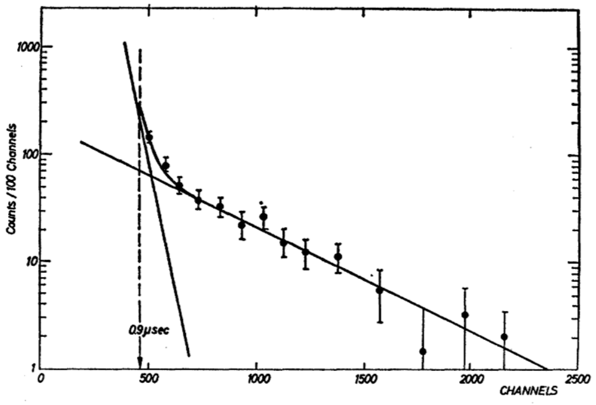

Figure 1.3: (from Ref. [3]) “Experimental time distribution of the neutron events after subtraction for the accidentals. The two straight lines correspond to the two components with 0.2 μs (iron events) and 2.2 μs (hydrogen events) lifetime. The TPHC figure was 2.95 ns/channel. The arrow shows the time cut used in the analysis.”

entrance, most muons that stopped directly in iron (stainless steel) had captured. The effect of remaining neutrons from capture on iron are visible in the neutron time spectrum shown in Fig. 1.3. The time spectrum was fit with the sum of two exponential decay curves to extract the number of events with the ≈ 2.2 μs lifetime, which were attributable to stops in hydrogen. They found the number of neutrons from muon capture on the proton to be $N_n = 315 \pm 23$ [3].

In addition to selecting events prepared in the μp atomic state, the further information required to apply Eq. 1.4 are the relevant number N_μ of μp atoms examined and the overall efficiency ϵ_n to detect any neutrons resulting from these N_μ atoms. A modified version of Eq. 1.4 was used [3]:

$$\Lambda_S^{\mathrm{expt}} = \lambda_0 \frac{N_n \epsilon_e}{N_e \epsilon_n} l \left(1 + \frac{N_n \epsilon_e l}{N_e \epsilon_n} \right), \tag{1.5}$$

in which N_μ is replaced (to a good approximation) with the number N_e of observed decay electrons from stops in V, divided by the overall efficiency ϵ_e to detect these electrons. The electrons were counted with the same detectors used for neutron counting but running in a charged-particle-selection mode. Neutron-counting and electron-counting data were taken alternately, and N_e was normalized to the same number M^*_{tot} of “master trigger” events (beam muons defined by coincidence of scintillation counters 1 and 2) as were present in the neutron-counting data. The result was $N_e = (5.07 \pm 0.05) \times 10^5$ (per M^*_{tot} master triggers), with an additional background level of 2%.

Evaluation of the overall efficiencies of neutron detection (ϵ_n) and of electron detection

(ϵ_e) required Monte Carlo calculations, which included models of beam distributions, multiple scattering, and detector acceptances and responses. In the case of ϵ_e, the acceptance solid angle Ω_e was calculated to be 12%, and the detector efficiency W for electrons had been determined experimentally to be $W = (74 \pm 2)\%$. The calculation of ϵ_n depended on details of the neutron counter and the various materials in the experimental apparatus. The result was $\epsilon_n = (3.90 \pm 0.15)\%$, and the authors note that the uncertainty was estimated by varying model parameters in the calculation.

In summary, the first measurement of muon capture in hydrogen gas reported [3] $N_n = 315 \pm 23$, $\epsilon_n = (3.90 \pm 0.15)\%$, $N_e = (5.07 \pm 0.05) \times 10^5$, $\epsilon_e = \Omega_e W = (8.88 \pm 0.27)\%$, leading to the result via Eq. 1.5 (with $l = 1.01$) of

$$\Lambda_S^{\text{expt}} = 651 \pm 57 \text{ s}^{-1}. \tag{1.6}$$

Although the total number of beam muons was reported to be $\approx 4.5 \times 10^9$, the fiducial cuts and low detector efficiencies reduced this to an effective number of μp observed of approximately $\epsilon_n N_e/\epsilon_e = 2.2 \times 10^5$. The uncertainty in the result appears to be statistics dominated (by $1/\sqrt{N_n}$) for a final precision of 7.3%, but uncertainties in the overall neutron and electron detection efficiencies are not far behind at 3.8% and 3.0%, respectively.

An independent measurement of muon capture in hydrogen gas at 41-atm pressure was reported a few years later by Bystritski\u{i} *et al.* [4]. Their measurement also involved detection of the 5.2-MeV neutrons, but they did not have proportional counters within the hydrogen volume to define stops away from the walls. Diffusion of μp into the walls was therefore significant, contributing, they report, a background of 20–30%. Special studies of this background were undertaken in order to accurately remove these events from the data. They reported a μp capture rate of $\Lambda_S = 686 \pm 88 \text{ s}^{-1}$ based on “278 ± 33 events of this type.” The uncertainty in Λ_S of 13% appears to be dominated by systematic uncertainties.

1.2.3 Ordinary Muon Capture in Liquid Hydrogen

The most accurate measurement of muon capture in hydrogen prior to the MuCap experiment utilized the lifetime technique to measure the capture rate in liquid hydrogen. The disappearance rates λ_μ^- of the μ^- and λ_μ^+ of the μ^+ were measured, and (apart from some small corrections) the capture rate Λ_c was given by

$$\Lambda_c = \lambda_\mu^- - \lambda_\mu^+; \tag{1.7}$$

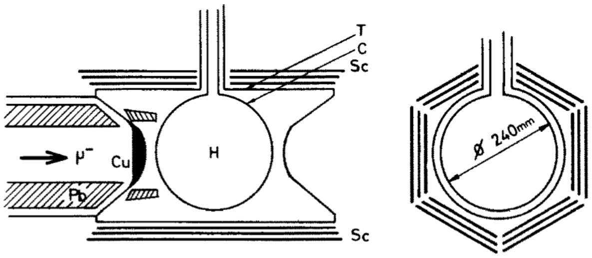

Figure 1.4: (from Ref. [5], an experiment to measure muon capture in liquid hydrogen) "Simplified scheme of the experimental arrangement: Pd = lead collimator; Cu = copper degrader; C = copper vessel; T = steel chamber; SC = plastic scintillator telescopes."

that is, the higher disappearance rate of the μ^- compared to the μ^+ is attributed to capture on the proton. The experiment, performed at Saclay in 1980 and described in an article by Bardin *et al.* [5] (with some additional details in Ref. [6]), is quite different than the measurement in hydrogen gas described above. The high density and low temperature (22 K) of the liquid hydrogen target each sharply reduce the diffusion length of μp atoms. This fact, combined with the narrower stopping distribution of muons obtainable in the denser target, rendered unnecessary the proportional counters of the gas experiment. Instead, the approach was to avoid muon stops in low-Z materials except hydrogen and delay electron counting until most muons on high-Z materials had disappeared. Since it was a lifetime measurement, the detector efficiencies did not need to be known absolutely, thus circumventing a key difficulty in the neutron counting experiments.

The liquid hydrogen was required to be of extremely high purity, both in terms of $Z > 1$ elements and deuterium. Careful preparation of the sample volume, and filling the hydrogen into the volume through a palladium filter, reduced $Z > 1$ impurities to the required level of 10^{-8} (as deduced by tests with the Pd filter [6]). Continued outgassing from the sample volume walls, a typical problem in very clean systems, was expected to be negligible because of the the low temperature of the target. A deuterium concentration of $c_d = 2.7 \pm 0.1$ ppm was reported based on mass spectrometer analysis; this amount turned out to be non-negligible, and a correction of -18 ± 4 s^{-1} to λ_μ^- was required.

A diagram of the experimental apparatus is shown in Fig. 1.4. The electron detectors were scintillator tiles arranged into six independent electron telescopes of three layers each. The authors state that 90% of incident muons stop in hydrogen, 10% in copper or lead, and stops in plastic (scintillator) or other low-Z material were fewer than 10^{-4} per incident muon. The beam was structured: a 3-μs-long burst arrived every 330 μs. Each data-taking interval was gated to begin 1 μs after the end of a beam burst and last 65 μs, and detector times were relative the start time of the gate. Only the time of the first three-fold coincidence in a given beam telescope was recorded per gate; in about 10% of the gate periods, a subsequent hit in the same detector occurred and triggered a pileup condition, according to which the data from that period were discarded (referred to as "multiple rejection" in [5]). A correction to the lifetime result for residual pileup — in particular from events in which a subsequent electron was missed due to detector deadtime or inefficiency — was effected by a zero-extrapolation procedure, in which special runs with high beam rate were taken to observe the change in lifetime compared to the production data with lower beam rate. The corrections for residual pileup were $-55\ \mathrm{s}^{-1}$ to λ_μ^- and $-100\ \mathrm{s}^{-1}$ to λ_μ^+, the latter of which apparently had a somewhat higher beam rate. The λ_μ^+ measurement used a sulfer target to depolarize the μ^+, which otherwise could have exhibited distortions in its decay time spectrum due to a combination of spin precession and detector asymmetries.

The reported results, in terms of lifetimes τ_μ, are $\tau_\mu^- = 2194.903 \pm 0.066$ ns and $\tau_\mu^+ = 2197.182 \pm 0.121$ ns. The capture rate is then $\Lambda_c^{\mathrm{expt}} = 467 \pm 29\ \mathrm{s}^{-1}$, in which a relativistic correction to the μ^- decay rate is included ($+12\ \mathrm{s}^{-1}$ [7], due to the μ^- orbital motion) as well as the correction for deuterium ($-18 \pm 4\ \mathrm{s}^{-1}$). The authors also report Λ_c based on the world average μ^+ lifetime updated with τ_μ^+ from their experiment. The present world average for this value, some 25 years later, is much more precise: $\tau_\mu^+ = 2197.019 \pm 0.021$ ns [8]. The resulting capture rate in the Saclay experiment is then

$$\Lambda_c^{\mathrm{expt}} = 433 \pm 15\ \mathrm{s}^{-1}. \tag{1.8}$$

The interpretation of Λ_c in terms of Λ_S is dependent on the rate λ_{op} of the ortho-para transition of the $p\mu p$ molecule. This fact was forseen, and a followup experiment was designed to constrain λ_{op}. The result was $\lambda_{\mathrm{op}}^{\mathrm{Ex1}} = (4.1 \pm 1.4) \times 10^4\ \mathrm{s}^{-1}$ [9], somewhat lower than the theoretical prediction of $\lambda_{\mathrm{op}}^{\mathrm{Th}} = (7.1 \pm 1.2) \times 10^4\ \mathrm{s}^{-1}$ [10]. The situation was further aggravated by a more recent measurement yielding the result $\lambda_{\mathrm{op}}^{\mathrm{Ex2}} = 11.7 \pm 1.7^{+0.9}_{-0.6}\ \mathrm{s}^{-1}$ [11], which is inconsistent with both theory and the previous measurement.

1.2.4 Radiative Muon Capture in Liquid Hydrogen

Radiative muon capture (RMC) on the proton,

$$\mu + p \rightarrow \nu_\mu + n + \gamma, \tag{1.9}$$

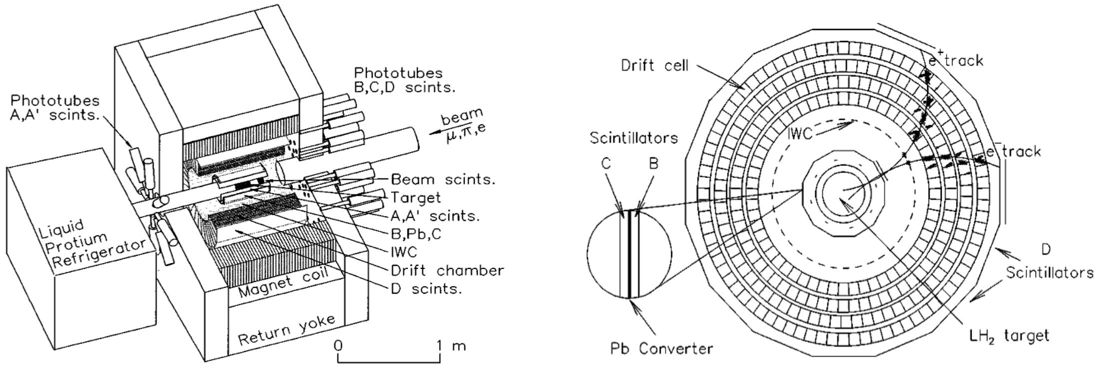

(a) The RMC pair spectrometer at TRIUMF. (b) X-Y view of converted photon event.

Figure 1.5: (both from Ref. [14]) Diagrams of the apparatus used to measure photons from radiative muon capture (RMC) in liquid hydrogen.

is $\sim 10^{-8}$ times as likely as muon decay for photon energies $E_\gamma > 60$ MeV. Above this energy the photon spectrum is sensitive to the pseudoscalar coupling g_p; therefore this process is another way to experimentally determine g_p, though the theoretical treatment is not as straightforward as in ordinary muon capture on the proton (see e.g. [12]).

A first measurement of the rare process of RMC on the proton was reported by G. Jonkmans *et al.* in 1996 [13] and described in more detail by Wright *et al.* [14]. Muons were stopped in liquid hydrogen contained within an apparatus designed to detect the energy and time spectra of photons produced in the target. The same requirements of high purity and low deuterium concentration apply as in the ordinary muon capture experiments. Similar to the Bardin *et al.* ordinary muon capture measurement, target walls were made of high-Z materials, and timing cuts were applied to remove photons from RMC captures on high-Z nuclei from the data. Likewise the enormous background of photons produced in nuclear capture of negative pions (a beam contaminant) was eliminated by cutting events prompt with particle entrances. Photons were detected after their conversion in lead to e^+e^- pairs: a spectrometer tracked these charged particles in an applied magnetic field, such that the photon energy could be inferred by the curvatures of the tracks (Fig. 1.5). Some of the copious bremsstrahlung photons, produced by electrons from muon decay with a maximum energy of $m_\mu/2 \approx 53$ MeV, "leaked" into the energy spectrum above 60 MeV due to resolution effects (Fig. 1.6a); as Wright *et al.* explain, this was the largest background after all analysis cuts, and it was subtracted based on the photon spectrum observed when μ^+ (which do not capture) were stopped in the target.

Comparison of the experimental RMC photon spectrum required knowledge of the de-

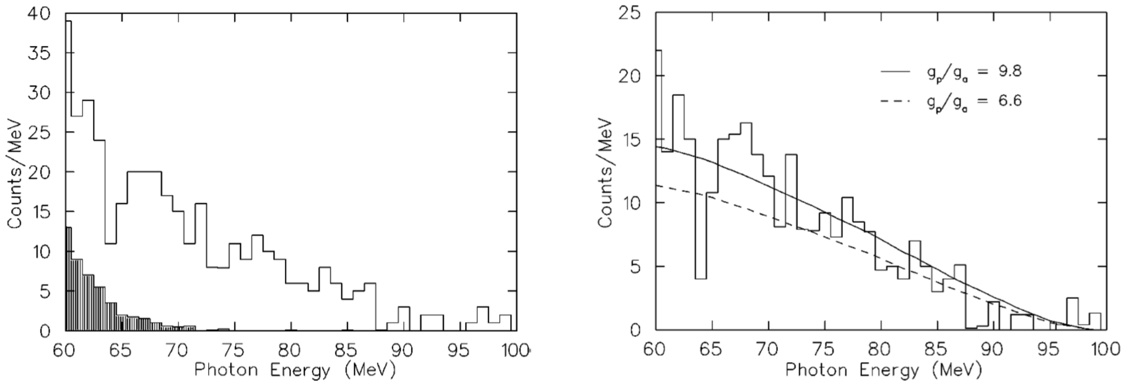

Figure 1.6: Results from the radiative muon capture experiment (both from Ref. [14]). (a) "Photon energy spectrum after all cuts and before background subtraction (unshaded) and bremsstrahlung background spectrum (shaded)." (b) "Photon energy spectrum after all cuts and background subtraction. Theoretical RMC spectra are shown for the best fit value of $g_p/g_a = 9.8$ (solid curve) and for $g_p/g_a = 6.6$ (dashed curve)."

tector response. Monte Carlo code was developed for this purpose and validated by stopping π^- in the target: the π^- stopping distribution and the known photon spectrum from π^- stopped in hydrogen were input into the computation, and the Monte Carlo results were shown to reproduce the observed spectrum. The theoretical RMC photon spectrum was calculated assuming certain values for g_p and $\lambda_{\rm op}$, and photons were generated in the virtual spectrometer with the Monte Carlo code drawing from the theoretical spectrum. These virtual data were analyzed with the same code as the real data, thus producing an RMC spectrum to compare with real data. The process was repeated for several different g_p until a best fit g_p for a given $\lambda_{\rm op}$ was obtained (Fig. 1.6b, in which $\lambda_{\rm op} = 4.1 \times 10^4$ s^{-1}). The result for g_p, over a wide range of $\lambda_{\rm op}$ values, lies significantly above the theoretical prediction. This discrepancy has not yet been explained [12].

1.3 Overview of the MuCap Experiment

The goal of the MuCap experiment is to measure the rate of ordinary muon capture in hydrogen gas to 1% precision, determining g_p to 6% precision and without ambiguities due to $\lambda_{\rm op}$. Innovative features of previous efforts are drawn upon to achieve this objective. As in the Alberigi-Quaranta *et al.* experiment [3], the target is hydrogen gas to minimize molecular formation, and a detector operating on the hydrogen gas itself defines a fiducial volume for muon stops well-away from the walls. The lifetime technique based on electron detection is employed, as in the Bardin *et al.* experiment [5], to avoid the uncertainties in absolute calibration of neutron detectors that would otherwise limit the measurement precision.

An essential, new technology of the MuCap experiment is the time projection chamber (TPC) operating with hydrogen gas. An active fiducial volume is defined by the TPC in which muons are tracked in 3-dimensions to their stop positions, without any $Z > 1$ material within the fiducial volume or on its surface. In a sense, the new TPC allows the logic to be inverted compared to the Alberigi-Quaranta *et al.* experiment: the previous experiment rejected an event if a muon stop was detected near the walls, while the present effort accepts an event only if a muon stop is positively detected away from the walls. Wires on the surface of the fiducial volume, unavoidable in the earlier experiment, are absent with the TPC. The TPC is also able to detect the recoil products of muon captures on $Z > 1$ impurities, providing *in situ* $Z > 1$ impurity monitoring of the hydrogen gas. Another innovation in this respect is a purification system that continuously cleans the hydrogen gas, maintaining a very low level of impurities over several weeks of data accumulation.

The MuCap goal of Λ_S to 1% precision requires a measurement of the muon (inverse) lifetime to $10^{-5}\,\lambda_{\mu}^{-}$, a technical challenge in itself. Electron detector acceptances, efficiencies, and background counts must be constant at this level. Many cross-checks were designed into the experiment to demonstrate accuracy of the result. A significant advantage over previous ordinary muon capture experiments is the ability to continuously record data from all detectors, independently of each another. In this way, offline data analyses can explore different detector combinations and various cuts, each of which may be expected to be more or less sensitive to certain systematic effects, to check for consistency in the final lifetime result. An additional accuracy check may be accomplished by comparing the μ^+ lifetime, measured with the MuCap electron detector, to the world average μ^+ lifetime from other experiments.

The implications, in terms of the proton's pseudoscalar coupling g_P, of a 1% precision measurement of the ordinary muon capture rate in the MuCap target is shown in Fig. 1.7 assuming different values of the ortho-para $p\mu p$ molecular transition rate λ_{op}. Also shown are the interpretations of the results from the TRIUMF radiative muon capture (RMC) and the Bardin *et al.* ordinary muon capture (OMC) experiments, both of which used liquid hydrogen. In the case of the OMC result, the dependence of g_P on λ_{op} is severe. The value of g_P implied by the RMC result is significantly higher than theory predicts over nearly the entire range of reasonable λ_{op} values. Furthermore, there is no region of mutual agreement between the OMC and RMC experiments and theory. A successful measurement

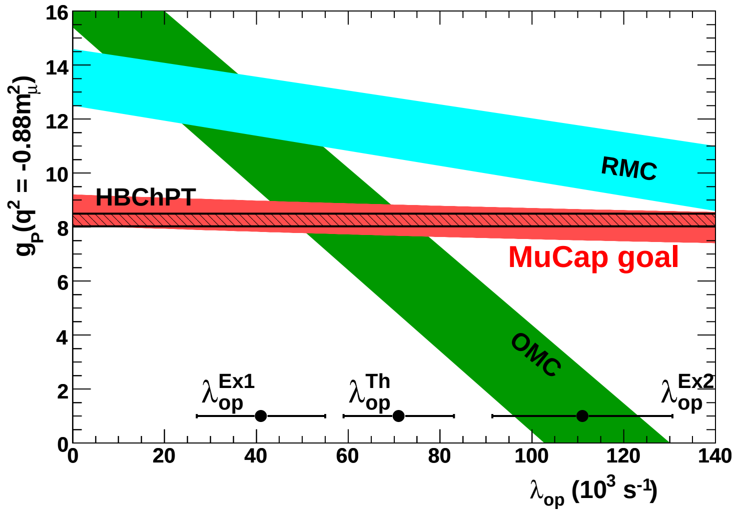

Figure 1.7: (from Ref. [15], MuCap band modified) Experimental and theoretical determinations of g_P, presented vs. the ortho–para transition rate λ_{op} of the $p\mu p$ molecule. The most precise previous OMC experiment [5] and the RMC experiment [14] both depend significantly on the value of λ_{op}, which itself is poorly known due to mutually inconsistent experimental ($\lambda_{\text{op}}^{\text{Ex1}}$ [9], $\lambda_{\text{op}}^{\text{Ex2}}$ [11]) and theoretical ($\lambda_{\text{op}}^{\text{Th}}$ [10]) results. A measurement of the OMC rate by MuCap will give a value for g_P that is nearly independent of molecular effects; here the uncertainty band corresponding to the precision goal of 1% in Λ_S is placed arbitrarily at the height of the theory prediction.

of OMC in MuCap to the design precision goal will provide an unambiguous, experimental determination of g_P that can be meaningfully compared to theory.

Chapter 2

Muon Capture Theory

2.1 Standard Model Formulation

As the momentum transfer q appropriate for muon capture is much smaller than the W boson mass m_W, i.e., $|q^2| \ll m_W^2$, the W propagator reduces to a constant factor m_W^{-2} which scales the weak coupling constant. The process is then well-described by the four-fermion interaction with Lorentz-invariant transition amplitude

$$\mathcal{M} = \frac{G_F V_{ud}}{\sqrt{2}} J^\alpha j_\alpha, \tag{2.1}$$

where J is the nucleon current (p → n), and j is the lepton current ($\mu \to \nu_\mu$); here the bare weak couplings are factored out of J and j to be included in G_F, which also contains the factor m_W^{-2} from the W-boson propagator. With the factor V_{ud} of the Cabibo-Kobayashi-Maskawa (CKM) and including conventional factors of $\sqrt{2}$, G_F is the same Fermi coupling constant familiar from muon decay ($\mu^- \to \nu_\mu + e^- + \bar{\nu}_e$) and other low-energy weak interactions. The lepton current is

$$j_\alpha = i\bar{\psi}_\nu \gamma_\alpha (1 - \gamma_5) \psi_\mu, \tag{2.2}$$

which represents purely vector-minus-axial-vector ("$V - A$") coupling of lepton states. The weak current of an individual quark is similar to that of a lepton: the only modification necessary is multiplication by the appropriate CKM matrix element (V_{ud}, factored out in Eq. 2.1) to account for the difference between the quark weak-interaction eigenstates and the mass eigenstates.

If the nucleon were similarly pointlike, in the general expression

$$J^\alpha = i\bar{\psi}_n \left(V^\alpha - A^\alpha\right) \psi_p, \tag{2.3}$$

we would have $V^\alpha = \gamma^\alpha$ and $A^\alpha = \gamma^\alpha \gamma_5$. Instead, to account for the QCD structure of the nucleon, V^α and A^α must be modified by form factors, $g_i(q^2), i = V, M, S, A, T, P,$

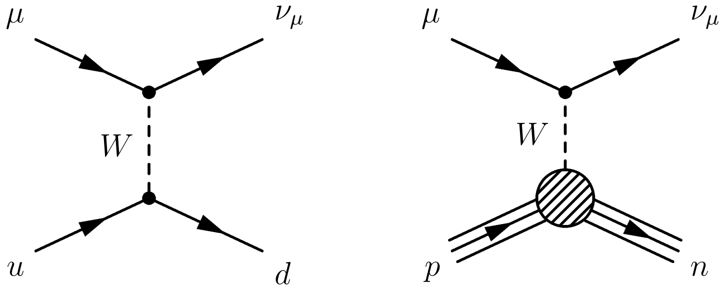

Figure 2.1: Feynman diagrams representing ordinary muon capture. Left: quark level. Right: nucleon level.

multiplying terms constructed from available Lorentz 4-vectors:

$$V^\alpha = g_V(q^2)\gamma^\alpha + i\frac{g_M(q^2)}{2m_N}\sigma^{\alpha\beta}q_\beta + g_S(q^2)q^\alpha, \tag{2.4}$$

and

$$A^\alpha = g_A(q^2)\gamma^\alpha\gamma_5 + ig_T(q^2)\sigma^{\alpha\beta}q_\beta\gamma_5 + \frac{g_P(q^2)}{m_\mu}\gamma_5 q^\alpha, \tag{2.5}$$

where the form factors may take complex values. Scaling of the g_M and g_P terms by $(2m_N)^{-1}$ and m_μ^{-1}, where m_N and m_μ are respectively the nucleon and muon mass, is by convention. In the Feynman diagrams of Fig. 2.1, representing muon capture on the quark level and nucleon level, the W-propagator has been retained for illustrative purposes.

A calculation of OMC at the quark level would require detailed knowledge of the low-energy QCD wavefunctions of the proton and neutron, and such an approach remains beyond modern capabilities. Instead, progess has been made with effective field theories (EFT's), which offer model-independent calculations of basic processes in terms of a few *a priori* undetermined "low-energy constants (LEC's)." Different physical processes are related by the same LEC's; thus, experimental data from other processes can be used to fix the LEC's, and quantitative predictions of muon capture can be made. Recent EFT calculations of muon capture on the proton are quoted below, but first the phenomenological approach is outlined, in which the nucleon is a basic particle and the various form factors are parameters that must be determined externally.

2.2 Knowledge of Nucleon Form Factors

Neglecting an overall complex phase in $\mathcal{M}$, the nucleon form factors amount to eleven parameters which must be known to calculate the rate of muon capture. Since the deviations of the form factors from their values in the absence of QCD (i.e., $g_V = g_A = 1$ and all others zero) are attributed to strong interaction effects, processes that are related by QCD-symmetric transformations of $\mathcal{M}$ are expected to have the same form factor values for a given q^2. Thus, QCD symmetries and approximate symmetries restrict the couplings in muon capture and relate them to processes measured in other experiments, in particular electron scattering off the proton and neutron, neutron β-decay, and antineutrino-neutron scattering. The important symmetry operations and their implications on the form factors are outlined below, followed by a summary of numerical values appropriate for the momentum transfer of OMC on the proton.

2.2.1 Time Reversal Invariance

The number of free parameters in equations 2.4 and 2.5 can immediately be reduced by requiring time reversal invariance of the observables, which are proportional to $|\mathcal{M}|^2$. As a consequence of this symmetry, all form factors must be relatively real [16].

2.2.2 Conserved Vector Current (CVC)

The CVC hypothesis stems from the invariance of the strong interaction under isospin rotation. That is, neglecting the small mass difference between the proton and neutron, the strong interaction is the same for a proton, a neutron, and arbitrary mixed proton-neutron states. Isospin rotations turn protons into neutrons and vice versa. As explained in the text by Commins and Bucksbaum [16, pages 165–167], CVC states that the vector part of the isospin lowering current V^α $(p \to n)$, its hermitian conjugate $V^{\alpha\dagger}$ $(n \to p)$, and the isovector portion of the electromagnetic current J_{EM}^{isov} $(N \to N)$ form an isospin triplet of conserved currents. The electromagnetic current between two proton states $|p, s\rangle$ and $|p', s'\rangle$ is written [16, Eq. 4.119]

$$\langle p', s'|J_{\mathrm{EM}}|p, s\rangle = e^{i(p'-p)\cdot x}\bar{u}(p', s')[C_p(q^2)\gamma^\alpha + iM_p(q^2)\sigma^{\alpha\nu}q_\mu + F_{3p}(q^2)q^2]u(p, s) \qquad (2.6)$$

and similarly for the current between two neutron states (with the symbol "p" in the EM form factors' subscripts changed to "n"). The scalar term $F_3(q^2)$ is shown to be zero by the conserved-current requirement, $\partial_\alpha J^\alpha_{\text{EM}} = 0$. In terms of the isovector electromagnetic form factors $C^{(1)}(q^2) = C_p(q^2) - C_n(q^2)$ and $M^{(1)}(q^2) = M_p(q^2) - M_n(q^2)$, applying CVC leads to the result [16]

$$\begin{aligned} g_V(q^2) &= C^{(1)}(q^2) = C_p(q^2) - C_n(q^2), && (2.7)\\ \frac{g_M(q^2)}{2m_N} &= M^{(1)}(q^2) = M_p(q^2) - M_n(q^2), && (2.8)\\ g_S(q^2) &= 0. && (2.9) \end{aligned}$$

2.2.3 G-parity

G-parity is the combined operation of charge conjugation and isospin rotation by π about the I_2 isospin axis, $G = Ce^{i\pi I_2}$. It is a symmetry of QCD, with violations allowed only on the level of isospin breaking. Applying G to the transition amplitude $\mathcal{M}$, it can be shown [16] that 1) g_S transforms differently than g_V and g_M; and 2) g_T transforms differently than g_A and g_P. g_S and g_T are called "second class" currents and are expected to be negligible.

2.2.4 Partially Conserved Axial Current (PCAC)

The discussion of the partially conserved axial current (PCAC) hypothesis in the text by Commins and Bucksbaum [16, pp. 169–172] is summarized in this subsection. Two minor changes are made for consistency: $g_3 \rightarrow g_P/m_\mu$, and the model reaction is OMC instead of β-decay.

The axial current A^α is conserved in the limit of zero pion mass, $\lim_{m_\pi \to 0} \partial_\alpha A^\alpha = 0$. The dominant contribution to g_P is represented by the Feynman diagram in Fig. 2.2. Other processes contribute to g_A [16]. The amplitude of the process involves the pion-nucleon coupling $g_{\pi NN}$, the pion propagator $(q^2 - m_\pi^2)^{-1}$, and the pion decay constant f_π. Reading off the terms in the diagram leads to the amplitude [16]

$$A = -V_{ud} G_F f_\pi g_{\pi NN} \frac{1}{q^2 - m_\pi^2} \bar{u}(n) q^\alpha \gamma_5 u(p) j_\alpha, \tag{2.10}$$

where u is the nucleon Dirac spinor. Comparing this with the pseudoscalar term in $\langle n|A^\alpha|p\rangle$ gives [16]

$$\frac{g_P(q^2)}{m_\mu} = -\frac{f_\pi g_{\pi NN} \sqrt{2} F(q^2)}{q^2 - m_\pi^2}, \tag{2.11}$$

in which the "slowly varying" function $F(q^2)$ is introduced to account for vertex corrections

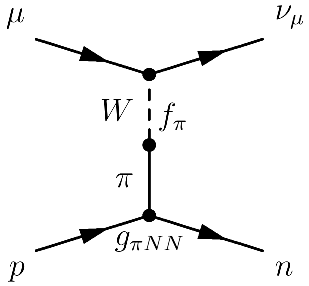

Figure 2.2: Feynman diagram representing one-pion exchange in muon capture. This is the dominant constribution to g_P at the momentum transfer q^2_{OMC}.

away from $q^2 = m_\pi^2$, where $g_{\pi NN}$ is measured. Now substitute Eq. 2.11 into the axial part of the nucleon current:

$$\langle n|A^\alpha(x)|p\rangle = e^{i(p_n - p_p)\cdot x}\bar{u}(n)\left[g_A(q^2)\gamma^\alpha - \frac{f_\pi g_{\pi NN}\sqrt{2}F(q^2)}{q^2 - m_\pi^2}q^\alpha\right]\gamma_5 u(p). \tag{2.12}$$

The partially conserved axial current hypothesis (PCAC) states that $\lim_{m_\pi\to 0}\partial_\alpha A^\alpha(x) = 0$, i.e., CAC in the limit of zero pion mass. Applying PCAC to Eq. 2.12, we have

$$0 = \lim_{m_\pi\to 0}\bar{u}(n)\left[g_A(q^2)(m_p + m_n) - \frac{f_\pi g_{\pi NN}\sqrt{2}F(q^2)}{q^2 - m_\pi^2}q^2\right]\gamma_5 u(p), \tag{2.13}$$

where the Dirac equation $(\partial_\alpha\gamma^\alpha - m)\psi(x) = 0$ has been used in the g_A term. Thus from result (Eq. 2.13) of PCAC applied to the expression (Eq. 2.12) for the axial current in which g_P is replaced with the one-pion exchange term from Fig. 2.2, and assuming $F(q^2)$ (for vertex corrections to $g_{\pi NN}$) is slowly varying $F(q^2) \approx 1$, we obtain the Goldberger-Treiman relation

$$g_A(0) \approx \frac{f_\pi g_{\pi NN}\sqrt{2}}{m_p + m_n}. \tag{2.14}$$

Equations 2.11 and 2.14 can be combined to express $g_P(q^2)$ in terms of $g_A(0)$:

$$\frac{g_P(q^2)}{m_\mu} \approx -\frac{2m_N g_A(0)}{q^2 - m_\pi^2}, \tag{2.15}$$

in which $m_N = (m_p + m_n)/2 \approx m_p$.

2.2.5 Further Information on g_P

Modern calculations of g_P use the framework of chiral perturbation theory (ChPT). The PCAC result is reproduced, and further corrections are systematically calculated in terms of small parameters (e.g., $m_\mu/m_N \sim 0.1$). Calculation to next-to-leading-order (NLO) [17] shows the correction term to Eq. 2.15 originally derived through current-algebra techniques [18]:

$$g_P(q^2) \approx -\frac{2m_\mu m_N g_A(0)}{q^2 - m_\pi^2} - \frac{1}{3} g_A(0) m_\mu m_N r_A^2, \tag{2.16}$$

where r_A is the axial radius (defined below). Higher-order (NNLO) corrections have been shown to be small [19]. We will use the value for g_P quoted in the review by Bernard *et al.* [20],

$$g_P(-0.88m_\mu^2) = (8.74 \pm 0.23) - (0.48 \pm 0.02) = 8.26 \pm 0.16, \tag{2.17}$$

in which the contributions from the PCAC and NLO terms are separated in the middle expression; the authors use the PCAC expression in terms of $g_{\pi NN}$ and f_π instead of $g_A(0)$ (related via Eq. 2.14), and the values $g_{\pi NN} = 13.10 \pm 0.35$ and $f_\pi = 92.4 \pm 0.3$ MeV.

2.2.6 Summary of Form Factor Values

We now assign numerical values to the weak form factors. At $q^2 = 0$, the electromagnetic form factor $C_p = 1$ ($C_n = 0$), and aside from a factor of the electron charge e, M_p (M_n) is the anomalous magnetic moment of the proton (neutron), $\kappa_p{-}1$ ($\kappa_n{-}0$). The proton and neutron magnetic moments are $\kappa_p = (2.792847351 \pm 0.000000028)\mu_N$ and $\kappa_n = (-1.91304273 \pm 0.00000045)\mu_N$ [21], respectively, where $\mu_N = e\hbar/2m_p$ is the nuclear magneton. Then the weak vector form factor is $g_V(0) = 1$, and the weak magnetic form factor is $g_M(0) = (\kappa_p - 1 - \kappa_n)/\mu_N$. The q^2-dependences of g_V and g_M are determined by electromagnetic electron-proton and electron-neutron scattering experiments. For sufficiently low energies, the dependence of an electromagnetic form factor F is parameterized by

$$F(q^2) = F(0)\left(1 + \frac{q^2}{6}\langle r^2\rangle\right), \tag{2.18}$$

where $\langle r^2\rangle$, called the "charge radius" of the form factor, is from fits to scattering data. A global fit to electromagnetic scattering data finds the radii $r_1^v = 0.765$ fm for $C^{(1)}$ and $r_2^v = 0.893$ fm for $M^{(1)}$ [22], each reported with an uncertainty of 1%. Equation 2.18 is applied directly to g_V and g_M with these radii.

	Value at $q^2 = 0$	Value at $q^2 = -0.88 m_\mu^2$	Comment
g_V	1	0.9755 ± 0.0005	Electron scattering and CVC
g_M	$3.70589008 \pm 0.00000045$	3.5821 ± 0.0025	Electron scattering and CVC
g_A	1.2695 ± 0.0029	1.24689 ± 0.0036	Neutron β-decay asymmetry
g_P		8.26 ± 0.16	PCAC with NLO term from ChPT
V_{ud}	0.97377 ± 0.00027	0.97377 ± 0.00027	Superallowed ($0^+ \to 0^+$) nuclear β-decay

Table 2.1: Summary of parameters relevant to the calculation of the muon capture rates Λ_S and Λ_T.

The weak axial form factor $g_A(0)$ is set from the current world average of measurements of the neutron β-decay asymmetry parameter, $\lambda \equiv -g_A(0)/g_V(0) = -1.2695 \pm 0.0029$ [21]. The $g_A(0)$ from beta decay is evolved to larger momentum transfers by applying Eq. 2.18, with an axial charge radius r_A — determined from fits to (anti) neutrino scattering data — of $\langle r_A^2 \rangle = 0.42 \pm 0.04\ \text{fm}^2$ [23].

Besides well-known fundamental constants such as the Fermi constant G_F and particle masses, the remaining parameter required for quantitative predictions of OMC on the proton is the CKM matrix element V_{ud}. Recent improvements in the calculation of electroweak radiative corrections to superallowed nuclear beta decays ($0^+ \to 0^+$ transitions) allows a precise value of V_{ud} to be extracted: $V_{ud} = 0.97377(27)$ [24].

2.3 Phenomenological Calculation

The treatment of ordinary muon capture in this section follows that in the texts by Commins [25] and (with fewer details) Commins and Bucksbaum [16]. It is a non-relativistic expansion of the Lagrangian to first order in the nucleon recoil velocity v_{nucleon}/c. The coupling constants g_i in what follows are the form factors $g_i(q^2)$ evaluated at the momentum-transfer q^2_{OMC} appropriate for OMC, i.e., $g_i \equiv g_i(q^2_{\text{OMC}})$. The sign conventions of these couplings vary in the literature; they are defined above in Eqs. 2.3–2.5 such that g_V, g_M, g_A, and g_P are positive.

2.3.1 Wavefunctions

The wavefunction of each particle is a solution to the Dirac equation,

$$(\partial_\alpha \gamma^\alpha - m)\psi(x) = 0, \tag{2.19}$$

where m is the mass of the particle. The nucleon may be considered as well-localized both before and after the capture reaction. In terms of Pauli matrices $\vec{\sigma} \equiv (\sigma_1, \sigma_2, \sigma_3)$ and bi-spinors χ, we have the following for the proton wavefunction:

$$\psi_p(x) = e^{-iE_p t}\psi_p(\vec{x}) = e^{-iE_p t}\begin{pmatrix} \chi_p(\vec{x}) \\ \frac{\vec{\sigma}_A \cdot \vec{p}_p}{2m_N}\chi_p(\vec{x}) \end{pmatrix}; \tag{2.20}$$

the subscript p labels the proton, m_N is the mass of the nucleon, which will be taken as the average of the p and n mass, and the subscript A on the Pauli matrices vector is to remind us that these matrices operate on the nucleon spinors. The neutron wavefunction $\psi_n(x)$ is given by the same expression with the subscript p replaced by n to indicate the neutron. The outgoing neutrino may be written as a plane wave ($m_\nu \approx 0$):

$$\psi_\nu(x) = e^{-iE_\nu t}\psi_\nu(\vec{x}) = \frac{1}{\sqrt{2}}e^{-iE_\nu t}e^{i\vec{p}_\nu \cdot \vec{x}}\begin{pmatrix} \chi_\nu \\ \vec{\sigma} \cdot \vec{p}_\nu \chi_\nu \end{pmatrix}, \tag{2.21}$$

where σ with no subscript reminds us that the matrix acts on the lepton spinor.

The muon is in a bound state with the much heavier proton, and its wavefunction is similar to that of the electron in the hydrogen atom:

$$\psi_\mu(x) = e^{-iE_\mu t}\psi_\mu(\vec{x}) = e^{-iE_\mu t}\phi_\mu(\vec{x})\begin{pmatrix} \chi_\mu \\ 0 \end{pmatrix}, \tag{2.22}$$

$$\phi_\mu(\vec{x}) = \frac{1}{\sqrt{\pi a_0^3}}e^{-r/a_0}, \tag{2.23}$$

where $r = |\vec{x}|$ and the Bohr radius, in terms of the reduced mass $m' = m_\mu m_p/(m_\mu + m_p)$ of the proton-muon system and the fine-structure constant α, is $a_0 = 1/(m'\alpha)$.

2.3.2 Kinematics

The total 4-momentum p_i of the initial state is the sum of the muon and proton rest mass, plus the muon-atomic binding energy $-\alpha^2 m'/2$; the final state 4-momentum p_f is the sum of neutrino and neutron 4-momenta. The 4-momenta of the particles are the following:

$$p_p = \begin{pmatrix} m_p \\ \vec{0} \end{pmatrix}, \quad p_\mu = \begin{pmatrix} m_\mu - \alpha^2 m'/2 \\ \vec{0} \end{pmatrix}, \tag{2.24}$$

$$p_n = \left(\begin{array}{c} \sqrt{m_n^2 + |\vec{p}_n|^2} \\ \vec{p}_n \end{array} \right) \quad p_\nu = \left(\begin{array}{c} E_\nu \\ E_\nu \hat{p}_\nu \end{array} \right). \tag{2.25}$$

In the spatial components of the neutrino 4-momentum vector, a unit vector $\hat{p}_\nu$ in the direction of $\vec{p_\nu}$ is introduced. Conservation of 3-momentum requires $\vec{p}_n = -E_\nu \hat{p}_\nu$, and we are left with the energy conservation equation and its solution for E_ν:

$$\sqrt{s} \equiv m_p + m_\mu - \alpha^2 m'/2 = \sqrt{m_n^2 + E_\nu^2} + E_\nu \Rightarrow E_\nu = \tfrac{s - m_n^2}{2\sqrt{s}}. \tag{2.26}$$

The momentum transfer squared of the reaction is $q^2_{\mathrm{OMC}} \equiv (p_n - p_p)^2 = -0.876 m_\mu^2$, which is expressed in terms of the muon rest mass.

2.3.3 Transition Rate

The differential transition probability per unit time is [25]

$$dW = \frac{2\pi\delta(E_p - E_n + E_\nu - m_\mu) d^3\vec{p}_\nu}{(2\pi)^3} |A|^2, \tag{2.27}$$

where the transition amplitude is

$$A = \frac{1}{\sqrt{2}} G_F V_{ud} \int d^3\vec{x} \bar{\psi}_n(\vec{x}) \hat{\mathcal{O}} \psi_p(\vec{x}), \tag{2.28}$$

with

$$\hat{\mathcal{O}} = g_V \gamma^\alpha j_\alpha + i\frac{g_M}{2m_N}\sigma^{\alpha\beta} q_\beta j_\alpha - g_A \gamma^\alpha \gamma_5 j_\alpha - \frac{g_P}{m_\mu}\gamma_5 q^\alpha j_\alpha, \tag{2.29}$$

and lepton current

$$j_\alpha(\vec{x}) = \bar{\psi}_\nu(\vec{x}) \gamma_\alpha (1 - \gamma_5) \psi_\mu(\vec{x}). \tag{2.30}$$

Substituting in the expressions for the muon and electron wavefunctions and using the Dirac representation of the gamma matrices gives the following “two-component” reduction of the lepton current:

$$j_0 = \frac{1}{\sqrt{2}} \chi_\nu^\dagger (1 - \vec{\sigma} \cdot \hat{p}_\nu) \chi_\mu e^{-i\vec{p}_\nu \cdot \vec{x}} \phi_\mu(\vec{x}) \tag{2.31}$$

$$\vec{j} = \frac{-1}{\sqrt{2}} \chi_\nu^\dagger (1 - \vec{\sigma} \cdot \hat{p}_\nu) \vec{\sigma} \chi_\mu e^{-i\vec{p}_\nu \cdot \vec{x}} \phi_\mu(\vec{x}) \tag{2.32}$$

Similar two-component reduction of the nucleon wavefunctions leads, after some algebra and dropping terms of second order in the nucleon recoil ($(v_{\mathrm{nucleon}}/c)^2 \sim (m_\mu/m_N)^2 \approx 1\%$), to an expression for the amplitude A in terms of 2-spinors and Pauli matrices [25]

$$\begin{aligned} A &= \frac{1}{2}\int d^3\vec{x}e^{-i\vec{p}_\nu\cdot\vec{x}}\phi_\mu(\vec{x})\chi_n^\dagger\chi_\nu^\dagger\mathcal{H}_{eff}\chi_\mu\chi_p, &(2.33)\\ \mathcal{H}_{eff} &= (1-\vec{\sigma}\cdot\hat{p}_\nu)(G_V+G_A\vec{\sigma}_A\cdot\vec{\sigma}+G_P\vec{\sigma}_A\cdot\hat{p}_\nu), &(2.34)\end{aligned}$$

The parameters in the effective Hamiltonian are defined in terms of the original couplings as follows:

$$\begin{aligned} G_V &= G_FV_{ud}g_V\left(1+\frac{E_\nu}{2m_N}\right), &(2.35)\\ G_A &= G_FV_{ud}\left(g_A+\frac{E_\nu}{2m_N}(g_M+g_V)\right), &(2.36)\\ G_P &= G_FV_{ud}\frac{E_\nu}{2m_N}\left(-\frac{E_\nu}{m_\mu}g_P+g_V-(g_V+g_M)\right). &(2.37)\end{aligned}$$

The spatial integral in equation 2.33 is simplified by noting that the neutrino wavefunction does not vary much over the extent of the nucleon: the plane-wave term in the integrand may be replaced by 1. The nucleon is considered as small and well-localized at the origin, so the muon orbital function is replaced with its value at $\vec{x}=0$. Some authors [26] include an overlap factor $C_p \approx 1$ to account for the nonzero extent of the nucleon. Thus we have the simplified expression for A:

$$A = \frac{1}{2}C_p\phi_\mu(0)\chi_n^\dagger\chi_\nu^\dagger\mathcal{H}_{eff}\chi_\mu\chi_p. \tag{2.38}$$

The quantity of interest in the transition rate is the amplitude squared,

$$A^\dagger A = \frac{1}{4}C_p^2\phi_\mu^2(0)\chi_\mu^\dagger\chi_p^\dagger\mathcal{H}_{eff}^\dagger\mathcal{H}_{eff}\chi_\mu\chi_p, \tag{2.39}$$

where we have used the completeness of the sum over final spins, $\Sigma\chi\chi^\dagger = 1$.

The total transition rate is the integral of equation 2.27 over the neutrino phase space. Using $d^3\vec{p}_\nu = E_\nu^2 dE_\nu d\Omega_\nu$, where $d\Omega_\nu$ is the solid-angle element of neutrino direction $\hat{p}_\nu$, and doing the integral over E_ν leads to

$$W = \frac{1}{4\pi}\frac{E_\nu^2}{1+E_\nu/\sqrt{m_n^2+E_\nu^2}}C_p^2\phi_\mu^2(0)\int\frac{d\Omega_\nu}{4\pi}\chi_\mu^\dagger\chi_p^\dagger\mathcal{H}_{eff}^\dagger\mathcal{H}_{eff}\chi_\mu\chi_p, \tag{2.40}$$

Integration over the neutrino direction, with the aid of several Pauli matrix identities, gives finally an explicit expression for the total transition rate [25]:

$$W = \frac{C_p^2}{2\pi^2 a_0^3}\frac{E_\nu^2}{1+E_\nu/\sqrt{m_n^2+E_\nu^2}}G_V^2(1+3\eta)\left(1-\frac{\langle\vec{\sigma}\cdot\vec{\sigma}_A\rangle\xi}{1+3\eta}\right), \tag{2.41}$$

where

$$\eta = \frac{1}{G_V^2}\left(G_A^2+\frac{1}{3}(G_P^2-2G_AG_P)\right), \tag{2.42}$$

$$\xi = 2\frac{1}{G_V^2}\left(G_A^2+\frac{1}{3}G_VG_P-G_VG_A-\frac{2}{3}G_AG_P\right), \tag{2.43}$$

and the neutrino energy E_ν was given earlier in equation 2.26. The term in angle brackets represents the expectation value in the initial μp state, which is $\langle\vec{\sigma}\cdot\vec{\sigma}_A\rangle_{F=0} = -3$ in the singlet state, or $\langle\vec{\sigma}\cdot\vec{\sigma}_A\rangle_{F=1} = 1$ in the triplet state. Putting in values for all physical constants and form factors, including an overlap factor of $C_p = 0.9956$ [26], and dividing by $\hbar$ to get the rate in inverse seconds, we have the singlet and triplet capture rates

$$W_{F=0} = 689.5\ \mathrm{s}^{-1},\quad W_{F=1} = 11.3\ \mathrm{s}^{-1}. \tag{2.44}$$

2.4 Chiral Perturbation Theory Calculations

The modern way to calculate the muon capture rate employs chiral perturbation theory (ChPT). Chiral perturbation theory is an effective field theory of low-energy QCD, in which a series expansion about a chirally-symmetric lagrangian, which obtains in the limit $m_u+m_d \to 0$, is developed. The expansion is in terms of the small parameter q/Λ_χ, where q is the momentum transfer scale and $\Lambda_\chi \sim 1$ GeV is the chiral scale. The calculations are in terms of a number of free parameters called "low-energy contants." Chiral perturbation theory is considered model independent in that it expresses the underlying symmetries of QCD and fixes the low-energy constants by comparing calculations to data.

Two published calculations using ChPT to find the rate for ordinary muon capture on the proton give slightly different results. The first, by Ando, Myhrer, and Kubodera [27], is a next-to-next-to-leading-order (NNLO) calculation which finds $\Lambda_\mathrm{S} = 695\ \mathrm{s}^{-1}$. A separate calculation by Bernard, Hemmert, and Meissner [28] included additional degrees of freedom for the nucleon Δ excitation. No significant difference in the chiral expansion was found, and the reported result for the capture rate is $\Lambda_\mathrm{S} = 687.4\ \mathrm{s}^{-1}$. Bernard *et al.* state that they "further demonstrate that both ordinary and radiative muon capture consitute systems with a very well-behaved chiral expansion, both in the standard chiral perturbation theory and in the small scale expansion" [28]. The numerical difference of ∼1% between the two Λ_S results, which in principle come from the same type of calculation, is not clear. Differences could arise trivially, for example from expanding the phase-space factor to order $(m_\mu/m_N)^2 \sim 1\%$ or from slightly different empirical input values for $g_{\pi NN}$ or g_A. For comparison with the MuCap experimental result, the two Λ_S predictions are averaged to $\Lambda_S^{\mathrm{Th}} = 691.2\ \mathrm{s}^{-1}$.

2.5 Radiative Corrections

The theoretical prediction for Λ_S is modified by radiative corrections. Historically, some radiative corrections were automatically included in the calculations of Λ_S, because the product $G_F V_{ud}$ was taken directly from β-decay measurements. More recent calculations, including ones quoted above, use for V_{ud} the value extracted from nuclear beta decay with radiative corrections taken into account; that is, electroweak radiative corrections common to both ordinary muon capture and beta decay were explicitly removed from the normalization factor. An additional correction specific to ordinary muon capture was calculated in 1972 by Goldman [29], who found a 0.6% increase in Λ_S due to vacuum polarization.

Very recently a more complete calculation of the radiative corrections for ordinary muon capture on the proton was done by Czarnecki, Marciano, and Sirlin [30]. They found a +2.4% correction for electroweak effects like the ones appearing in neutron beta decay. The additional vacuum polarization effect was found to be +0.4%, somewhat smaller than Goldman's result. The total correction to Λ_S is +2.8%, a significant amount compared to the present and expected precision of the MuCap result. The chiral perturbation theory prediction will be increased by this amount for comparison with experiment.

2.6 Sensitivity of Λ_S to External Parameters

Uncertainties in the form factor values translate into uncertainties in the theoretical prediction for Λ_S. The sensitivity factor of a parameter C is defined as $K(C) \equiv \frac{\partial\Lambda_S}{\partial C}\frac{C}{\Lambda_S}$. It is straightforward to compute this from the phenomenological calculation results (Eqs. 2.41–2.43), though we opt to simply use the (nearly identical) values for $K(C)$ from Govaerts and Martinez [26]. Values of $K(C)$ and $C(q^2_{\mathrm{OMC}})$ are in Table 2.2, along with their contributions to the uncertainty of the Λ_S prediction. The derivatives $\partial\Lambda_S/\partial C$ can be easily calculated

C	Value at $q^2 = -0.88m_\mu^2$	$\frac{\partial\Lambda_S}{\partial C}\frac{C}{\Lambda_S}$	$\frac{\delta\Lambda_S}{\Lambda_S}$
g_V	0.9755 ± 0.0005	$+0.466$	0.024%
g_M	3.5821 ± 0.0025	$+0.151$	0.011%
g_A	1.24689 ± 0.0036	$+1.567$	0.45%
g_P	8.26 ± 0.16	-0.184	0.36%
V_{ud}	0.97399 ± 0.00027	2	0.055%

Table 2.2: Effect on Λ_S of the uncertainties in the phenomenological parameters C. All sensitivity factors $K(C) \equiv \frac{\partial\Lambda_S}{\partial C}\frac{C}{\Lambda_S}$ are directly from Govaerts and Martinez [26] except the last (V_{ud}), which is trivially calculated from $\Lambda_S \propto V_{ud}^2$. The effect of uncertainty a form factor C is calculated with $\frac{\delta\Lambda_S}{\Lambda_S} = K(C)\frac{\delta C}{C}$. The form factor values are transferred from Table 2.1.

from $K(C)$:

$$\frac{\partial\Lambda_S}{\partial C} = \left(\frac{\partial\Lambda_S}{\partial C}\frac{C}{\Lambda_S}\right)\frac{\Lambda_S}{C} \equiv K(C)\frac{\Lambda_S}{C}. \tag{2.45}$$

Applying Eq. 2.45 to find $\partial\Lambda_S/\partial g_P$ from $K(g_P)$, we use $\Lambda_S = 688.4\ \mathrm{s}^{-1}$ and $g_P = 8.475$, since these are the values used to calculate $K(g_P)$ in Ref. [26] (they used the larger value of $g_{\pi NN} = 13.37$ to get g_P): this gives $\partial\Lambda_S/\partial g_P = -14.9\ \mathrm{s}^{-1}$. Including the radiative correction factor 1.028, the derivative and its inverse become

$$\partial\Lambda_S/\partial g_P = -15.4\ \mathrm{s}^{-1}, \tag{2.46}$$

$$\partial g_P/\partial\Lambda_S = -0.065\ \mathrm{s}. \tag{2.47}$$

The latter quantity will be used in the Results chapter to compute the change in g_P, from its theoretical value, implied by the experimental result for Λ_S.

2.7 Other Capture Rates

Ordinary muon capture rates from other muonic states relevant to later discussions are presented in this section.

Muon capture from a $p\mu p$ molecule depends on the configuration: ortho molecular (proton spins aligned) or para molecular (proton spins opposite). The capture rates Λ_{OM} (ortho) and Λ_{PM} (para) can be written in terms of the singlet and triplet μp capture rates and molecular overlap factors γ_{O}, γ_{P} [31]:

$$\Lambda_{\mathrm{OM}} = 2\gamma_{\mathrm{O}}(\frac{3}{4}\Lambda_S + \frac{1}{4}\Lambda_T), \tag{2.48}$$

$$\Lambda_{\mathrm{PM}} \quad = \quad 2\gamma_{\mathrm{P}}(\frac{1}{4}\Lambda_S + \frac{3}{4}\Lambda_T). \tag{2.49}$$

The overlap factors are calculated to be $2\gamma_{\mathrm{O}} = 1.009 \pm 0.001$ and $2\gamma_{\mathrm{P}} = 1.143 \pm 0.001$ [10]. Since $\Lambda_T \ll \Lambda_S$, the singlet capture rate dominates from either state, and $\Lambda_{\mathrm{OM}} \approx \frac{3}{4}\Lambda_S$, $\Lambda_{\mathrm{PM}} \approx \frac{1}{4}\Lambda_S$.

The capture rate Λ_d from the μd atomic state is similar to Λ_S. Theoretical predictions give $\Lambda_d \approx 370$–410 s^{-1}, consistent with experiments.

The nuclear capture rate Λ_Z of μZ atoms can be estimated based on overlap of the muon orbital wavefunction and the nucleus. The overlap $\phi_\mu^2(0) \propto Z^3$, where ϕ_μ is the orbital wavefunction. Multiplying by the number of protons in the nucleus, we see that $\Lambda_Z \sim Z^4\Lambda_S$. Nuclear structure causes significant deviations from this simple relation, but it is sufficient in the present context to note that $\Lambda_Z \gg \Lambda_S$. Measurements of Λ_Z covering a wide range of nuclei are tabulated in Ref. [32].

Chapter 3

Muon Kinetics in Hydrogen

The interpretation of experiments to measure muon capture on the proton requires knowledge of the initial muon-proton state at the moment of capture. Real experiments involve bringing negative muons to rest inside a medium, in this case hydrogen, where bound states form between the muons and protons. During the relatively long muon lifetime, the μp atom undergoes several transitions, many involving interactions with H_2 molecules or impurities (isotopic or elemental) of the medium. Mu-atomic and molecular transition rates in hydrogen effected by collisional processes are conventionally defined at the density of liquid hydrogen, $N_{\mathrm{LH2}} = 4.25 \times 10^{22}$ atoms/cm^3. Density relative to liquid hydrogen is represented by the symbol ϕ. We will see that a target density of $\phi \approx 0.01$ is optimal for most captures to take place from the μp singlet atomic state, and the hydrogen target must be deuterium-depleted and free of $Z > 1$ contaminants.

3.1 Stopping of Energetic Muons

Charged particles traveling through material deposit increasing amounts of energy per path length as they are slowed, leaving the largest amount of energy at the end of the path. The peak of ionization energy near the stop point is called the Bragg peak. An analytic relation between the range R versus kinetic energy T of an incident particle can be found by fits to empirical data. The range-energy relation thus found is [33]

$$T = \left(\frac{R}{k}\right)^{1/1.8}, \tag{3.1}$$

where the constant k appropriate for the MuCap target is $k = 57.89$ with R in mm and T in MeV. Equation 3.1 may be differentiated by R to get the ionization energy per unit length,

dE/dx, at a distance R from the stop position:

$$\frac{dE}{dx} = \frac{1}{1.8k(R/k)^{1-1/1.8}}. \tag{3.2}$$

3.2 Atomic Capture and Transitions

After being stopped in hydrogen, a negative muon undergoes a series of atomic-scale processes until it disappears through decay or nuclear capture.

1. *Atomic Formation.* A muonic hydrogen (μp) atom is initially formed with the muon's orbital radius similar to that of the electron it replaced. The initial atomic state energy level is correspondingly $n \approx \sqrt{m_\mu/m_e} \approx 14$ [1]. The muon then cascades to the mu-atomic ground state at a rate enhanced by collisions with the medium. The μp atom quickly (within $\sim 10^{-10}$ s at density $\phi = 0.01$) de-excites to the $n = 4$ state via two mechanisms [34]: dissociation of H_2 ($p\mu^{**} + \mathrm{H}_2 \rightarrow p\mu^* + \mathrm{H} + \mathrm{H}$), and an "external" Auger effect on the electron of another atom. The final transition from $n = 4$ to the ground state, by radiative transitions, occurs in less than $\sim 10^{-9}$ ns [35]. The ground-state ($n = 1$) muonic atom is formed in either the singlet (total spin $F = 0$) or triplet ($F = 1$) hyperfine state with statistical probability, i.e., the probabilities to form the singlet and triplet state are $P(F = 0) = 1/4$ and $P(F = 1) = 3/4$.

2. *Atomic Hyperfine Transition.* The hyperfine splitting between the single and triplet states is $\Delta E_{\mathrm{hf}} = 0.195$ eV, much greater than the room-temperature thermal energy scale $kT \approx 0.025$ eV. Irreversible triplet-to-singlet transitions take place via the collisional charge-exchange process, $(\mu p)_{\uparrow\uparrow} + p \rightarrow (\mu p)_{\uparrow\downarrow} + p$, at the density-dependent rate $\phi\lambda_{\mathrm{hf}}$, after the μp atom has thermalized. For a hydrogen density of $\phi \geq 0.01$, the triplet μp transitions to the singlet state well-within 100 ns [36].

3. *Molecular Formation, Transfer to $Z > 1$ Impurity, or Transfer to Deuteron.* The μ^- binds more tightly to all other nuclei than to the proton. This fact, combined with the ability of the μp — a small, neutral object — to penetrate within the charge cloud of an atom and interact directly with the nucleus, leads to high transfer rates away from the muonic hydrogen state. Since these are collisional processes, the rates scale by the density of the impurity nuclei, $c_X\phi$, where c_X is the relative concentration of the impurity and the subscript X labels the species.

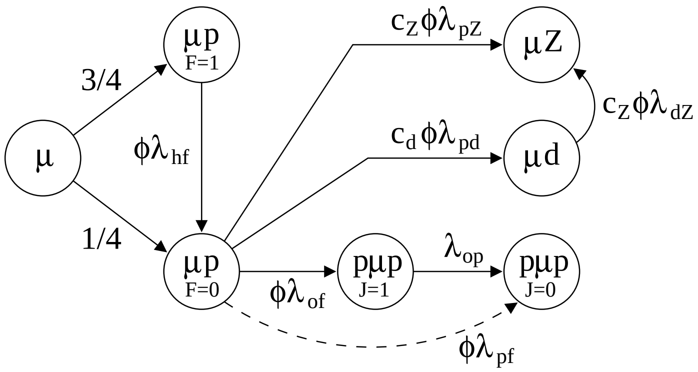

Figure 3.1: Simplified kinetics diagram for a negative muon in hydrogen of density ϕ relative to LH$_2$. Muon decay can occur from every state, and nuclear muon capture can occur from each of the bound states.

λ_{of} (10^6 s^{-1})	Ref.	Comment
1.8	[37]	Theory
1.89 ± 0.20	[38]	Expt., Liquid H$_2$
2.55 ± 0.18	[39]	Expt., Liquid H$_2$
2.34 ± 0.17	[40]	Expt., Gaseous H$_2$
3.21 ± 0.18	[41]	Expt., Solid H$_2$

Table 3.1: Determinations of the $pp\mu$ ortho molecular formation rate, normalized to liquid hydrogen density ($\phi = 1$).

The various muonic states, and transitions between them, are diagrammed in Fig. 3.1. The processes of the last step outlined above — transitions away from the singlet μp state — are represented in the right half of the figure and further described below.

3.2.1 Molecular Formation and Transitions

The mu-molecular $pp\mu$ formation rates into the ortho (angular momentum $J = 1$) and the lower-energy para ($J = 0$) states occur with very different rates. The dominant formation mechanism is S-wave scattering of $p\mu + p$ with an E1 dipole transition coupled to an orbital electron, resulting in an ortho $pp\mu$ molecule (the electron is ejected) [34]. A theoretical calculation [37] predicts the density-dependent formation rates $\lambda_{\text{of}} = 1.8 \times 10^6$ s^{-1} for ortho and $\lambda_{\text{pf}} = 0.0074 \times 10^6$ s^{-1} for para, each normalized to $\phi = 1$. Experimental measurements of λ_{of} vary somewhat more than their stated uncertainties (see Table 3.1).

While direct formation into the para molecular state can be ignored, transitions from the ortho to para state are significant. As explained by Bakalov *et al.* [10], the ortho-para

λ_{op} (10^4 s^{-1})	Ref.	Comment
7.1 ± 1.2	[10]	Theory
4.1 ± 1.4	[9]	Expt., Liquid H_2
$11.7 \pm 1.7^{+0.9}_{-0.6}$	[11]	Expt., Liquid H_2

Table 3.2: Determinations of the ortho-para transition rate of the $pp\mu$ molecule.

transition is forbidden in the nonrelativistic limit, since it involves a change of total nuclear spin from $I = 1$ to $I = 0$. The $\Delta I = 1$ transition is only allowed through coupling to the small component of the relativistic wave functions. The mechanism involves molecular complexes $[(pp\mu)^+p2e] + \mathrm{H}_2]$, $[(pp\mu)^+2p2e]^+ + \mathrm{H}]$, etc., which form very quickly (rates $\sim 10^{13}$ s^{-1} in liquid hydrogen) [10], much faster than the subsequent ortho-para transition even at lower densities $\phi \sim 0.01$. Thus the rate λ_{op} for the ortho-para transition, calculated to be $\lambda_{\mathrm{op}} = (7.1 \pm 1.2) \times 10^4$ s^{-1} [10] in liquid hydrogen, is also appropriate for MuCap conditions of $\phi = 0.01$ without scaling by ϕ. Two experimental studies of λ_{op} report values that are inconsistent with each other and with the theoretical prediction (see Table 3.2); this is precisely the cause of the ambiguity in the interpretation of muon capture experiments in liquid hydrogen, in which capture takes place from the molecular state.

3.2.2 Transfer to $Z > 1$ Impurity

The binding energy $E_{\mathrm{B}}(Z)$ of the ground state of a μZ atom approximately follows $E_{\mathrm{B}}(Z) \propto Z^2$. All $Z > 1$ atoms are more strongly bound than the μp, and the transfer rate λ_{pZ} of the muon from μp to μZ is fast, $\lambda_{pZ} \sim 10^{11}$ s^{-1}. Once the μZ is formed, cascade to the ground state via Auger and radiative transitions is immediate, and nuclear capture proceeds with rate $\Lambda_Z \gg \Lambda_{\mathrm{S}}$. The transfer rate λ_{pZ} scales with the impurity density $c_Z\phi$, for an effective transfer rate $\tilde{\lambda}_{pZ} = c_Z\phi\lambda_{pZ}$. Specific calculations of the effect of $Z > 1$ impurities on the μ^- lifetime in hydrogen are presented later in this chapter.

3.2.3 Transfer to the Deuteron

Due to the difference in reduced mass, the μd is more tightly bound than the μp by $\Delta E_{pd} = 135$ eV [34], and irreversible transfer of the muon to the heavier isotope, $p\mu + d \rightarrow d\mu + p$, takes place with rate $c_d\phi\lambda_{pd}$, where c_d is the deuterium concentration and $\lambda_{pd} \sim 10^{10}$ s^{-1}. The newly-formed μd has an initial kinetic energy of ≈ 45 eV [34], which, combined with an anomalously small $\mu d + p \rightarrow \mu d + p$ scattering cross section, can lead to large displacements on the time scale of the muon lifetime (see Section 3.5). The muon of a μd can also transfer to a $Z > 1$ impurity as in the case of μp. In general the transfer rate $\lambda_{dZ} \neq \lambda_{pZ}$ due to atomic and molecular effects. For deuterium-depleted, low density, and high-purity hydrogen gas, the transfer from μd to Z is entirely negligible.

3.3 Kinetics Equations

The kinetics processes diagrammed in Fig. 3.1 may be expressed as a system of linear differential equations. In addition to the transitions shown in the diagram, muon decay from each state and nuclear muon capture from the bound states must be included. Let $n_i(t)$ represent the number of muons in atomic/molecular state i at time t: $i = 1$ for singlet μp atoms, $i = 2$ for ortho $p\mu p$ molecules, $i = 3$ for para $p\mu p$, and $i = 4$ for μZ impurity atoms; triplet μp atoms are not considered, since they quickly transition to the singlet state. Transfer to deuterium is neglected for now, but it can be easily included for special studies involving significant deuterium concentrations. The muon decay rate from any state is set to a common value $\lambda_0 \approx \lambda_\mu^+$, a good approximation except in μZ states with heavy nuclei, which have significant bound-state effects on muon decay [7]. The following system of equations express the change in the populations:

$$\begin{aligned}
\frac{dn_1}{dt} &= -(\lambda_0 + \Lambda_{\mathrm{S}} + \phi\lambda_{pp} + \tilde{\lambda}_{pZ})n_1 && (3.3)\\
\frac{dn_2}{dt} &= \phi\lambda_{\mathrm{of}}n_1 - (\lambda_0 + \Lambda_{\mathrm{om}} + \lambda_{\mathrm{op}})n_2 && (3.4)\\
\frac{dn_3}{dt} &= \phi\lambda_{\mathrm{pf}}n_1 + \lambda_{\mathrm{op}}n_2 - (\lambda_0 + \Lambda_{\mathrm{pm}})n_3 && (3.5)\\
\frac{dn_4}{dt} &= \tilde{\lambda}_{pZ} - (\lambda_0 + \Lambda_Z)n_4 && (3.6)
\end{aligned}$$

Lower-case lambdas are transition rates, and upper-case lambdas are nuclear capture rates. The effective impurity transfer rate $\tilde{\lambda}_{pZ}$ and the total molecular formation rate λ_{pp} are

$$\begin{aligned}
\tilde{\lambda}_{pZ} &= \phi\lambda_{pZ}c_Z, && (3.7)\\
\lambda_{pp} &= \lambda_{\mathrm{of}} + \lambda_{\mathrm{pf}} \approx \lambda_{\mathrm{of}}. && (3.8)
\end{aligned}$$

The solution to the kinetics equations is given in appendix A.1 and plotted in Fig. 3.2 for $c_Z = 0$ and two different hydrogen densities.

Functional forms for the time spectra $y_X(t)$ of the various final state particles — electrons

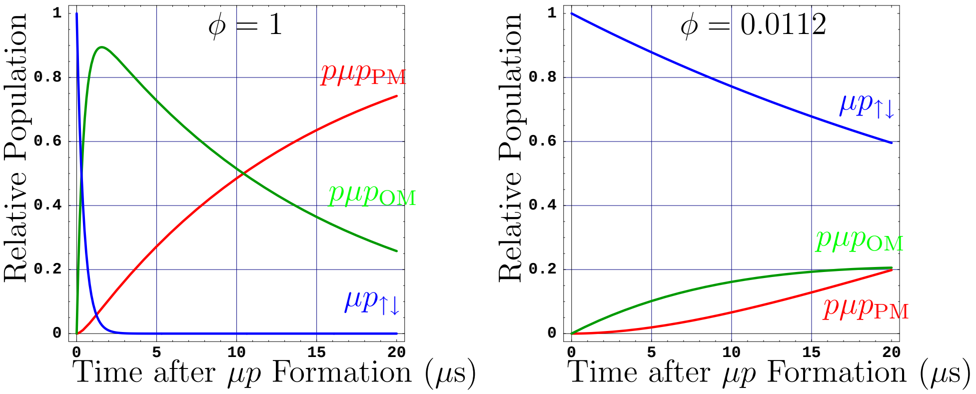

(a) High density, $\phi = 1$. (b) Low density, $\phi = 0.0112$.

Figure 3.2: Relative populations of the singlet μp state (blue), the ortho $p\mu p$ state (green), and the para $p\mu p$ state (red).

from muon decays, neutrons from captures on protons, and recoil nuclei from muon captures on impurities — are calculated in terms of the solution to the kinetics equations. The appearance-time spectrum of electrons is the total muon population in any state multiplied by the decay rate λ_0, i.e.,

$$y_e(t) = \lambda_0 \sum_i n_i(t). \tag{3.9}$$

In contrast, the different bound states are each weighted by the appropriate nuclear capture rate to give the neutron time spectrum:

$$y_n(t) = \Lambda_{\mathrm{S}} n_1(t) + \Lambda_{\mathrm{om}} n_2(t) + \Lambda_{\mathrm{pm}} n_3(t). \tag{3.10}$$

The time spectrum of $Z > 1$ capture events is

$$y_Z(t) = \Lambda_Z n_4(t). \tag{3.11}$$

3.4 Effects of $Z > 1$ Impurities

The solution to the kinetics equations may be used to predict the effect of a small amount of $Z > 1$ impurity on the muon disappearance rate. We are interested in the case appropriate for the MuCap target: low density of $\phi \approx 1\%$ and low impurity concentration of up to $c_Z \approx 10^{-5}$ (for special impurity-doped runs — much less for production runs). Under these conditions molecular formation and $Z > 1$ impurities amount to small corrections to the electron time spectrum approximated as a simple exponential decay,

$$y_e(t) \approx f_e(t) = N\lambda e^{-\lambda t}, \tag{3.12}$$

where N is the total number of decay electrons observed and, in terms of corrections for molecular formation and $Z > 1$ impurities,

$$\lambda = \lambda_0 + \Delta\lambda_{p\mu p} + \Delta\lambda_Z. \tag{3.13}$$

The parameter λ in Eq. 3.12 can be found from the full kinetics solution $y_e(t)$ by taking the first moment:

$$\lambda^{-1} = \lambda_{\text{1st}}^{-1} \equiv \frac{\int_0^\infty t y_e(t)dt}{\int_0^\infty y_e(t)dt}. \tag{3.14}$$

The result depends on the parameters of $y_e(t)$: $\lambda = \lambda_{\text{1st}}(\lambda_0, \Lambda_{\text{S}}, \lambda_{pZ}, c_Z, ...)$. The correction $\Delta\lambda_Z$ for a given impurity concentration c_Z is then the difference of λ_{1st} with $c_Z = 0$ to the same with $c_Z > 0$:

$$\Delta\lambda_Z = \lambda_{\text{1st}}(c_Z = 0) - \lambda_{\text{1st}}(c_Z). \tag{3.15}$$

The molecular formation correction may be calculated similarly by setting $c_Z = 0$ and comparing λ_{1st} with $\lambda_0 + \Lambda_{\text{S}}$. A somewhat different approach is described in Appendix A.2 which connects more closely to the data-analysis reality of fitting an observed spectrum over a finite time interval: a lifetime spectrum is generated with the full-kinetics function (Eq. 3.9) and then fit via χ^2-minimization with the single exponential function f_e of Eq. 3.12. Similar to the first-moment method, variation $\Delta\lambda$ of the fit result as the parameter-of-interest (e.g., c_Z) of the full kinetics function is changed gives the effect of that parameter.

In the discussion of systematic corrections to the MuCap result in chapter 6, the correction $\Delta\lambda_Z$ is developed from essentially a zero-extrapolation procedure based on the observed $Z > 1$ capture yield (i.e., the integral of $y_Z(t)$ in Eq. 3.11 mulitiplied by the detection efficiency ϵ) and calibration data in which the impurity concentration of the target gas was increased. Calculation of $\Delta\lambda_Z$ from Eq. 3.15, which requires knowing the absolute impurity concentration and species, and furthermore accurate literature values for the impurity transfer and capture rates, is thus circumvented. However, theoretical predictions for certain $Z > 1$ capture observables will be used for consistency checks and minor adjustments to the impurity calibration method. The adjustments are necessary, as explained in section 6.5, for two reasons: 1) we cannot be sure what were the relative fractions of different impurities in the production data, and 2) the calibration data were taken under slightly different conditions (detector gain). The quantities of interest are defined as follows:

$$\beta_Z \equiv \Delta\lambda_Z/Y_Z, \tag{3.16}$$

$$\gamma_Z \equiv \tilde{\lambda}_{pZ}/Y_Z, \tag{3.17}$$

$$R_Z \equiv \Delta\lambda_Z/\tilde{\lambda}_{pZ}. \tag{3.18}$$

Theoretical predictions for β_Z, γ_Z, and R_Z require calculations of the capture yield Y_Z (number of $Z > 1$ capture events per muon stop) and the lifetime effect $\Delta\lambda_Z$. The total capture yield is the integral of Eq. A.23:

$$Y_Z = \int_0^\infty y_Z(t)dt = \frac{\Lambda_Z \tilde{\lambda}_{pZ}}{(\lambda_0 + \Lambda_Z)(\lambda_0 + \Lambda_S + \phi\lambda_{pp} + \tilde{\lambda}_{pZ})}, \tag{3.19}$$

which approximately scales with the impurity concentration c_Z if $\tilde{\lambda}_{pZ} \ll \lambda_0 + \Lambda_S + \phi\lambda_{pp}$. For the calculation of $\Delta\lambda_Z$ from Eq. 3.15 and the solution to the kinetics equations $y_e(t)$, we may neglect capture from the μp state by setting $\Lambda_S = 0$. Molecular formation should be retained, however, because muons in the molecular $p\mu p$ state are no longer available to transfer to an impurity. In terms of ratios of rates,

$$x_{pZ} = \tilde{\lambda}_{pZ}/\lambda_0, \tag{3.20}$$

$$X_Z = \Lambda_Z/\lambda_0, \tag{3.21}$$

$$m = \phi\lambda_{pp}/\lambda_0, \tag{3.22}$$

the result of the moment method is [42]

$$\begin{aligned}\Delta\lambda_Z \approx\ & x_{pZ}X_Z\,(2 + m + x_{pZ} + X_Z)\,/\,\Big\{x_{pZ}^2 + (1+X_Z)^2 + m^2(1+X_Z)^2 \\ & + x_{pZ}(2+X_Z) + m[2(1+X_Z)^2 + x_{pZ}(2 + 2X_Z + X_Z^2)]\Big\}.\end{aligned} \tag{3.23}$$

If x_{pZ} is much less than both 1 and X_Z (i.e., $\tilde{\lambda}_{pZ} \ll \lambda_0$, $\tilde{\lambda}_{pZ} \ll \Lambda_Z$), a condition met even in the impurity-doped calibration data of MuCap, all factors of x_{pZ} can be neglected except the overall scaling term in the numerator; we see that $\Delta\lambda_Z$ scales with the transfer rate $\tilde{\lambda}_{pZ}$. This observation supports the validity of the linear correction procedure described in section 6.5.

In the end we apply the fitting (χ^2-minimum shift) method of Appendix A.2 to best match the experimental conditions of finite observation time interval, and results for $\Delta\lambda_Z$

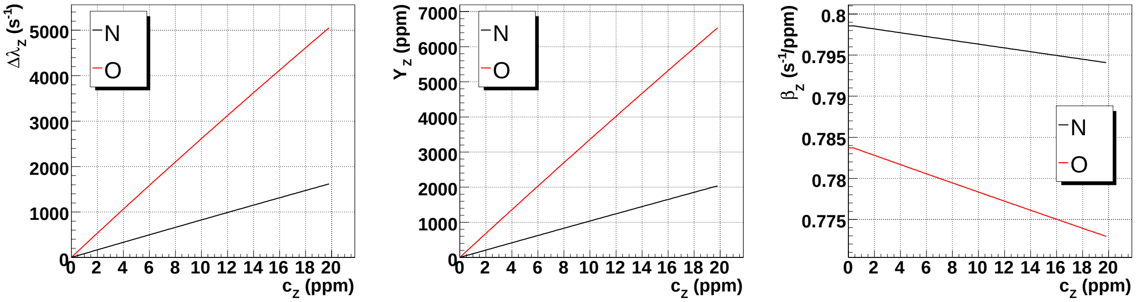

(a) $\Delta\lambda_Z$.

(b) Y_Z.

(c) β_Z.

Figure 3.3: Calculated $Z > 1$ impurity observables vs. impurity concentration c_Z, for $Z = \mathrm{N}$ (nitrogen) and $Z = \mathrm{O}$ (oxygen).

Element	λ_{pZ} (10^{11} s^{-1})	Λ_Z (10^6 s^{-1})	Y_Z (ppm)	$\Delta\lambda_Z$ (s^{-1})	β_Z (s^{-1}/ppm)	γ_Z (s^{-1}/ppm)	R_Z
C	0.95 (Ref. [43])	0.0376	168.3	136.1	0.809	6.32	0.128
N	0.34 (Ref. [44])	0.0693	104.4	83.4	0.798	3.65	0.219
O	0.85 (Ref. [45])	0.1020	361.3	283.1	0.784	2.63	0.297
Ne	0.08 (Ref. [46])	0.2350	63.4	46.2	0.729	1.41	0.515
Ar	1.63 (Ref. [47])	1.4000	2850.3	1561.4	0.548	0.64	0.855

Table 3.3: $Z > 1$ impurity quantities for $c_Z = 1$ ppm. The references for the transfer rates λ_{pZ} are listed in brackets next to the values The total capture rates Λ_Z are from Ref. [32]. The capture yields Y_Z are based on Eq. 3.19, and the lifetime deviations $\Delta\lambda_Z$ are found from the fit method described in the text.

versus the impurity concentration c_Z are shown in Figure 3.3 for $Z = \mathrm{N}$ (nitrogen) and $Z = \mathrm{O}$ (oxygen). Values for β_Z, based on the fitting method for $\Delta\lambda_Z$ and Eq. 3.19 for the impurity capture yield, are presented in the right panel of Fig. 3.3. The insensitivity of β_Z to c_Z confirms the linear scaling of $\Delta\lambda_Z$ with c_Z. The other impurity capture quantities defined above, γ_Z and R_Z, are similarly insensitive to c_Z. Predictions for these values are shown in Table 3.3 for $c_Z = 1$ ppm of the common impurities carbon, nitrogen, and oxygen, and the heavier elements neon and argon. Calculated $Z > 1$ capture time spectra for nitrogen, oxygen, and argon are in Fig. 3.4.

The prediction from Table 3.3 of nearly equal values of β_Z for carbon, nitrogen, and oxygen is of note. If we observe with perfect efficiency a particular capture yield Y_Z without knowing which of these species contribute, we can still approximately calculate the effect of impurities on the lifetime:

$$\Delta\lambda_Z \approx (0.8\ \mathrm{s}^{-1}/\mathrm{ppm})Y_Z, \tag{3.24}$$

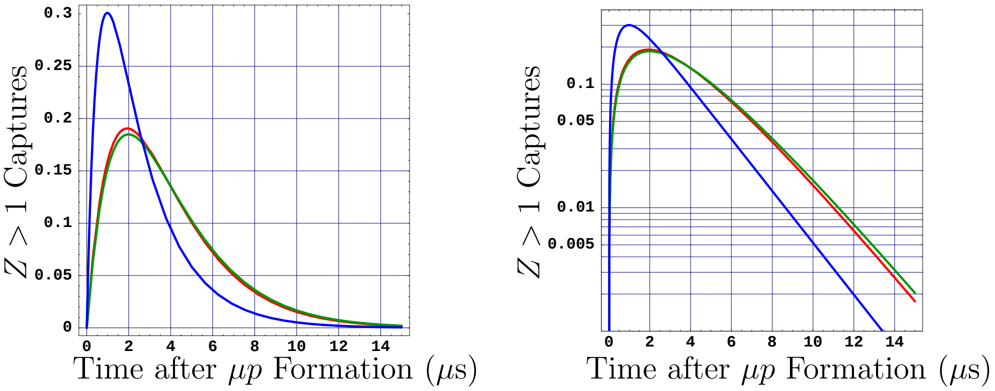

(a) Linear scale.

(b) Log scale.

Figure 3.4: Calculated $Z > 1$ capture time spectra $y_Z(t)$, each normalized to the respective total capture yield Y_Z (Eq. 3.19), for nitrogen (green), oxygen (red), and argon (blue). Impurity concentrations of $c_Z = 1$ ppm were specified for these plots.

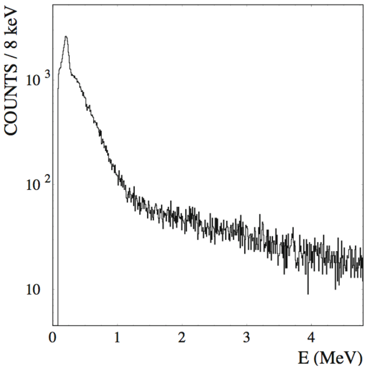

Figure 3.5: (from Ref. [48]) Energy spectrum of muon capture on nitrogen measured in a high-pressure hydrogen ionization chamber with 140 ppm N_2 added to the H_2 gas.

where Z is C, N, or O. There is one major caveat: in a real experiment there will be an energy threshold to detect $Z > 1$ capture events and a corresponding reduction of the observed yield, $Y_Z^{\text{obs}} = \epsilon_Z Y_Z$, with some efficiency factor $\epsilon_Z < 1$. The final states of capture on $Z > 1$ nuclei are generally complicated and dependent on details of nuclear structure [49]. The final-state nucleus may break up be left in an excited state, leading to a broad kinetic-energy spectrum. An example muon capture energy spectrum, as measured in an ionization chamber, is shown in Fig. 3.5 for nitrogen.

The dependence of ϵ_Z on the impurity species and experimental energy threshold has implications for the impurity correction in MuCap. Since both $\Delta\lambda_Z$ and the yield Y_Z scale with impurity concentration c_Z, a convenient method to correct for impurities is a zero-extrapolation procedure based on the observed yield and calibration data in which c_Z is increased. The extrapolation is valid as long as the $Z > 1$ capture detection efficiency ϵ_Z remains the same. The ideal case of calibration data with the same impurity species and $Z > 1$ capture detection threshold — therefore the same ϵ_Z — was not achieved in the 2004 MuCap run. Fortunately, a high level of purity was maintained in the MuCap production target, and the required correction to the lifetime is small. Practical details are described later in Section 6.5 of the Systematic Effects chapter.

3.5 Diffusion

In addition to the high transfer rates of the muon to $Z > 1$ nuclei, another consequence of the neutrality of μp and μd atoms is their ability to diffuse significant distances before the muon disappears through capture or decay. The cross sections for $\mu p + \mathrm{H}_2$ and $\mu d + \mathrm{H}_2$ scattering are shown in Fig. 3.6. For $\mu d + \mathrm{H}_2$ scattering, there is a minimum in the scattering cross section between 1 to 100 eV due to the Ramsauer-Townsend effect. Since the reaction $\mu p + d \to p + \mu d$ imparts 10's of eV to the μd, much longer diffusion lengths occur compared to μp. The diffusion of μp in H_2 is itself not entirely neglible in the target conditions of the MuCap experiment ($\phi = 0.01$ and temperature $T = 300$ K), in part because of an initial "epithermal" (energy greater thermal energy scale $kT \approx 0.03$ eV) component of the μp kinetic energy distribution. Detailed Monte Carlo studies were performed for the original MuCap proposal [50], and results are published in Ref. [36] (from which Figs. 3.6 and 3.7 are taken). The effect of deuterium contamination is particularly clear in the right panel of Fig. 3.7, the distribution of radial displacements of the simulated μp's and μd's at the time of muon decay: the formation and diffusion of the μd are responsible for the long tail,

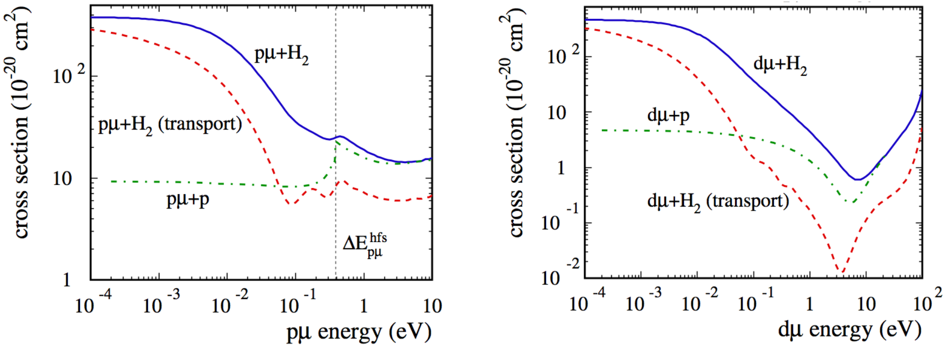

Figure 3.6: (from Ref. [36]) Calculated cross sections for $\mu p + \mathrm{H}_2$ and $\mu d + \mathrm{H}_2$ scattering. The transport cross section (dashed lines), defined as $\sigma_{\mathrm{trans}} = \int d\Omega(1-\cos\theta)\frac{d\sigma(\theta)}{d\Omega}$, takes into account the anisotropy of the scattering, which in this case is strongly forward-peaked [36]. Solid lines are total cross sections.

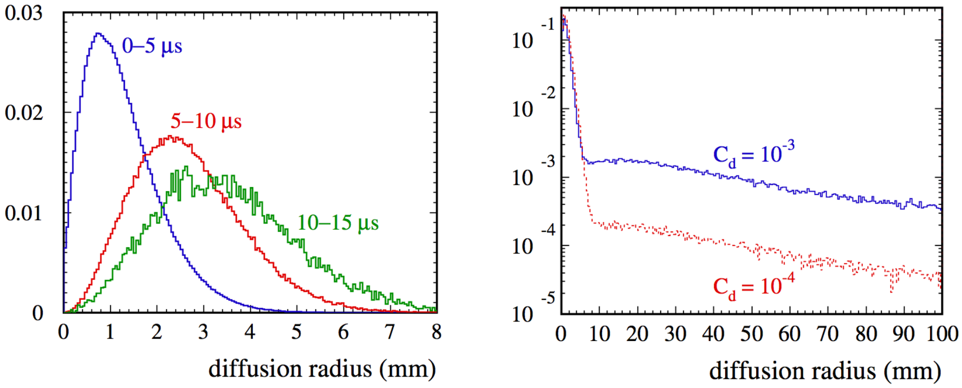

Figure 3.7: (from Ref. [36]) Radial distributions of μ^- decays in a simulation of μp and μd diffusion in hydrogen gas ($\phi = 0.01$) at temperature $T = 300$ K. Left: distributions for decays in the indicated time intervals. Right: distributions in hydrogen gas with the specified deuterium concentrations, for decays with $t < 20$ μs. The tail in the distribution extending out to ~ 10 cm is due to the small cross section for $\mu d + p$ scattering.

which extends out to ~ 10 cm, perhaps far enough to reach the walls of a vessel containing the hydrogen gas in a real experiment. The left panel of Fig. 3.7 demonstrates the much smaller scale of the μp displacements, which are very unlikely to result in collision with wall material if the initial μp formation is more than ≈ 1 cm away. The μp diffusion cannot be completely dismissed, though, because of a subtle but important effect in the MuCap experiment related to tracking decay electrons back to the muon stop positions; this issue will be explained in Section 6.6 of the Systematics chapter.

Chapter 4

The MuCap Experiment

4.1 Design Considerations

In order to avoid ambiguities in the interpretation of the result, muons must be stopped in hydrogen gas that is extremely pure — elementally and isotopically — and has a density of $\phi \sim 1\%$ of liquid hydrogen density. At this density, the muon-atomic hyperfine transition from the $n = 1$ triplet to singlet state is fast, such that all μp atoms are in the singlet ground state well-within 100 ns. Also, the rate of muon-molecular ($p\mu p$) formation is relatively slow, and only $\approx 4\%$ of all muons reach the molecular state before disappearing. To avoid lifetime corrections from transfers to $Z > 1$ nuclei, elemental impurity concentrations c_Z must be less than $\sim 10^{-8}$. Finally, the deuterium concentration must be small principally because of the anomalously small cross-section for $\mu d + p$ scattering, such that the μd can scatter ~ 10 cm, far enough to encounter the walls of the vessel containing the hydrogen.

The low target density presents a challenge to reliably stop incident muons in the gas and away from all $Z > 1$ materials. Given the small branching ratio of muon capture on the proton ($\approx 0.16\%$) and the desired precision of the result (Λ_S to 1%), wall stops must be avoided to better than 10^{-5}. This is accomplished with the central detector of MuCap, a Time Projection Chamber (TPC) operating on the target gas itself; the TPC is the key enabling technology of MuCap. Whereas a previous measurement in hydrogen gas employed veto counters around the walls of the target [3], in MuCap only muons that stop within the TPC fiducial volume are accepted in the data analysis. The practical difference in the present approach, of accepting “good” muons rather than rejecting “bad” muons, is that the detectors need not have extremely high efficiency, and muon stops in detector wires are not problematic.

The all-neutral final state of muon capture on the proton presents an additional experimental challenge. An absolute measurement based on neutron detection would involve simply counting the number of good muon stops with subsequent emission of a 5.2 MeV neutron, and dividing by the total number of good muon stops. The capture rate is then approximately this branching ratio multiplied by the free muon decay rate, i.e., $\Lambda_S \approx \lambda_\mu^+ N_{neutrons}/N_{muons}$, where $N_{neutrons}$ is the number of good muon stops followed by neutron emission, and N_{muons} the number of good muon stops. The problem with this method is the combination of low efficiencies (generally $\sim$ 10%) and difficulty of absolute calibration of neutron detectors, and the large background of Michel electrons. For a 1% precision measurement of Λ_S, the neutron detector efficiency would have to be known to the same relative precision.

Because of the difficulties with neutron detection, the MuCap experiment instead uses the "lifetime technique": the capture rate is approximately determined by the difference between the μ^- lifetime in hydrogen and the free μ^+ lifetime. Assuming CPT invariance (equal lifetimes of the free μ^- and μ^+), $\lambda_\mu^- = \lambda_\mu^+ + \Lambda_S + \Delta\lambda_{corr}$, where $\Delta\lambda_{corr}$ is a small correction for molecular formation and a bound-state modification to the free muon lifetime. An absolute measurement is therefore not required; only the shape of the electron or neutron appearance time spectrum needs to be measured. The tradeoff is we are subtracting two large numbers, λ_μ^+ from λ_μ^-, to get the $\sim 10^{-3}$ smaller Λ_S. Therefore, to get Λ_S to 1% precision, λ_μ^- and λ_μ^+ must be known to $\sim 10^{-5}$ precision. Such a high-precision lifetime measurement presents its own challenges, as all time-dependent detection efficiencies correlated to the muon entrance time must be understood.

4.2 Overall Scheme

A simplified cross-sectional diagram of the MuCap detector, including the various detector elements, is shown in Fig. 4.1. Each detector element is named according to its measurement principle — scintillator (SC), multiwire proportional chamber (PC), or time projection chamber (TPC) — and, except for the TPC, the particle it is intended to measure — muon (μ) or electron (e). In chronological order of the detectors encountered by the example muon decay event shown in the figure, there are the muon detectors: 1) the μSC for fast timing, giving the muon (absolute) time t_μ; 2) the μPC for additional pileup protection of spatially separated muon entrances; 3) the TPC for tracking to the stop position. Next are the electron detectors traversed by the decay electron: 4) ePC1, the inner cylindrical wire chamber, for (ϕ, z) detection at a smaller radius; 5) ePC2, the outer cylindrical wire chamber, for (ϕ, z) detection at a larger radius; 6) the eSC for fast timing, giving the (absolute) electron time t_e. A muon decay time spectrum is built up from the time differences $\Delta t = t_e - t_\mu$ of many such events. A fit of the time spectrum to a simple exponential function yields, apart

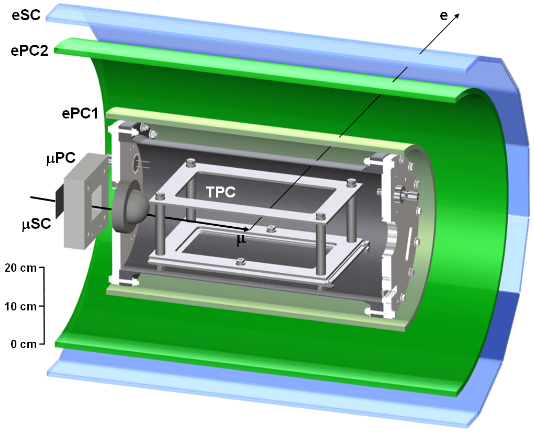

Figure 4.1: Simplified cross-sectional diagram of the MuCap apparatus, showing the muon and electron detectors described in the text. The particle paths of an example event, a muon entrance followed by decay into an electron (neutrinos are not shown), are indicated by the arrows.

from small corrections, the desired μ^- lifetime in the singlet μp atomic state.

Key features of the MuCap experiment are the following:

- Muons are stopped in purified, deuterium-depleted hydrogen gas at 10 bar and room temperature. The density at this pressure and temperature is $\phi = 0.0112$ relative to liquid hydrogen, and most muons are in the singlet atomic state.

- Muons are fully tracked by a time projection chamber (TPC) operating on the target gas itself. Only those that stop well-within the TPC fiducial volume are accepted.

- The target gas is continuously circulated through cryogenic adsorbers to maintain low levels of $Z > 1$ impurities.

- The effect of non-negligible deuterium in the production data is corrected for by a zero-extrapolation procedure, in which a calibration point is based on data with ~ 100 times the deuterium concentration of the production data.

- The effect of residual $Z > 1$ impurities is corrected for by *in situ* impurity capture monitoring by the TPC combined with calibration data at much higher impurity concentration.

- The measurement of Λ_S is based on the lifetime technique. Electrons from muon decay are detected and timed to build up an electron appearance time spectrum, giving the net lifetime of the μ^- in hydrogen. Comparison with the μ^+ lifetime gives the additional loss rate of μ^- in hydrogen, which (aside from small corrections) is attributed to muon capture.

- The muon decay electrons are tracked to allow reduction of background events by requiring that the electron track points to the parent muon stop position. These vertex cuts also enable *in situ* deuterium concentration monitoring, in which tighter vertex cuts result in higher loss rates from μd atoms diffusing away from the allowed regions.
- Muon and electron detectors are kept as separate as possible to avoid any interference or cross talk that could distort the precision lifetime measurement.
- Muon pileup events, i.e., events in which an additional muon entrance is detected within a certain time interval of a given muon entrance, are rejected, a condition called "pileup protection." Allowing only one muon at a time circumvents many problems due to TPC tracking ambiguities and detector deadtimes, which would otherwise distort the lifetime spectrum.

The major subsystems of the MuCap experiment — devoted to muon detection, electron detection, hydrogen gas handling, and data acquisition — are presented below with selected details. This chapter is concluded with a summary of the different experimental conditions during the 2004 data-taking period, which define data sets of interest in the analysis.

4.3 Muon Beam

The experiment was installed in the πE3 area at the Paul Scherrer Institute for the experimental running period of late September through November of 2004. The beamline was tuned to transport muons with central momentum $P = 32.6$ MeV/c and rate 20 kHz (direct current). Background electrons in the beam were reduced by an $\vec{E} \times \vec{B}$ separator set to allow only muons of the central momentum to pass. In the ideal situation, each muon would be stopped in the center of the hydrogen target, and no other muons would enter during the measurement period of 25 μs. In practice, the muons are stopped over a broad distribution of positions within the low-density hydrogen target, due to 1) the finite momentum distribution of muons transported by the beam, and 2) range straggling in materials placed before the hydrogen target. A beam tune was developed to minimize the momentum spread,

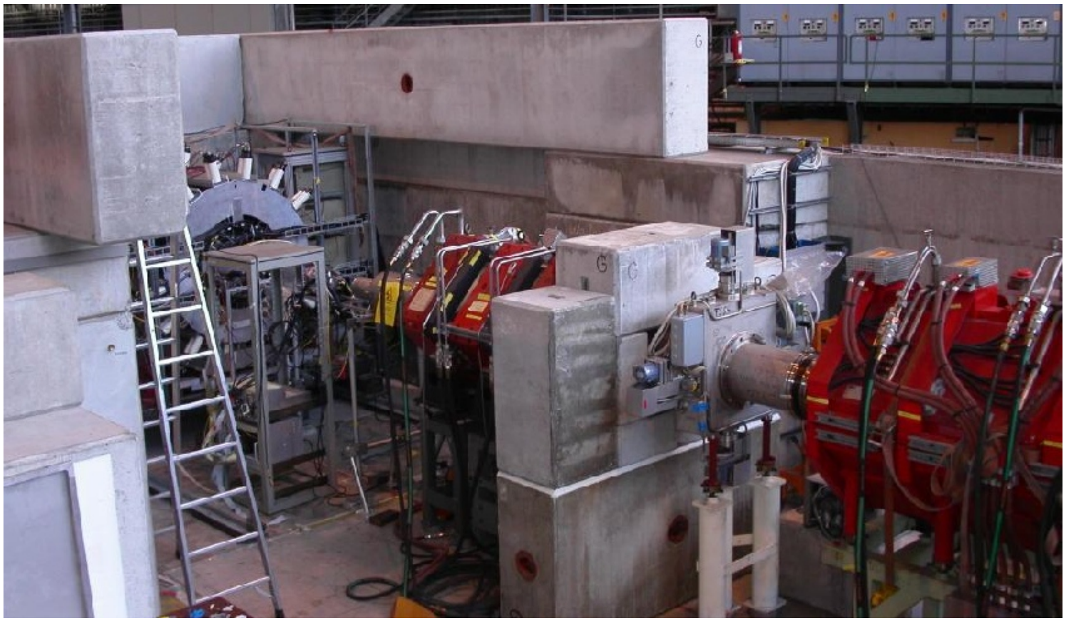

Figure 4.2: Photo of the last beamline elements before the detector, showing the focusing quadruple magnets and the last set of variable beam apertures (slits). The *e*-detector is visible on the left in its rolled-back position.

and material in front of the hydrogen was minimized as much as possible. The net result was a gaussian distribution of muon stop positions in the hydrogen gas, as measured with the muon detectors described below, having longitudinal spread $\sigma_z = 8.0$ cm and transverse spread $\sigma_x = \sigma_y = 3.1$ cm. Approximately 65% of incident muons stopped within the active region of the central muon detector within the hydrogen gas. The beam rate of 20 kHz was optimal in terms of the net rate of incident muons that are separated in time from all others by at least 25 μs.

4.4 Muon Detection

The muon detectors allow selection of each event in which an incident muon stopped in the hydrogen gas away from any $Z > 1$ material, and no other muon entered within ± 25 μs.

4.4.1 Entrance Detectors

Entrance muon detectors provide timing of incident beam muons and enable selection of events in which only one muon entered the target ("pileup protection"). The detectors are designed to avoid degrading the beam, which would adversely affect the spatial stopping distribution of muons within the hydrogen gas. The elements between the beam window and the entrance window of the pressure vessel containing the H_2 are described below in the order encountered by a beam particle.

The first detector is a thin muon scintillator, the μSC, to privide a fast timing signal for t_μ. In the early part of the 2004 data-taking period (Run8), a 500-μm-thick scintillator served as the μSC. Later it was changed to a scintillator of half the thickness in an effort to reduce material in the beam path, but the improvement to the stopping distribution in the target was marginal. The inefficiency of the μSC, however, increased severely in going to the thinner target. After the μSC is the μSCA, a scintillator with a 35-mm-diameter hole in the middle to allow most beam particles to pass. Its purpose is to veto muons that are too far off the beam axis. Immediately behind the μSCA and aligned to it is a lead collimator also with a 35-mm-diameter hole.

A multiwire proportional chamber, the μPC, follows the lead collimator. The μPC has two anode planes, each with 24 wires, and 25-μm-thick aluminized mylar cathode planes. The anode planes are oriented such that one provides horizontal (x) positions of beam particles, and the other provides vertical (y) positions. The μPC greatly improves the pileup-protection efficiency compared to the μSC alone. It was indispensible in this respect, as will be demonstrated in Chapter 6.

4.4.2 Time Projection Chamber

The time projection chamber (TPC) detects ionizing particles within a 15×12×28-cm sensitive volume free of $Z > 1$ material. An incident muon leaves an ionization trail in the hydrogen gas with increasing intensity as it slows, depositing the most amount of energy per track length at the stop position (see Section 3.1). Electrons from the ionization track drift in a uniform 2 kV/cm electric field towards a multiwire proportional chamber (MWPC) at the bottom of the volume. When the electrons enter the region of high electric field around the small-diameter anode wires of the MWPC, a cascade process begins: electrons are accelerated and collide with gas molecules with enough energy to ionize the H_2, releasing more electrons to do the same until a large number reach an anode and are detected. Ions created in the process drift back to the cathode planes of the MWPC, where they are also detected.

A photograph of the TPC is shown in Fig. 4.3a. Most wires are not visible in the photograph, with the exception of the large wires wrapped around the posts. The upper

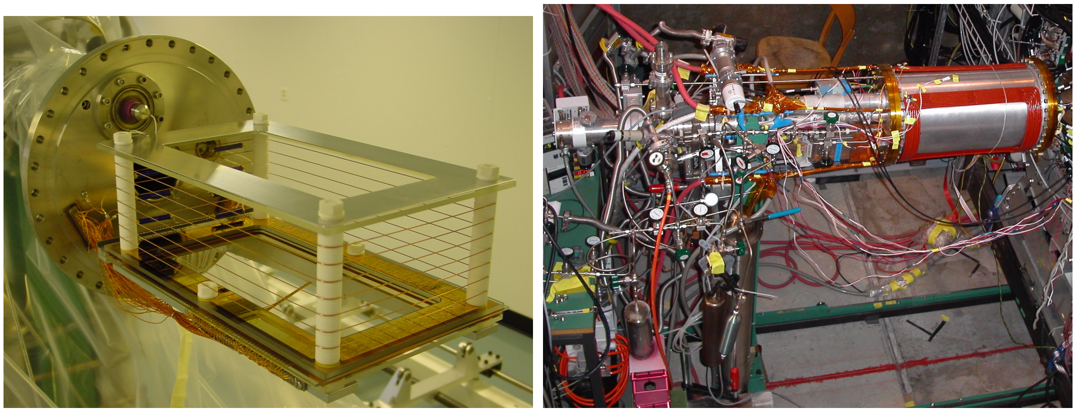
(a) TPC.

(b) Pressure vessel.

Figure 4.3: (a) Photo of TPC with the pressure vessel removed and (b) photo of the aluminum pressure vessel, containing the hydrogen gas and TPC, pulled back from its docking position in the center of the e-detector. In these views, muons enter from the right side. (The red coils mounted on the pressure vessel are parts of a $\cos\theta$ magnet to provide a ~ 50 Gauss μSR field for μ^+ measurements, which are not discussed in this document.)

frame, which has wires strung across it to define an equipotential surface, is held at a voltage of ≈ 30 kV creating the 2 kV/cm drift field, leading to a drift velocity of electrons in the 10-bar hydrogen of $v_{\text{drift}} \approx 5.5\ mm/\mu$s. The wires wrapped around the posts are connected to a voltage divider, which sets the potentials of these wires improve the field uniformity in the drift region. The MWPC is composed of the closely-spaced frames at the bottom. An anode plane with 4-mm-spaced, 25-μm-diameter tungsten-gold wires running transverse to the long axis of the TPC is sandwiched between two cathode planes. Each cathode plane has 1-mm-spaced, 50-μm-diameter wires strung parallel to the long axis. The cathode planes are held at ≈ -5.0 kV, while the anode plane is at ground potential. The TPC frame materials were carefully chosen to be compatible with baking at 115 C, an important step in the preparation of a high-purity target volume. At an operating voltage of -5.0 kV across the 3.5-mm spacing ("half-gap") between the anode and cathode planes, the gain of the MWPC is about 60, doubling for every ~ 200 V the voltage is increased.

Each of the 75 anode wires is connected to a charge-integrating preamplifier. Cathode wires are tied together into 35 groups (strips), each comprising four adjacent cathode wires except the edge strips, which include a few more. Each cathode strip is connected to a charge-integrating preamplifier. An example of the signal produced by the MWPC anode wires is shown in Fig. 4.4 for a muon stop followed by a $Z > 1$ capture event (a rarity in MuCap). Analog data like that shown in Fig. 4.4a is recorded for special events, such as

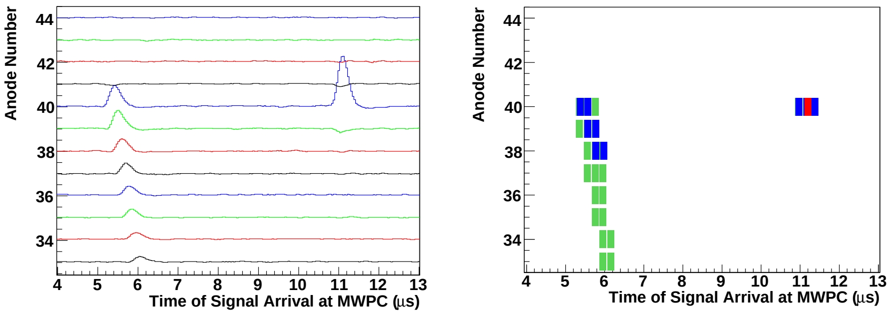

(a) FADC data. (b) TDC data.

Figure 4.4: Example of raw data from a muon stop event for several adjacent wires of the TPC. The times are with respect to a muon entrance at $t_\mu = 0$. The analog signals are displayed in (a), and the corresponding 3-level discriminated data are in (b). The discriminator levels are set low (green) for fast muons, high (blue) for slow muons and stops, and very high (red) for recoil nuclei from $Z > 1$ captures. This example is a $Z > 1$ capture event, a rare occurance in the high-purity hydrogen maintained in MuCap.

$Z > 1$ impurity captures, that involve anode wires in a middle section of the TPC. Data from all wires and every event is recorded in the coarse-grained form shown in Fig. 4.4b. The analog signals are sent to discriminators with three treshold settings: the lowest ("EL") is set above noise to trigger on fast muons, the high ("EH") threshold is set to pick up the larger signal from slow muons and stops (the Bragg peak), and the very-high ("EVH") threshold is set above the Bragg peak to trigger on the heavily-ionizing recoil nuclei from $Z > 1$ captures. Custom data-acquisition modules record the state of all discriminator outputs every 200 ns (zero-words, when no signal out of a group of sixteen wires are above threshold, are suppressed).

The position of a muon stop in 3-D can be determined from the TPC data. The anode and strip that the muon stops on is unambiguously given by high-threshold hits preceded by a line of low-threshold hits. The anode (strip) gives the location in z (x). The height y in the TPC is not completely determined by the TPC data itself, but requires knowing when the event occurred. The height from the bottom of the drift region is

$$\Delta y = v_{\text{drift}}(T_{\text{drift}} - t_0), \tag{4.1}$$

where T_{drift} is the time delay after the muon entrance for the signal to be detected in the MWPC, and t_0 is the drift time across the 3.5-mm half gap of the MWPC (~ 500 ns). The distribution of stop positions determined this way are shown in Fig. 4.5.

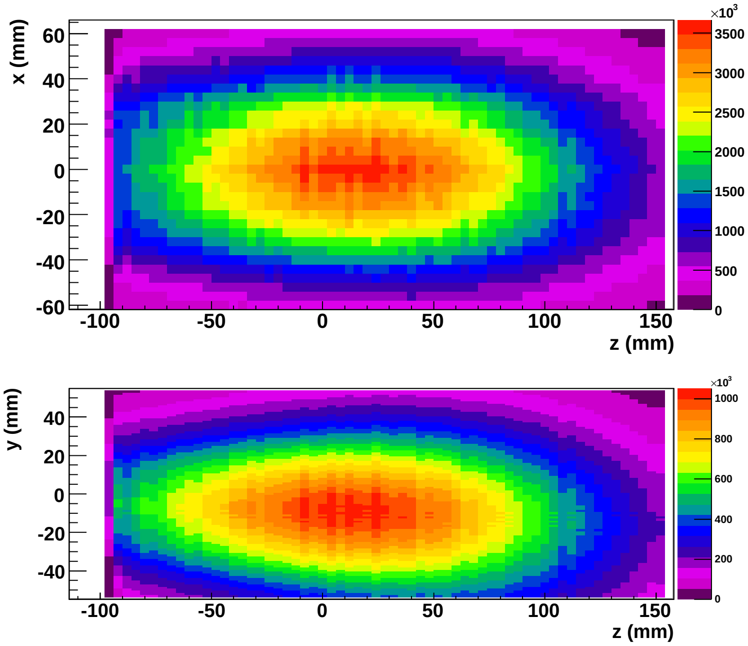

Figure 4.5: Distribution of muon stop positions determined by the TPC. The projection onto the xz- (yz-) plane is displayed in the top (bottom) panel. The z-axis is parallel to the beam axis, and muons enter from the left.

The TPC operates within an aluminum pressure vessel containing hydrogen gas at 10 bar and room temperature. The wall of the vessel is made of aluminum and is as thin as safety allows to minimize scattering of decay electrons. The 4-mm-thick aluminum wall is the primary scatterer for the majority of electrons that do not hit the TPC frames, limiting the ability of the electron detector to track back to the muon stop position. Figure 4.3b shows the pressure vessel installed in the experimental area. The pressure vessel is docked in the middle of the electron detector during data-taking.

4.5 Electron Detection

The electron detector times and tracks decay electrons originating from within pressure vessel. Its cylindrical geometry covers approximately 3π solid angle of the TPC active volume placed in its geometric center. An outer scintillator hodoscpe barrel provides the times t_e of electrons. Tracking in two concentric, cylindrical wire chambers allows selection of events in which the electron points back to the muon stop position, reducing background and permitting a method to monitor the deuterium content of the target. Figure 4.6 is a diagram

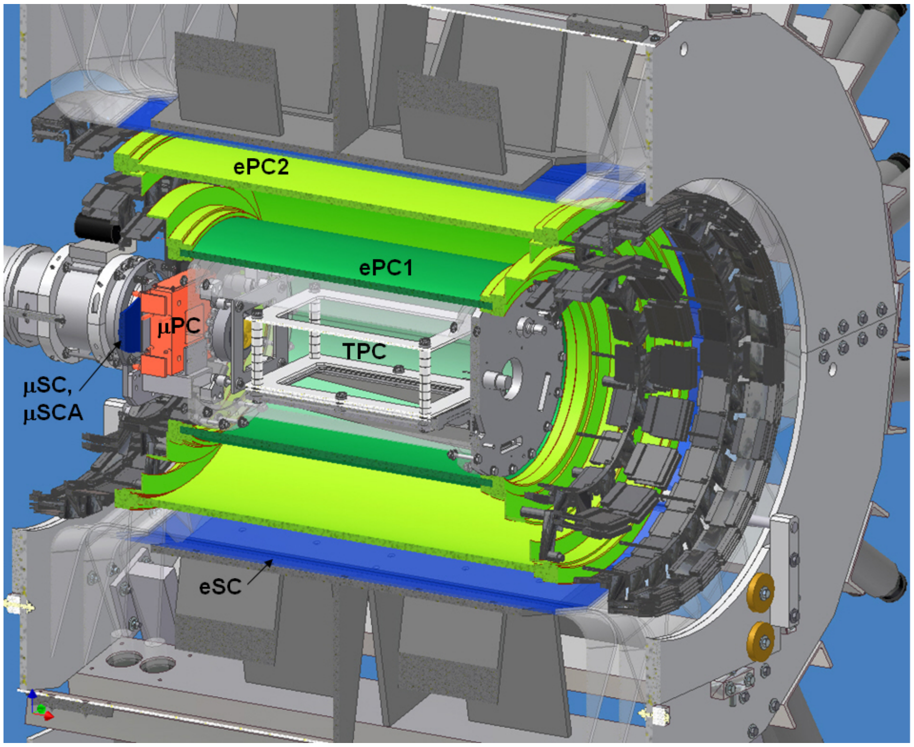

Figure 4.6: Cutaway diagram of the MuCap apparatus showing more of the support structure than in Fig. 4.1.

of the key MuCap detectors and may be a helpful reference in the following descriptions of electron detector components.

4.5.1 Scintillator Hodoscope Barrel

Fast timing of electrons is the purpose of the eSC, a scintillator hodoscope comprising sixteen segments, each with an active area of 90×15 cm placed with the long axis parallel to the beam axis, together forming a barrel with a diameter of 78 cm. Each eSC segment has two 5-mm-thick scintillating plastic layers, each viewed on both ends by photomultiplier tubes.

The total of 64 photomultiplier signals are input via discriminators to data acquisition modules (CAEN V767 time-to-digital converters) that record the time of each leading edge with 1.25 ns precision. The time difference between detection by the upstream and downstream photomultipliers provides some information about where the particle hit along the length of the segment. A study that involved placing a beta-source along the length of one of the segments found $v_{\text{gond}} = 67$ mm/ns in the relation $z = v_{\text{gond}}(t_{\text{upstream}} - t_{\text{downstream}})$, where t is the time of detection at the indicated end.

Parameter	ePC1	ePC2
Number of anode wires	512	1024
Number of inner cathode strips	192	320
Number of outer cathode strips	192	320
Operating voltage	+2.6 kV	+2.8 kV
Half-gap	4 mm	4 mm
Diameter at anodes	384 mm	640 mm
Active length	580 mm	800 mm
Anode spacing	2.356 mm	1.963 mm
Inner cathode screw angle	43.81 deg.	44.31 deg.
Outer cathode screw angle	46.19 deg.	45.74 deg.

Table 4.1: Physical parameters of the electron proportional chambers (ePCs).

All four photomultipliers on a given segment are required to be in coincidence in the data analysis. The 4-fold coincidence reduces the level of random noise from the eSC, generally leaving only signals from real particles.

4.5.2 Cylindrical Multiwire Proportional Chambers

The electron tracking detectors are two concentric, cylindrical multiwire proportional chambers, each with readout of anodes and cathode strips, to give the complete (ϕ, z) positions (in cylindrical coordinates) of an electron track at two different radii. The smaller chamber (ePC1) sits just outside the pressure vessel. The larger chamber (ePC2), with about twice the diameter as the smaller one, sits somewhat inside the scintillator hodoscope barrel (eSC). Anode wires run parallel to the cylinder axis, and cathode strips wrap around the chamber making an angle of ≈ 45 degrees with the anodes. The inner and outer cathode planes wind in opposite directions, providing redundancy if the anode and both cathode planes of a chamber are required. Physical parameters of ePC1 and ePC2 are given in Table 4.1.

The anode and cathode planes are fully instrumented with chamber-mounted, charge-integrating-preamp-discriminator cards. Although mounting the preamps directly on the chambers reduced electronic noise into the sensitive preamplifiers, it was necessary to shield the cards and the entire chamber from external electromagnetic interference. Copper mesh was placed 1) inside ePC1, 2) inside ePC2, and 3) outside ePC2 (see Fig. 4.7). The outputs of the preamp/discriminator cards are connected to custom data acquisition modules through 40-wire twisted pair cables (32 wires are used for signals, the remaining for for threshold setting and preamp power), and each cable is wrapped in braided wire shielding. The custom data-acquisition modules, called compressors, are based on FPGA circuitry. The

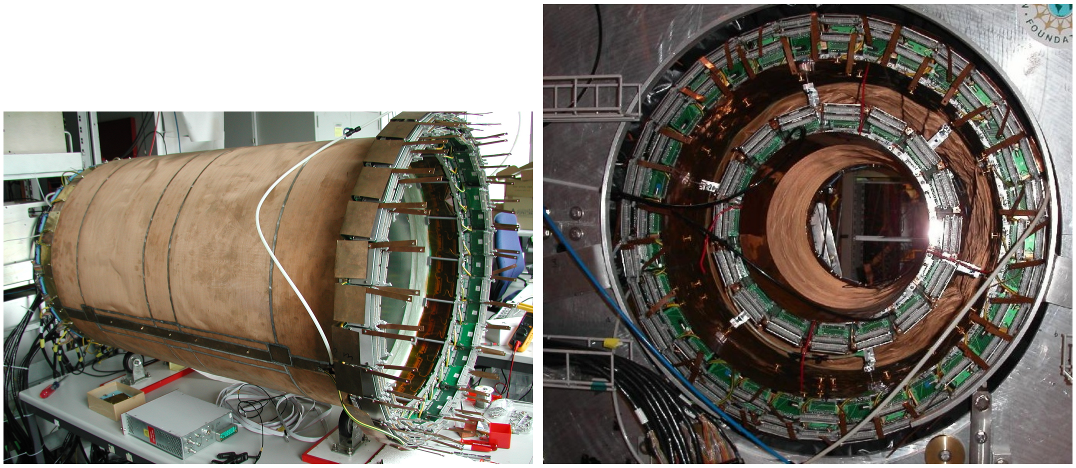

Figure 4.7: Photos showing (left) ePC2 in the lab during high-voltage training and electronics tests, and (right) the downstream end of the MuCap electron detector with both ePCs in place prior to cabling. The copper shielding mesh is visible in the photos.

discriminated signals from the ePC electronics are transmitted as low-voltage differential signals (LVDS) to the compressors, which encode them into time–channel words that are saved in a buffer.

4.6 Hydrogen Gas System

4.6.1 Protium Production

The protium gas is produced by electrolysis of deuterium depleted water and filled into the target volume through a palladium filter. The 40-liter target volume required 400 STP liters of protium for the gas pressure of 10 bar. An additional 800 STP liters of protium was produced to fill the circulating system described below.

The deuterium concentration of the target gas must be known to correct for its effect on the MuCap lifetime result. Measurement of the low concentration of residual deuterium content is difficult, but a system based on accelerator mass spectrometry developed recently at ETH Zürich [51] was adapted to this purpose to measure the MuCap production gas. The deuterium concentration was found to be $c_d = 1.44 \pm 0.13$ ppm. An alternate method to determine c_d based on MuCap data analysis is described in Chapter 6.

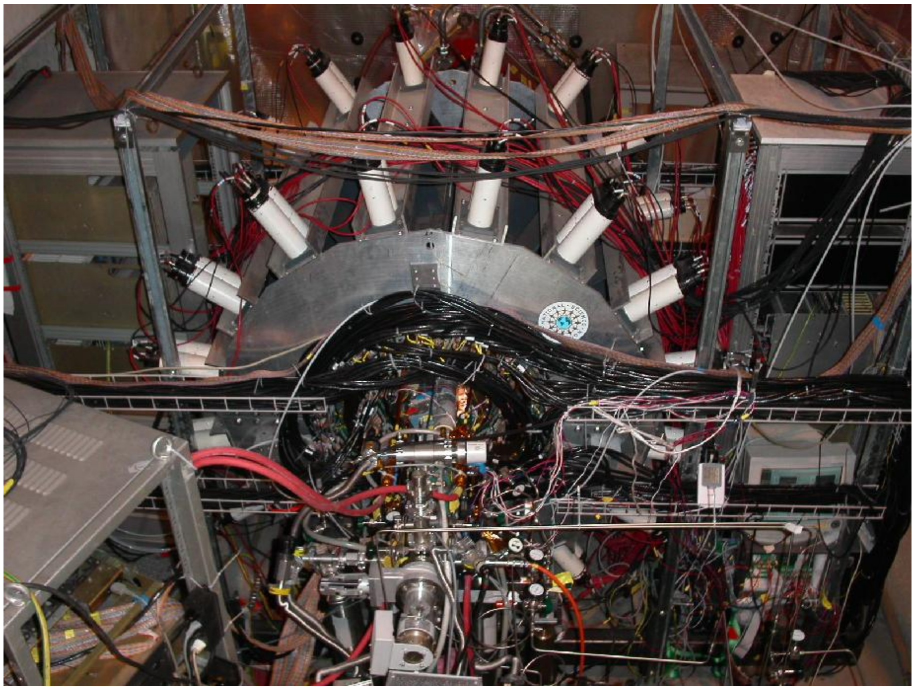

Figure 4.8: Photo of the downstream end of the MuCap apparatus with the TPC pressure vessel docked in the middle of the e-detector.

4.6.2 Circulating Hydrogen Ultra-Purification System

A system was developed for the MuCap experiment to continuously circulate the 10-bar hydrogen gas through cryogenic adsorbers, thereby maintaining a very low level of $Z > 1$ impurities. The circulating hydrogen ultra-high purification system (CHUPS) [52] employs an adsorption cryopump, which alternately adsorbs hydrogen through a one-way valve into liquid-nitrogen-cooled, activated carbon, and heats the carbon to release the hydrogen through another valve. The flow is directed through zeolite adsorbers for purification. The impurity levels throughout the Run8 experimental period are shown in Fig. 4.9. External measurements were made of the nitrogen and oxygen concentrations at a few points during Run8, confirming these to be very low after purification by CHUPS. The $Z > 1$ capture yield was measured *in situ* by the observation of recoil nuclei by the TPC, giving a signal proportional to the impurity concentration as described in Chapter 3. The capture yield itself does not reveal the exact impurity species, but subsequent measurements with a humidity sensor installed inline to the circulation system confirm water as the primary contaminant. The impurity level was low enough that it can be corrected for to sufficient accuracy through the arguments of Chapter 6.

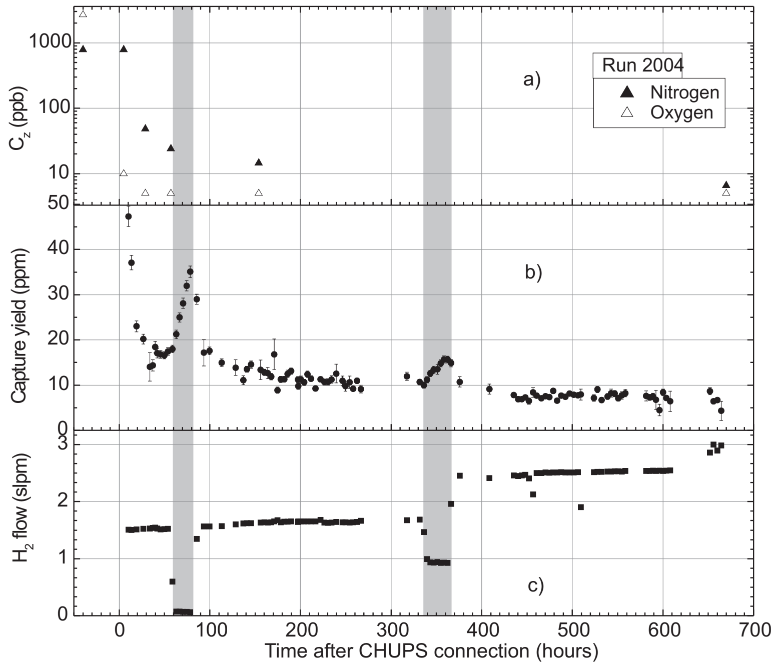

Figure 4.9: (from ref. [52]) Hydrogen flow rate, gas chromotography measurement results, and observed impurity capture yield (from the analysis described in Chapter 6) vs. time. The grey bands highlight periods when the purification system was turned off or reduced, and outgassing of impurities from interior surfaces of the target volume is evident by the increase of the capture yield.

4.7 Data Acquisition

The data acquisition system collects data from the various subsystems into raw data files for offline analysis. Data are collected in cycles of continuous readout from each detector for an average "live time" period of 120 ms, followed by a few milliseconds pause to clear out certain buffers. The cycle is repeated, maintaining a live time of better than 90%.

Most of the raw data consists of times of discriminated signals from individual muon and electron detector channels. Muon and electron signals were routed into different modules, following the principle of keeping muon and electron paths as separate as possible to avoid undue interference. Signals from the muon entrance detectors, MuSC and MuPC, were handled by a CAEN V767 time-to-digital conversion (TDC) module. Discriminated photomultiplier signals were routed into a separate CAEN V767 TDC. The custom-build data acquisition modules developed for the TPC and a separate system for the ePCs were both mentioned above. Data were continuously transferred from the modules via PowerPC

Data Set	TPC HV	Target Condition	Comment
Prod52	5.2 kV	production gas	early runs
Prod50	5.0 kV	production gas	most data
Prod48	4.8 kV	production gas	late runs
CalibN	4.8 kV	nitrogen-doped production gas	$Z > 1$ calibration
CalibD	4.8 kV	deuterium-doped production gas	c_d calibration
CalibNat	4.8 kV	natural hydrogen	c_d calibration

Table 4.2: Data sets defined by different run conditions.

VME controllers to PCs across gigabit ethernet.

In addition to the TDC data, some analog-to-digital (ADC) data were stored for special studies. Analog signals from sixteen anodes in the center of the TPC were recorded by flash ADCs. They were read out at most once per 120-ms live time block, allowing only one event per block to be recorded by these modules. Trigger logic was implemented to catch $Z > 1$ capture candidates, and some muon stops were recorded for normalization. These data provide a method to find the $Z > 1$ capture yield for muons stopped in the center of the TPC. The other method, described later in Chapter 6, is to use the TDC data. The additional information in the flash ADC data can be used to find the energy spectrum of the recoil products.

4.8 Run Conditions

The 2004 run period ("Run8") was mainly devoted to taking data with μ^- stopped in ultrapure, deuterium-depleted hydrogen. This is considered the production data, the primary measurement of MuCap. Some μ^+ data were accumulated to study backgrounds, such as those relevant to the $Z > 1$ capture identification. After the main production period, calibration data were taken in which the target conditions were changed, for example by adding a small, known amount of a $Z > 1$ impurity. Runs with natural hydrogen were also taken to calibrate the effect of deuterium on the lifetime measurement. The total raw data volume (compressed) was about 5 TB on disk.

The production data is subdivided depending on the high voltage setting of the TPC's multiwire proportional chamber. It was originally planned to set the voltage to 5.4 kV or higher to detect rare events of interest, in particular the Alvarez muon from $p\mu d$ fusion, which would have given another means to infer the deuterium content of the production gas. Instead a hot spot appeared in the TPC, that is a point where sparking was occuring, preventing operation at the anticipated 5.4 kV. After some early data with the TPC at 5.2 kV, the voltage was reduced further to 5.0 kV, where it remained for most of the production period. A few production runs were taken at 4.8 kV, enough to see the relatively large signals from slow muons. The results of the 2004 analysis are from the data set with the TPC at 5.0 kV.

Calibration runs followed the production running period. The purification system was bypassed, and nitrogen was mixed into the production gas for a concentration $c_{\mathrm{N}} \approx 11$ ppm. The data set defined by this target condition is called CalibN and will be used to relate the observed $Z > 1$ capture yield to the effect of the impurities on the muon lifetime.

Two calibration sets were intended to inform the correction for deuterium. After the CalibN runs, the purification system cleaned out the production gas and was again bypassed. Natural hydrogen, with deuterium concentration $c_d \approx 122$ ppm, was mixed into the production gas through a palladium filter for a net deuterium concentration of $c_d \approx 17$ ppm. The data under these conditions is called CalibD. For unknown reasons the $Z > 1$ capture yield, as monitored by the TPC, was more than ten times higher than in the production data. The high level of $Z > 1$ contaminants could spoil the calibration for deuterium, and the target gas could not be cycled through the purification system without isotopically contaminating the entire system. It was decided to throw away the CalibD gas and refill natural hydrogen again through a palladium filter, but this time without diluting with the production gas. The data with natural hydrogen comprise a set called CalibNat.

Additional calibration data were taken in the 2006 run period. A water permeation tube was installed in the hydrogen circulation system to maintain a low, steady-state concentration of water. Other calibration data were taken again with nitrogen-doped production gas. The TPC high voltage was set to 5.45 kV in the 2006 run period. These data sets are used to determine the correction for $Z > 1$ impurities as described in Chapter 6.

Chapter 5

Data Analysis

The analysis software is designed to translate raw data into a collection of "physics objects" — mainly muon stops in the TPC and electron tracks through the e-detector — from which quantities will be derived and filled into histograms depending on various selection criteria ("cuts"). For example, muon–electron time differences are filled into histograms to build up muon decay-time spectra, perhaps requiring the reconstructed electron track to be within a certain impact parameter (distance of closest approach) with respect to the muon stop position. Basic indicators of detector performance, rates, and data-quality are also studied.

Two independent analyses of the 2004 MuCap data were performed: the one described in this document was developed by the author at the University of Illinois at Urbana-Champaign (UIUC). The other analysis was conducted at the University of California, Berkeley (UCB). Individuals involved directly or peripherally in either analysis were blinded to the actual master clock frequency, which was known to be detuned from the nominal $f_{\mathrm{clock}} = 100$ MHz by $\sim 10^{-3} f_{\mathrm{clock}}$, the exact amount known to only two people. It is assumed throughout the analysis that f_{clock} is exactly 100 MHz until a final unblinding step, when λ^{MuCap}, the observed μ^- disappearance rate with all internal systematic corrections applied, is adjusted based on the actual clock frequency $f_{\mathrm{clock}}^{\mathrm{actual}}$ by a factor $f_{\mathrm{clock}}^{\mathrm{actual}}/(100\ \mathrm{MHz})$. As an additional level of blinding intended to prevent false convergence of UIUC and UCB results, each person adjusted their own results by an individual, secret offset $\sim 10^{-3}$ before reporting them to the rest of the collaboration. No such additional offset is imposed in this document.

The analysis steps to form muon and electron objects may be considered "low-level," in the sense that individual detector elements are studied in detail. This is in contrast to the generally "high-level" construction of lifetime histograms and the studies of systematic effects in Chapter 6, which are based on properties of the muon and electron objects identified in the low-level analysis. The low-level analysis reads the raw data produced in the experiment. Each raw data file contains consecutive DAQ live-time periods ("blocks") of ≈ 120 ms, during which all data from every detector were recorded without interruption. The software operates on these 120-ms blocks individually, finding coincidences within detector planes and between them, filling in a series of diagnostic histograms, identifying muon tracks in the TPC data, finding coincidences between e-detector planes, ultimately constructing muon and electron objects according to specified definitions. Once these objects are formed, they are written to file for subsequent higher-level analyses. By design, the UIUC analysis maintains logical separation of muon and electron signals when forming the physics objects.

Many of the systematics studies involve varying the muon or electron definition, and this is anticipated in the low-level analysis. Several versions of electron objects are constructed in parallel, with more or less strict inter-plane coincidence requirements: for example, an electron could be defined by the eSC only or by coincidence between all ePC and eSC planes. In the case of muon stops, objects formed per the minimal definition — a single hit in one entrance detector plane and a track in the TPC — comprise a superset of all other muon definitions studied; thus, parameters are included in each muon object for possible rejection at a later stage if it fails a stricter cut, such as smaller fiducial volume or coincidence with additional entrance detector planes.

5.1 Muon Definition

The minimal muon stop definition requires 1) a hit in the MuSC separated from all other MuSC hits ("pileup protected"), or any MuSCA hit, by at least 25 μs, and 2) a TPC high-threshold ("EH") signal within 0–25 μs of the MuSC hit. The muon entrance time is provided by the MuSC, and the presence of an EH hit in the TPC indicates a possible Bragg peak of a muon stop. Pileup protection is necessary to avoid ambiguities in associating tracks in the TPC with the correct entrance time. Muon stops are identified in the TPC data and characterized by stop positions and track-quality indicators for later selection.

5.1.1 Muon Entrances

Although pileup protection with the MuSC rejects on average $\approx 99\%$ of the events in which an additional muon entered, much better rejection is achieved by including the MuPC. The MuPC has two independent planes, one with anodes running vertically to give the x-position, and the other with anodes running horizontally to give the y-position. Time-coincident singles hits in a given plane are clustered together if the wires are next- or next-nearest neighbors — the usual treatment of a multiwire proportional chamber, in which a single

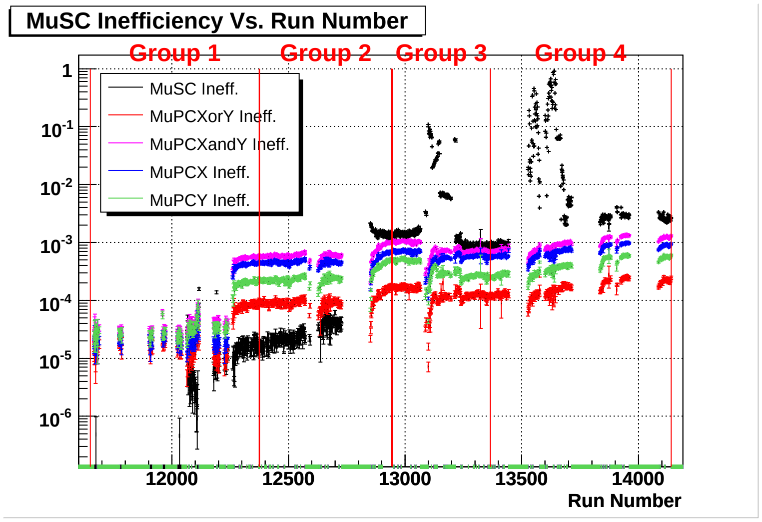

Figure 5.1: Relative counting inefficiencies of the muon entrance detectors vs. time (here a "Run" is a data-taking period of typically 12 minutes). The vertical red lines show the subdivision of the Prod50 data into chronological groups of similar total statistics. The MuSC was changed from a 500 μm-thick scintillator to one of half the thickness after about 12750 on the horizontal axis, corresponding to a 100-fold increase in MuSC inefficiency. Other periods of especially poor MuSC efficiency are obvious from this study.

particle may be detected in more than one nearby channel. Clusters in the MuPC x- and y-planes can be checked for interplane coincidences to define (x, y) coordinates of muon entrances. In case of pairing ambiguities such as two hits in the x-plane time-coincident with a hit in the y-plane, the analysis creates a separate (x, y) pair for each possibility.

In the strictest muon entrance definition, the MuSC hit must be coincident with a single MuPC (x, y) hit, and there can be no other hits in the MuSC, MuSCA, or any MuPC wire within the ± 25 μs pileup-protection gate. The pileup protection by the MuPC stabilized what would otherwise have been vastly different levels of undetected pileup during the run.

A special study was performed to check the relative efficiencies of the entrance detector planes. The trigger is a MuSC hit (pileup-protected with itself) with a coincident muon stop in the TPC, and the fraction of triggers with coincident hits in MuPC planes is found. In a variation to check the MuSC, the trigger is a MuPC (x, y) hit (pileup-protected with all MuPC wires) coincident with a muon stop, and the fraction of triggers with coincident MuSC hits is found. The results are shown in Fig. 5.1. A different study, described in Section 6.2 of Chapter 6, finds the overall pileup-protection inefficiency to be $\sim 10^{-5}$ throughout Run8 if the MuPC planes are included.

5.1.2 Muon Stops

The concepts involved in characterizing events in the TPC are briefly described in this section.

Region of Interest (ROI). Each muon entrance time t_μ defines a ROI in the TPC data of $0 \leq t_{\mathrm{TPC}} - t_\mu < 25$ μs, where t_{TPC} is the absolute signal arrival time at the MWPC of the TPC. Since the maximum drift time in the TPC is ≈ 22 μs, the ROI contains all events in the TPC coincident with the muon entrance time. The pileup protection by the entrance counters means, to the extent the entrance counters are efficient, up to one muon track per ROI is expected.

Pixel Space Mapping. The TPC data are the 200-ns-discretized times-over-threshold of signals in each anode and (4 tied together) cathode wire of the MWPC. A pixel space $(\tilde{x}, \tilde{y}, \tilde{z})$ is defined that maps to real space (x, y, z) (divided into a lattice of points) assuming all events are prompt with the muon entrance. More precisely, projections of the spaces onto 2-D are observed. TPC anodes data give the projection onto the $\tilde{z}\tilde{y}$ plane:

$$\tilde{z} = (\text{Anode Number}) \leftrightarrow z, \tag{5.1}$$

$$\tilde{y} = (t_{\mathrm{TPC}} - t_\mu)/(200 \text{ ns}) \leftrightarrow y; \tag{5.2}$$

TPC cathodes data give the projection onto the $\tilde{x}\tilde{y}$ plane:

$$\tilde{x} = (\text{Cathode Number}) \leftrightarrow x, \tag{5.3}$$

with the same relation in the y-dimension as for the anodes. In terms of the wire spacing and drift velocity $v_{\mathrm{drift}} = 5.54 \times 10^{-3}$ mm/ns (based on $t_{\mathrm{TPC}} - t_\mu$ coincidence time histograms),

$$\frac{\partial x}{\partial \tilde{x}} = 4 \text{ mm}, \tag{5.4}$$

$$\frac{\partial y}{\partial \tilde{y}} = v_{\mathrm{drift}} \times (200 \text{ ns}) \approx 1.1 \text{ mm}, \tag{5.5}$$

$$\frac{\partial z}{\partial \tilde{z}} = 4 \text{ mm} \tag{5.6}$$

An example of TPC data represented in pixel space is shown in Fig. 5.2a. Each non-zero pixel corresponds to a low-threshold (EL) hit, represented by a green pixel. If the signal was large enough to be over the high threshold (EH), which usually indicates the Bragg peak of a muon stop or an impurity capture event, the pixel in the display is blue. In the rare case

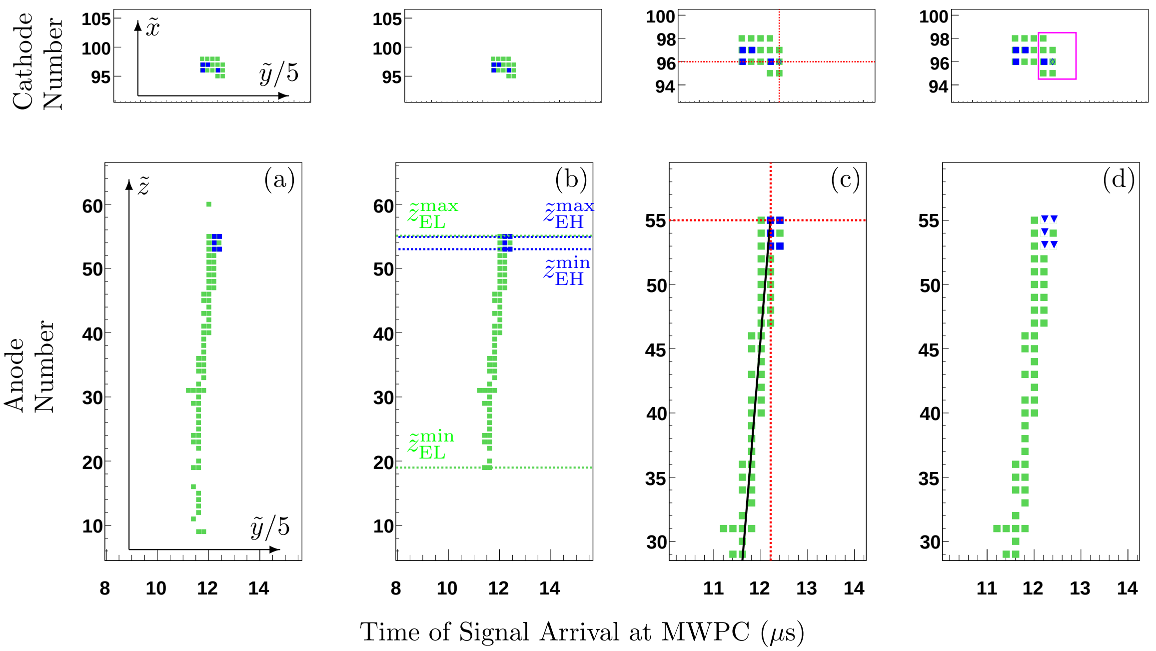

Figure 5.2: Illustration of the analysis steps to identify a muon stop in the TPC data. Actual data from a muon entrance are shown, and the muon enters from the bottom in each panel. (a) The raw data of a muon stop, represented in “pixel” space, is shown for anodes (bottom panel) and cathodes (top panel). Green pixels for low-threshold hits and blue are for high-threshold hits. The remaining panels show the results of analysis steps applied to the data in (a). (b) These are the anode pixels connected by next-nearest neighbors into a single cluster that includes at least one high-threshold pixel. (c) The cross-hairs (dashed red lines) show the location of the muon stop as determined in the analysis. (d) The anode pixels identified as part of the Bragg peak are displayed as inverted triangles, and the cathode pixels used for fiducial volume cuts are contained within the purple box in the upper panel.

of a very-high-threhold (EVH) hit, as from an impurity capture event, a red pixel is drawn (none are present in Fig. 5.2).

Pixel Clustering. Anode pixels within the ROI are clustered into “pixel islands,” groups of connected low-threshold (EL) pixels with at least one high-threhold (EH) pixel in the group. A gap of one pixel is allowed in the clustering, so each pixel is connected to the rest of the island by a neighboring or next-nearest-neighboring pixel. Each pixel island is a candidate muon stop event. In Fig. 5.2b, pixels included in the island are displayed. The maximum and minimum extents of the EL and EH pixels included in the island — denoted by $\tilde{z}^{\max}_{\mathrm{EL}}$, $\tilde{z}^{\min}_{\mathrm{EL}}$, $\tilde{z}^{\max}_{\mathrm{EH}}$, and $\tilde{z}^{\min}_{\mathrm{EH}}$ — are indicated by the horizontal dashed lines in the figure. Only one EH-containing island is found in this ROI, the predominant situation after muon entrance pileup protection. If another pixel island had been found, it would have been handled as a separate muon object with the same entrance time t_μ.

Muon Stop Definition. The requirements a pixel island must satisfy to be considered a muon stop event are very simple:

$$\tilde{z}_{\mathrm{EL}}^{\max} - \tilde{z}_{\mathrm{EH}}^{\max} \leq 2,, \tag{5.7}$$

$$\tilde{z}_{\mathrm{EH}}^{\min} - \tilde{z}_{\mathrm{EL}}^{\min} \geq 5. \tag{5.8}$$

Equation 5.7 cuts tracks that have too many EL pixels downstream of the apparent Bragg peak, which would be inconsistent with an actual muon stop traveling in that direction. Equation 5.8 further ensures the track is consistent with a muon orginating from upstream, which should have sufficient EL pixels leading up to a Bragg peak. The reason for such a simple track definition, as explained in Section 6.3 of the Systematics chapter, is to avoid a time-dependent cut caused by interference from decay-electron-induced EL pixels included in the pixel island.

Muon Stop Location. Typically the position of the earliest (minimum $\tilde{y}$) of the most downstream anode EH pixels (i.e., anode EH pixels with $\tilde{y} = \tilde{y}_{\mathrm{EH}}^{\max}$) is taken as the stop position $(\tilde{y}_{\mathrm{stop}}, \tilde{z}_{\mathrm{stop}})$ in the $\tilde{y}\tilde{z}$-plane. In the rare case of a track having a large angle with respect to the $\tilde{z}$ axis, an anode EH pixel that better represents the stop position is chosen according to slightly different criteria that will not be discussed here. The stop position in $\tilde{x}$ is taken as the average of all cathode EL pixels with $\tilde{y} = \tilde{y}_{\mathrm{stop}}$. The stop position thus found is shown by the intersection of the dashed lines in Fig. 5.2c (along with a best-fit line to the EL pixels). If there are no cathode EL pixels with exactly this $\tilde{y}$ position, then the search for cathode EL pixels is repeated with $\tilde{y}_{\mathrm{stop}} - 1$, then $\tilde{y}_{\mathrm{stop}} + 1$, etc.; the search is expanded in $\tilde{y}$ as far as $\tilde{y}_{\mathrm{Bragg}}^{\min} - 1 \leq \tilde{y} \leq \tilde{y}_{\mathrm{Bragg}}^{\max} + 1$, where the subscript "Bragg" refers to anode EH pixels of the identified Bragg peak. The anode EH pixels included in the Bragg peak, marked by inverted triangles in the lower panel of Fig. 5.2d for the example track, are found by next-nearest-neighbor clustering of anode EH pixels starting on $(\tilde{y}_{\mathrm{stop}}, \tilde{z}_{\mathrm{stop}})$. A muon stop without a coincident cathode pixel is not rejected outright but will fail the subsequent fiducial volume cut, since the x-position is undetermined.

Fiducial Volume Cut. The purpose of this selection is to keep only muons stopped well-away from the edges of the TPC's active volume. Two fiducial volumes are imposed: an "outer" volume, within which all anode EL pixels of a track must be contained, and a slightly smaller "inner" volume, within which the stop position must lie. The outer volume nearly fills the entire TPC drift region, rejecting only pixel islands that include an edge cathode, anode, or 1.1-mm drift unit — i.e., the outermost pixels of the drift region. The $\tilde{x}$-limits used for the outer fiducial cut are based on the cathode pixels with $\tilde{y}^{\rm min}_{\rm Bragg} - 1 \leq \tilde{y} \leq \tilde{y}^{\rm max}_{\rm Bragg} + 1$; this is illustrated in Fig. 5.2d by the box in the upper panel of Fig. 5.2d. The inner volume is nested within the outer, with each bound smaller by 4 mm in x and z (1 unit in each of $\tilde{x}$ and $\tilde{z}$) and 5.5 mm in y (5 units of $\tilde{y}$). Muons stopped within the inner volume are more than 6 mm away from the bounds of the TPC drift region and even further from any $Z > 1$ material.

The purpose of two fiducial volumes, with the looser one applied to the EL pixels, is to avoid a time-dependent track acceptance in the following situation: 1) a muon stops near the boundary of the inner fiducial volume, 2) some time later the muon decays, and 3) the electron produces a knock-on electron that is detected as an EL pixel included in the pixel island, extending the island outside the fiducial cut. These knock-on or delta electrons are discussed further in Chapter 6. It could be argued, in principle, that the outer fiducial volume in the y-dimension should be brought one or two pixels further from the bounds to perhaps catch more $\mu + p$ scatter events (see Sec. 6.4); in practice, however, the cut appears to be adequate as will be demonstrated by the consistency studies of Chapter 6.

5.2 Electron Definition

In the ideal case, a decay electron is detected in one channel of each plane of the tracking chambers (ePCs) and and by each photomultiplier channel of a segment of the scintillator hodoscope (eSC), and no signals are present on any other channel until the next electron, well-separated in time, is detected. An example electron trajectory through the detector is shown in the detector diagram Fig. 4.1, which gives the name of each particle detector in MuCap. The analysis of the ideal case would form an electron object simply by finding time-coincidences between all detector planes. In practice it is more complicated because a single particle can create signals on more than one wire in an ePC plane, or it can fail to produce a signal on some planes. Ambiguities in the case of multiple signals in a single detector, such as from a cosmic particle traversing the detector at the same time as the decay electron, require making a choice of which hit on one plane to pair with which in the other.

The details of the electron analysis are not necessary to understand the discussion of systematic effects in Chapter 6. It is sufficient to understand that choices are made of how to define an electron event, and some variations of these choices are executed in parallel. Different versions of the electron objects can be used to construct the muon lifetime histograms, testing the effect of the choice of electron definition on the measured lifetime. The algorithms used by the analysis to form electron objects are covered in Appendix C.

5.3 Lifetime Fit Method

Lifetime spectra are fit with an exponential plus flat background,

$$f(t) = N\lambda w e^{-\lambda t} + B, \tag{5.9}$$

where w is fixed to the lifetime histogram bin width of 40 ns, and N, λ, and B are fit parameters. Unless otherwise noted, the lifetime spectra with complete electron detector tracking, requiring an OR of the cathodes in each ePC, is used. The standard fit range is 100 ns to 24000 ns. Considering the binning phase of the lifetime spectra, the effective fit range is 120 ns to 24000 ns after the muon stop.

Some of the lifetime histograms are filled requiring only one electron in the range -10 μs to 24.5 μs. In addition, for these "1e" spectra an e-detector ambiguity (flagged in the raw data analysis stage) within this gate also vetos the event. Bin errors are corrected for double counting in the flat background due to throughgoing particles (see Section 6.1), except in the case of "1 electron gated" spectra, which exclude double counting events by construction.

Chapter 6

Systematic Effects

An advantage of the MuCap experiment over previous measurements of ordinary muon capture in hydrogen is demonstrated by the generally model-independent evaluation of the small systematic corrections, and by the availability of numerous unbiased cross checks of the lifetime result. Required systematics corrections are small in part because of the low background of $Z > 1$ capture events, either from impurities within the hydrogen gas itself, from μp diffusion of muons stopped near wall materials, or from transfer to deuterium and subsequent diffusion into wall materials. Selecting only one muon at a time ("pileup protection"), which is enabled by the muon entrance counters, avoids distortions to the lifetime spectrum that would otherwise occur due to electron detector dead times and muon tracking ambiguities in the time projection chamber (TPC).

Many cross checks of the lifetime result are possible because data from each detector were continuously, independently recorded. The electron definition, for example, can be made more or less strict by the number of electron detector planes required. Care is required in the analysis of the electron proportional chambers because of, e.g., their slow response or the possibility of electronic pickup by the sensitive preamplifiers. The wire chambers can be entirely removed from the electron definition, retaining only the fast scintillators, and the lifetime result can be compared to that when all planes are included.

The studies presented in this chapter are data-driven whenever possible. A parameter in the analysis is varied, and the effect on the (inverse) lifetime λ is observed. If λ exhibits linear behaviour with the variations in a way that is understood, then a systematic correction $\Delta\lambda_{(sys)}$ is applied to λ. The statistical uncertainty in λ of $\sigma_{\text{stat}} = 12\ \text{s}^{-1}$ should be compared to each $\Delta\lambda_{(sys)}$. Effects leading to a correction much smaller than σ_{stat} can be neglected, and non-negligible but small corrections may be adequately covered by assigning a systematic uncertainty to an estimated upper bound of the effect.

6.1 Doubly-Counted Background Events

Particles that traverse the electron detector, starting from external sources, can lead to double counting in the backgrounds of lifetime spectra. Figure 6.1 illustrates a throughgoing track, and figure 6.2 shows evidence of these in the data. As will be demonstrated, the effect of double counting on the lifetime result appears to be minimal, ≈ 0.4 s^{-1}. It will also be shown that we can attribute approximately half of the flat background to doubly-

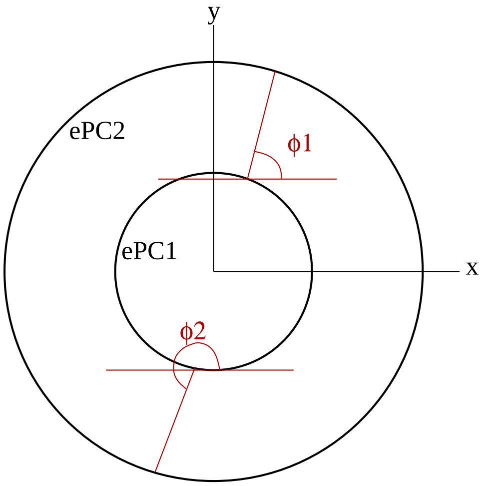

Figure 6.1: Beam-view diagram of ϕ of electron track. Time-coincident electron tracks with $|\phi_1 - \phi_2| > 2.6$ are considered throughgoing tracks.

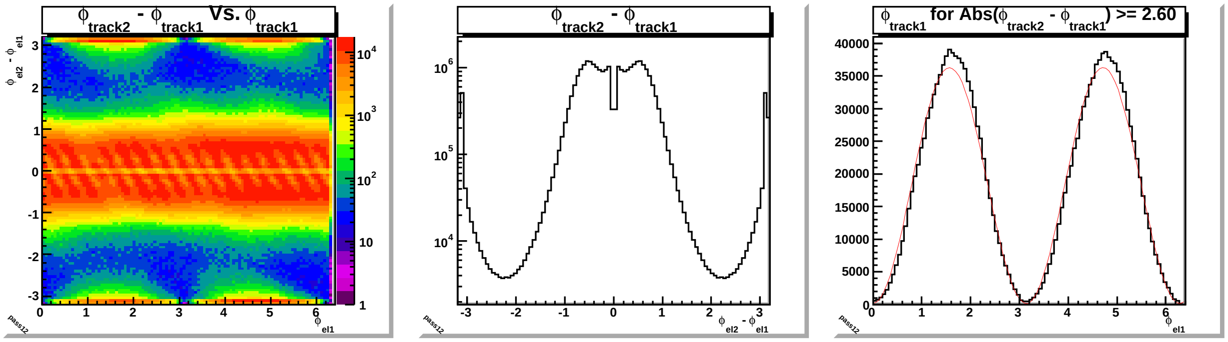

Figure 6.2: Relative angle in the (x, y)-plane of time-coincident e-detector tracks, 120 mm impact parameter cut with the muon stop location. Left: $\Delta\phi$ vs. ϕ of one of the tracks; Middle: projection of the leftmost histogram onto the $\Delta\phi$ axis; Right: projection of the leftmost histogram onto the ϕ axis for $|\Delta\phi| \geq 2.6$. Time-coincident electron tracks with $|\Delta\phi| > 2.6$ are considered throughgoing tracks.

counted, throughgoing tracks, regardless of whether or not a 120 mm impact parameter cut is imposed.

The calculation of how to correct the bin errors for double counting in the flat background begins by defining a given bin as composed of signal S and background B. Here, B comprises contributions from particles that are doubly-counted B_{double} and singly-counted B_{single}. If each particle were counted only once, instead of $B = B_{single} + B_{double}$, we would have $B_{correct} = B_{single} + B_{double}/2$. If uncorrected, the error of B is taken to be the usual $\sigma_B = \sqrt{B}$. However, the single and double components should be considered separately and their errors added in quadrature:

$$\begin{aligned}
\sigma_{B,single} &= \sqrt{B_{single}}, \\
\sigma_{B,double} &= 2\sqrt{B_{double}/2} = \sqrt{2B_{double}}, \\
\sigma_B &= \sqrt{\sigma^2_{B,single} + \sigma^2_{B,double}} = \sqrt{B_{single} + 2B_{double}}.
\end{aligned}$$

The last equation, for the corrected error of B, can be rewritten in terms of the fraction of the flat background due to doubly-counted particles, $m = B_{double}/B$:

$$\sigma_B = \sqrt{B + mB} = \sqrt{(1+m)B}. \tag{6.1}$$

The total error for a given histogram bin with contents C is $\sigma_C = \sqrt{\sigma_B^2 + \sigma_S^2}$. Rewriting $S = C - B$ and some substitutions gives:

$$\sigma_C = \sqrt{(1+m)B + C - B} = \sqrt{C + mB}. \tag{6.2}$$

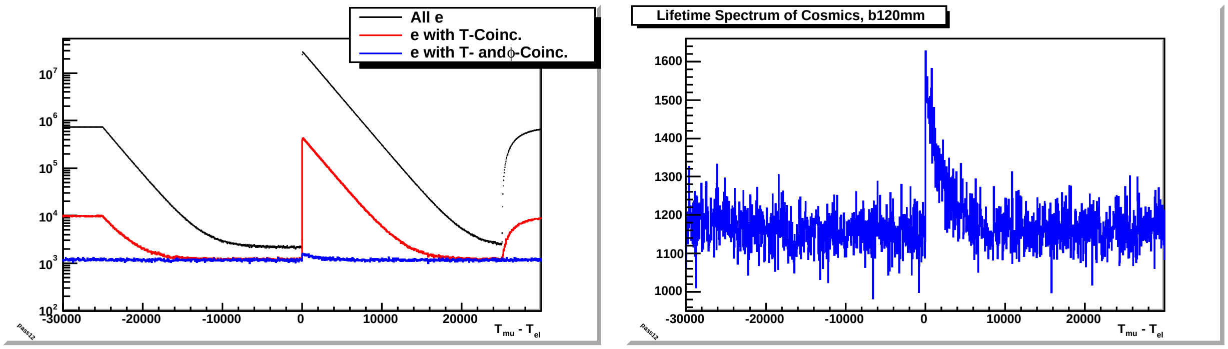

Figure 6.3: Spectra of Throughgoing Tracks Study, 120 mm Impact Parameter Cut. Muons are stopped within the TPC fiducial volume; electrons are fully tracked (eSC×ePC1×ePC2); and a 120 mm impact parameter cut is imposed.

Bin	N	λ [s^{-1}]	B/N	χ^2/DOF
all e	1.603×10^9	455430.0 ± 12.2	1.344×10^{-6}	1.05 ± 0.06
T-coinc. e	2.474×10^7	455405.0 ± 109.1	4.832×10^{-5}	1.84 ± 0.06
T-coinc. e and $\lvert\phi_2 - \phi_1\rvert > 2.6$	2.015×10^4	506885.4 ± 21368.2	5.749×10^{-2}	1.83 ± 0.06
T-coinc. e and $\lvert\phi_2 - \phi_1\rvert \leq 2.6$	2.472×10^7	455337.9 ± 98.0	1.371×10^{-6}	1.99 ± 0.06
all e, errs. adjusted, $m = 0.54$	1.603×10^9	455429.6 ± 12.2	1.344×10^{-6}	0.97 ± 0.06

Table 6.1: Fits to spectra of throughgoing tracks study, 120 mm impact parameter cut. The fit function is $y = Nw\lambda e^{-\lambda t} + B$, where w is the (fixed) bin width of 40 ns; the fit range is 0.1 μs to 24 μs. Muons are stopped within the TPC fiducial volume; electrons are fully tracked (eSC×ePC1×ePC2); and a 120 mm impact parameter vertex cut is imposed. "T-coinc. e" means time-coincident electron tracks. The fit of the last row is of the lifetime spectrum after correcting bin errors by the procedure outlined in this section.

The procedure used to correct the bin errors of a given lifetime spectrum, for example the black spectrum of figure 6.3, is the following:

1. Under the same conditions as the lifetime spectrum, fill a similar histogram selecting only electron tracks that are time coincident with another track, and have $|\phi_1 - \phi_2| > 2.6$. This is the blue spectrum in figure 6.3.

2. Fit both spectra (the original and the "cosmics"), and take the ratio of the B-terms to find m, $m = B_{cosmics}/B_{all}$. Table 6.1, rows 1 and 3 show these fits, and we see that $m \approx 0.5$.

3. For each bin of the lifetime spectrum, recalculate the errors according to equation 6.2.

4. Fit the spectrum again using the corrected bin errors. Results for the example are shown in the last row of table 6.1 and should be compared to the first row, which is the fit with uncorrected bin errors.

Fits to spectra as described by the above procedure are shown in table 6.1 for the lifetime spectra having a 120 mm impact parameter cut; it is observed that about half of the background is composed of doubly-counted events. The same procedure was also applied to the spectra having no impact parameter cut. In both cases, and in spite of quite different background levels ($\sim$ 5 times larger for the no-cut spectrum), the fraction of the background due to throughgoing tracks is $m \approx 0.5$. Comparing the spectrum of all time-coincident electrons with the spectrum of time-coincident, ϕ-opposite electrons shows that the flat backgound of the former is almost entirely accounted for by the latter.

6.2 Entrance Counter Inefficiency

Entrance counter inefficiencies come in two varieties: time dependent, especially due to the MuSC dead time, and time independent, i.e., uncorrelated to a given muon entrance. The effects of each type are examined in turn.

6.2.1 Time-Dependent Inefficiency

The important inefficiency time structure is that due to the 10-ns dead time of the MuSC. If two muons arrive simultaneously and within the spatial pair resolution of the MuPC, only one signal will be detected. If one of the muons further goes on to stop in the TPC, while the other stops in some $Z > 1$ material, a decay electron from the latter may be detected and associated with the former, good muon stop. A distortion of the lifetime spectrum can also be caused by the "wrong electron" effect, in which one muon sets the entrance time t_μ, and the time t'_e of an electron from an unobserved muon entrance is associated with the entrance at t_μ. Here, the "wrong electron" effect is not expected to be a problem, because 1) it shifts the lifetime spectrum of some muon decay events to the right by up to the dead time, and 2) the dead time is shorter than the 120-ns start time of lifetime fits.

To investigate the overall effect of the MuSC dead time on the lifetime measurement, the artificial dead time (ADT) was increased, from the standard $T_{\mathrm{ADT}} = 10$ ns, to 30 ns, 60 ns, 100 ns, and 150 ns. The rest of the analysis was run as usual, including the MuPC treatment, and lifetime spectra were created for the different MuSC ADTs. From the fit results $\lambda_{\mathrm{fit}}(T_{\mathrm{ADT}})$ of these spectra the nominal λ_{fit} based on the best (10 ns) ADT was subtracted, generating a set of lifetime deviations $\Delta\lambda_{\mathrm{fit}}(T_{\mathrm{ADT}})$ attributed to the increase in the dead time. Figure 6.4 shows $\Delta\lambda_{\mathrm{fit}}(T_{\mathrm{ADT}})$ plotted against T_{ADT}, revealing a monotonically increasing λ_{fit} as T_{ADT} increases. Two sets of points are plotted: the blue circles are from fits to the usual lifetime spectra in which the electron track is required to point back at the muon stop position to within a 120-mm impact parameter; the red triangles are for the spectra of all electrons regardless of their impact parameter with the muon stop position. The reduced sensitivity of the 120-mm-impact-parameter-cut lifetime spectrum to increases in artificial deadtime is consistent with the expectation that the vertex cut rejects many of the electrons from bad muon stops.

The observed linear dependence of $\Delta\lambda_{\mathrm{fit}}$ on T_{ADT} is also expected, since the number per muon entrance of undetected-pileup ("sneaky") muons that enter within the ADT interval of another muon is $N_{\mathrm{sneaky}} = R_{\mathrm{beam}} T_{\mathrm{ADT}}$, where R_{beam} is the (constant) beam rate. We

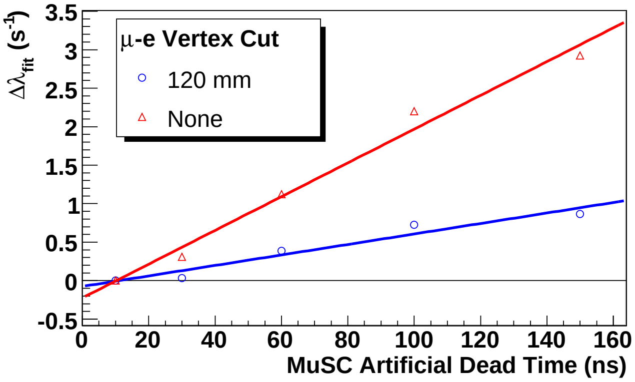

Figure 6.4: Lifetime vs. MuSC Artificial Deadtime setting, with and without the muon-electron vertex cut. The rates $\Delta\lambda_{\rm fit}$ are with respect to $\lambda_{\rm fit}$ of the spectrum with the standard (10 ns) MuSC artificial dead time and the specified muon-electron vertex cut. The lines through the data are linear fits based on equal weighting of each point for a given vertex cut.

could go further here with some order-of-magnitude estimates. The difference in the number of sneaky muons, when the dead time is 100 ns instead of 10 ns, is $\Delta N_{\rm sneaky} \approx 20000 \times 90 \times 10^{-9} = 1.8 \times 10^{-3}$ for a 20 kHz beam, for which $\Delta\lambda(b < 120\text{ mm}) = 0.7\text{ s}^{-1}$, and $\Delta\lambda(b < \infty) = 2.2\text{ s}^{-1}$. The effect on the lifetime for the no-impact-parameter-cut case is tiny, ~ 4 ppm, and three times smaller for the 120-mm-cut case. We could estimate 35% of $N_{\rm sneaky}$ stop outside of the TPC fiducial volume, leaving $\sim 6 \times 10^{-4}$ that are potentially "dangerous." Now the MuPC recovery fraction must be considered: perhaps ≈ 95–98% of the sneaky muons will be spatially separated from the first muon and be detected by one of the MuPC planes. A few times 10^{-5} remain, which must collectively have $\lambda \sim 10\%$ higher than the good stops. Many could be rejected by the e-detector acceptance even if no explicit cut is made, and many of those that stop in high-Z material like iron will disappear before the 120-ns start time of the lifetime fits. A type of elemental analysis could be performed by including high-Z lifetimes in the model function and fitting the difference of the standard lifetime spectrum from the spectrum with long ADT. In the end, however, it is not necessary to understand this type of undetected pileup further, because a linear extrapolation of $\lambda_{\rm fit}$ for the standard lifetime spectrum (120-mm impact parameter cut, $T_{\rm ADT} = 10$ ns) to the ideal case of $T_{\rm ADT} = 0$ implies a systematic correction of $\Delta\lambda \approx -0.06\text{ s}^{-1}$, completely negligible.

A similar study was carried out in which the MuPC per-wire dead time was varied from its standard setting of 650 ns to 300 ns and and to 1500 ns. The effects on the lifetime were minimal and consistent with statistically allowed deviations.

6.2.2 Time-Independent Inefficiency

In the following discussion, "time-independent inefficiency of entrance pileup protection" refers to the entrance-time-independent probability κ of an undetected ("sneaky") muon entrance within the ± 25-μs pileup-protection gate of an apparently isolated muon entrance. For pileup protection with only the MuSC detector, this type of inefficiency varied by orders of magnitude throughout the 2004 experimental run period (see Fig. 5.1). Pileup protection with the logical "or" of all entrance counters has much lower inefficiency, leading to a very small effect in the observed lifetime.

Time-independent inefficiency of the entrance detectors results in a non-flat background in the lifetime spectrum in the following way:

1. A muon entrance is detected at time t_μ, defining a region of interest (ROI), and more importantly a fiducial volume in the TPC equivalent to a coincidence time interval of approximately $2 < t_{\rm TPC} - t_\mu < 21$ μs, where $t_{\rm TPC}$ is the absolute time the pixel identified as the stop position is detected by the wires of the TPC.

2. Muon entrances are uncorrelated to each other (neglecting the ≈ 50 MHz beam microstructure), so an additional muon entrance that goes completely undetected (a "sneaky" muon) is not dangerous regardless of whether or not its decay electron is detected. The problem is rather that the probability that the sneaky muon stops in the TPC, with a stop pixel detection time $t'_{\rm TPC}$ that satisfies $2 < t'_{\rm TPC} - t_\mu < 21$ μs, depends on when the sneaky muon enters with respect to t_μ; there is a time-dependent acceptance of these background decay events.

The acceptance probability ϵ of the sneaky muon can be written in terms of the distribution $F_{\rm drift}(t_{\rm TPC} - t_\mu)$ of stop times $t_{\rm TPC}$ for muons that enter at t_μ, and the fiducial cut bounds $T_{\rm fid}^{\rm min} \approx 2$ μs, $T_{\rm fid}^{\rm max} \approx 21$ μs:

$$\begin{aligned}\epsilon(t'_\mu - t_\mu) &= \int_{-\infty}^{\infty} dt'_{\rm TPC} F_{\rm drift}(t'_{\rm TPC} - t'_\mu) \\ &\quad \times \Theta(t'_{\rm TPC} - t_\mu - T_{\rm fid}^{\rm min}) \Theta(T_{\rm fid}^{\rm max} - (t'_{\rm TPC} - t_\mu)), \qquad (6.3)\end{aligned}$$

where the $\Theta(x) = 1$ if $x > 1$ and zero otherwise. The contribution to the background of the

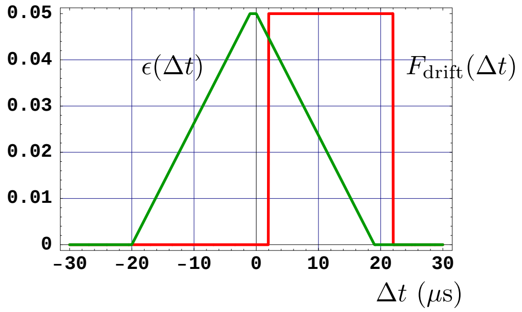

Figure 6.5: Time-dependent acceptance $\epsilon(t'_\mu - t_\mu)$ (green line) of a sneaky muon allowed by time-independent pileup-protection inefficiency, given a uniform drift-time distribution $F_{\mathrm{drift}}(t_{\mathrm{TPC}} - t_\mu)$ (red line) and application of Eq. 6.3.

lifetime spectrum if the electron of the sneaky muon is detected is then

$$f_{\mathrm{BG}}(t'_e - t_\mu) = \int_{-\infty}^{\infty} dt'_\mu \epsilon(t'_\mu - t_\mu)\lambda e^{-\lambda(t'_e - t'_\mu)}\Theta(t'_e - t'_\mu). \tag{6.4}$$

This leads to a slow component in the lifetime spectrum with characteristic time similar to the maximum TPC drift-time. An example of Eq. 6.3 applied to a uniform drift-time distribution is shown in Fig 6.5. Another way undetected pileup can distort the lifetime spectrum is if the sneaky muon "approves" a wall stop by providing the muon stop signature in the TPC.

The actual effect on the lifetime is observed in a data-driven manner by changing the fraction of sneaky muons contributing to the lifetime spectrum. Varying the level of entrance counter inefficiency can be effected by imposing less stringent pileup-protection requirements than the standard case, which takes an OR of all planes for the highest possible efficiency.

An estimate of the overall pileup protection inefficiency is needed. This is accomplished by histogramming the differences between the times of muon stop signal arrivals at the TPC's MWPC, and the MuSC signal times, i.e, $t_{\mathrm{TPC}} - t_{\mathrm{MuSC}}$, where the t_{TPC} are for identified muon stops. The time difference is normally used to calculate the height y of an event in the TPC under the assumption it is prompt with the muon entrance. Here we are interested in the out-of-time or background events — muon stops that could not have occurred at the MuSC time because they fall outside the drift-time interval. Drift-time histograms under different levels of pileup protection are displayed in Fig. 6.6b. Overall pileup protection inefficiencies are estimated as the ratio of the background of TPC drift-time histograms (average bin content in the range -1.5 μs $< t_{\mathrm{TPC}} - t_{\mathrm{MuSC}} < -0.2$ μs) to the correlated part of the drift-time histograms (average bin content in the range 0 μs $< t_{\mathrm{TPC}} - t_{\mathrm{MuSC}} < 23.0$ μs). This ratio

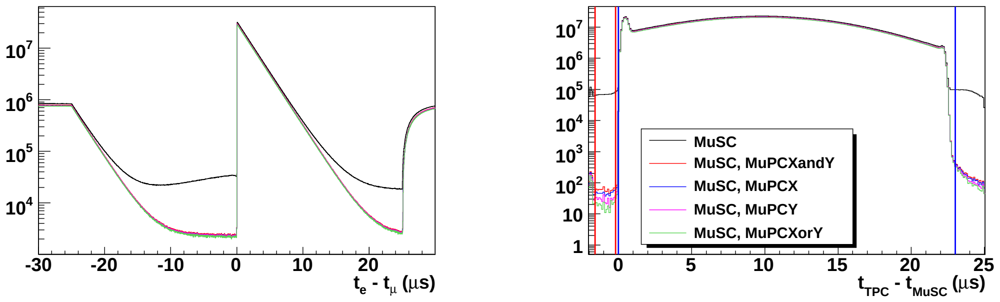

(a) Lifetime Spectra

(b) Drift Time Histograms

Figure 6.6: Lifetime and drift-time spectra with different levels of pileup protection. The legend in (b), which lists the pileup-protection condition, also applies to the spectra in (a). In both panels the curve with the largest background is for the MuSC-only, which had a rather high inefficiency of $\approx 10^{-2}$ (averaged over the 2004 experimental period). Vertical lines in (b) indicate the background (left side) and correlated regions of the drift-time plot.

is multiplied by a factor of 2.1 [53], which is a function of the beam rate and the drift-time interval, to give the time-independent inefficiency κ. The estimate for the inefficiency of the standard (best) pileup-protection is $\kappa = 3.40 \times 10^{-6}$.

The values of κ under different levels of pileup protection are correlated with the results of fits to the lifetime spectra (Fig. 6.6a) under the same conditions, and a zero-extrapolation procedure is suggested. Convenient "calibration" data sets are subsets of the production (Prod50) data with different κ(MuSC-only). The Prod50 set is divided into four chronological subsets of similar statistics. An additional calibration set comprises a period of Prod50 in which κ(MuSC-only) was stable and approximately 10^{-3}. Results are summarized in Table 6.2. The calibration values for λ_{fit} and κ are from the entire Prod50 set and the Prod50 subsets just described, each with MuSC-only pileup protection (MuPC planes are ignored). Here, $\Delta\lambda$ and $\Delta\kappa$ are calculated with respect to the standard Prod50 λ_{fit} and κ and plotted in Fig. 6.7, showing a linear relationship over a wide range of $\Delta\kappa$ except for Prod50-4, which has a very large κ, and Prod50-1, which has a very small κ that may have some background. The remaining calibration groups suggest a correction to λ^{MuCap} of $\Delta\lambda_\kappa \approx +0.8$ s^{-1}. No correction is applied, but the possibility of an offset in the estimate for κ is conservatively covered by assigning a systematic uncertainty of $\Delta\lambda_\kappa = 0 \pm 3$ s^{-1} for entrance counter inefficiency.

Calib. Group	κ_{Calib} (ppm)	$\Delta\lambda$ (s^{-1})	$\Delta\lambda/\Delta\kappa$ (s^{-1}/ppm)	Correction[a] $\Delta\lambda$ (s^{-1})	Best κ (ppm)
All	10792.44 ± 0.69	-2529.78 ± 17.18	-0.23 ± 0.00	0.80 ± 0.01	3.40 ± 0.01
1	10.48 ± 0.04	-58.82 ± 26.17	-8.30 ± 3.69	28.20 ± 12.55	2.45 ± 0.02
2	290.50 ± 0.22	-47.78 ± 25.94	-0.17 ± 0.09	0.57 ± 0.31	2.40 ± 0.02
3	5290.35 ± 0.94	-1380.42 ± 26.18	-0.26 ± 0.00	0.89 ± 0.02	1.29 ± 0.02
4	39732.37 ± 2.73	-7477.92 ± 29.27	-0.19 ± 0.00	0.64 ± 0.00	8.17 ± 0.04
Set001	1076.57 ± 0.59	-296.06 ± 34.23	-0.28 ± 0.03	0.94 ± 0.11	2.46 ± 0.03

---

[a] Using Prod50 overall inefficiency for MuSC+MuPCXorY pileup protection, $\kappa = 3.40 \pm 0.01$ ppm

Table 6.2: Results of time-independent pileup protection inefficiency study described in the text. The change in lifetime $\Delta\lambda$ and the change in pileup protection efficiency $\Delta\kappa$ are with respect to λ_{fit} and κ of the entire Prod50 group under the standard (best) pileup protection condition. The values in the last column, "Best κ," demonstrate that the pileup protection inefficiency is low throughout the experimental run when the MuPCs are included in the pileup protection.

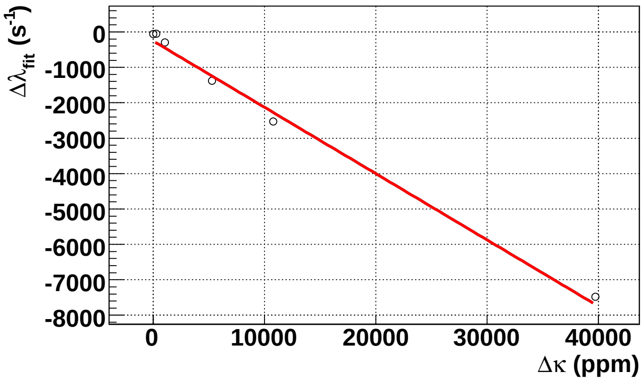

Figure 6.7: Change in lifetime $\Delta\lambda_{\text{fit}}$ vs. change in overall pileup protection inefficiency $\Delta\kappa$. $\Delta\lambda_{\text{fit}}$ and $\Delta\kappa$ are with respect to λ_{fit} and κ under the standard (best) pileup protection condition. The line through the data, a linear fit based on equal weighting of each point, is meant only as a guide.

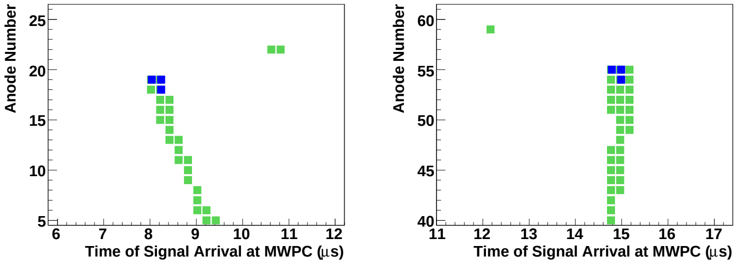

(a) (b)

Figure 6.8: Displays of muon stops with stray pixels in the same regions of interest. In each panel, the muon enters from the bottom.

6.3 Delta Electrons in the TPC

Pattern recognition of good muon stops in the TPC must be decay-time independent to avoid distortion of the lifetime measurement. Potential sources of decay-time dependent track acceptance, it turns out, are "extra EL" pixels around the muon track pixels. Extra EL pixels are low-threshold hits in the TPC data, within the same region-of-interest (0 to 25 μs of a muon entrance) as a muon track but not connected to the muon track. Two examples of muon stops accompanied by extra EL pixels are shown in figure 6.8. Extra EL pixels are present in approximately 2% of all muon stops and appear throughout the TPC fiducial region. These extra EL pixels come in clusters of up to five or six hits, the number of such events dropping exponentially as cluster size increases.

The reason to be concerned with these extra EL pixels is evident in figure 6.9, which shows the results of lifetime fits to spectra requiring both 1) a particular eSC segment, and 2) no extra EL pixels or one extra EL pixel. There should be no variation beyond statistical in the fit results versus eSC segment (direction of the electron); yet, a dramatic variation is observed when selecting either zero or one extra EL pixel. The residuals to the lifetime fits, displayed in the right panel of the figure, exhibit distortions except in the case of no cut on extra EL pixels (black points). Not explicitly selecting on the extra EL pixels results in statistically consistent fits across eSC segments. Thus, we cannot cut an event based on stray EL pixels in the region of interest. [1]

It will be shown in this section that most extra EL pixels are explained by "delta" or "knock-on" electrons — electrons of the medium to which relatively large amounts of kinetic

---

[1] However, as described in section 6.4, a line of extra EL pixels is often the signature of a $\mu + p$ scatter event, which we do want to cut.

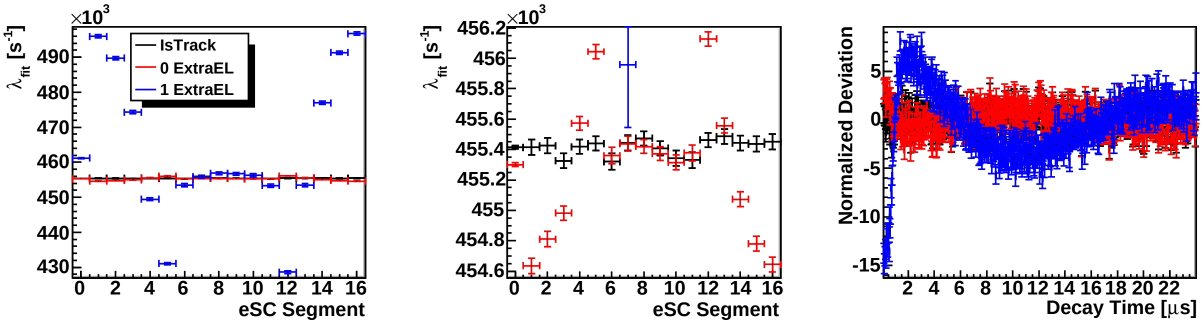

Figure 6.9: Lifetime fits vs. eSC segment, with no requirement on the number of extra EL pixels (black), with exactly 0 extra EL pixels required (red), and with exactly 1 extra EL pixel required (blue). Left panel: λ_{fit}; the leftmost bin is the fit to the sum over all eSC segments. Middle panel: zoomed-in version of the left panel. Right panel: fit residuals (normalized) to the fits of the sum of all eSC segments.

energy were imparted by energetic particles. The energetic particles in this case are the muon decay electrons. The delta electrons of interest are those with greater than the low-threshold (EL) setting of the TPC, around 25 keV. Since the probability a delta electron is produced decreases exponentially as its energy increases, most above-EL-threshold delta electrons do not have energy much higher than the EL threshold. The range of electrons with these energies in 10-bar hydrogen is expected to be smaller than the TPC pixel dimensions, so the full delta-electron energy should be deposited within a single pixel.

The correlation of extra EL pixels with both muon stop position and muon decay time is apparent in figure 6.10: the positions of extra EL pixels relative to the muon stop position, that is, $\Delta z = z(\text{ExtraEL}) - z(\mu\ \text{Stop})$ and similarly for Δy, are plotted. The left panel of the figure shows $(\Delta y, \Delta z)$ for events with muon decay times t_{Decay} in the early interval $0 \leq t_{\text{Decay}} < 1\ \mu\text{s}$; the right panel is for later decays, $6 \leq t_{\text{Decay}} < 7\ \mu\text{s}$. The peak of the distribution for early decays is near the muon stop position, while that for the late decays appears to be shifted vertically to a larger y-coordinate. Here we must recall the relation between the TPC drift time and the determination of the y-coordinate of an event: the y-coordinate is assigned with the assumption that the ionization source was prompt with the muon entrance time as detected by the separate entrance counters. If the source is prompt with the muon entrance time, its y-coordinate is assigned correctly. If the source is delayed somewhat, its inferred y-coordinate y_{TPC} will be above its actual position y_{actual}, according to

$$y_{\text{TPC}} - y_{\text{actual}} = v_{\text{drift}} \Delta t, \tag{6.5}$$

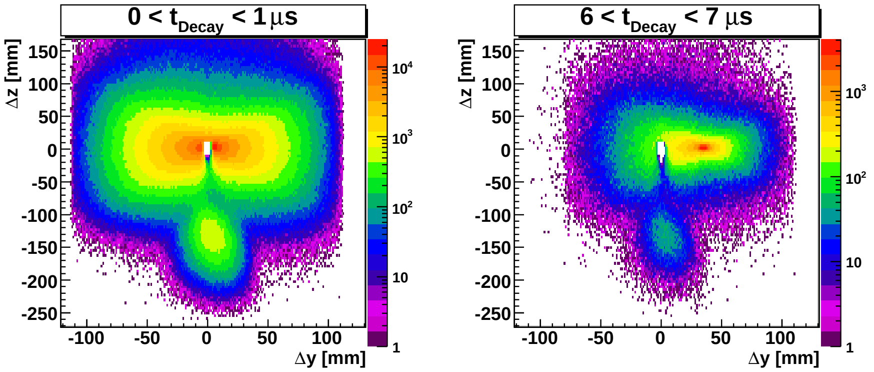

Figure 6.10: Distribution of delta electrons with respect to the muon stop position. Left: early muon decays ($0 \leq t_{Decay} < 1$ μs). Right: late muon decays ($6 \leq t_{Decay} < 7$ μs).

where v_{drift} is the TPC drift velocity, and Δt is the difference between the source time and the muon entrance time. The histograms of figure 6.10 are two in a series for different decay time intervals. A plot of Δy of the peak versus average t_{Decay} of the corresponding decay time interval follows a line with a slope of exactly v_{drift}, i.e.,

$$\Delta y_i^{\text{peak}} = v_{\text{drift}} \langle t_{\text{Decay}} \rangle_i, \tag{6.6}$$

where the subscript i labels the decay time interval, and the angle brackets indicate averaging over the time interval. The shift of the peak position with muon decay time is expected from applying equation 6.5 to sources of extra EL pixels that are centered on the muon stop positions and occur at the muon decay times.

Further evidence that the sources of extra EL pixels are delta electrons deposited along the path of the decay electrons is shown in figure 6.11. The distibutions are for a particular decay time interval ($3 \leq t_{\text{Decay}} < 4$ μs) and selecting electrons that are seen by a specific eSC segment, one at the top of the electron detector (left panel of figure) and the other at the bottom (right panel). Considering the acceptances of the eSC segments, the shape of each distribution is expected from signals deposited locally and uniformly along the decay electron path. A numerical study, in which a simplified detector geometry (approximate TPC active volume and eSC acceptances) was incorporated, and it was assumed that delta electrons are deposited with constant probability per unit path length p_δ, demonstrated rough quantitative agreement with observations if $p_\delta \sim 10^{-3}$ cm^{-1}.

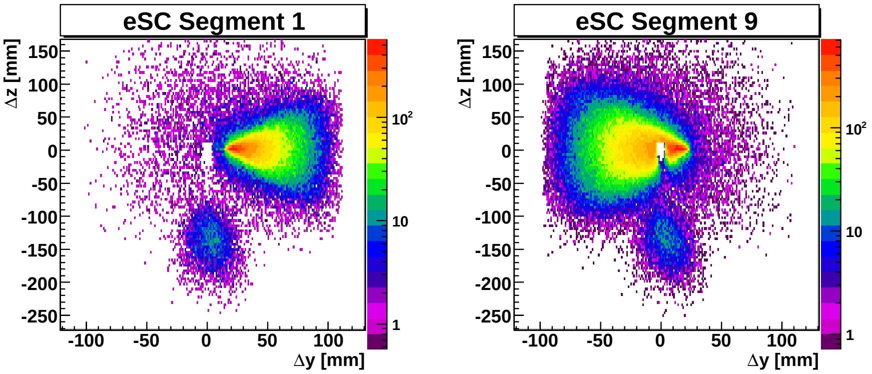

Figure 6.11: Distribution of delta electrons with respect to the muon stop position, cutting on electrons detected at the top (eSC Segment 1) and bottom (eSC Segment 9) of the electron detector. The decay times are required to be in the interval $3 \leq t_{Decay} < 4$ μs.

6.4 Muon-Proton Scatters

In a small fraction events, the incident muon scatters significantly off a proton. The proton recoils, traveling only a short distance (less than the space between TPC anodes) before its kinetic energy is lost to ionization of the gas. In terms of the resolution of the TPC, all of the recoil energy is deposited at a single pixel. Meanwhile, the scattered muon continues, possibly into a wall. The scatter leg of the muon track may escape detection for two reasons: 1) low-threshold TPC tracks are viewed only in projection onto the yz-plane, so a path straight into or out of the plane (along an anode) is not recognized as a track; 2) the efficiency of the TPC varies somewhat with particle direction, generally becoming less efficient for muons travelling along the drift ($\pm y$) direction. Thus, there are events that exhibit lead-up pixels to a $\mu + p$ collision point, and sparse or absent pixels leading away from that point. If the proton's recoil energy is above the high TPC threshold, EH pixels will appear at the end of the lead-up track and be confused with the muon's Bragg peak. In this way we can have "fake" muon stop events. These fake stops are particularly dangerous if the muon is scattered downwards because the muons may stop in the aluminum plate situated just below the MWPC of the TPC. Simulations have shown, and data analysis confirms (see below), that most muons scattered in other directions harmlessly stop in the hydrogen before hitting the pressure vessel wall.

Most of the $\mu + p$ scatter events do show signs of the muon scatter leg and can be identified in the data analysis. Four different types of scatter event signatures are defined, and an example of each is shown in Fig. 6.12:

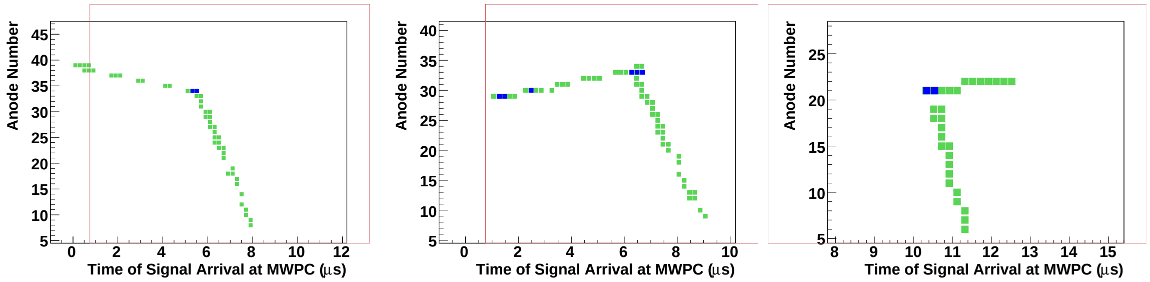

(a) “ExtraEL” Scatter (b) “TrackTrack” Scatter (c) “Cutoff” Scatter

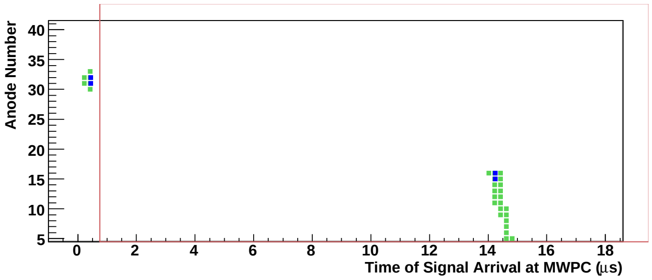

(d) “MWPC” Scatter

Figure 6.12: Examples of the four types of $\mu + p \rightarrow \mu + p$ scatter event signatures in the TPC data. In each panel, a muon enters from the bottom and Coulomb scatters off a proton, leaving a high-threshold signal (blue pixels) deposited by the recoil proton. The muon then continues to the boundary of the fiducial volume, indicated in panels a, b, and d by the vertical red line at ≈0.75 μs. The labels under the figures are explained in the text.

- **ExtraEL Scatters.** These are characterized by at least six extra EL pixels, somewhere in the region of interest, which fall along a straight line that points to the apparent Bragg peak. The requirement of at least six extra EL pixles is sufficient to avoid misidentifying decay-electron-induced delta electrons with this scatter event signature.

- **TrackTrack Scatters.** In this type of event, an apparently good muon stop has another muon track (with Bragg peak) pointing back to it. The troubling situation is when the scatter leg stops outside of the desired fiducial volume, for example near the wires of the TPC’s MWPC. The length of the scatter leg must be long enough to avoid confusing this event with a delayed, $Z > 1$ capture event (see section 6.5).

- **Cutoff Scatters.** An event of this type has a line of EL pixels, connected to each other and to the apparent stop position, extending beyond the fake stop position. Here the length of the scatter leg must be long enough that it could not have been caused by a delta electron from the muon decay electron.

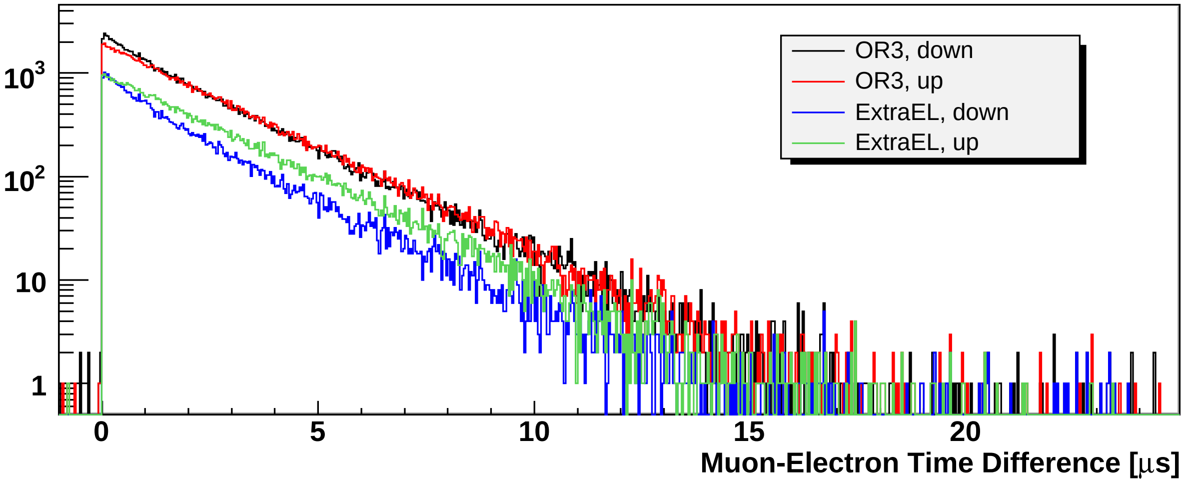

Figure 6.13: Lifetime spectra of identified $\mu + p$ scatter events. The legend indicates the scatter signature ("OR3" for any of the four types in Fig. 6.12, "ExtraEL" for the type of Fig. 6.12a) and the direction (upwards or downwards) of the scatter leg.

- **MWPC Scatters.** This is identified by a prompt (with respect to the muon entrance time), high-threshold hit in the MWPC region of the TPC. The motivation for this search is that muons scattered into the MWPC can make a larger signal (relative to the drift region) because of the effectively shorter drift time within the MWPC, and also because some of these muons may stop in wires and quickly capture, creating a large signal. Minor sparking in the MWPC or other noise could conceivably be mistaken for this type of scatter event, but these are found to be very infrequent.

Events that exhibit at least one of the scatter signatures are tagged and removed from the final muon lifetime spectrum. Lifetime spectra of these identified scatter events are shown in Fig. 6.13; the events are divided into those that scatter upwards and those that scatter downwards. It is found that the lifetime of the upwards scatters is consistent with the lifetime of the non-scatters. Evidently, the upwards scatters eventually stop in hydrogen and present no distortion to the desired measurement. The lifetime spectrum of the downwards scatters reveals quite different behavior: the spectrum is visibly steeper at early times, consistent with a significant fraction of these muons stopping in the aluminum plate below the TPC.

The removal of all identified scatter events from the standard muon track selection reduces the statistics by 121 ppm and lowers the final muon disappearance rate, λ_{μ}^{-}, by $\Delta\lambda_{\rm sc}^{\rm obs} = 2.5\ {\rm s}^{-1}$ (= 5.5 ppm of λ_{μ}^{-}), about 18% of the final statistical error. This is a small shift of the lifetime, but one must ask: how many scatter events were missed, and what is their effect

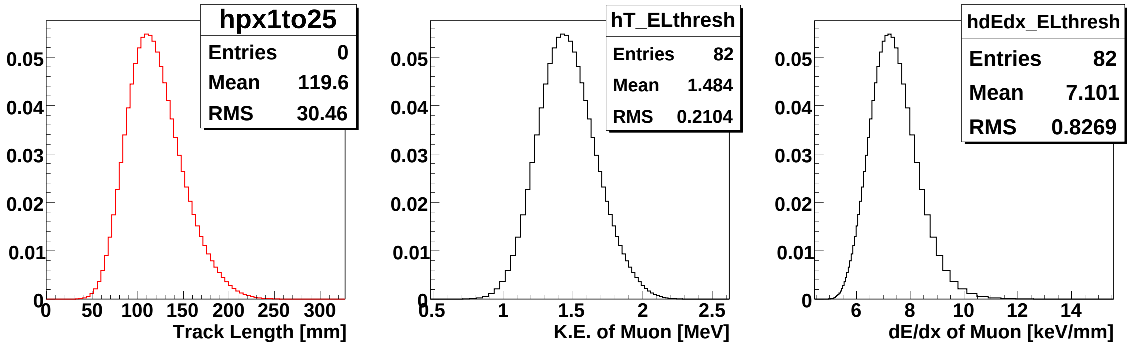

(a) (b) (c)

Figure 6.14: Left: histogram of observed muon track lengths for tracks that start on anodes 6 through 25. Middle: muon kinetic energy at the start of the observed tracks, calculated from the track lengths of left panel. Right: muon energy loss per track length (dE/dx) at the start of the observed tracks, calculated from the track lengths of the left panel.

on the result? To answer this question we need to know the efficiency to catch a scatter event faking a good muon stop, and especially the efficiency to catch those that eventually stop in wall material. This efficiency was estimated by comparing the observed distibutions of scatter events to the same produced from simulated muons stopping in hydrogen.

The simulated events were generated with the Monte Carlo software package, SRIM [54], with the momentum distibution, beam spread, and beam divergence set to closely resemble these properties observed in the MuCap data. To further connect with reality, the length of the track leading up to the location of a $\mu + p$ scatter must be set correctly. A scatter event in which the muon's energy prior to the collision is too high to leave enough lead-up pixels for a contiguous and sufficiently long track will not pass the track length cut; it will not be mistaken for a good muon stop. The maximum muon kinetic energy T_{EL} to leave a continuous track is estimated from the MuCap data from the observed set of track lengths $\{R_i\}$ for muon stops and the analytic range-energy relation (Eq. 3.1 in Chapter 3). The distribution of track lengths is shown in the left panel of Fig. 6.14. Only tracks entirely contained within the TPC active volume, that is, not cut off by the boundaries, are histogrammed and used in the calculation of the T_{EL} distibution (middle panel of Fig. 6.14). Similarly, Eq. 3.2 is applied to the track lengths to get the ionization energy per unit length dE/dx at the point where the track becomes contiguous. This is shown in the right panel of Fig. 6.14, and the mean value of the distribution, multiplied by the TPC anode spacing (4 mm), is an estimate of the low-threshold (EL) setting of the TPC.

The final requirement to compare simulation with data is knowledge of the TPC's high-

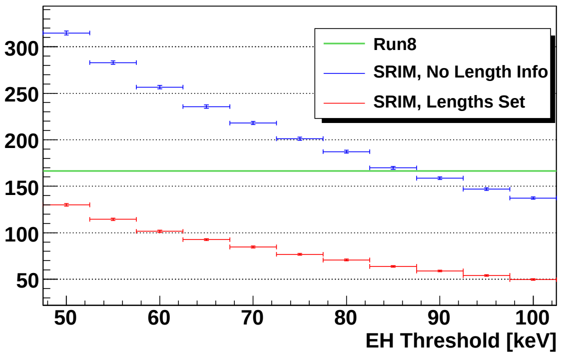

Figure 6.15: Total fraction of simulated $\mu + p$ scatter events with and without the lead-up track cut. The fraction observed in MuCap is indicated by the green horizontal line.

threshold (EH) setting, which we need to cut simulated scatter events with recoil energy below this setting. An independent study based on FADC data has indicated that the EH threshold was set in the range 80–90 keV [55]. The total scatter fraction in the simulation, with and without the lead-up track length cut, is shown in figure 6.15 as a function of the assumed EH threshold setting. Across the entire range of reasonable threshold settings, the total fraction of scatter events with the lead-up track length cut fall well below the total fraction observed in the data. It turns out the lead-up track length cut in the simulation is far too severe: often in the MuCap data, sparse lead-up pixels upstream of the contiguous part of the track connected to the apparent Bragg peak are enough for a fake stop event to pass the cut. This was confirmed by examination with an event display of the lead-up pixels to many typical muon stops.

The distribution of scattering angle θ_2 — the angle in the yz plane of the muon track after the collision — is shown in Fig. 6.16 for scatters identified in the MuCap data and for the SRIM simulation assuming an EH threshold of 85 keV. Results are displayed for the simulated muons with and without the lead-up track length cut, and with and without selection of events in which the scattered muons stop in the aluminum plate. The peaks in the data at $\theta_2 = \pm\pi$ is a discretization effect: the θ_2-reconstruction resolution is poor for scatter legs that travel steeply up or down, especially for paths that do not leave the charge-collection region of a given anode. The θ_2-distibutions of data and simulation (without the lead-up cut) are in rough quantitative agreement, but uncertainty remains in how to correctly set the lead-up lengths of the simulated muons.

Since the only scatter events that affect the lifetime measurement are those that stop in wall material, primarily the aluminum plate beneath the TPC, the relevent quantity is the

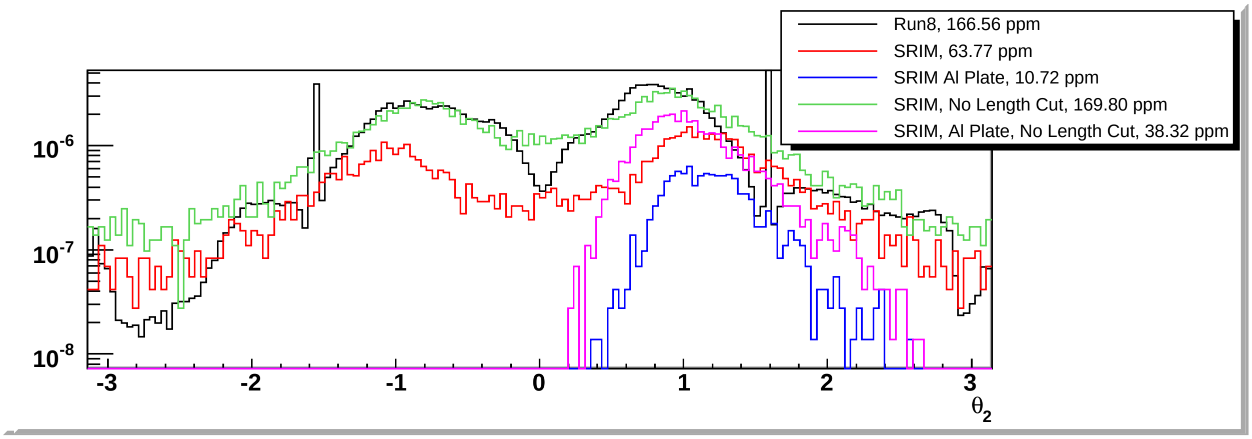

Figure 6.16: Angle θ_2 of scatter legs of identified $\mu+p$ scatter events, compared to simulated scatter events assuming an EH threshold of 85 keV and with and without setting the track lengths as described in the text. Note: in the track parameterization, $\theta_2 > 0$ for a downwards scatter.

	Standard Muon Def.	Relaxed Muon Def.	SRIM	SRIM No Length Cut
Total	120.8 ± 0.2 ppm	166.6 ± 0.3 ppm	63.8 ± 0.9 ppm	169.8 ± 1.5 ppm
Down	73.0 ± 0.2 ppm	92.6 ± 0.2 ppm	37.8 ± 0.7 ppm	94.4 ± 1.1 ppm
Al	[11.0 ± 1.2 ppm][a]	[12.6 ± 1.3 ppm][b]	10.7 ± 0.4 ppm	38.3 ± 0.7 ppm
$0.7 \le \theta_2 \le 1.5$				
Down'	46.2 ± 0.1 ppm	48.7 ± 0.1 ppm	22.2 ± 0.6 ppm	50.5 ± 0.8 ppm
Al'	[7.2 ± 1.0 ppm][c]	[7.2 ± 1.0 ppm][d]	8.7 ± 0.3 ppm	28.2 ± 0.6 ppm

---

[a] $N_Z/N_{\text{Down}} = 0.158 \pm 0.015$, $(1 - \alpha_{Z1}) = 0.959 \pm 0.042$.

[b] $N_Z/N_{\text{Down}} = 0.141 \pm 0.014$, $(1 - \alpha_{Z1}) = 0.966 \pm 0.041$.

[c] $N_Z/N_{\text{Down}'} = 0.160 \pm 0.020$, $(1 - \alpha_{Z1}) = 0.980 \pm 0.052$.

[d] $N_Z/N_{\text{Down}'} = 0.151 \pm 0.019$, $(1 - \alpha_{Z1}) = 0.974 \pm 0.054$.

Table 6.3: Comparison of scatter fractions in Run8 and SRIM (with $E_{\text{recoil}} > 85$ keV). The Run8 fraction of stops in aluminum, $X_{\text{Al}}^{\text{obs}}$, is calculated based on the high-Z lifetime fit to the downward scatters: $X_{\text{Al}}^{\text{obs}} = X_{\text{down}}^{\text{obs}}(1 - \alpha_{Z1})N_Z/N$, where $X_{\text{down}}^{\text{obs}}$ is the observed downward scatter fraction, and α_{Z1}, N_Z and N are parameters from the lifetime fit; these parameters are listed in footnotes to the table.

fraction $X_{\rm Al}^{\rm unobs}$ of aluminum stops present in the final lifetime spectrum after all observed scatters are removed. The systematic error due to these unobserved aluminum stops is then estimated by scaling the effect on the lifetime of removing all observed scatters:

$$\Delta\lambda_{\rm sc}^{\rm unobs} \approx \frac{X_{\rm Al}^{\rm unobs}}{X_{\rm Al}^{\rm obs}} \Delta\lambda_{\rm sc}^{\rm obs}. \tag{6.7}$$

The fraction of observed scatters $X_{\rm Al}^{\rm obs}$ is estimated by fitting the lifetime spectrum of downward scatters (Fig. 6.13) with a fit function modified to include stops in aluminum and tungsten (for the MWPC wires):

$$f_{\rm withZ}(t) = N\lambda w e^{-\lambda t} + B + N_Z w \left(\alpha_{Z1}\lambda_{\rm W} e^{-\lambda_{\rm W} t} + (1-\alpha_{Z1})\lambda_{\rm Al} e^{-\lambda_{\rm Al} t}\right), \tag{6.8}$$

where w is fixed to the lifetime histogram bin width of 40 ns, and N, λ, and B are the standard fit parameters. Of the new parameters, the rates will be fixed: $\lambda_{\rm W} = 12.76 \times 10^6$ s^{-1} for the muon inverse lifetime on tungsten (gold has a similar total capture rate), and $\lambda_{\rm Al} = 1.157 \times 10^6$ s^{-1} for the muon inverse lifetime on aluminum. In this parameterization, the fraction of stops in aluminum is given by

$$X_{\rm Al}^{\rm obs} = \frac{N_Z}{N}\left(1-\alpha_{Z1}\right). \tag{6.9}$$

The results of this estimate for the fraction of stops in aluminum present in the final lifetime spectrum is included in the column labeled "Standard Muon Def." in table 6.3. The next column, labeled "Relaxed Muon Def.," gives the scatter fractions based on tracks without the standard muon definition cut of Eq. 5.7 (the cut of Eq. 5.8 still applies); these can be compared directly to the SRIM fractions. The last two rows are for a restricted range of scatter angles in an attempt to enhance the contribution from the aluminum stops, but the fractions $N_Z/N_{\rm Down}$ come out very similarly. Depending on the lead-up cut in the simulation, it appears we are missing somewhere between zero and about two-thirds of the dangerous scatters into aluminum.

In the end we assign a systematic error based on a 50% efficiency to catch these events, i.e., $X_{\rm Al}^{\rm unobs}/X_{\rm Al}^{\rm obs} \approx 1$. Inserting this ratio and $\Delta\lambda_{\rm sc}^{\rm obs} = 2.5$ s^{-1} into Eq. 6.7, our estimate for the systematic error due to $\mu + p$ scatter events faking good stops is $\delta\lambda_{\rm sc}^{\rm unobs} \approx 3$ s^{-1}, where the lower-case delta indicates an uncertainty, not a correction to the lifetime. In principle this is a one-sided uncertainty, $0 \leq \Delta\lambda_{\rm sc}^{\rm unobs} \leq 3$ s^{-1}; we conservatively make it symmetric to ease inclusion into the final, overall systematic uncertainty.

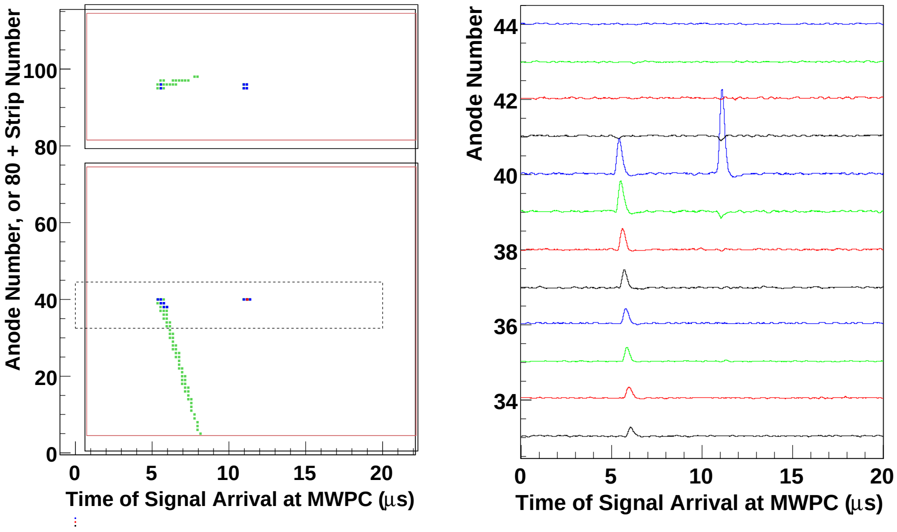

(a) (b)

Figure 6.17: Display of a $Z > 1$ impurity capture event. (a) TDC data. (b) FADC data.

6.5 Elemental Impurities

One of the powerful features of the MuCap experiment is the ability to monitor *in situ* the $Z > 1$ gas impurities. When nuclear muon capture occurs from a μZ atom, a localized, relatively high-energy signal is deposited in the TPC by the recoiling $Z - 1$ nucleus. An event display of a typical $Z > 1$ capture is shown in Fig. 6.17. The signature of these events is distinct: a good muon stop is followed by a very-high-threshold (EVH) hit on the same or adjacent anode (z-dimension) and cathode (x-dimension) as the muon stop. There is the usual TPC ambiguity between the y-position and timing of a source; here, we assume the capture occurred also at the same height (y-dimension) as the muon stop. The time delay t_{cap} between the muon stop and the capture event is simply the difference in signal arrival times at the MWPC. Normalizing the total number of identified $Z > 1$ capture events by the total number of muon stops gives the observed capture yield Y_Z^{obs}, which differs from the actual yield $Y_Z^{\epsilon=1}$ by the efficiency factor ϵ_Z of the capture search, i.e., $Y_Z^{\text{obs}} = \epsilon_Z Y_Z^{\epsilon=1}$.

For low concentrations of $Z > 1$ impurities, the effect on the overall muon lifetime is proportional to the impurity capture yield:

$$\Delta\lambda_Z = \beta_Z^{\epsilon=1} Y_Z^{\epsilon=1} = \beta_Z^{\text{obs}} Y_Z^{\text{obs}}, \tag{6.10}$$

where β_Z is a factor to be determined by either 1) calculation using the full kinetics equations, giving $\beta_Z^{\epsilon=1}$, or 2) calibration using an impurity-doped dataset, giving β_Z^{obs}. Application of $\beta_Z^{\epsilon=1}$ has the disadvantage that the efficiency to observe the capture events in the TPC, ϵ_Z, must be known to correct the observed yield to the perfect-efficiency case. Instead we use the second method with the β_Z^{obs} determined from calibration data in which the protium gas is doped with a specific impurity at greater than 100 times the concentration in the clean fill. The β_Z^{obs} factor is then simply calculated from the observed change in the muon disappearance rate in the calibration data compared to the clean (Prod.) data, divided by the observed change in the $Z > 1$ capture yield:

$$\beta_Z^{\mathrm{obs}} = \frac{\lambda^{\mathrm{Calib}Z} - \lambda^{\mathrm{Prod}}}{Y_Z^{\mathrm{Calib}Z} - Y_Z^{\mathrm{Prod}}}. \tag{6.11}$$

Although the theoretical values $\beta_Z^{\epsilon=1}$ are close to each other for the most common impurities, carbon, nitrogen, and oxygen (water) (see Section 3.4), the recoil energy spectra may be quite different; in general the fraction ϵ_Z of $Z > 1$ capture events that make it over the TPC very-high (EVH) threshold depends on the impurity species. In an ideal calibration, the TPC gain and threshold are unchanged from the production settings, and the target is doped with the same impurity species that was present in the clean fill. Technical difficulties prevented such an ideal situation in the 2004 MuCap run.

Fortunately, we are able to relate the 2004 conditions to calibration data from later MuCap experimental runs, and an impurity correction can be assigned with a conservative systematic uncertainty of less than half the statistical error of the final λ^{MuCap} result. The issues are the following:

1. The dominant impurity in the clean fill is not known, but there is circumstantial evidence that it is water. External measurements (gas chromotography) showed very low levels of the common impurities nitrogen (N_2) and oxygen (O_2). Water concentration measurements were attempted with a humidity sensor in an external apparatus, requiring intermediate storage in a sample volume, but the results are inconclusive. Water tends to stick to internal surfaces, and equilibrium between outgassing and absorption in the sample volume must be reached for a reliable humidity measurement. Installation in 2005 of an inline humidity sensor in the target gas circulation system confirmed that water is the dominant impurity in the target gas.

2. Calibration data in the 2004 running period were successfully taken only with nitrogen.

Oxygen doping did not produce useful data because of the high electronegativity of O_2: drift electrons tended to be atomically captured by oxygen atoms before reaching the MWPC of the TPC, severly attenuating the signals. Water-doping on the ppm level requires some technical effort to effect an equilibrium condition with target materials, and this was accomplished in a later MuCap running period (2006) via installation of a water permeation tube.

3. The high voltage of the TPC was not the same during the calibration runs as during the production (Prod50) runs. The high voltage of the TPC was reduced by 200 V to 4.8 kV for the nitrogen-doped (CalibN2) data, lowering the MWPC gain by about half. The water-doped (CalibH2O) data were taken during a different experimental period (2006) and with a higher TPC voltage of 5.45 kV. An additional nitrogen-doped data set was also recorded in 2006 at the higher TPC voltage of 5.45 kV. Connection with the 2004 production data can still be made, however, because discriminator threshold settings were commensurately changed, such that the energy thresholds for the high (EH) and very-high (EVH) thresholds were nearly the same for the different data sets. Here, the Bragg peaks of muon stops were convenient reference sources: the EVH threshold was in all cases set just above nearly all of the Bragg peaks. We can be confident that we are integrating over a similar range of recoil energies in the calibration runs as in the Prod50 runs.

The third issue, the connection of calibration to production data, is the key to an accurate impurity correction and a continuing point of discussion within the MuCap collaboration. The final recommendation [56] for the impurity correction to the 2004 data is based on adjusting the $\beta_{\mathrm{O}}^{\mathrm{obs}}$ value from the 2006 water-doped data to account for differences in efficiency ϵ_{O}. This adjustment is estimated by comparing parameters from analyses of the respective nitrogen-doped data sets of the two running periods. The $\beta_{\mathrm{O}}^{\mathrm{obs}}$ of the water-doped dataset is scaled by the change in the efficiency ϵ_{N} of nitrogen capture detection:

$$\beta_{\mathrm{O}}^{\mathrm{obs}}(2004) \approx \frac{\beta_{\mathrm{N}}^{\mathrm{obs}}(2004)}{\beta_{\mathrm{N}}^{\mathrm{obs}}(2006)} \beta_{\mathrm{O}}^{\mathrm{obs}}(2006). \tag{6.12}$$

With $\beta_{\mathrm{N}}^{\mathrm{obs}}(2004) = 1.30 \pm 0.08\ \mathrm{s}^{-1}/\mathrm{ppm}$, $\beta_{\mathrm{N}}^{\mathrm{obs}}(2006) = 1.38 \pm 0.03\ \mathrm{s}^{-1}/\mathrm{ppm}$, and $\beta_{\mathrm{O}}^{\mathrm{obs}}(2006) = 1.58 \pm 0.12\ \mathrm{s}^{-1}/\mathrm{ppm}$, equation 6.12 gives $\beta_{\mathrm{O}}^{\mathrm{obs}}(2004) \approx 1.49 \pm 0.15\ \mathrm{s}^{-1}/\mathrm{ppm}$.

The estimate for $\beta_{\mathrm{O}}^{\mathrm{obs}}$ is further modified by drawing on the results of fits to the lifetime spectra of the impurity-doped data with the solution $y_e(t)$ (Eq. 3.9) to the full kinetics equation. In the fit, the lifetime parameters are fixed, and the effective transfer rate $\tilde{\lambda}_{pZ}$ is allowed to float. The results of the fit can be used to calculate the additional quantity γ_Z,

$$\gamma_Z^{\text{obs}} = \tilde{\lambda}_{pZ}^{\text{obs}} / Y_Z^{\text{obs}}. \tag{6.13}$$

The ratio of β_Z and γ_Z, called R_Z in the Kinetics chapter, is particularly interesting because it is not affected by the efficiency ϵ_Z, depending only on the electron time spectrum:

$$R_Z^{\text{obs}} = \beta_Z^{\text{obs}} / \gamma_Z^{\text{obs}} = \Delta\lambda_Z^{\text{obs}} / \tilde{\lambda}_{pZ}^{\text{obs}}. \tag{6.14}$$

R_Z can be directly compared to the theoretical predictions in Table 3.3. Fits to the 2004 nitrogen-doped calibration data show $\gamma_{\text{N}}^{\text{obs}}(2004) = 5.9 \pm 0.3$ s^{-1}/ppm. Calculating $R_{\text{N}}^{\text{obs}}$ from this and the similar quantity based on the simple-exponential fit, $\beta_{\text{N}}^{\text{obs}}(2004) = 1.30 \pm 0.08$ s^{-1}/ppm, gives $R_{\text{N}}^{\text{obs}}(2004) = 0.220 \pm 0.002$, in good agreement with the theoretical prediction of 0.219. Similar fits to the 2006 calibration data find [56] $R_{\text{N}}^{\text{obs}}(2006) = 0.210 \pm 0.00014$ and $R_{\text{O}}^{\text{obs}}(2006) = 0.269 \pm 0.0024$, lower than the theoretical predictions by 5% and 10%, respectively. The latter discrepancy is attributed to a result for $\Delta\lambda_{\text{O}}^{\text{obs}}(2006)$ that is lower than expected based on the value for $\gamma_{\text{O}}^{\text{obs}}(2006)$. We choose to account for this by adjusting the $\beta_{\text{O}}^{\text{obs}}(2004)$ from Eq. 6.12 up by 10%. Setting a conservative systematic uncertainty of 25% results in the slope that will applied to the production data to correct for oxygen (water) impurities:

$$\beta_{\text{O}}^{\text{obs}}(2004, \text{adjusted}) = 1.65 \pm 0.45 \text{ s}^{-1}/\text{ppm}. \tag{6.15}$$

In the case of the CalibNat data set, which has a significant deuterium concentration $c_d \approx 120$ ppm, further modification of the β_Z^{obs} may be motivated. We can estimate the fraction of muons that transfer to deuterium as $X_d \sim \phi c_d \lambda_{pd}/\lambda_0$, which is about 4% for the conditions of the CalibNat target. These μd proceed to diffuse cm-scale distances (see Kinetics chapter). Muons that transfer from μd to μZ and subsequently capture are not recognized as impurity capture events, since the EVH signal is likely spatially displaced in x and z. Therefore we see a reduction in the observed yield Y_Z compared to the case with no deuterium, but the effect $\Delta\lambda_Z$ on the lifetime is unchanged. Thus, the β_Z from the impurity-doped calibration data is not entirely appropriate, and should be increased for the CalibNat $Z > 1$ correction. A further complication stems from an isotopic effect on the transfer rates to Z, such that $\lambda_{pZ} \neq \lambda_{dZ}$. For example, the transfer rate from μd to nitrogen was measured

Data Set	Yield [ppm]	α_N	β_N [s^{-1}/ppm]	β_O [s^{-1}/ppm]	$\Delta\lambda_Z$ [s^{-1}]
Prod50	10.65 ± 0.08	0.05 ± 0.05	1.30 ± 0.08	1.65 ± 0.45	-17.4 ± 4.6
CalibN2	726.93 ± 2.84	1.00 ± 0.00	1.30 ± 0.08	1.65 ± 0.45	-948.1 ± 56.8
CalibNat	44.13 ± 0.81	0.50 ± 0.50	1.57 ± 0.28	1.65 ± 0.45	-70.9 ± 11.9
CalibD2	105.79 ± 0.70	0.50 ± 0.50	1.30 ± 0.08	1.65 ± 0.45	-156.3 ± 30.3

Table 6.4: Practical impurity corrections. Y_Z is the observed $Z > 1$ capture yield, and α_N is the fraction of the observed yield attributed to captures on nitrogen. β_N and β_O are the slopes based on calibration data, and $\Delta\lambda_Z$ is the resulting correction to be applied to the listed data set.

to be $\lambda_{d\text{N}} = 1.45(2) \times 10^{11}\ \text{s}^{-1}$[57], approximately five times higher than $\lambda_{p\text{N}}$; i.e., muons that transfer to deuterium ($\sim 4\%$ in CalibNat) have an enhanced rate to subsequently transfer to nitrogen. Therefore, we modify β_Z to be used for the CalibNat correction in the following way:

$$\beta_Z^{\text{obs}}(\text{CalibNat}) \approx \frac{\phi c_d \lambda_{pd}}{\lambda_0} \frac{\lambda_{dZ}}{\lambda_{pZ}} \beta_Z^{\text{obs}}(CalibZ). \tag{6.16}$$

In the case of nitrogen, β_N for CalibNat is increased by $\approx 0.04 \times 5 = 20\%$. Detailed numerical studies with the full kinetics equations support this estimate [42]. In the case of oxygen, the transfer rate from μd ($\lambda_{d\text{O}} = 6.3 \pm 0.5$ [41]) is similar to the rate from μp ($\lambda_{p\text{O}} = 8.5 \pm 0.2$ [58]), so no modification of β_O is necessary.

The final step to implement the impurity correction is to specify the composition of $Z > 1$ impurities in the target gas and weight the correction accordingly. The gas chromotography result of very little nitrogen in the production target is expected to be reliable. We attribute 0 to 10% of the capture yield Y_Z^{obs} in the production data to nitrogen and the remainder to oxygen (water). Let α_N represent the fraction of the yield due to captures on nitrogen. Then the impurity correction is

$$\Delta\lambda_Z = -\left(\alpha_\text{N}\beta_\text{N} + (1 - \alpha_\text{N})\beta_\text{O}\right), \tag{6.17}$$

where the β_Z are the values adjusted as described above. The $Z > 1$ corrections for the production (Prod50) and other data sets are summarized in Table 6.4.

6.6 Diffusion

The presence of deuterium in the target gas leads to a systematic shift of the lifetime measurement. While the somewhat different capture rate of μd compared to μp is not important at MuCap deuterium concentration, the effect of μd diffusion out of μ–e vertex (impact parameter) cuts, perhaps into wall material, can be severe. Our approach to correct for this is zero-extrapolation procedure. In addition to the main production data with deuterium-depleted hydrogen, with $c_d^{\text{Prod}} \sim 1$ ppm, data with higher c_d were taken: CalibD with $c_d^{\text{CalibD}} \approx 18$ ppm, and CalibNat with $c_d^{\text{CalibNat}} \approx 120$ ppm. The zero-extrapolation can be done with either the CalibD or CalibNat data sets, though the latter is favored since the effect is larger and still sufficiently linear [59]. We define the ratio of deuterium concentrations:

$$\tilde{c} \equiv \frac{c_d^{\text{calib}}}{c_d^{\text{Prod}}}, \tag{6.18}$$

where "calib" is either CalibNat or CalibD. In terms of $\tilde{c}$, the correction to the production data is

$$\Delta\lambda_d = \frac{-\tilde{c}^{-1}}{1-\tilde{c}^{-1}}(\lambda^{\text{calib}} - \lambda^{\text{Prod}}), \tag{6.19}$$

in which the λ have been corrected for $Z > 1$ impurities, and the same geometrical cuts have been applied to both data sets.

The correction $\Delta\lambda_d$ requires accurate knowledge of the deuterium concentrations in the production and calibration sets. An external measurement of c_d for the production gas was quoted in Section 4.6.1 of Chapter 4. Given the difficulty of these external measurements and the strong dependence of $\Delta\lambda_d$ on which impact parameter cut is applied, a cross check of the correction is warranted. In fact, the "cross check" that is described below was originally developed to infer $\tilde{c}$ from the MuCap data without relying on external measurements; it was only in 2006 that the ETH-Zürich accelerator technique was available to precisely measure c_d^{Prod}. Moreover, the MuCap data-analysis study to find $\tilde{c}$ quantified an additional systematic effect related to μp diffusion that would have otherwise been neglected.

6.6.1 Data-Analysis Technique to Determine c_d

The data-analysis technique begins with a signal $y^{(\text{set})}(b_{\text{cut}})$ intended to be directly proportional to c_d of the data set for a given impact parameter cut b_{cut}:

$$y^{(\text{set})}(b_{\text{cut}}) = \lambda^{(\text{set})}(b_{\text{cut}}) - \lambda^{(\text{set})}(b_{\text{cut}}^{\max}), \tag{6.20}$$

where the λ are the fit results to lifetime spectra with the specified impact parameter cut, and $b_{\text{cut}}^{\max}$ is large. Recall that the μd's in the MuCap target can diffuse ~ 10 cm during the

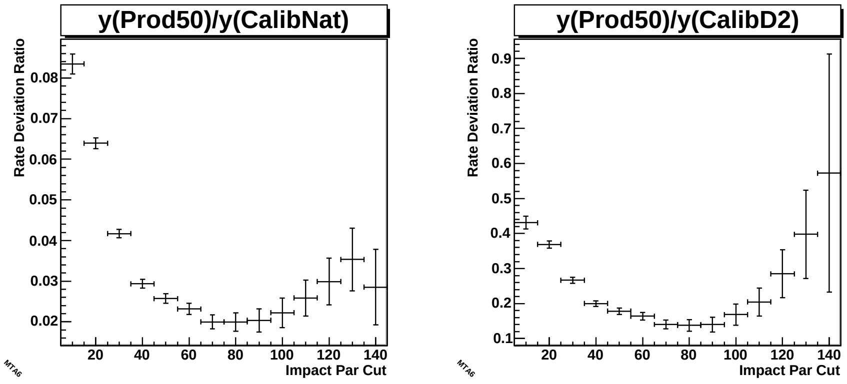

Figure 6.18: Results of applying the naïve Eq. 6.21 to infer the deuterium concentration (inverse) ratio $\tilde{c}^{-1}$ from the data. Left: using CalibNat as the calibration data set; Right: using CalibD2 instead. $b_{\text{cut}}^{\text{max}}$ is set to 150 mm in Eq. 6.20.

muon lifetime (see Fig. 3.7 of Chapter 3). Therefore, we expect a higher λ for smaller b_{cut} settings, since μd diffusion out of the acceptance region represents an additional muon loss channel. Assuming scaling by c_d, $y^{(\text{set})}(b_{\text{cut}}) = c_d^{(\text{set})}\tilde{y}(b_{\text{cut}})$ for some c_d-independent function $\tilde{y}$, and we find

$$\tilde{c}^{-1} = \frac{y^{\text{Prod}}(b_{\text{cut}})}{y^{\text{calib}}(b_{\text{cut}})}, \tag{6.21}$$

which, if true, must give the same value for any b_{cut}. The results of applying Eq 6.21 to the data are shown in Fig. 6.18. Equation 6.21 is clearly not valid. Further studies showed what appeared to be an anomalous increase in λ by as much as $\sim 1000\ \text{s}^{-1}$ for the smallest b_{cut} studied (10 mm).

It turns out the additional rate deviation is caused by the following mechanism: the ~ 1 mm diffusion of μp atoms, combined with the broad spatial resolution function of the electron detector, causes a few more events to be misreconstructed with impact parameter $b > b_{\text{cut}}$ at later decay times than at early decay times. As a preliminary to the full treatment worked out in Appendix B, a simpler 1-dimensional argument and numerical demonstration is presented to explain the issue. Consider an electron-detector resolution function $F_{\text{res}}(x_e - x_{\mu p})$, in which x_e is the reconstructed location of an electron that was actually emitted from $x_{\mu p}$; then the impact parameter is the difference, $b = x_e - x_{\mu p}$, and $F_{\text{res}}(b)$ represents the probability density to reconstruct the event as having impact parameter b. $F_{\text{res}}(b)$ would be a δ-function at $b = 0$ if the μp did not move, and the event reconstruction was perfect. In reality the detector resolution is rather broad, on the order of several centimeters, due to scattering in the pressure vessel walls and other materials. Let $x_{\mu p}$ be the actual position of the μp with respect to its original stopping location, and let the function $F_{\mu p}(x_{\mu p}|t)$ represent the distribution of $x_{\mu p}$ for decays at time t. The observed impact parameter distribution for decays at t is the convolution of $F_{\mu p}$ and F_{res}:

$$F_b(b) = \int_{-\infty}^{\infty} F_{\mu p}(x_{\mu p}) F_{\text{res}}(b - x_{\mu p}) dx_{\mu p}. \tag{6.22}$$

In the limit of very early muon decays, the μp atoms have not had time to move: $\lim_{t\to 0} F_{\mu p}(x_{\mu p}|t) = \delta(x_{\mu p})$. We can identify the observed impact parameter distribution $F_b(b|t < t_1)$, for early muon decays before time t_1, with the resolution function:

$$F_{\text{res}}(b) = \lim_{t_1 \to 0} \frac{F_b(b|t < t_1)}{\int_{-\infty}^{\infty} F_b(b|t < t_1) db}. \tag{6.23}$$

The next steps are to 1) choose a model for $F_{\mu p}$, 2) convolute per Eq. 6.22 $F_{\mu p}$ with the experimentally-determined resolution function (Eq. 6.23), and 3) calculate the relative change in acceptance of an impact parameter cut, as a function of time, with respect to the undiffused acceptance. We choose $F_{\mu p}$ appropriate for isotropic thermal diffusion,

$$F^{\text{ex}}_{\mu p}(x_{\mu p}) = \frac{1}{\sigma_{\mu p}\sqrt{2\pi}} e^{-x^2_{\mu p}/2\sigma^2_{\mu p}}, \tag{6.24}$$

where $\sigma_{\mu p} \propto \sqrt{t}$. For the sake of this 1-dimensional demonstration, we choose a gaussian with fixed parameters for the detector resolution,

$$F^{\text{ex}}_{\text{res}}(\Delta x) = \frac{1}{\sigma_{\text{res}}\sqrt{2\pi}} e^{-(\Delta x)^2/2\sigma^2_{\text{res}}}. \tag{6.25}$$

The resulting $F^{\text{ex}}_b(b)$ are shown in Fig. 6.19a for $\sigma_{\text{res}} = 15$ cm and $\sigma_{\mu p} = 0$ mm, 1 mm, and 2 mm; F^{ex}_b appears very similar $F^{\text{ex}}_{\text{res}}$ in all cases, as expected since the former is just a gaussian with $\sigma_b = \sqrt{\sigma^2_{\text{res}} + \sigma^2_{\mu p}} \approx \sigma_{\text{res}}$. The acceptance of particular impact parameter cut b_{cut} is

$$\epsilon_{bcut} = \int_0^{b_{\text{cut}}} F_b(b) db. \tag{6.26}$$

The differences between $F^{\text{ex}}_b(b|t)$ and $F^{\text{ex}}_b(b|0)$ are shown in Fig. 6.19, illustrating how events are lost outside of $b < b_{cut}$ for increasing $\sigma_{\mu p}$. The relative decrease of ϵ_{bcut}, from changing $\sigma_{\mu p}$ from zero to 1 mm, is $\Delta\epsilon_{50}/\epsilon_{50} = 2.3 \times 10^{-5}$ for $b_{\text{cut}} = 50$ mm, and $\Delta\epsilon_{10}/\epsilon_{10} = 1.9 \times 10^{-3}$ for $b_{\text{cut}} = 10$ mm. Therefore, if during the muon lifetime the μp diffuse a distance characterized by $\sigma_{\mu p} = 1$ mm, the absolute effect on λ in this demonstration is roughly

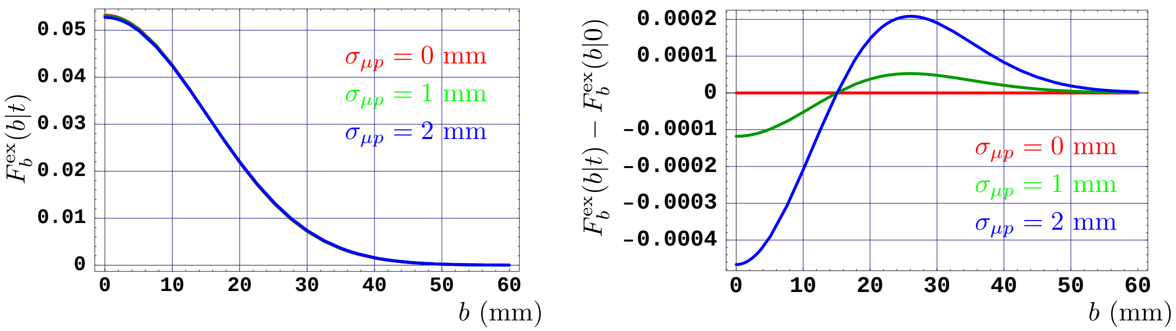

(a) b-Distributions Diffused by 0, 1 mm, and 2 mm.

(b) Differences from Undiffused b-Distribution.

Figure 6.19: Plots from the simple numerical demonstration of how a small diffusion, convoluted with a broad resolution function, leads to time-dependent acceptance once an impact parameter cut is imposed. The curves (which overlap) in the left plot are the example impact parameter distributions $F_b^{\rm ex}(b|t)$ for decays at different times t corresponding to a gaussian μp distribution spread out by $\sigma_{\mu p} = 0$ mm (red), $\sigma_{\mu p} = 1$ mm (green), $\sigma_{\mu p} = 2$ mm (blue). The curves on the right are the differences between the diffused distributions $F_b^{\rm ex}(b|t)$ and the undiffused $F_b^{\rm ex}(b|0)$.

$\Delta\lambda_{bcut} \sim \lambda_0 \Delta\epsilon_{bcut}/\epsilon_{bcut}$: $\Delta\lambda_{50} \sim 10$ s^{-1} if $b_{\rm cut} = 50$ mm, and $\Delta\lambda_{10} \sim 870$ s^{-1} if $b_{\rm cut} = 10$ mm. Even the fairly large impact parameter cut of 50 mm, which accepts 99.9% of the events in this demonstration, leads to a $\Delta\lambda$ similar to the statistical precision of the real data.

The full calculation in terms of the (effectively) 2-dimensional electron-tracking geometry and actual impact parameter distributions is explained in detail in Appendix B. The calculation is model independent until a specific μp diffusion distribution is introduced, which depends on the single free parameter k in $\sigma_{\mu p} = k\sqrt{t}$ of a gaussian distribution. The lifetime effect $\Delta\lambda_k$ is based on the time-dependent acceptance $\epsilon(t)$, for given $b_{\rm cut}$ and k, and a first moment integral over the muon decay exponential. The "diffusion parameter" k is fixed by requiring consistency of $\tilde{c}^{-1}$ (Eq. 6.21) vs. $b_{\rm cut}$, after μp diffusion is accounted for in $y^{(\rm set)}$. We write

$$y^{(\rm set)}(b_{\rm cut}) = y_d^{(\rm set)}(b_{\rm cut}) + y_p(b_{\rm cut}), \tag{6.27}$$

where y_d is the contribution from the presence of deuterium and y_p is due to μp diffusion:

$$y_d^{(\rm set)}(b_{\rm cut}) = \Delta\lambda_d(b_{\rm cut}) - \Delta\lambda_d(b_{\rm cut}^{\rm max}), \tag{6.28}$$

$$y_p^{(\rm set)}(b_{\rm cut}) = \Delta\lambda_k(b_{\rm cut}) - \Delta\lambda_k(b_{\rm cut}^{\rm max}). \tag{6.29}$$

A convenient modification is to work in terms of non-overlapping impact parameter interval

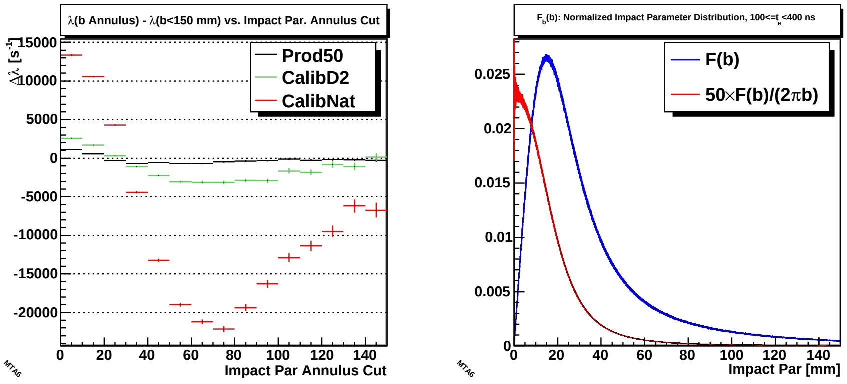

Figure 6.20: Left: Rate deviations $y^{(\mathrm{set})}(b_{\mathrm{cut1}}, b_{\mathrm{cut2}})$ of impact parameter "annulus" cuts with respect to the 150 mm "disc" cut. The impact parameter annulus cuts are indicated on the x-axis: the lower edge of a bin is b_{cut1}, and the upper edge is b_{cut2}. Right: observed impact parameter distribution $F_b(b)$ (blue), and the same divided by a phase-space factor (red, arbitrarily scaled).

cuts, or "annuli", defined by b_{cut1} and b_{cut2}: an event is accepted only if $b_{\mathrm{cut1}} \leq b < b_{\mathrm{cut2}}$, i.e., the only difference is now we are specifying a lower bound on b. The rate deviations in this case are defined as

$$y^{(\mathrm{set})}(b_{\mathrm{cut1}}, b_{\mathrm{cut2}}) = \lambda^{(\mathrm{set})}(b_{\mathrm{cut1}}, b_{\mathrm{cut2}}) - \lambda^{(\mathrm{set})}(0, b_{\mathrm{cut}}^{\mathrm{max}}), \tag{6.30}$$

and the arguments in the expressions for y_d and y_p are similarly modified. Figure 6.20a shows the results of Eq. 6.30 applied to actual data for the annuli $b_{\mathrm{cut2}} = b_{\mathrm{cut1}} + 10$ mm, for $b_{\mathrm{cut1}} = 0, 10, 20, \cdots, 140$ mm. y_p is calculated for each of these annuli, and we have the desired signal

$$y_d^{(\mathrm{set})}(b_{\mathrm{cut1}}, b_{\mathrm{cut2}}) = y^{(\mathrm{set})}(b_{\mathrm{cut1}}, b_{\mathrm{cut2}}) - y_p(b_{\mathrm{cut1}}, b_{\mathrm{cut2}}). \tag{6.31}$$

Note that $y_p(b_{\mathrm{cut1}}, b_{\mathrm{cut2}})$ is the same for all data sets, since it depends only on the impact parameter distribution (Fig. 6.20b), which is nearly the same across data sets. In practice, the deuterium signal is large enough in the CalibNat set that the y_p correction is only important in the Prod set, but we apply it to both just the same. Finally, we calculate the c_d ratio,

$$\tilde{c}^{-1}(b_{\mathrm{cut1}}, b_{\mathrm{cut2}}) = \frac{y_d^{\mathrm{Prod}}(b_{\mathrm{cut1}}, b_{\mathrm{cut2}})}{y_d^{\mathrm{calib}}(b_{\mathrm{cut1}}, b_{\mathrm{cut2}})}. \tag{6.32}$$

The uncertainties of $y_d^{(\mathrm{set})}$ (for a particular data set) are still not completely independent because of correlations via the common reference rate $\lambda^{(\mathrm{set})}(0, b_{\mathrm{cut}}^{\mathrm{max}})$, but the uncertainties of

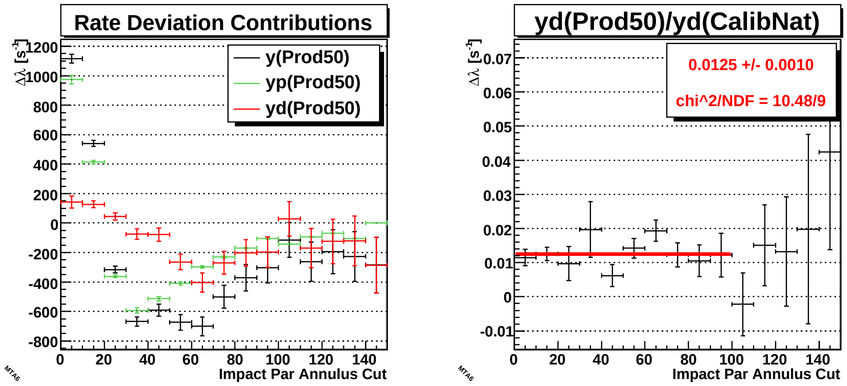

Figure 6.21: Left: observed Prod50 rate deviations $y(b_{\text{cut1}}, b_{\text{cut2}})$ (black points, same as the black points in Fig. 6.20:left); calculated effect $y_p(b_{\text{cut1}}, b_{\text{cut2}})$ due to μp diffusion (green points); and the differences $y_d(b_{\text{cut1}}, b_{\text{cut2}})$ between the black and green points attributed to μd (red points). Right: Prod50-to-CalibNat $\tilde{c}^{-1}(b_{\text{cut1}}, b_{\text{cut2}})$ after subtracting the effects of μp diffusion. The model parameter k was varied to minimize χ^2 of the constant fit (red line in figure) to $\tilde{c}^{-1}$ of the first ten annulus cuts.

$\lambda^{(\text{set})}(b_{\text{cut1}}, b_{\text{cut2}})$ are much larger than that of the reference rate. It is therefore reasonable to consider the $\tilde{c}^{-1}$ determined from non-overlapping annuli as statistically independent, which facilitates a χ^2 check of consistency.

The figure-of-merit, χ^2 of a constant fit across determinations of $\tilde{c}^{-1}$ from different annuli cuts, is used to set an optimal value for k, the only free parameter in the calculation. The calibration set can be either CalibNat or CalibD2. The "signal" y^{Prod50} from the production data is shown in Fig. 6.21a, along with y_p calculated from the optimal k, and the signal y_d^{Prod50} attributed to deuterium. The fit across $\tilde{c}^{-1}(b_{\text{cut1}}, b_{\text{cut2}})$ with the optimal k is shown in Fig. 6.21b. The χ^2 vs. k of such fits is well-behaved over a wide range of k, and the optimal value was found with standard MINUIT subroutines. Results using the two different calibration sets, and even using CalibD as the "Prod" set, are in Table 6.5. The value and error for k indicated in the table are as reported by MINUIT (MIGRAD), where the minimization is on the χ^2 of the constant fit, and $\tilde{c}^{-1}$ in the table is the value from the same constant fit. This data-analysis technique is only sensitive to deuterium ratios, and this is all that is required for the zero-extrapolation. For the sake of comparison with the external c_d measurements of the Prod gas, this quantity implied by $\tilde{c}^{-1}$ and the externally-measured c_d^{calib} are shown in the table and found to be consistent with the external ETH-Zürich measurement of $c_d^{\text{Prod}} = 1.44 \pm 0.13$ ppm. The external measurement of c_d^{CalibD} was indirect from volumetric considerations (natural hydrogen was mixed into the protium), and

Data Sets	Fitted $\tilde{c}^{-1}$	χ^2/NDF	c_{calib} (Meas.)	$c_{prod} = \tilde{c}^{-1} c_{calib}$
Prod50/CalibNat	0.0125 ± 0.0010	10.5/9	122.2 ppm	1.531 ± 0.124 ppm
Prod50/CalibD2	0.0923 ± 0.0078	10.0/9	17.8 ppm	1.638 ± 0.139 ppm
CalibD2/CalibNat	0.1341 ± 0.0030	8.9/9	122.2 ppm	16.386 ± 0.361 ppm

μp Diffusion Parameter $k = 0.4909 \pm 0.0072\ mm/\sqrt{\mu s}$

Table 6.5: Results of constant fits as in fig. 6.21b are shown in columns 2 and 3. In Column 4, c_d^{calib}, the values are from an external measurements of the calibration gas. Column 5 is the deuterium concentration of the production gas (or CalibD2 gas, in the last row) derived from the columns 2 and 4 by the formula indicated in the column label.

the reported value of 17.8 ppm may have a significant error. As stated previously, we prefer CalibNat as the calibration set because of the larger deuterium signal compared to CalibD; also, a much higher impurity capture yield was observed in CalibD than CalibNat, so the $\Delta\lambda_Z$ of the former is substantial.

The agreement between the data-analysis technique and external measurements means we can use either in the zero-extrapolation, and the calculated correction will be the same within its reported uncertainty. An advantage of the data-analysis technique, which could be considered an *in situ* measurement of c_d^{Prod}, is that c_d^{Prod} can be tracked thoughout the running period by dividing the data into chronological subsets. The external measurement reports only c_d at the beginning of the running period, when the gas sample was taken. In the course of the experiment more protium was produced from the same deuterium-depleted water to replace target hydrogen removed, e.g., for external $Z > 1$ impurity analysis. It is well known that electrolysis of water leads to deuterium enrichment in the remaining water, so there was some concern that the target gas produced later had a higher deuterium concentration. As shown in Fig. 6.22, there is no evidence for a large increase in c_d^{Prod} during the data-taking period. Even if there were a change in c_d^{Prod}, the $\tilde{c}^{-1}$ result from the data-analysis technique is the average over exactly the data we would like to correct, and it is therefore completely appropriate for a linear correction.

6.6.2 Summary of Diffuson Corrections

The correction for deuterium uses the data-analysis result of

$$\frac{c_d^{\mathrm{Prod}}}{c_d^{\mathrm{CalibNat}}} = \tilde{c}^{-1} = 0.0125 \pm 0.0010. \tag{6.33}$$

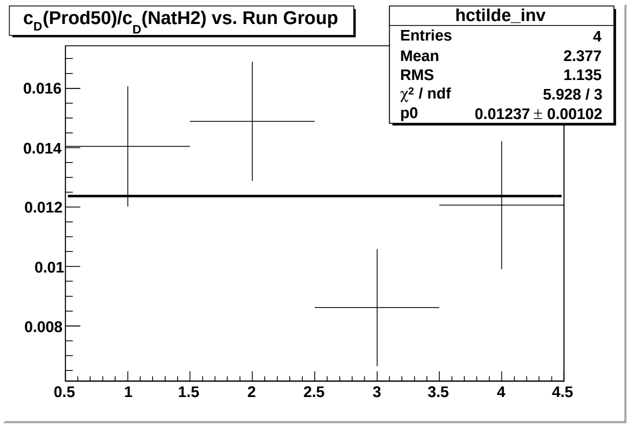

Figure 6.22: Prod50/CalibNat Diffusion concentration ratio $\tilde{c}^{-1}$ vs. Prod50 run group. The runs groups are in chronological order, formed arbitrarily by dividing the data file list evenly (by number of files) into four groups. The diffusion parameter k is set to the value found from optimization over all Prod50 data. There was some concern that the c_d concentration in the production gas may have increased in the course of the run when more gas was produced from the same light water, but no evidence of an increase is observed in this study.

An additional correction $\Delta\lambda_k$ for μp diffusion is also applied. The $y_p(b_{\text{cut}})$ ("disc" cuts) calculated with the optimal μp diffusion parameter $k = 0.4909 \pm 0.0072$ mm/$\sqrt{\mu\text{s}}$ — as determined from the annulus cuts — is shown in Table 6.6 along with the effect attributed to μd diffusion. Recall that y_p and y_d are rate deviations with respect to $\lambda(b_{\text{cut}}^{\max})$, which itself has offsets due to deuterium and μp diffusion; i.e.,

$$\Delta\lambda_k(b_{\text{cut}}) = \Delta\lambda_k(b_{\text{cut}}^{\max}) + y_p(b_{\text{cut}}). \tag{6.34}$$

Actually, it is $\Delta\lambda_k(b_{\text{cut}})$ that was calculated, and $\Delta\lambda_k(b_{\text{cut}}^{\max}) = 1.4$ s^{-1} was subtracted to get $y_p(b_{\text{cut}})$. We should not forget this offset when reading the μp diffusion correction from Table 6.6. For an impact parameter cut of 120 mm, the μp diffusion correction is then

$$\Delta\lambda_k = 3.1 \pm 0.1 \text{ s}^{-1}. \tag{6.35}$$

6.6.3 Further Comments

Some notes concerning the reliability of the above calculation of the μp diffusion correction are listed.

- There is some theoretical preference to using decays starting at the lifetime fit start time ($\approx$ 100 ns) to construct $F_b(b)$: by this time many of the epithermal μp have ther-

b_{cut} [mm]	$y(b_{cut})$ [s^{-1}]	$y_p(b_{cut})$ [s^{-1}]	$y_d(b_{cut})$ [s^{-1}]
10	1115.3 ± 30.0	972.0 ± 28.3	143.4 ± 41.3
20	735.1 ± 14.4	601.7 ± 17.5	133.4 ± 22.7
30	374.3 ± 9.3	270.4 ± 8.0	103.8 ± 12.2
40	191.4 ± 6.7	118.8 ± 3.5	72.6 ± 7.6
50	115.0 ± 5.2	57.3 ± 1.7	57.7 ± 5.5
60	68.9 ± 4.1	29.7 ± 0.9	39.2 ± 4.2
70	39.1 ± 3.3	16.9 ± 0.5	22.2 ± 3.4
80	24.6 ± 2.7	10.0 ± 0.3	14.6 ± 2.7
90	15.9 ± 2.2	6.3 ± 0.2	9.5 ± 2.2
100	10.9 ± 1.8	4.5 ± 0.2	6.4 ± 1.8
110	8.0 ± 1.4	2.7 ± 0.1	5.3 ± 1.4
120	5.4 ± 1.0	1.7 ± 0.1	3.6 ± 1.0
130	3.3 ± 0.7	1.1 ± 0.1	2.1 ± 0.7
140	1.3 ± 0.4	0.4 ± 0.1	0.8 ± 0.4

μp Diffusion Parameter $k = 0.4909 \pm 0.0072$ *$mm/\sqrt{\mu s}$*

$\Delta\lambda_k(b_{\mathrm{cut}}^{\max} = 150\ mm) = 1.4\ \mathrm{s}^{-1}$

Table 6.6: Contribution to the rate deviation due to an impact parameter *disc* cut. The y-column is from Prod50 data, $y(b_{cut}) = \lambda(b_{cut}) - \lambda(150mm)$. $y_p(b_{cut})$ is the expected rate shift due to μp diffusion, where the uncertainties in the values are from the uncertainty in the diffusion parameter k. $y_d(b_{cut}) = y(b_{cut}) - y_p(b_{cut})$ is attributed to μd diffusion.

malized, and the spreading of μp stop position is folded into $F_b(b)$ and automatically accounted for in the y_p calculation. The time acceptance interval should not extend too late, however, because then F_b would already be somewhat spread by thermal diffusion and possibly μd diffusion. The $F_b(b)$ used in the calculations of this section is based on decay times in the interval 100–400 ns. Different decay-time intervals were studied, and the results for $\tilde{c}^{-1}$ were always within the reported error. As noted in Section B.1, to a good approximation $\Delta\lambda_k(b_{\mathrm{cut}})$ depends only on the slope $dF_b(b_{\mathrm{cut}})/db$.

- It is argued in Section B.4 that the derivations of Section B.1 are actually quite general, in that by using the observed impact parameter distribution, we are already taking into account the TPC resolution and electron detector resolution asymmetries.

- A possible source of systematic error is from the diffusion model, which was taken to be thermal diffusion, represented by a gaussian distribution with $\sigma = k\sqrt{t}$. The average μp diffusion displacement in *3D* at time t is $R(t) = 2\sqrt{2/\pi}\,k\,\sqrt{t}$; putting in the value for the model parameter k gives $R(t) = 0.78\,\sqrt{t}$. The original MuCap proposal [50] covers the kinetics of μp diffusion in detail, and in the Appendix 10.2 of the proposal, titled “Simple analytical estimation of diffusion,” the following estimation for the mean diffusion range R is quoted:

$$R \sim \sqrt{\frac{vt}{\sigma N}}, \tag{6.36}$$

where v is the mean velocity, σ here is “the transport cross section averaged over the thermal distribution of the μp atoms and target molecules,” and N is the molecular density. The proposal further gives numerical values for the parameters in equation 6.36 relevant for MuCap conditions of temperature 300 K and density 0.01 of LN_2: $v = 0.26$ cm/μs, and $1/(\sigma N) = 0.023$ cm. With these values, equation 6.36 becomes $R \sim 0.77\sqrt{t}$ (R in mm and t in μs), in excellent quantitative agreement with $R(t)$ calculated with the model diffusion used in this note. We can at least conclude that the value of $k = 0.49$ mm/$\sqrt{\mu\text{s}}$, necessary to give consistency of $\tilde{c}^{-1}$ with impact parameter cut, is entirely reasonable.

6.7 Lifetime Fit Consistency Checks

There are many parameters in the analysis that can be varied with the expectation that the results will not change. Any non-statistical variations in the results must be explained and possibly promoted to a systematic correction. A few of these consistency checks are presented in the following subsections.

6.7.1 Lifetime vs. eSC Segment

In this study, lifetime histograms are filled based on which eSC segment (1 – 16) is included in the electron track. The results $\{\lambda^i_{\text{fit}}\}$, where i labels the eSC segment, are plotted in Fig. 6.23; the leftmost point is from the fit to the lifetime spectrum summed over all eSC segments. The statistical consistency of the λ^i_{fit} is demonstrated by the constant fit shown in Fig. 6.23a.

It is worth mentioning that this study has a special place in the history of the MuCap analysis, since early results showed deviations of at least three times what is statistically allowed. This was a puzzle for some time, until it was discovered that delta electrons — in combination with a fragile muon stop definition of the early analysis versions — were creating a decay-time-dependent efficiency to accept a muon track. The much more robust algorithm of the present analysis does not suffer these same distortions, as has been discussed above.

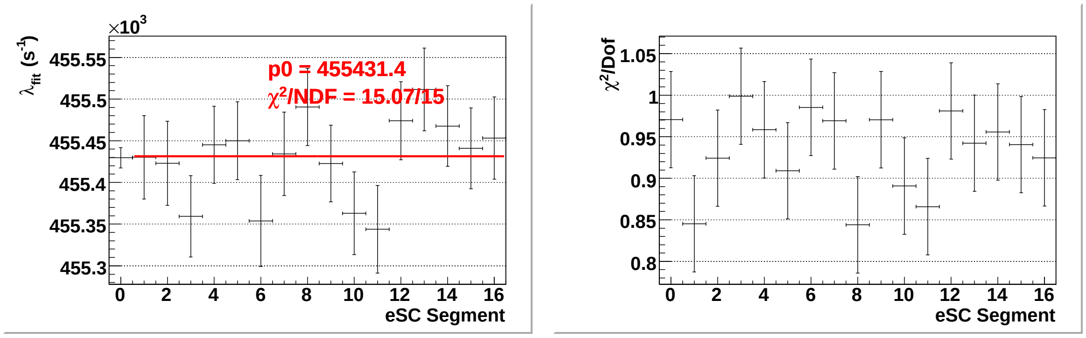

(a) Fit Parameter λ (b) χ^2/Dof of Fit

Figure 6.23: Lifetime vs. eSC Segment. Segment "0" is the sum over all eSC segments. The value of a constant $p0$ fit across the λ^i_{fit}, where i labels the eSC segment $(1-16)$, is shown in (a) along with the χ^2/Dof of this constant fit.

6.7.2 Lifetime vs. TPC Fiducial Volume

The purpose of this study is to confirm that the standard fiducial volume is sufficiently far from TPC boundaries. The TPC volume is logically divided into a series of nested boxes, starting with the largest fiducial volume possible and becoming successively smaller. The space V_i between each box and the next smaller one is a fiducial volume shell. Since there is no overlap between different volume shells, the lifetime spectra vs. volume shell are statistically independent. Fit results are shown in figure 6.24. The standard fiducial volume, indicated by the vertical green line in the figures, appears to be fine, and a constant fit across all $\lambda_{\text{fit}}(V_i)$ with the standard fiducial volume demonstrates statistical consistency.

6.7.3 Lifetime vs. Muon Track Cut

The purpose of the muon track "head cut," part of the muon track definition and illustrated in Fig 5.2b, is to veto tracks that continue beyond an apparent stop point. This cut on the difference between the most downstream EL pixel and the most downstream EH pixel is set to 2 anode spacings, or "AnodeMaxEL $-$ AnodeMaxEH ≤ 2." If not for extraEL pixels from delta electrons of the Michel electrons, the head cut could be made quite strict, say ≤ 1 to cut scatters but keep events with the Bragg peak just overlapping the next anode. The head cut of ≤ 2 avoids most vetos on an extraEL included by next-nearest-neighbor pixel clustering into the muon track. It could be argued to relax the cut to ≤ 3, so events that have an EL pixel from the Bragg peak extending a bit onto the next anode are not vetoed by an extraEL pixel at stop anode $+\,3$; however, the combined probability of this event veto

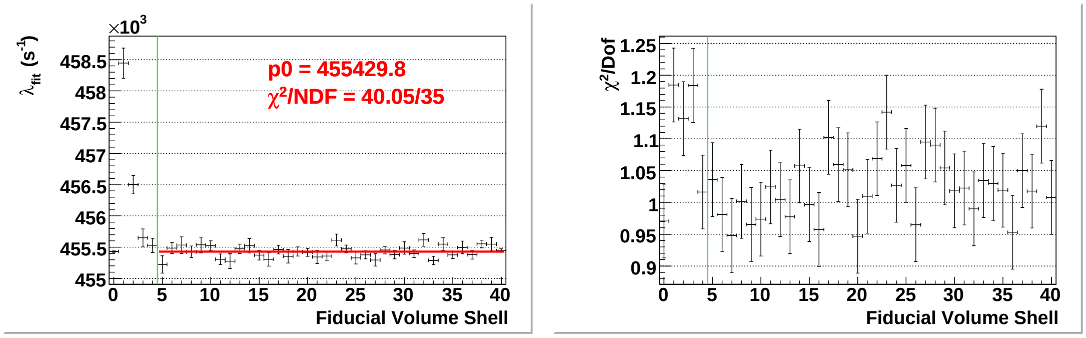

(a) Fit Parameter λ (b) χ^2/Dof of Fit

Figure 6.24: Lifetime vs. TPC Fiducial Volume Shell. The fit parameter in the leftmost bin is for reference: it is from stops in the standard fiducial volume, which are well away from the walls. The rest of the fits represent statistically independent data of muon stops in successively smaller, nested volume shells V_i. The shells are of uniform thickness ≈1.1 mm, except the volume corresponding to the rightmost bin, which does not have an inner bounding surface. The sum of all events included in the fits to the right of the vertical green line are those of the standard UIUC fiducial volume. The result $p0$ of a constant fit across the $\lambda_{\mathrm{fit}}(V_i)$, for the V_i within the standard fiducial volume, is shown in the figure along with its χ^2/Dof.

is quite small, perhaps 10^{-4} as will be argued based on the lifetime spectra of this section.

To check for the influence of the head cut on the lifetime, this cut is varied from 0 to up to 7, and then to ≥ 8; The standard cut of ≤ 2 anodes is included as a reference. Fit results are in Table 6.7. The effect of relaxing the head cut to ≤ 3 anodes can be estimated from the table by comparing the parameters for the ≤ 2 anodes head cut to those for the differential head cut of 3 anodes: $N_{=3}/N_{\leq 2} \approx 10^{-4}$, $\Delta\lambda \approx (\lambda_{=3} - \lambda_{\leq 2})10^{-4} \approx 2$ Hz. This observed $\Delta\lambda > 0$ could be from avoiding a time-dependent veto via the more relaxed cut, implying the standard cut is too strict; another possibility is the relaxed cut allows some $\mu + p$ scatter events into the lifetime spectrum, slightly raising the rate from the more accurate value at the standard cut. Therefore it seems reasonable to include an entry in the systematic errors table, called "muon track definition" or the like, of 0 ± 2 Hz.

6.7.4 Fit Start Time Scan

Varying the time range $[t_{\mathrm{start}}, t_{\mathrm{stop}}]$ of the lifetime fits is a good way to check for subtle distortions the lifetime spectrum that would not be reflected in the χ^2 of the fit. For example, if the singlet-to-triplet hyperfine transition rate λ_{hf} of the μp atom were slower than expected, some triplet μp could still be present beyond the start time of the lifetime fit.

maxEL - maxEH	N	λ [s^{-1}]	B	χ^2/DOF
<= 2 anodes	1.603×10^9	455430.0 ± 12.2	2154.9 ± 5.1	1.05 ± 0.06
= 0 anodes	1.261×10^9	455364.9 ± 13.7	1695.2 ± 4.5	1.13 ± 0.06
= 1 anodes	3.410×10^8	455587.0 ± 26.4	456.4 ± 2.3	1.20 ± 0.06
= 2 anodes	9.325×10^5	489016.9 ± 552.4	1.8 ± 0.1	1.34 ± 0.06
= 3 anodes	1.941×10^5	475516.0 ± 1178.8	0.4 ± 0.1	1.07 ± 0.06
= 4 anodes	2.101×10^4	484079.5 ± 4218.4	0.5 ± 0.1	0.84 ± 0.08
= 5 anodes	9.063×10^3	494330.9 ± 7048.5	0.5 ± 0.1	1.04 ± 0.08
= 6 anodes	8.048×10^3	498180.0 ± 7574.2	0.6 ± 0.1	0.99 ± 0.08
= 7 anodes	5.325×10^3	514457.0 ± 10152.4	0.6 ± 0.1	0.84 ± 0.08
> 8 anodes	1.467×10^4	477077.7 ± 5095.7	0.5 ± 0.1	0.97 ± 0.08

Table 6.7: Lifetime vs. Track Head Cut. The fit range is 100 to 12000 ns for all fits except the first three, which have enough statistics that the fit can be done over the full 100 to 24000 ns range. Bin errors are not increased to account for double counting in the background.

Then there would be some component of the lifetime at early times characterized by rate $\lambda_0 + \Lambda_\mathrm{T}$, significantly lower than the desired $\lambda_0 + \Lambda_\mathrm{S}$. In this hypothetical case, the result $\lambda_\mathrm{fit}(t_\mathrm{start})$ would be larger for later t_start. Another example is the effect of including some $Z > 1$ stops in the spectrum, which would tend to go the opposite way as that just discussed: $\lambda_\mathrm{fit}(t_\mathrm{start})$ would decrease for later t_start as the $Z > 1$ component decays away faster than the singlet μp component. The last example that will be given here is not hypothetical, and that is the effect of $p\mu p$ molecular formation. The relative populations of the singlet μp, ortho and para molecular states shown in the Fig. 3.2 of the Kinetics chapter. The ortho $p\mu p$ has a somewhat lower muon capture rate $\Lambda_\mathrm{om} \approx \frac{3}{4}\Lambda_\mathrm{S}$, and that on the para $p\mu p$ is lower still, $\Lambda_\mathrm{pm} \approx \frac{1}{4}\Lambda_\mathrm{S}$. Quantitative calculations show that molecular formation under MuCap conditions does not appreciably affect the fit start time scan at the current statistical precision, and the lifetime should be consistent as t_start is varied. Results of the start time scan, in which t_stop is held fixed at its standard 24 μs and t_start is varied, are shown in Figure 6.25; the lines in (a) indicate the 1-σ statistically allowed deviation with respect to the result with the standard fit time range of $[0.1, 24.0]$ μs (leftmost point in the figure). $\lambda_\mathrm{fit}(t_\mathrm{start})$ does not vary more than expected.

6.7.5 Fit Stop Time Scans

This study is similar to the start time scan, except here t_start is held fixed and t_stop is varied. Results are shown in Figure 6.26. The interpretation of this study is not as obvious as for the start time scan, but no problems are evident.

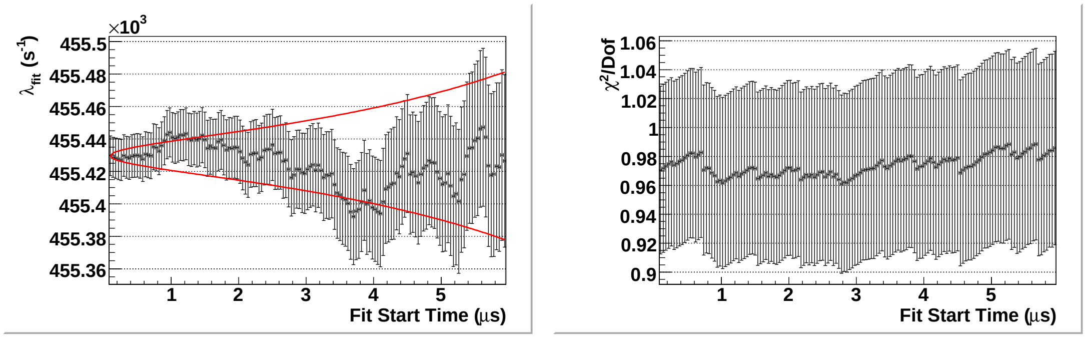

(a) Fit Parameter λ (b) χ^2/Dof of Fit

Figure 6.25: Fit Start Time Scan of the Lifetime Spectrum. The time range of the lifetime fit is varied, and results are plotted vs. the beginning of the range t_{start}; the end of the time range t_{stop} is fixed to 24 μs. The red curves in (a) indicate the statistically allowed (at 1σ) deviation with respect to the λ_{fit} from the standard fit range of 0.1 to 24 μs.

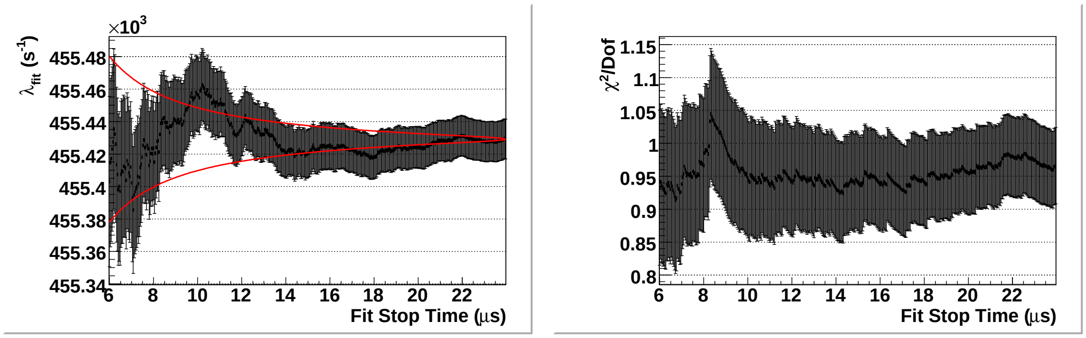

(a) Fit Parameter λ (b) χ^2/Dof of Fit

Figure 6.26: Fit Stop Time Scan of the Lifetime Spectrum. The time range of the lifetime fit is varied, and results are plotted vs. the end of the range t_{stop}; the beginning of the time range t_{start} is fixed to 0.1 μs. The red curves in (a) indicate the statistically allowed (at 1σ) deviation with respect to λ_{fit} from the standard fit range of 0.1 to 24 μs (rightmost point).

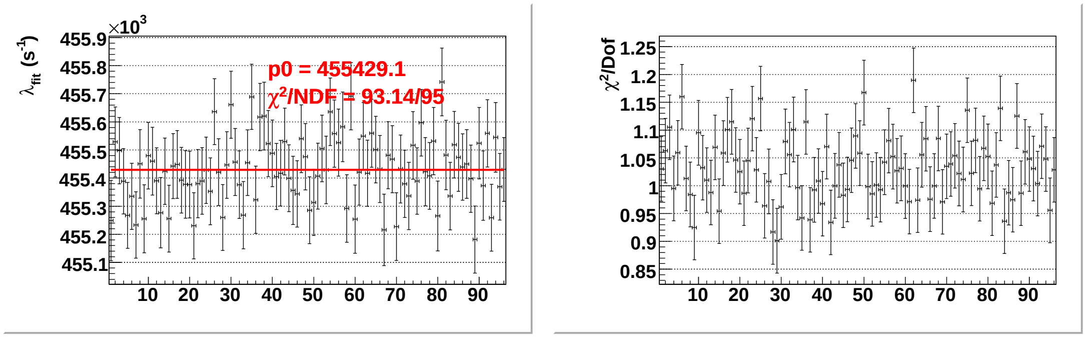

(a) Fit Parameter λ

(b) χ^2/Dof of Fit

Figure 6.27: Lifetime vs. Prod50 Run Group. The divisions are the Prod50 data set divided into 96 chronological pieces of approximately equal statistics. A constant fit across all λ_{fit} is shown in (a).

6.7.6 Lifetime vs. Run Group

The Prod50 data set is split into 96 chronological subgroups, each with similar numbers of μ-e events. Lifetime spectra frome each subgroup are fit, and the results $\lambda_{\text{fit}}(G_j)$ and $\chi^2(G_j)/\text{Dof}$, where G_j is the j^{th} subgroup, are displayed in Fig. 6.27. The results are found to be statistically consistent, and a constant fit to the set of $\lambda_{\text{fit}}(G_j)$ is shown in the figure. There is no evidence that a systematic effect is caused by slow changes — such as in ambient temperature, which affects the density of the hydrogen and therefore the gain of the TPC — throughout the course of the experimental running period.

6.8 Choice of *e*-Definition

The final consistency check before unblinding is the lifetime versus choice of electron definition in the analysis. Possibilities are combinations of the following items in italics.

- *Combination of Electron Detector Planes.* Three options are studied:

  1. **eSC.** The ePC's are ignored;
  2. **CathAND.** Full *e*-detector tracking (eSC, ePC1, and ePC2 coincidence), in which the anode, inner and outer cathode planes of each ePC are required;
  3. **CathOR.** Full *e*-detector tracking (eSC, ePC1, and ePC2 coincidence), in which each ePC hit requires the anode and at least one cathode plane.

- *Electron Gating.* There are two options:

    1. **All Electrons Accepted.** Each electron time t_e enters the lifetime spectrum after subtraction of each good muon time t_μ;
    2. **One Electron Gated.** Only events that have one electron time that satisfies $t_\mu - 10\ \mu\text{s} < t_e < t_\mu + 20\ \mu\text{s}$ ("unique" electrons) are filled into the lifetime spectrum.

- *b Cut.* b is the distance of closest approach (impact parameter) of an electron tracked back to the muon stop position. Only μ-e events that satisfy $b < b_{\text{cut}}$, for some specified b_{cut}, enter the lifetime histogram. This option is not compatible with the eSC-only specification, since electron tracking requires the ePC's. Two different impact parameter cuts are studied:
    1. **b < 120 mm.** This is a loose enough cut that diffusion corrections are not too big;
    2. **No b Cut.** No explicit cut on b is imposed. The diffusion corrections are smaller, but the lifetime spectrum has ~ 5 times the background level as the one subject to the 120-mm impact parameter cut. Also, it is possible that more $Z > 1$ stops are included for example from undetected pileup or $\mu + p$ scatters that fake good muon stops.

Recall that the $b < 120$ mm, all-electrons-accepted, CathOR lifetime spectrum is the standard thus far, used in all the above studies except where noted.

No completely convincing reason has been offered to favor one electron definition over to the others, but it was agreed upon within the MuCap collaboration to base the final result for Run8 on the "$b < 120$ mm", "All Electrons Accepted" lifetimes, averaging the "CathOR" and "CathAND" λ's into a single value, which we will call λ^{MuCap}. The choice of the 120-mm impact parameter cut is due to a preference for the much lower background level and well-defined b_{cut}, the latter suggested by the diffusion systematics studies. Accepting all electrons instead of only the single-electron events, one could argue, avoids a (marginal) loss in statistics. The "one electron gated" requirement leads to the harmless dead time effect, if it is present, of a background contribution that decays away with the same lifetime as the desired measurement. No consequences to λ_{fit} of electron-detector dead time effects were found in any case. The original choice in the UIUC analysis to use CathOR e-detector tracking was motivated by the higher efficiency and reduced dead time response of the overall electron detector in this treatment; however, perhaps the CathAND treatment reduces the effects of afterpulsing or detector noise. Thus, the prescription set by collaboration is followed, and the other e-definitions are used to set a conservative "consistency" systematic uncertainty.

Comparison of the λ's from the various e-definitions is best performed after diffusion corrections are applied, since the sensitivities to diffusion effects may be explicitly or implicitly different. The diffusion correction in turn is more accurately calculated after the respective impurity corrections are added to the Prod50 and CalibNat λ_{fit}'s. The results of lifetime fits, corrected for impurities, extrapolated to zero deuterium concentration, and then with the μp diffusion effect correction subtracted off, are shown in table 6.8. The remaining systematic studies — unseen $\mu + p$ scatters, muon track definition, and entrance counter time-independent inefficiency — give uncertainties that will be applied uniformly to all of the λ's. Aside from these yet-to-be-applied, small increases in their uncertainties, the values for the corrected λ's, in the last column of the table, may now be checked for consistency with λ^{MuCap}.

The sets of events resulting from the different e-definitions overlap each other by at least 77% and as much as $\approx$ 95%, depending on which sets are compared, so we cannot simply fit a constant across the $\lambda(e\text{Def.})$ and expect a meaningful χ^2. Differences of the $\lambda(e\text{Def.})$ from λ^{MuCap} are plotted in Fig. 6.28; the errors indicated are those on $\lambda(e\text{Def.})$, ignoring correlations with and the uncertainty of λ^{MuCap}. The overlap factors can be calculated from N_{fit}'s when one set is an obvious subset of another, such as between the "unique e" and "all e" sets for the same ePC treatment and b_{cut}, but care must be taken if the background fractions are significant and very different. The MuCap collaboration opted to add a conservative systematic uncertainty of ± 5 s^{-1} for "analysis methods," which covers most of the observed deviations within this analysis, within the UCB analysis, and between the two analyses.

6.9 Summary of Internal Systematic Corrections

The systematic errors discussed in this chapter are summarized in Table 6.10. These are dependent on details of the experiment and are therefore designated "internal" systematic errors. The final step, before interpreting the result for λ in terms of Λ_S, is unblinding of the clock frequency. The actual clock frequency was 100.001000 MHz, compared to the frequency assumed in the analysis of exactly 100 MHz. Thus, the final λ^{MuCap} is multiplied by a factor of 1.001 to convert to actual s^{-1}. The final value for λ^{MuCap} in terms of actual

e-Definition		Prod50 $\lambda_{\text{fit}} + \Delta\lambda_Z$[a]	Deuterium Correction[b]	μp Diffusion Correction[c]	Corrected λ
All Electrons Accepted	CathOR $b < 120$ mm	455412.2 ± 13.0	-12.2 ± 1.8	-3.1 ± 0.1	455396.8 ± 13.2
	CathAND $b < 120$ mm	455405.6 ± 13.4	-12.0 ± 1.8	-3.1 ± 0.1	455390.5 ± 13.5
	CathOR No b Cut	455397.4 ± 13.1	-8.1 ± 1.5	—	455389.3 ± 13.2
	CathAND No b Cut	455392.8 ± 13.5	-7.8 ± 1.6	—	455385.0 ± 13.6
	eSC	455401.8 ± 13.5	-7.8 ± 1.6	—	455394.0 ± 13.6
One-Electron Gated	CathOR $b < 120$ mm	455410.5 ± 13.4	-12.3 ± 1.8	-2.5 ± 0.1	455395.7 ± 13.5
	CathAND $b < 120$ mm	455404.6 ± 13.7	-12.0 ± 1.8	-2.5 ± 0.1	455390.2 ± 13.8
	CathOR No b Cut	455400.2 ± 13.4	-9.0 ± 1.6	—	455391.1 ± 13.5
	CathAND No b Cut	455396.2 ± 13.7	-8.6 ± 1.6	—	455387.6 ± 13.8
	eSC	455400.6 ± 13.0	-8.8 ± 1.6	—	455391.8 ± 13.1

---

[a] Using $Y(Z,\text{obs}) = 10.6 \pm 0.08$ ppm, $\beta_N = 1.30 \pm 0.08$ s^{-1}/ppm, $\beta_O = 1.65 \pm 0.45$ s^{-1}/ppm, and $\alpha = 0.05 \pm 0.05$.

[b] Using $\tilde{c}^{-1} = 0.0125 \pm 0.0010$, and adding 0.50 s^{-1} to the error on this correction to account for nonlinearity at $c_D = 122$ ppm.

[c] Using model diffusion parameter $k = 0.4909 \pm 0.0072$ mm/$\sqrt{\mu\text{s}}$

Table 6.8: Summary of λ results with different electron detector treatments. The complete Prod50 fit parameters are in table 6.9.

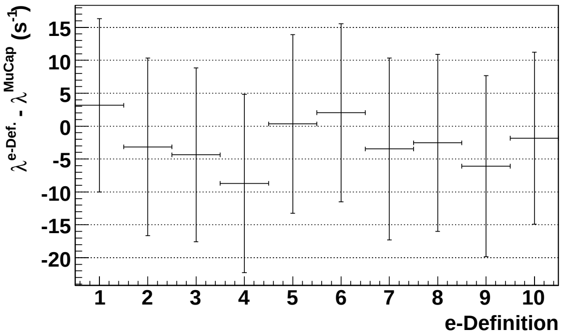

Figure 6.28: The corrected λ's from Table 6.8 with λ^{MuCap} (the average of the two "all electrons accepted, $b < 120$ mm" λ's) subtracted off.

e-Definition		N_{fit}	λ_{fit}	B_{fit}	X_{BG}	χ^2/Dof
All Electrons Accepted	CathOR $b < 120$ mm	1.603×10^9	455429.6 ± 12.2	2.154×10^3	8.022×10^{-4}	0.97 ± 0.06
	CathAND $b < 120$ mm	1.511×10^9	455423.0 ± 12.6	2.008×10^3	7.931×10^{-4}	0.98 ± 0.06
	CathOR No b Cut	1.679×10^9	455414.8 ± 12.3	9.921×10^3	3.527×10^{-3}	1.09 ± 0.06
	CathAND No b Cut	1.581×10^9	455410.2 ± 12.7	9.240×10^3	3.488×10^{-3}	1.08 ± 0.06
	eSC	1.786×10^9	455419.2 ± 12.7	4.765×10^4	1.593×10^{-2}	1.01 ± 0.06
One-Electron Gated	CathOR $b < 120$ mm	1.454×10^9	455427.9 ± 12.6	2.030×10^2	8.336×10^{-5}	0.97 ± 0.06
	CathAND $b < 120$ mm	1.387×10^9	455422.0 ± 12.9	2.436×10^2	1.049×10^{-4}	0.97 ± 0.06
	CathOR No b Cut	1.499×10^9	455417.5 ± 12.6	1.267×10^3	5.044×10^{-4}	0.96 ± 0.06
	CathAND No b Cut	1.431×10^9	455413.6 ± 12.9	1.447×10^3	6.036×10^{-4}	0.96 ± 0.06
	eSC	1.703×10^9	455418.0 ± 12.2	8.383×10^3	2.938×10^{-3}	0.89 ± 0.06

Table 6.9: Parameters from the fits to Prod50 lifetime spectra with different electron detector treatments. N_{fit}, λ_{fit} and B_{fit} are the results of the fit with the model function $f(t) = Nw\lambda e^{-\lambda t} + B$, where w is the fixed histogram bin width of 40 ns. The total background fraction X_{BG} is derived from the fit parameters and the number N_{bins} of histogram bins included in the fit via $X_{\text{BG}} = (B_{\text{fit}} N_{\text{bins}}/w)/N_{\text{fit}}$: this is the ratio of the number of events in the flat background to the number in the lifetime part.

Source	Correction (s^{-1})	Uncertainty (s^{-1})
$Z > 1$ impurities ($\Delta\lambda_Z$)	-17.4	4.6
Deuterium ($\Delta\lambda_d$)	-12.1	1.8
μp Diffusion ($\Delta\lambda_k$)	-3.1	0.1
Unseen $\mu + p$ scatters ($\Delta\lambda_{\mathrm{sc}}$)	0.0	3.0
μ stop definition ($\Delta\lambda_{\mathrm{tr}}$)	0.0	2.0
μ pileup veto inefficiency ($\Delta\lambda_\kappa$)	0.0	3.0
Analysis methods ($\Delta\lambda_{\mathrm{Ana}}$)	0.0	5.0
Total	-32.6	± 8.4

Table 6.10: Summary of internal experimental corrections to λ.

inverse seconds is presented in Table 7.2 of the next chapter.

Chapter 7

Results

7.1 Λ_{S} from MuCap λ_μ^-

After the adjustments described in Chapter 6 for impurities, deuterium, and μp diffusion are applied, we arrive at an experimental result for the muon disappearance rate λ_μ^- of negative muons stopped in hydrogen gas of density $\phi = 0.0112$ and temperature $T = 300$ K. The target conditions are such that most muons are prepared in the singlet μp atomic state; however, the small amount of molecular formation is significant and must be accounted for to accurately interpret λ_μ^- in terms of the singlet capture rate Λ_{S}. Fitting the observed μ^- lifetime spectrum with a single-exponential function leads to a result

$$\lambda_\mu^- = \lambda_0 + \Lambda_{\mathrm{S}} + \Delta\lambda_{p\mu p}, \tag{7.1}$$

where the last term represents the effect of molecular formation and λ_0 is the muon disappearance rate in the absence of any muon capture.

The calculation of $\Delta\lambda_{p\mu p}$ is described in Chapter 3 and Appendix A. The approach is to generate a lifetime spectrum using the full kinetics equation, fit a single-exponential model function, and thus observe a shift of λ_μ^- from its value in the absence of molecular formation ($\lambda_0 + \Lambda_{\mathrm{S}}$) by an amount $\Delta\lambda_{p\mu p}$. Rates of ortho molecular formation λ_{of} and ortho-para transition λ_{op} are set to $\lambda_{\mathrm{of}} = (2.3 \pm 0.5) \times 10^6\ \mathrm{s}^{-1}$ and $\lambda_{\mathrm{op}} = (6.9 \pm 4.3) \times 10^4\ \mathrm{s}^{-1}$ to cover most literature values (see Tables 3.1 and 3.2). The rates Λ_{om} and Λ_{pm} of muon capture from the ortho and para molecular states are functions of Λ_{S}; consequently, $\Delta\lambda_{p\mu p}$ depends on Λ_{S} itself, and there is a slight loss of sensitivity in Eq. 7.1 between Λ_{S} and the observed rate λ_μ^-. The reduction in sensitivity can be seen by rearranging Eq. 7.1 and Taylor expanding $\Delta\lambda_{p\mu p}$ about some reasonable value Λ_{S}^0 of the singlet capture rate:

$$\Lambda_{\mathrm{S}} = \lambda_\mu^- - \lambda_0 - \left\{ \Delta\lambda_{p\mu p}(\Lambda_{\mathrm{S}}^0) + \frac{\partial \Delta\lambda_{p\mu p}}{\partial \Lambda_{\mathrm{S}}} \left(\Lambda_{\mathrm{S}} - \Lambda_{\mathrm{S}}^0 \right) + \cdots \right\}. \tag{7.2}$$

Λ_{S} (s^{-1})	λ_{of} ($\mu\mathrm{s}^{-1}$)	λ_{op} ($\mu\mathrm{s}^{-1}$)	$\Delta\lambda_{p\mu p}$
723.00	2.30	0.000	-17.34
723.00	1.80	0.069	-18.35
723.00	2.30	0.069	-23.06
723.00	2.80	0.069	-27.63
723.00	2.30	0.026	-19.71
723.00	2.30	0.069	-23.06
723.00	2.30	0.112	-25.84
703.00	2.30	0.069	-22.41
743.00	2.30	0.069	-23.71

Table 7.1: Corrections for molecular formation for different values of λ_{of} and λ_{op}. The variations in the parameters are the recommended 1-σ values, so the error on $\Delta\Lambda_{p\mu p}$ due to that on λ_{of} (λ_{op}) can be estimated from rows 2 – 4 (5 – 7). The last two rows can be used to find the senstivity of the correction on Λ_S (i.e., $\partial\Delta\Lambda_{p\mu p}/\partial\Lambda_S$).

A fluctuation in $(\lambda_\mu^- - \lambda_0)$ by an amount $\delta\lambda$ produces a change $\delta\Lambda_{\mathrm{S}}$ in the extracted value of Λ_{S}, with the relation

$$\delta\Lambda_{\mathrm{S}} \approx \left(1 + \frac{\partial\Delta\lambda_{p\mu p}}{\partial\Lambda_{\mathrm{S}}}\right)^{-1} \delta\lambda. \tag{7.3}$$

We will account for this by scaling the final uncertainty of Λ_{S} according to Eq. 7.3. Table 7.1 shows $\Delta\lambda_{p\mu p}$ calculated with an array of values for Λ_{S}, λ_{of}, and λ_{op}. Each molecular rate parameter is varied by its uncertainty while the other and Λ_{S} are held at their central values. In that way the uncertainty of $\Delta\lambda_{p\mu p}$ due to that in each molecular parameter is determined. The partial derivative with respect to Λ_{S} is computed similarly to be $\frac{\partial\Delta\lambda_{p\mu p}}{\partial\Lambda_{\mathrm{S}}} = -3.2\%$, meaning the final Λ_{S} error should be increased by a sensivity factor $\alpha_{\mathrm{sens}} = (1 - 0.032)^{-1} = 1.034$.

We turn now to the value for λ_0, the parameter in Eq. 7.1 that represents the μ^- decay rate in the absence of nuclear capture. Assuming CPT invariance of muon decay, and apart from a small bound-state correction $\Delta\lambda_{\mu p}$ to the decay rate of a μ^- in the μp atomic state, λ_0 is equivalent to the free μ^+ decay rate λ_μ^+; i.e.,

$$\lambda_0 = \lambda_\mu^+ + \Delta\lambda_{\mu p}. \tag{7.4}$$

The positive muon lifetime $\tau_\mu^+ = 1/\lambda_\mu^+$ has been measured in several experiments, and the previous world average $\tau_\mu^+ = (2.19703 \pm 0.00004) \times 10^{-6}$ s [21] was recently updated to a value with even higher precision: $\tau_\mu^+ = (2.197019 \pm 0.000021) \times 10^{-6}$ s [8].

The last quantity to determine, before extracting the experimental result for Λ_{S} based on Eqs. 7.1 and 7.4, is $\Delta\lambda_{\mu p}$. As pointed out by several authors ([7], [60], [61]), the bound-state

	Value (s^{-1})	Uncertainty (s^{-1}) Stat.	 Syst.
MuCap λ_μ^-	455849.1	12.4	8.4
Molecular Formation (λ_{of}) Correction	17.3		4.7
Molecular Transitions (λ_{op}) Correction	5.7		3.4
Bound State Correction ($\Delta\lambda_{\mu p}$)	12.3		
World Average λ_μ^+	455162.2	4.4	
MuCap Λ_S[a]	722.2	13.6	10.6

---

[a] The uncertainties are increased by a factor 1.034 to account for the sensitivity of the molecular correction to Λ_S.

Table 7.2: Final determination of Λ_S from the UIUC analysis of the MuCap Run8 data. Uncertainties are divided into statistical (Stat.) and systematic (Syst.) contributions, and all errors are added in quadrature for the last row.

effect on the muon lifetime may be understood in terms of a few competing contributions: 1) relativistic time dilation of the muon due to its orbital motion; 2) reduction of the phase-space available to the decay electron because of the initial binding energy (i.e., the muon is off-shell); and 3) the Coulomb interaction of the final-state electron with the proton, which may be considered as either increasing the overlap between the muon and electron wavefunctions, or as a downward shift in the electron's energy spectrum. In leading order, the latter two contributions exactly cancel, leaving only the time-dilation effect. The result for R, the ratio of free to bound (μZ) muon lifetimes, is $R = \lambda_0/\lambda_\mu^+ = 1 - (Z\alpha)^2/2$ [7], where α is the fine structure constant. Including a nuclear recoil correction modifies R by an additional $-0.06(Z\alpha)^2 m_\mu/m_p$ [60] ($\approx 1\%$ of the leading-order term) and we have (setting $Z = 1$):

$$\Delta\lambda_{\mu p} = -\left(\frac{1}{2}\alpha^2 + 0.06\alpha^2\frac{m_\mu}{m_p}\right)\lambda_\mu^+ = -12.3\ \text{s}^{-1}. \tag{7.5}$$

The final determination of the singlet capture rate Λ_S from the UIUC analysis of MuCap Run8 (2004) data is summarized in Table 7.2. The recommended value is $\Lambda_S^{\text{Mucap}} = 722.2 \pm 17.2\ \text{s}^{-1}$, where the statistical and systematic uncertainties are added in quadrature. The average of this analysis and that of the independent UC-Berkeley analysis is the result submitted by the MuCap collaboration for publication [15],

$$\Lambda_S^{\text{MuCap}} = 725.0 \pm 13.7_{\text{stat}} \pm 10.7_{\text{syst}}\ \text{s}^{-1}. \tag{7.6}$$

The difference between the two analyses is 5 s^{-1}, and as mentioned at the end of Chapter 6, an additional conservative systematic error for "analysis methods" is included in λ_μ^-. This new measurement of Λ_S is more precise than all previous experimental results, and its implications in terms of the underlying theory are described in the following section.

7.2 Determination of g_P

The pseudoscalar coupling $g_P(q^2_\text{OMC})$ can be calculated from the difference between Λ_S^MuCap and the theoretical prediction Λ_S^Th:

$$g_P^\text{MuCap} = g_P^\text{Th} + \frac{\partial g_p}{\partial \Lambda_S}\left(\Lambda_S^\text{MuCap} - \Lambda_S^\text{Th}\right). \tag{7.7}$$

The average of the two next-to-next-to-leading-order ChPT calculations for the singlet capture rate [28] [27] quoted in Chapter 2 is $(687.4\ \text{s}^{-1} + 695\ \text{s}^{-1})/2 = 691.2\ \text{s}^{-1}$. Applying radiative corrections of +2.8% [30] gives $\Lambda_S^\text{Th} = 710.6\ \text{s}^{-1}$. We use $g_P^\text{Th} = 8.26$ [20] and a value for $\partial g_P/\partial \Lambda_S$ based on the phenomenological calculation [26] of Λ_S. After a small adjustment to account for the different value of g_P used in [26], scaling by radiative corrections gives $\partial g_P/\partial \Lambda_S = -0.065$ s. Applying Eq. 7.7, we find the MuCap determination of g_P to be

$$g_P^\text{MuCap} = 7.3 \pm 1.1. \tag{7.8}$$

This result is consistent with g_P^Th and insensitive to the assumed muon molecular ortho-para transition rate λ_op.

A plot of g_P^MuCap vs. the assumed value of λ_op is shown in Figure 7.1, along with g_P implied by other muon capture experiments. Previous determinations [12] of g_P from ordinary muon capture assumed the λ_op from the earlier experiment by Bardin *et al.*, $\lambda_\text{op}^\text{Ex1} = (4.1 \pm 1.4) \times 10^4\ \text{s}^{-1}$ [9], notwithstanding the disagreement with the theoretical value $\lambda_\text{op}^\text{Th} = (7.1 \pm 1.2) \times 10^4\ \text{s}^{-1}$ [10]. With the more recent experimental result $\lambda_\text{op}^\text{Ex2} = (11.7 \pm 1.7^{+0.9}_{-0.7}) \times 10^4\ \text{s}^{-1}$ [11] in disagreement with both theory and the previous measurement, the ortho para transition rate must be considered uncertain over much of the range covered by the plot in Fig. 7.1. The widths of the uncertainty bands of the previous most precise muon capture measurements (labeled "OMC" and "RMC" in the figure), which used liquid hydrogen targets, are similar to that of this first result from the MuCap experiment; however, the MuCap result varies little over the entire range of reasonable λ_op due to the small amount of molecular formation in the low-density target. The previous experiment [3] in hydrogen gas, like MuCap, is nearly insensitive to λ_op, but its reported uncertainty is more than three times larger. MuCap is the

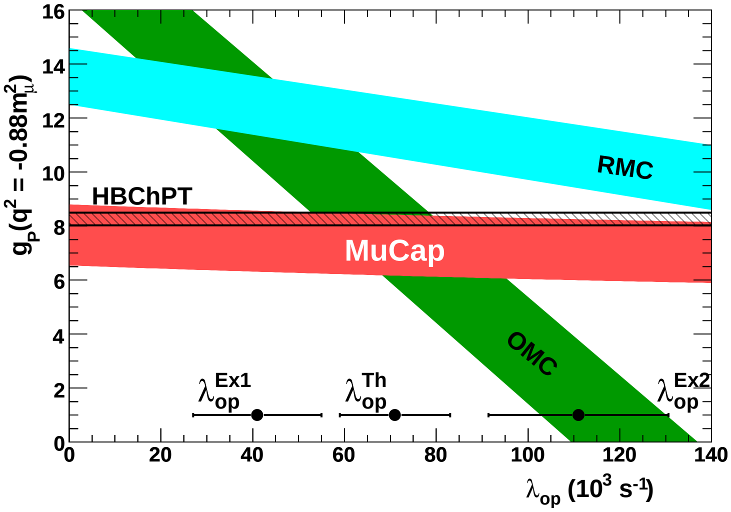

Figure 7.1: (from Ref. [15]) Experimental and theoretical determinations of g_P, presented vs. the ortho–para transition rate λ_{op} of the $p\mu p$ molecule, and updated with the new MuCap result. The most precise previous OMC experiment [5] and the RMC experiment [14] both depend significantly on the value of λ_{op}, which itself is poorly known due to mutually inconsistent experimental ($\lambda_{\text{op}}^{\text{Ex1}}$ [9], $\lambda_{\text{op}}^{\text{Ex2}}$ [11]) and theoretical ($\lambda_{\text{op}}^{\text{Th}}$ [10]) results.

first experiment to determine g_P both precisely and unambiguously. The disagreement with the chiral symmetry prediction originally implied by the RMC experiment is not supported.

Updated determinations of g_P from previous measurements, following the procedure described in Appendix D, are presented in Fig. 7.2. The differences from the g_P values reported in Table II of the 2004 review by Gorringe and Fearing [12] are mainly due to 1) the recent radiative corrections calculation of +2.8% [30], increased from the previous value of +0.6% [29], and 2) the different central value and much larger uncertainty of the $p\mu p$ ortho-para transition rate used in the present analysis, $\lambda_{\text{op}} = (6.9 \pm 4.3) \times 10^4\ \text{s}^{-1}$. For given values of the kinetic parameters, the value of g_P in the theoretical prediction of the capture rate is adjusted to match the observed capture rate. For each bubble-chamber and neutron-counting experiment, the capture rates and the average time t_1 muons spend in the hydrogen before counting begins are taken directly from Table II (the column labeled Δt) of Ref. [12]. The previous experiment employing the lifetime technique, that of Bardin *et al.* [5], is updated with the most recent world-average positive muon lifetime [8]. The new "world-average" g_P values shown in the lower part of Fig. 7.2 actually come out less precise than the present MuCap determination alone because the simple weighted average of the g_P vs. λ_{op} plots, which is what the study described in Appendix D uses, results in a

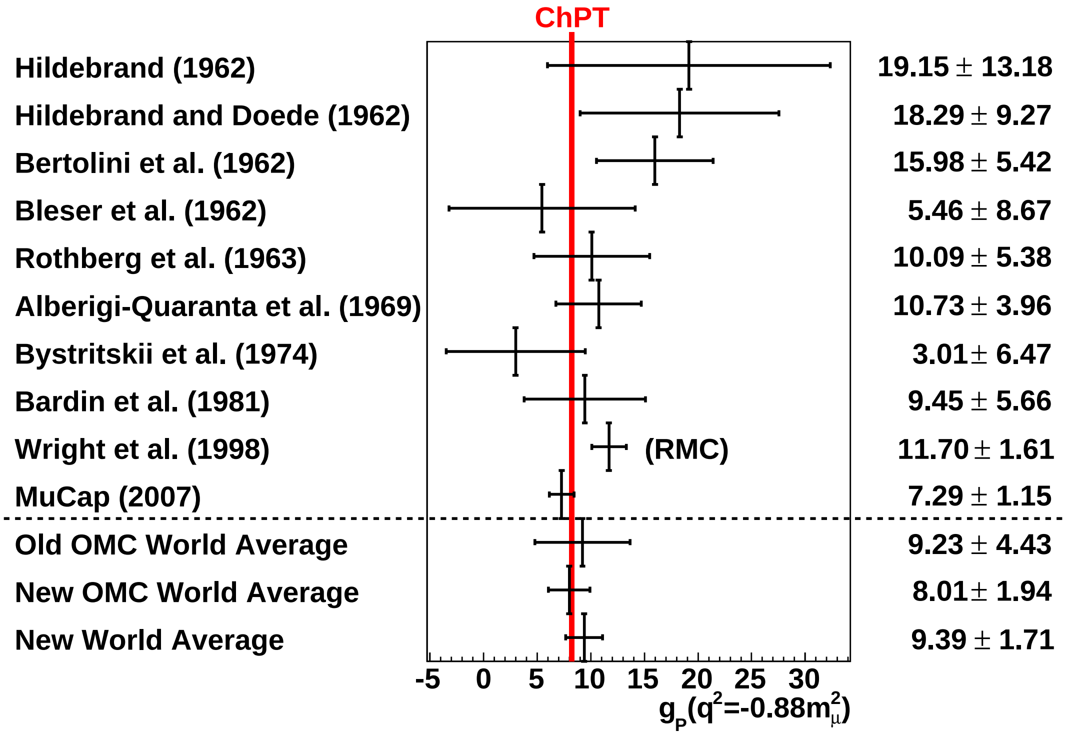

Figure 7.2: Updated experimental determinations of g_P from measurements of muon capture on the proton, using the same $p\mu p$ molecular trasition rates as in the MuCap analysis, i.e., $\lambda_{\mathrm{of}} = (2.3 \pm 0.5) \times 10^6\ \mathrm{s}^{-1}$ and $\lambda_{\mathrm{op}} = (6.9 \pm 4.3) \times 10^4\ \mathrm{s}^{-1}$. The values and uncertainties for g_P (plotted, and listed to the right) are based on the g_P vs. λ_{op} plots shown in Appendix D, Fig. D.1. As in the review by Gorringe and Fearing [12], the oldest three measurements, which used bubble chambers, are excluded from the "world average" determinations. The "old OMC world average" includes Bleser *et al.* through Bardin *et al.*; the "new OMC world average" additionally includes the present MuCap result; and the "new world average" further includes the Wright *et al.* radiative muon capture (RMC) determination.

net λ_{op} dependence. Unless the inconsistent situation with λ_{op} is resolved, the most precise determination of g_P is from the MuCap result unaveraged with previous experiments.

Appendix A

Full Kinetics Equations

A.1 Solution to Differential Equations

The differential equations can be written in terms of a matrix M and vector $\vec{n}$ as $\frac{d\vec{n}}{dt} = M\vec{n}$, with

$$M = \begin{pmatrix} -(\lambda_0 + \Lambda_S + \phi\lambda_{pp} + \tilde{\lambda}_{pZ}) & 0 & 0 & 0 \\ \phi\lambda_{\mathrm{of}} & -(\lambda_0 + \Lambda_{\mathrm{om}} + \lambda_{\mathrm{op}}) & 0 & 0 \\ \phi\lambda_{\mathrm{pf}} & \lambda_{\mathrm{op}} & -(\lambda_0 + \Lambda_{\mathrm{pm}}) & 0 \\ \tilde{\lambda}_{pZ} & 0 & 0 & -(\lambda_0 + \Lambda_Z) \end{pmatrix}$$

$$\vec{n} = \begin{pmatrix} n_1 \\ n_2 \\ n_3 \\ n_4 \end{pmatrix}.$$

The solution is written symbolically as

$$\vec{n}(t) = Ae^{Mt}\vec{n}(0), \tag{A.1}$$

where A is a scalar constant and $\vec{n}(0)$ is the initial population distribution. The matrix exponentiation is effected by first diagonalizing M: $M = SLS^{-1}$, where the diagonal matrix L is composed of the eigenvalues of M, and S is constructed with linearly independent eigenvectors $-\lambda_i$ of M.

$$e^{Mt} = e^{SLS^{-1}t} = Se^{Lt}S^{-1} = S \begin{pmatrix} e^{-\lambda_1 t} & 0 & 0 & 0 \\ 0 & e^{-\lambda_2 t} & 0 & 0 \\ 0 & 0 & e^{-\lambda_3 t} & 0 \\ 0 & 0 & 0 & e^{-\lambda_4 t} \end{pmatrix} S^{-1}$$

The eigenvalues of M are

$$\lambda_1 = \lambda_0 + \Lambda_S + \phi\lambda_{pp} + \tilde{\lambda}_{pZ}, \tag{A.2}$$

$$\lambda_2 = \lambda_0 + \Lambda_{\text{om}} + \lambda_{\text{op}}, \tag{A.3}$$

$$\lambda_3 = \lambda_0 + \Lambda_{\text{pm}}, \tag{A.4}$$

$$\lambda_4 = \lambda_0 + \Lambda_Z. \tag{A.5}$$

Equation A.1 is also conveniently solved in Mathematica with the `MatrixExp` function; the initial condition $\vec{n}(0) = (1, 0, 0, 0)^T$ and $A = 1$ leads to

$$n_1(t) = b_1 e^{-\lambda_1 t} \tag{A.6}$$

$$n_2(t) = b_2(e^{-\lambda_2 t} - e^{-\lambda_1}) \tag{A.7}$$

$$n_3(t) = b_3 e^{-\lambda_2 t} + b_4 e^{-\lambda_3 t} + b_5 e^{-\lambda_1 t} \tag{A.8}$$

$$n_4(t) = b_6(e^{-\lambda_4 t} - e^{-\lambda_1 t}), \tag{A.9}$$

the coefficients b_j defined as

$$b_1 = 1, \tag{A.10}$$

$$b_2 = \frac{\phi\lambda_{\text{of}}}{\Lambda_S - \Lambda_{\text{om}} - \lambda_{\text{op}} + \phi\lambda_{pp} + \tilde{\lambda}_{pZ}}, \tag{A.11}$$

$$b_3 = \frac{\phi\lambda_{\text{of}}\lambda_{\text{op}}}{(\Lambda_{\text{om}} + \lambda_{\text{op}} - \Lambda_{\text{pm}})(\Lambda_{\text{om}} + \lambda_{\text{op}} - \phi\lambda_{pp} - \Lambda_S - \tilde{\lambda}_{pZ})}, \tag{A.12}$$

$$b_4 = \frac{(\phi\lambda_{\text{of}}\lambda_{\text{op}} + \phi\lambda_{\text{pf}}(\Lambda_{\text{om}} + \lambda_{\text{op}} - \Lambda_{\text{pm}}))}{(\Lambda_{\text{om}} + \lambda_{\text{op}} - \Lambda_{\text{pm}})(\phi\lambda_{pp} - \Lambda_{\text{pm}} + \Lambda_S + \tilde{\lambda}_{pZ})}, \tag{A.13}$$

$$b_5 = \frac{\phi\lambda_{\text{of}}(\lambda_{\text{op}} - \phi\lambda_{\text{pf}}) + \phi\lambda_{\text{pf}}(\Lambda_{\text{om}} + \lambda_{\text{op}} - \phi\lambda_{\text{pf}} - \Lambda_S - \tilde{\lambda}_{pZ})}{(-\Lambda_{\text{om}} - \lambda_{\text{op}} + \phi\lambda_{pp} + \Lambda_S + \tilde{\lambda}_{pZ})(\phi\lambda_{pp} - \Lambda_{\text{pm}} + \Lambda_S + \tilde{\lambda}_{pZ})}, \tag{A.14}$$

$$b_6 = \frac{\tilde{\lambda}_{pZ}}{\phi\lambda_{pp} + \Lambda_S - \Lambda_Z + \tilde{\lambda}_{pZ}}. \tag{A.15}$$

Muons decay from each state with rate λ_0, so the electron appearance rate at time t is $\lambda_0(n_1(t) + n_2(t) + n_3(t) + n_4(t))$. Including a factor N for the total number of μ–e events and adding a constant background term B, the electron time spectrum $y(t)$ is

$$y_e(t) = N\lambda_0(c_1 e^{-\lambda_1 t} + c_2 e^{-\lambda_2 t} + c_3 e^{-\lambda_3 t} + c_4 e^{-\lambda_4 t}) + B, \tag{A.16}$$

the coefficients c_i given by

$$\begin{align}
c_1 &= 1 - \frac{\phi\lambda_{\mathrm{of}}}{\Lambda_S - \Lambda_{\mathrm{om}} - \lambda_{\mathrm{op}} + \phi\lambda_{pp} + \tilde{\lambda}_{pZ}} - \frac{\tilde{\lambda}_{pZ}}{\phi\lambda_{pp} + \Lambda_S - \Lambda_Z + \tilde{\lambda}_{pZ}} \tag{A.17}\\
&\quad + \frac{\phi\lambda_{\mathrm{of}}(\lambda_{\mathrm{op}} - \phi\lambda_{\mathrm{pf}}) + \phi\lambda_{\mathrm{pf}}(\Lambda_{\mathrm{om}} + \lambda_{\mathrm{op}} - \phi\lambda_{\mathrm{pf}} - \Lambda_S - \tilde{\lambda}_{pZ})}{(\Lambda_S - \Lambda_{\mathrm{om}} - \lambda_{\mathrm{op}} + \phi\lambda_{pp} + \tilde{\lambda}_{pZ})(\phi\lambda_{pp} - \Lambda_{\mathrm{pm}} + \Lambda_S + \tilde{\lambda}_{pZ})}, \tag{A.18}\\
c_2 &= \frac{\phi\lambda_{\mathrm{of}}}{-\Lambda_{\mathrm{om}} - \lambda_{\mathrm{op}} + \phi\lambda_{pp} + \Lambda_S + \tilde{\lambda}_{pZ}} \tag{A.19}\\
&\quad + \frac{\phi\lambda_{\mathrm{of}}\lambda_{\mathrm{op}}}{(\Lambda_{\mathrm{om}} + \lambda_{\mathrm{op}} - \Lambda_{\mathrm{pm}})(\Lambda_{\mathrm{om}} + \lambda_{\mathrm{op}} - \phi\lambda_{pp} - \Lambda_S - \tilde{\lambda}_{pZ})}, \tag{A.20}\\
c_3 &= \frac{(\phi\lambda_{\mathrm{of}}\lambda_{\mathrm{op}} + \phi\lambda_{\mathrm{pf}}(\Lambda_{\mathrm{om}} + \lambda_{\mathrm{op}} - \Lambda_{\mathrm{pm}}))}{(\Lambda_{\mathrm{om}} + \lambda_{\mathrm{op}} - \Lambda_{\mathrm{pm}})(\phi\lambda_{pp} - \Lambda_{\mathrm{pm}} + \Lambda_S + \tilde{\lambda}_{pZ})}, \tag{A.21}\\
c_4 &= \frac{\tilde{\lambda}_{pZ}}{\phi\lambda_{pp} + \Lambda_S - \Lambda_Z + \tilde{\lambda}_{pZ}}. \tag{A.22}
\end{align}$$

An explicit expression for the $Z > 1$ capture time spectrum follows from Eq. 3.11 and the expression for $n_4(t)$:

$$y_Z(t) = \Lambda_Z \frac{\tilde{\lambda}_{pZ}}{\phi\lambda_{pp} + \Lambda_{\mathrm{S}} - \Lambda_Z + \tilde{\lambda}_{pZ}} \left(e^{-(\lambda_0+\Lambda_Z)t} - e^{-(\lambda_0+\Lambda_S+\phi\lambda_{pp}+\tilde{\lambda}_{pZ})t}\right) \tag{A.23}$$

A.2 Calculation of Correction for Molecular Formation

The deviation due to molecular formation of λ of the single-exponential ($f(t)$, equation 5.9) fit, from $\lambda_0+\Lambda_S$, has been determined by generating a lifetime spectrum from the full kinetics solution $y(t)$ and either calculating the first moment or fitting with $f(t)$.[1] Fitting $y(t)$ with $f(t)$ has the advantage over the moment method of incorporating the fit time range and including the effect of the background term B; therefore, this procedure is implemented and with the generated lifetime spectrum binned exactly as in the analysis of Run8 data. An alternative to explicit fitting is also offered: the shift in the minimum of the χ^2 function is calculated based on the difference of $y(t; \lambda_0, \Lambda_S, ...)$ and $f(t; \lambda = \lambda_0 + \Lambda_S)$.

---

[1] See Run8 Analysis ELog, Message 74: "Analysis of Time Distributions in MuCap Experiment," S. Clayton, P. Kammel, and B. Kiburg.

A.2.1 General Calculation of the Shift of the χ^2 Minimum

Consider a model function $f_m(x;\{\nu_q\})$ to fit data distributed according to a $y(x;\{\nu_q^0\},\{\mu_r^0\})$, where the superscript "0" indicates central ("truth") values, $\{\nu_q\}$ is the set of N_{par} model parameters ($q = 1, 2, 3, ...N_{\text{par}}$), and $\{\mu_r^0\}$ characterize data structure in reality but not in the model. The goal is to accurately find the parameters $\{\nu_q^0\}$ of y. Fluctuations are included for each data point x_i by adding to $y(x_i)$ a stochastic variable ξ_i, gaussian distributed with mean zero and deviation σ_i.

The fitting procedure finds the minimum in parameter space of

$$\chi^2 = \sum_i \frac{1}{\sigma_i^2}\left(\xi_i + y(x_i;\{\nu_q^0\},\{\mu_r^0\}) - f_m(x_i;\{\nu_q\})\right)^2 \tag{A.24}$$

Deviations of the fit results from the truth values $\{\nu_q^0\}$ are expected to be small, so we first-order Taylor expand f_m in model space around $\{\nu_q^0\}$:

$$f_m(x_i;\{\nu_q\}) = f_m(x_i;\{\nu_q^0\}) + \sum_q \left.\frac{\partial f_m}{\partial \nu_q}\right|_{x_i;\{\nu_q^0\}} \Delta\nu_q + ... \tag{A.25}$$

Substituting this expression for f_m into equation A.24 and defining a function $\alpha(x_i; ...)$ as the difference between the model and reality,

$$\alpha(x;\{\nu_q^0\},\{\mu_r^0\}) = y(x;\{\nu_q^0\},\{\mu_r^0\}) - f_m(x;\{\nu_q^0\}), \tag{A.26}$$

the expression for χ^2 becomes, to first order in the Taylor expansion,

$$\chi^2 = \sum_i \frac{1}{\sigma_i^2}\left(\xi_i + \alpha(x_i;\{\nu_q^0\},\{\mu_r^0\}) - \vec{\nabla} f_m(x_i;\{\nu_q^0\}) \cdot \Delta\vec{\nu}\right)^2, \tag{A.27}$$

where the vector space is defined by the model parameters $\{\nu_q\}$. Now we minimize the χ^2 of equation A.27 with respect to the deviations $\Delta\nu_q$, yielding a set of N_{par} equations:

$$\frac{\partial\chi^2}{\partial\Delta\nu_q} = -2\sum_i \frac{1}{\sigma_i^2}\left(\xi_i + \alpha(x_i;\{\nu_q^0\},\{\mu_r^0\}) - \vec{\nabla} f_m(x_i;\{\nu_q^0\}) \cdot \Delta\vec{\nu}\right) \left.\frac{\partial f_m}{\partial \nu_q}\right|_{x_i;\{\nu_q^0\}}. \tag{A.28}$$

Defining a matrix K and vector $\vec{J}$,

$$K = \sum_i \frac{1}{\sigma_i^2} \vec{\nabla} f_m(x_i;\{\nu_q^0\}) \otimes \vec{\nabla} f_m(x_i;\{\nu_q^0\})^T \tag{A.29}$$

$$\vec{J} \;=\; \sum_i \frac{1}{\sigma_i^2} \left(\xi_i + \alpha(x_i; \{\nu_q^0\}, \{\mu_r^0\})\right) \vec{\nabla} f_m(x_i; \{\nu_q^0\}), \tag{A.30}$$

and equating the expression in equation A.28 to zero, we have $\vec{J} - K\Delta\vec{\nu} = 0$, giving a solution for the deviations $\Delta\nu_q$,

$$\Delta\vec{\nu} = K^{-1}\vec{J}. \tag{A.31}$$

Notable features of this solution for $\Delta\vec{\nu}$ include the following:

1. The matrix K depends only on partial derivatives, with respect to the fit parameters and weighted by $1/\sigma_i$, of the model function evaluated at the "true" parameter values $\vec{\nu}^0$. In the case of counting statistics we can set $\sigma_i \approx \sqrt{f_m(x_i; \{\nu_q\})}$ as long as none of the $y(x_i)$ and $f_m(x_i)$ are too far apart. For small deviations of model and reality, K does not depend on the additional reality parameters $\{\mu_r\}$.

2. The differences between model and reality enter via $\vec{J}$, so this vector must be recomputed as the reality parameters $\{\mu_r\}$ are varied.

3. The stochastic variables ξ_i enter linearly; therefore, the average solution for $\Delta\vec{\nu}$ over many simulations, that is generating different sets of ξ_i and solving for $\Delta\vec{\nu}$, is the same as setting all ξ_i to their central values and solving once.

A.2.2 Calculation of $\Delta\lambda$ vs. λ_{OF} and λ_{OP}

The effects of nonzero λ_{OF} and λ_{OP} are found by generating lifetime spectra according to equation A.16 and calculating the shifts $\Delta\lambda$ of the simple exponential fits. The full kinetics spectra are also fit with Minuit as a cross check. Figure A.1 shows the results of a study in which spectra were generated with full kinetics, bin contents were gaussian smeared ("S" option in TH1::Eval), and the shifts in λ from the true values were 1) calculated with equation A.31 and 2) found by fitting (TH1::Fit); agreement is found to be good.[2]

With the validity of equation A.31 demonstrated, we can now turn to calculating $\Delta\lambda$, due to molecular parameters, suitable for entry into the MuCap error table. The binning, N, B of the generated full-kinetics spectrum are set to the same values as the Run8 lifetime spectrum. The range of the fit is also the same as that used for the MuCap result. Results are shown in figure A.2.

---

[2] The "More" option of the Minuit fit, which more precisely finds the minimum value of the χ^2 function, is important in this comparison; Without this option the fit differs by as much as 1 s^{-1} from the calculation.

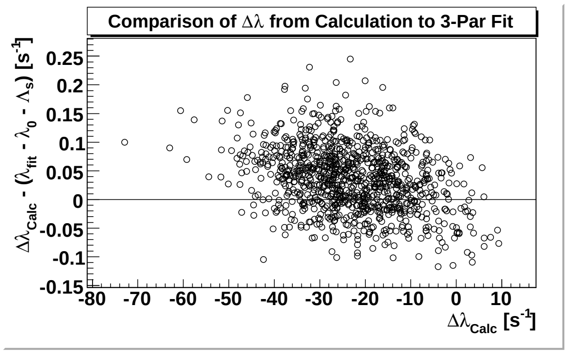

Figure A.1: Comparison of the calculation of $\Delta\lambda$ with $\lambda_0 + \Lambda_s - \lambda_{fit}$, where λ_{fit} is the result of the simple-exponential fit to the simulated full kinetics spectrum.

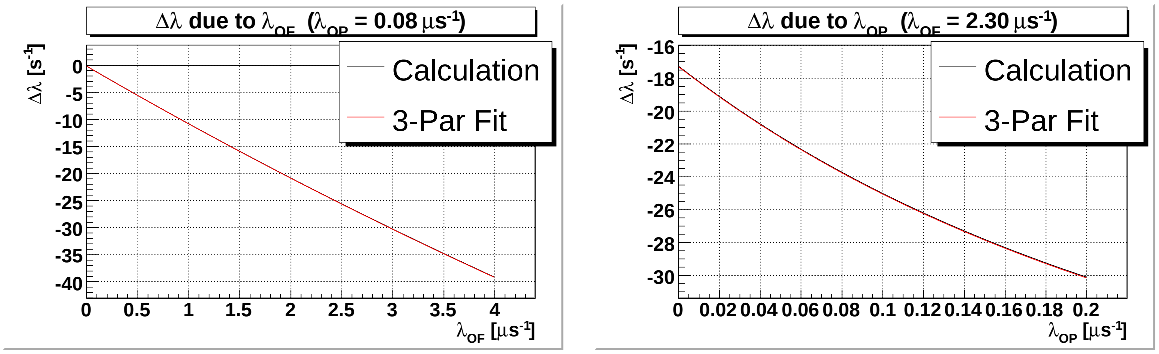

(a) Effect of λ_{OF} on λ_{fit} of the simple exponential fit.

(b) Effect of λ_{OP} on λ_{fit} of the simple exponential fit.

Figure A.2: Calculations of the correction $\Delta\lambda$ to the simple exponential fit result vs. molecular formation and transition rates. The generated full-kinetics spectra are gaussian smeared. In both plots the red line (from simple-exponential fit) lies on top of the result from equation A.31.

A.3 Fits to Data with Full Kinetics Equation

At MuCap target conditions, the full kinetics solution amounts to small deviations from the single-exponential decay with $\lambda = \lambda_0 + \Lambda_S$. The smallness of these deviations allows them to be corrected for in steps, as is done in the Results chapter of this report. The alternative is to fit the lifetime spectrum with the full kinetics solution, fixing as many parameters as possible. In fitting equation A.16 to the production data, N, Λ_S, and B will be the only parameters allowed to float; the rest must be fixed from calibration data and literature. Effects not present in equation A.16 will shift Λ_S from its correct value in the same way λ of the single-exponential fit is shifted. To be entirely consistent, all significant distortions of the lifetime spectrum should be included in the model function, such as that from μd diffusion.

A study is presented here to check the consistency of full kinetic fits to the key data sets — Prod50, CalibN2, and CalibNat — in light of the corrections applied in the standard 3-parameter fit procedure. The steps of the analysis for a particular time spectrum are enumerated:

1. The time axis of the lifetime histogram is rescaled by the unblinding factor, 1/1.001.

2. The histogram is fit with the 3-parameter function; bin errors are increased to account for 50% of the background as double counted.

3. The full kinetics function N and B parameters are initialized to those found in the 3-parameter fit. Remaining parameters, except Λ_S, are fixed, including the following (rates in s^{-1}): triplet capture rate $\Lambda_T = 12.0$; orthomolecular overlap factor $\gamma_O = 1.009/2.$; paramolecular overlap factor $\gamma_P = 1.143/2.$; hydrogen density $\phi = 0.0112$; atomic-to-paramolecular transfer rate $\lambda_{PF} = 7400$; atomic-to-orthomolecular transfer rate $\lambda_{OF} = 2300000$; ortho-para transition rate $\lambda_{OP} = 80000$. Remaining fixed parameters are λ_0, rates related to high-Z kinetics, and quantities to account for deuterium diffusion; these require some care in setting and are described in following steps.

4. The parameter for the μ^+ decay rate, λ_0, is initially set to the MuLan result, 455162.20. Corrections added to this rate are 1) 3.15 for μp diffusion, 2) 3.16 for averaging with the CathodeAND spectrum, 3) -12.00 Huff factor. It these small corrections are not included in λ_0, they will be reflected in the fit results for Λ_S.

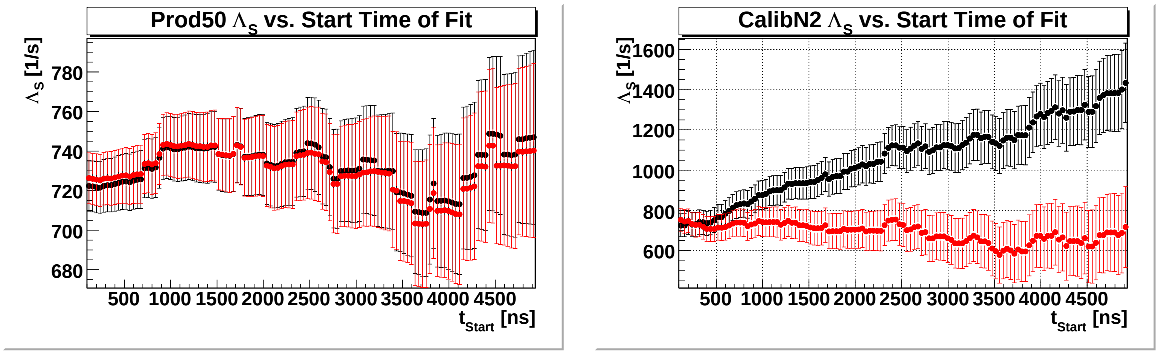

(a) Λ_S from fit to Prod50 data.

(b) Λ_S from fit to CalibN2 data.

Figure A.3: Start time scans with full kinetics function: Λ_S from Prod50, and Λ_S from CalibN2. See text for full description.

5. High-Z effects can be dealt with either by adjusting the λ_0 value based on previous 3-parameter fits, or by setting an effective transfer rate and a capture rate. In the latter case, the parameters are fixed as suggested by the MuCap note, "Practical Impurity Corrections," by P. Kammel and B. Kiburg. The full kinetics function is extended to include two different impurity species. In the present study, we use $\gamma_N = 528\ \text{s}^{-1}/\text{ppm}$ and $\gamma_O = 525\ \text{s}^{-1}/\text{ppm}$. The fraction of the observed capture yield from nitrogen is $\alpha = 0.05$ for Prod50, and $\alpha = 1.00$ for CalibN2. Then for Prod50, $\Lambda_{pN} = \gamma_N \alpha Y_Z$, $\Lambda_{pO} = \gamma_O \alpha Y_Z$, $Y_Z = 10.6$. Similarly for CalibN2, except $\alpha = 1$ and $Y_Z = 726.9$.

6. The full kinetics version of deuterium diffusion is less developed than for High-Z, but it is attempted here just the same. The parameterization of diffusion effects described in the MuCap note, "Analysis of Time Distributions in MuCap Experiment," are implemented; the parameterization is based directly on the ratio of the Prod50 to CalibNat time spectra. Results of this study indicate this parameterization is problematic; therefore, except in the case of CalibNat fits, we use instead the deuterium correction from the 3-parameter fits (adding it to λ_0).

7. With most parameters fixed, the full-kinetics fit is performed; only N, B, and Λ_S are allowed to float.

Fit start time scans, with the full kinetics function and following the above steps, are in figures A.3 and A.4, together comprising four plots.

- Figure A.3a: Prod50 Λ_S vs. Start Time of Fit. All parameters are fixed except N, B, and Λ_S; deuterium is accounted for by including an offset in λ_0. The black points are

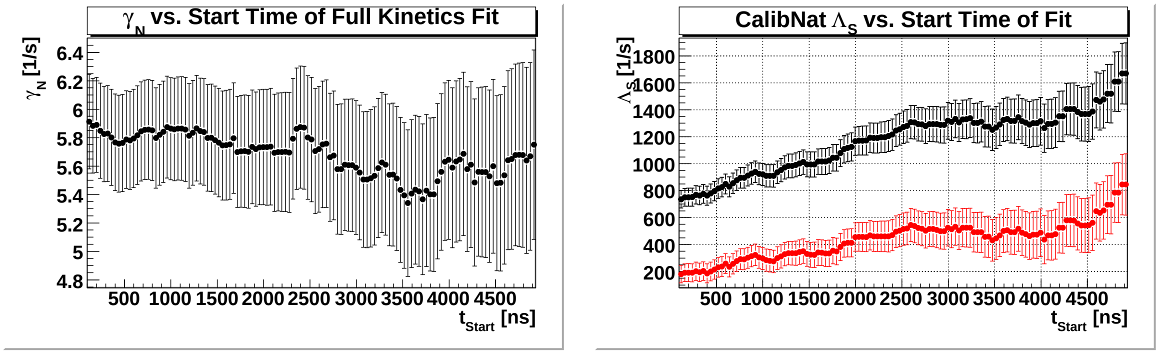

(a) γ_Z from fit to CalibN2 data.

(b) Λ_S from fit to CalibNat data.

Figure A.4: Start time scans with full kinetics function: γ_N from CalibN2, and Λ_S from CalibNat. See text for full description.

fit results when high-Z effects are treated by adding to λ_0 and setting $\Lambda_{pZ} = 0$. Red points are the results with high-Z included in the full-kinetics function (nonzero Λ_{pZ}). The slight disagreement of the red and black points at the start time of 120 ns must be due to slight inconsistency between γ_Z (full kinetics) and β_Z (3-parameter).

- Figure A.3b: CalibN2 Λ_S vs. Start Time of Fit. All parameters are fixed except N, B, and Λ_S; deuterium is accounted for by including an offset in λ_0. The black points are fit results when high-Z effects are treated by adding to λ_0 and setting $\Lambda_{pZ} = 0$. Red points are the results with high-Z included in the full-kinetics function (nonzero Λ_{pZ}).

- Figure A.4a: CalibN2 γ_N vs. Start Time of Fit. All parameters are fixed except N, B, and in this case Λ_{pZ}; deuterium is accounted for by including an offset in λ_0. The singlet capture rate is fixed to $\Lambda_S = 722.42$.

- Figure A.4b: Calibnat Λ_S vs. Start Time of Fit. All parameters are fixed except N, B, and Λ_S; high-Z is accounted for with the full kinetics. The black points are fit results when deuterium effects are treated by adding to λ_0. Red points are the results with deuterium included in the full-kinetics function via the parameterized Prod50/CalibNat ratio. The full-kinetics deuterium function seems to be much too aggressive, since it drops Λ_S by several hundred hertz.

Appendix B

Calculation of Correction for Diffusion

B.1 Impact Parameter Cut Acceptance Derivation

This is a two-dimensional problem. We observe only the direction of the electron, therefore μp displacement along that direction has no effect. A convenient coordinate system is one defined by the direction of the electron, with the x- and y-axes orthogonal to this direction; that is, each muon decay event has its own coordinate system. We consider a displacement of the μp of distance R_d, which will define the x-axis. Later, a model for μp diffusion will be imposed which takes into account phase space of the diffusion, etc., but until then the derivation is model independent.

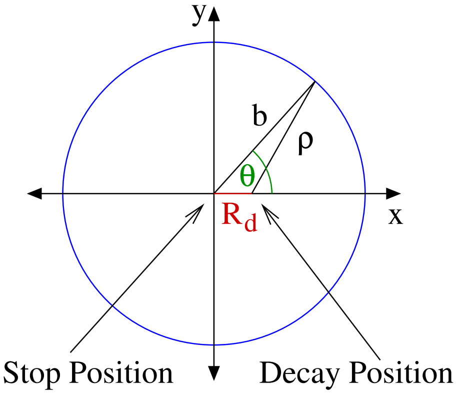

Figure B.1: Illustration of the coordinate system used in this section. The observed stop position is at the origin, the decay electron direction is out of the page (z-axis), and we consider the muon to be displaced by R_d at the time of decay. ρ is the "actual" impact parameter, which is distributed according to the electron detector resolution $g_b(b)$; b is the observed impact parameter distribution, which will be distributed somewhat differently from ρ due to the displacement R_d.

F_b is the *undiffused* impact parameter distribution scaled such that $\int_0^\infty db\, F_b(b) = 1$. $g_b(b)$ is the effective detector resolution function, which is simply $F_b(b)$ divided by the phase space factor $2\pi b$: $g_b(b) \equiv \frac{F_b(b)}{2\pi b}$. g_b will be expressed in terms of F_b for most of the derivation, since it is F_b that is more directly observed in the data. Integration of $g_b(b)$ over the 2D space shows that the normalization is correct.

$$\int_0^\infty db \int_0^{2\pi} b\, d\theta\, g_b(b) = \int_0^\infty db \int_0^{2\pi} b\, d\theta \frac{F_b(b)}{2\pi b} = \int_0^\infty db\, F_b(b) = 1 \tag{B.1}$$

To find the acceptance $\epsilon_{bcut}(R_d)$ given a particular impact parameter cut b_{cut} and μp displacement R_d, we integrate $g_b(\rho)$ over the area in our coordinate system bounded by $b = b_{cut}$ (see Figure B.1).

$$\epsilon_{bcut}(R_d) = \int_0^{b_{cut}} db \int_0^{2\pi} b\, d\theta\, \frac{F_b(\rho)}{2\pi\rho} \tag{B.2}$$

where ρ is found from the cosine law to be

$$\rho = \sqrt{R_d^2 + b^2 - 2R_d b \cos\theta} \tag{B.3}$$

Normalization must hold in the limit $b_{cut} \to \infty$

$$\lim_{b_{cut}\to\infty} \epsilon_{bcut}(R_d) = \int_0^\infty db \int_0^{2\pi} b\, d\theta\, \frac{F_b(\rho)}{2\pi\rho} = 1$$

which can be seen by shifting the origin to the decay position at $x = R_d$ and using Eq. B.1. We are interested in the change in the acceptance compared to no displacement ($R_d = 0$)

$$\Delta\epsilon_{bcut}(R_d) \equiv \epsilon_{bcut}(R_d) - \epsilon_{bcut}(0) \tag{B.4}$$

$\epsilon_{bcut}(0)$ is found from a simple integration over $F_b(b)$, which can be accurately computed from the experimental impact parameter distribution histogram:

$$\epsilon_{bcut}(0) = \int_0^{b_{cut}} db\, F_b(b) \tag{B.5}$$

$\epsilon_{bcut}(R_d)$ needs to be treated with more care, however, because the ρ in the denominator of the integrand in Eq. B.2 does not immediately cancel; numerical integration with discretely-binned F_b could result in large systematic errors around $\rho = 0$. The pole can be avoided by changing the limits of integration and using normalization:

$$\epsilon_{bcut}(R_d) = 1 - \int_{b_{cut}}^\infty db \int_0^{2\pi} b\, d\theta\, \frac{F_b(\rho)}{2\pi\rho} \tag{B.6}$$

While much less important for large b_{cut}, direct numerical integration still makes mistakes because of the discrete binning of F_b. There is a practical limit to how fine the binning can be made due to finite statistics. Intuitively, $\Delta\epsilon_{bcut}(R_d)$ should depend on the shape of $F_b(b)$ only in the neighborhood, of order R_d, around $b = b_{cut}$.

B.1.1 Exact Derivation for the Change in Acceptance

Here $\Delta\epsilon_{bcut}(R_d)$ is formulated in a way that makes clear the dependence on F_b only in the neighborhood of order R_d around b_{cut}. This will be accomplished by considering the same coordinate system described above and shown in Figure B.1, but with the stop position at $x = R_d$ and the decay position at the origin. The detector resolution function g_b, which as before is a function of the distance from the muon decay position, is centered on the origin of these coordinates. $\epsilon_{bcut}(R_d)$ is the integral of g_b over a circle of radius b_{cut} displaced by R_d from the origin. As illusrated in Figure B.2, the change in acceptance can be found by integrating g_b over the difference of the region (C_1) contained by a circle of radius b_{cut} centered at the origin with that (C_2) contained by the same circle displaced by R_d from the origin.

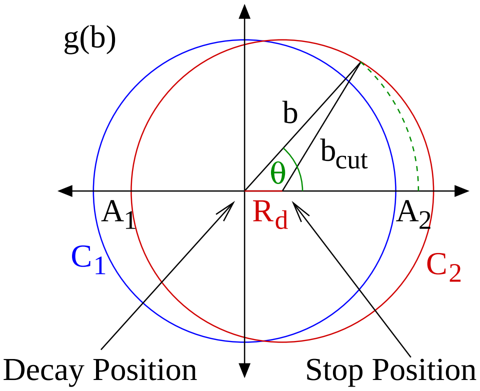

Figure B.2: Illustration of integration areas. C_1 (C_2) is the region bounded by the blue (red) circle; A_1 and A_2 are the differences of C_1 and C_2. The triangle in the first quadrant illustrates how to find the curve $b(\theta)$ that describes the boundary of C_2. The dashed green arc shows the integration path for constant b.

$$\Delta\epsilon_{bcut}(R_d) = \int_{C_2 - C_1} db\, b\, d\theta\, \frac{F_b(b)}{2\pi b} \tag{B.7}$$

The integral over θ for given b is twice the arc length indicated in Figure B.2 by the green dashed line; the $\theta > 0$ endpoint is given by

$$\sqrt{b^2 + R_d^2 - 2R_d r \cos\theta_b} = b_{cut} \tag{B.8}$$

Then the integration over θ in Eq. B.7 gives

$$\Delta\epsilon_{bcut}(R_d) = -\int_{b_{cut}-R_d}^{b_{cut}} db(1 - \frac{\theta_b}{\pi})F_b(b) + \int_{b_{cut}}^{b_{cut}+R_d} db\frac{\theta_b}{\pi}F_b(b) \tag{B.9}$$

with

$$\theta_b = \cos^{-1}\left(\frac{b^2 + R_d^2 - b_{cut}^2}{2R_d b}\right) \tag{B.10}$$

The advantage of Eq. B.9 is that it is clear that $\Delta\epsilon_{bcut}(R_d)$ depends only on $F_b(b)$ in the range $b_{cut} - R_d \leq b \leq b_{cut} + R_d$. The expression can further be rewritten in terms of a weighting factor $w(b)$ as

$$\Delta\epsilon_{bcut}(R_d) = \int_{b_{cut}-R_d}^{b_{cut}+R_d} db\, w(b)F_b(b) \tag{B.11}$$

with

$$w(b) = \begin{cases} \theta_b(b)/\pi - 1 & \text{if } b \leq b_{cut} \\ \theta_b(b)/\pi & \text{if } b > b_{cut} \end{cases} \tag{B.12}$$

Figure B.3 shows plots of $\theta_b(b)$ and $w(b)$ for a particular choice of b_{cut} and R_d. We see that $w(b)$ is approximately antisymmetric about b_{cut} for $R_d \ll b_{cut}$ by defining $\Delta b = b - b_{cut}$ and dropping terms of order R_d/b_{cut}; the argument of the inverse cosine of equation B.10 becomes

$$\cos\theta_b = \frac{b^2 + R_d^2 - b_{cut}^2}{2R_d b} \approx \frac{\Delta b}{R_d} + \mathcal{O}\left(\frac{R_d}{b_{cut}}\right). \tag{B.13}$$

Taylor expansion of $F_b(b)$ about $b = b_{cut}$ in equation B.11 gives

$$\begin{aligned} \Delta\epsilon_{bcut}(R_d) &\approx \textstyle\int_{b_{cut}-R_d}^{b_{cut}+R_d} db\, w(b)\left(F_b(b_{cut}) + (b - b_{cut})F_b'(b_{cut}) + ...\right) \\ &\approx F_b'(b_{cut})h(b_{cut}, R_d), \end{aligned} \tag{B.14}$$

where we have used the antisymmetry of $w(b)$ over the integral bounds to remove even derivatives of $F_b(b)$, and a new function,

$$h(b_{cut}, R_d) = \int_{b_{cut}-R_d}^{b_{cut}+R_d} db\, w(b)(b - b_{cut}), \tag{B.15}$$

is introduced.

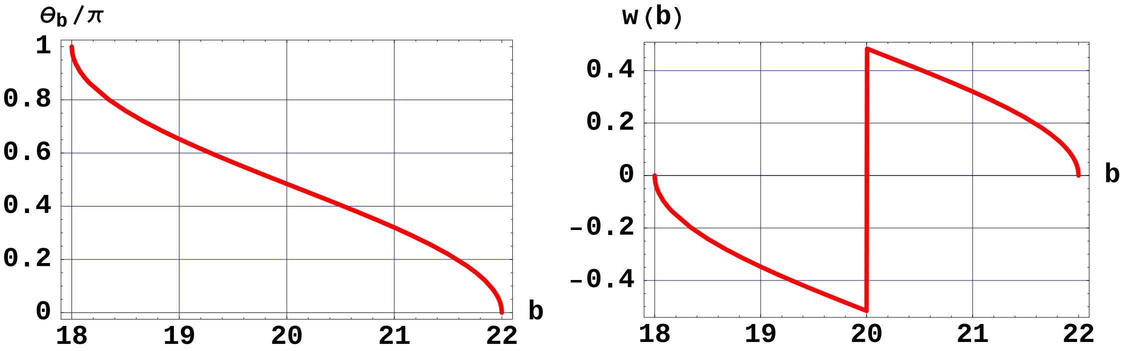

(a) (b)

Figure B.3: (a) Plot of θ_b/π vs. b for $b_{cut} = 20$ and $R_d = 2$. (b) Plot of $w(b)$ vs. b for $b_{cut} = 20$ and $R_d = 2$. (The vertical line at $b = 20$ is an artifact of plotting a discontinuous function in Mathematica.)

B.1.2 Impact Parameter Interval Cuts

In the type of impact parameter cut considered so far, we accept events with impact parameter b less than a certain b_{cut}. An alternative is to accept events bounded by two specified impact parameters, $b_{cut1} \leq b < b_{cut2}$. Lets call the former a *disc cut* and the latter an *annulus cut.* The annulus cuts have the advantage that the data subsets formed of these cuts are statistically independent for non-overlapping annuli.

Using the diagrams in Figure B.4 results in an expression for the change in acceptance of an impact parameter annulus cut given a μp displacement R_d.

$$\begin{array}{rcl} \Delta\epsilon_{bcut1,2}(R_d) & = & -\int_{\max(b_{cut2}-R_d,b_{cut1})}^{b_{cut2}} db(1-\frac{\theta_{b,2}}{\pi})F_b(b) \\ & & +\int_{\max(b_{cut2},b_{cut1}+R_d)}^{b_{cut2}+R_d} db\frac{\theta_{b,2}}{\pi}F_b(b) \\ & & +\int_{b_{cut1}-R_d}^{\min(b_{cut1},b_{cut2}-R_d)} db(1-\frac{\theta_{b,1}}{\pi})F_b(b) \\ & & -\int_{b_{cut1}}^{\min(b_{cut1}+R_d,b_{cut2})} db\frac{\theta_{b,1}}{\pi}F_b(b) \end{array} \tag{B.16}$$

with

$$\theta_{b,n} = \cos^{-1}(\frac{b^2+R_d^2-b_{cutn}^2}{2R_d b}). \tag{B.17}$$

In the limits of the integrals of Eq. B.16, note that the first argument of the max/min functions are used when $R_d \leq b_{cut2} - b_{cut1}$, and the second argument otherwise. The same approximate factorization as in equation B.14, here applied to the two cuts b_{cut1} (modifying

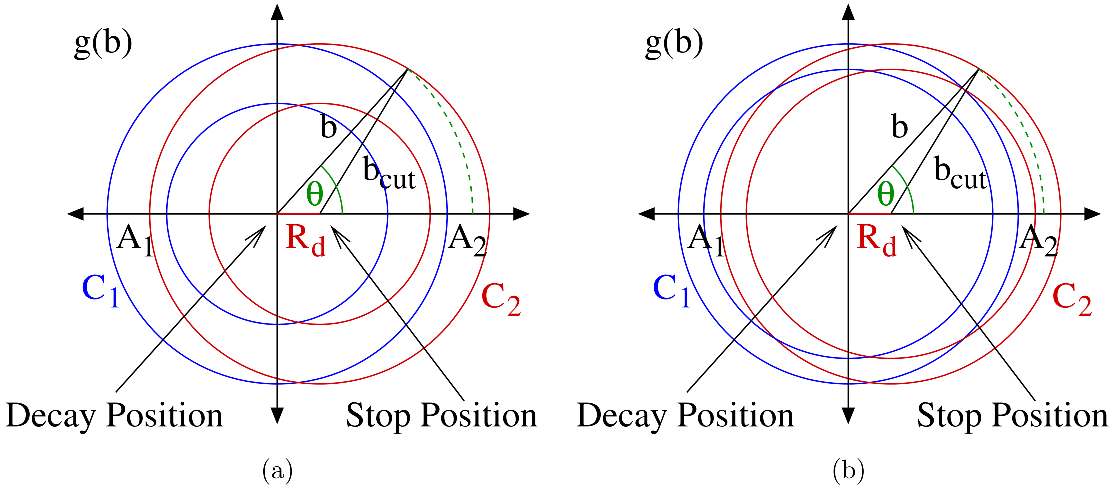

Figure B.4: Diagram of integration areas for an impact parameter annulus cut. The area between the blue (red) circles is integrated over to obtain $\epsilon_{bcut1,2}(0)$ ($\epsilon_{bcut1,2}(R_d)$). (a) Case $R_d < b_{cut2} - b_{cut1}$. (b) Case $R_d > b_{cut2} - b_{cut1}$.

$h(b_{cut1}, R_d)$ with an overall minus sign) and b_{cut2}, is valid as long as $R_d < b_{cut2} - b_{cut1}$.

B.2 $\Delta\epsilon_{bcut}(R_d)$ from Observed Impact Parameter Distribution

In order to predict the experimental muon decay rate deviation with impact parameter cut, we first need to find F_b, the normalized impact parameter distribution *with an undiffused source*: the derivation of the previous section is for F_b with the source at the origin, that is, with perfect muon stop position resolution. Normalization is simple enough – just divide by the integral over all bins in the impact parameter distrubution histogram.

The requirement of a source at the origin is less obvious due to finite TPC resolution and perhaps μp epithermal effects at early times. Even if we take only the earliest decays for the impact parameter distribution, before there is time for diffusion, uncertainty in the muon stop position could affect the results. Since this uncertainty is relatively small compared to the characteristic length scale of F_b, we will ignore it for now and proceed. $F_b(b)$ found from the Prod-50 μ^- data is shown in figure 6.20, which is the normalized impact parameter distribution for decays within 1 μs of the muon entrance time. Recall that the impact parameter b in MuCap is the distance of closest approach of the reconstructed electron track with the muon stop position as determined by the TPC.

B.2.1 Impact Parameter Disc Cuts

Figure B.5a shows the results of numerical integration of equation B.9 for several values of b_{cut} and R_d and using the experimentally determined $F_b(b)$ in figure 6.20. Figure B.5b is the relative change in acceptance, a number more directly related to the effect on the measured muon lifetime.

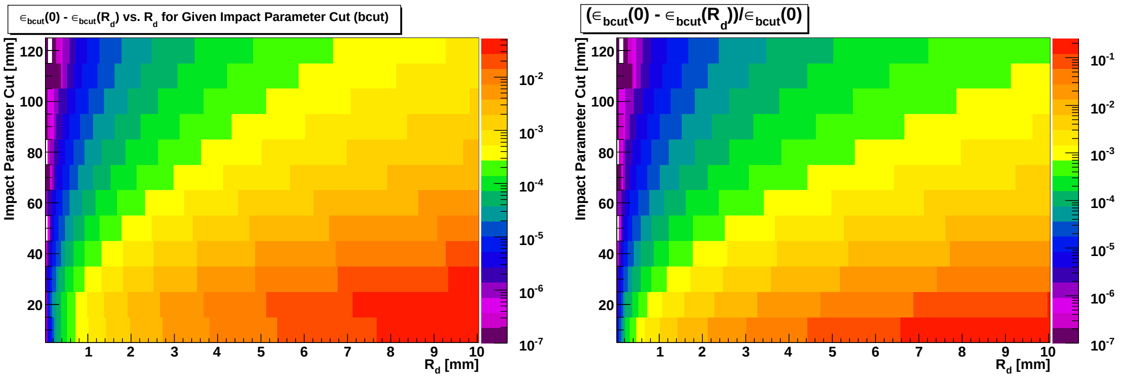

(a) (b)

Figure B.5: (a) Change in acceptance for a given impact parameter cut for a decay position displaced by R_d from the stop position compared to no displacement: $\epsilon_{bcut}(0) - \epsilon_{bcut}(R_d)$. These are calculated by numerical integration of Eq. B.9 with the experimental impact parameter distribution (Fig. 6.20). (b) Relative change in acceptance: $(\epsilon_{bcut}(0) - \epsilon_{bcut}(R_d))/\epsilon_{bcut}(0)$. $\epsilon_{bcut}(0)$ is the integral of $F_b(b)$ from zero to b_{cut}.

Figure B.6 is the slice of the plot in Figure B.5b for $b_{cut} = 10$. Figure B.7 is the slice of the plot in Figure B.5b for $b_{cut} = 80$. The fourth-order polynomial fits will be used to calculate the expected effect on the measured muon lifetime in the next section; the parameters are shown in Table B.1.

B.2.2 Impact Parameter Annulus Cuts

Figure B.8 shows the results of numerical integration of equation B.16 for given R_d and successive impact parameter cut annuli ($b_{cut1} \leq b < b_{cut2}$) and using the experimentally determined $F_b(b)$ of figure 6.20. The curves of acceptance vs. R_d for given (b_{cut1}, b_{cut2}) are fit to fourth-order polynomials, and the parameters are shown in Table B.2.

b_{cut}	$A[mm^{-1}]$	$B[mm^{-2}]$	$C[mm^{-3}]$	$D[mm^{-4}]$
10	-5.848897×10^{-5}	3.053354×10^{-3}	-1.836551×10^{-5}	-3.487593×10^{-6}
20	1.311007×10^{-5}	1.211282×10^{-3}	3.125804×10^{-6}	-3.865416×10^{-7}
30	2.679104×10^{-6}	4.855824×10^{-4}	-2.382571×10^{-8}	1.677439×10^{-7}
40	-9.250635×10^{-7}	2.138383×10^{-4}	7.151510×10^{-8}	7.847068×10^{-8}
50	-3.127169×10^{-7}	1.071523×10^{-4}	-2.491725×10^{-7}	4.943574×10^{-8}
60	4.843679×10^{-6}	5.544919×10^{-5}	4.689749×10^{-7}	-1.070464×10^{-8}
70	-6.623036×10^{-7}	3.511335×10^{-5}	-6.344084×10^{-8}	1.063847×10^{-8}
80	1.734878×10^{-6}	2.148329×10^{-5}	1.647239×10^{-7}	-5.458363×10^{-9}
90	1.013937×10^{-6}	1.485015×10^{-5}	8.846502×10^{-8}	-2.876537×10^{-9}
100	2.342871×10^{-7}	1.065840×10^{-5}	6.326233×10^{-8}	-2.353117×10^{-9}
110	-2.707013×10^{-6}	9.500100×10^{-6}	-2.212691×10^{-7}	1.264452×10^{-8}
120	-9.683916×10^{-7}	6.914395×10^{-6}	-1.248112×10^{-7}	7.536558×10^{-9}

Table B.1: Fit results of $f_{pol4}(R_d) = AR_d + BR_d^2 + CR_d^3 + DR_d^4$ to $(\epsilon_{bcut}(0) - \epsilon_{bcut}(R_d))/\Delta\epsilon_{bcut}(0)$ derived from the experimental impact parameter distribution.

b_{cut1}	b_{cut2}	$A[mm^{-1}]$	$B[mm^{-2}]$	$C[mm^{-3}]$	$D[mm^{-4}]$
0	10	-5.8489×10^{-5}	3.0534×10^{-3}	-1.8366×10^{-5}	-3.4876×10^{-6}
10	20	5.4217×10^{-5}	4.9760×10^{-5}	1.5927×10^{-5}	1.6213×10^{-6}
20	30	-9.8232×10^{-6}	-1.2330×10^{-3}	-5.7190×10^{-6}	1.3739×10^{-6}
30	40	-1.6093×10^{-5}	-1.2952×10^{-3}	1.2993×10^{-6}	-4.5671×10^{-7}
40	50	1.9545×10^{-5}	-1.0221×10^{-3}	-1.6871×10^{-6}	-3.6650×10^{-7}
50	60	9.2735×10^{-5}	-8.4027×10^{-4}	1.2570×10^{-5}	-1.0320×10^{-6}
60	70	-1.1121×10^{-4}	-5.1975×10^{-4}	-9.2064×10^{-6}	2.9332×10^{-7}
70	80	1.0573×10^{-4}	-4.8972×10^{-4}	1.0740×10^{-5}	-7.2202×10^{-7}
80	90	-3.5033×10^{-5}	-3.1037×10^{-4}	-3.8350×10^{-6}	1.3518×10^{-7}
90	100	9.5819×10^{-6}	-2.9628×10^{-4}	5.9886×10^{-6}	-3.9312×10^{-7}
100	"∞"	-3.9110×10^{-6}	-1.7792×10^{-4}	-1.0560×10^{-6}	3.9281×10^{-8}

Table B.2: Fit results of $f_{pol4}(R_d) = AR_d + BR_d^2 + CR_d^3 + DR_d^4$ to the change in acceptance of impact parameter annulus cuts, $(\epsilon_{bcut1,2}(0) - \epsilon_{bcut1,2}(R_d))/\Delta\epsilon_{bcut1,2}(0)$, derived from the experimental impact parameter distribution.

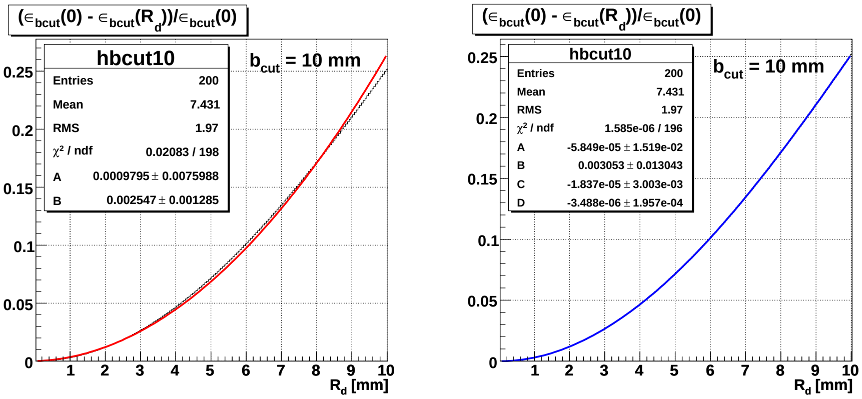

(a) (b)

Figure B.6: Slice of Figure B.5b for $b_{cut} = 10$, with polynomial fits. The experimental curve (black line) does not have errors calculated, so the χ^2 of the fits and errors on the fit parameters are not meaningful. (a) Second order fit (red): $f_{pol2}(R_d) = AR_d + BR_d^2$. The fit is actually quite good if the range is restricted to $R_d < 5$. (b) Fourth order fit (blue): $f_{pol4}(R_d) = AR_d + BR_d^2 + CR_d^3 + DR_d^4$. The curve and data match well over the entire range of R_d shown.

B.3 Model Effect on Measured Decay Rate vs. Impact Parameter Cut

We start with the normalized decay time distribution

$$n_{e0}(t) = \lambda_0 \, e^{-\lambda_0 t} \tag{B.18}$$

where λ_0 in this case would be the decay rate observed if there were perfect acceptance. λ_0 is found from $n_{e0}(t)$ by taking the first moment:

$$\int_0^\infty dt \, t \, n_{e0}(t) = \lambda_0^{-1} \tag{B.19}$$

Time-dependent detection acceptance can be included

$$\lambda^{-1} = \int_0^\infty dt \, t \, n_{e0}(t)\epsilon(t) / \int_0^\infty dt \, n_{e0}(t)\epsilon(t) \tag{B.20}$$

where $\epsilon(t)$ is a time-dependent acceptance and λ is the observed decay rate.

Let $F_{\mu p}(R_d)$ be a 2-dimensional distribution function for R_d with the phase-space factor included, where R_d represents displacement from the muon stop position, normalized such

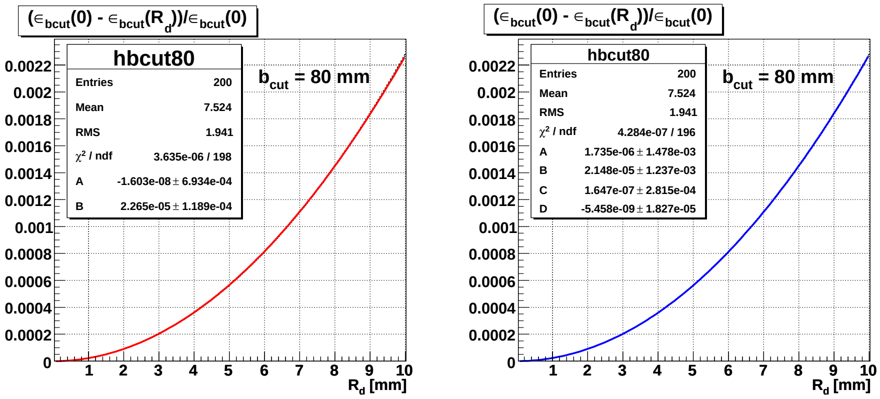

(a) (b)

Figure B.7: Slice of Figure B.5b for $b_{cut} = 80$, with polynomial fits. The experimental curve (black line) does not have errors calculated, so the χ^2 of the fits and errors on the fit parameters are not meaningful. (a) Second order fit (red): $f_{pol2}(R_d) = AR_d + BR_d^2$. At this impact parameter cut, the data are well-described by a second order polynomial over the entire fit range shown. (b) Fourth order fit (blue): $f_{pol4}(R_d) = AR_d + BR_d^2 + CR_d^3 + DR_d^4$.

that $\int_0^\infty dR_d\, F_{\mu p}(R_d) = 1$. $F_{\mu p}(R_d)$ will implicitly be a function of time. Then the acceptance for a given impact parameter cut is

$$\epsilon(b_{cut}) = \int_0^\infty dR_d\, \epsilon_{bcut}(R_d) F_{\mu p}(R_d). \tag{B.21}$$

Putting this in Eq. B.20, dividing by $\epsilon_{bcut}(0)$, and rearranging results in an expression for the change in observed lifetime due to the time dependence of $F_{\mu p}(R_d)$ and a particular impact parameter cut.

$$\begin{aligned} \mathcal{I}_t &\equiv \textstyle\int_0^\infty dt\, t\, n_{e0}(t)(1 + \int_0^\infty dR_d\, F_{\mu p}(R_d)\, \Delta\epsilon_{bcut}(R_d)/\epsilon_{bcut}(0)) \\ &= \lambda_0^{-1} + \textstyle\int_0^\infty dt\, t\, \lambda_0\, e^{-\lambda_0 t} \int_0^\infty dR_d\, F_{\mu p}(R_d)\, \Delta\epsilon_{bcut}(R_d)/\epsilon_{bcut}(0) \end{aligned} \tag{B.22}$$

$$\begin{aligned} \mathcal{I}_{norm} &\equiv \textstyle\int_0^\infty dt\, n_{e0}(t)(1 + \int_0^\infty dR_d\, F_{\mu p}(R_d)\, \Delta\epsilon_{bcut}(R_d)/\epsilon_{bcut}(0)) \\ &= 1 + \textstyle\int_0^\infty dt\, \lambda_0\, e^{-\lambda_0 t} \int_0^\infty dR_d\, F_{\mu p}(R_d)\, \Delta\epsilon_{bcut}(R_d)/\epsilon_{bcut}(0) \end{aligned} \tag{B.23}$$

$$\Delta\lambda_{bcut} = \frac{\mathcal{I}_{norm}}{\mathcal{I}_t} - \lambda_0 \tag{B.24}$$

$-\Delta\epsilon_{bcut}(R_d)/\epsilon_{bcut}(0)$ is precisely that calculated in section B.2 from the experimental impact parameter distribution and well-fit by fourth order polynomials (Table B.1). For $F_{\mu p}(R_d)$, we must choose a model.

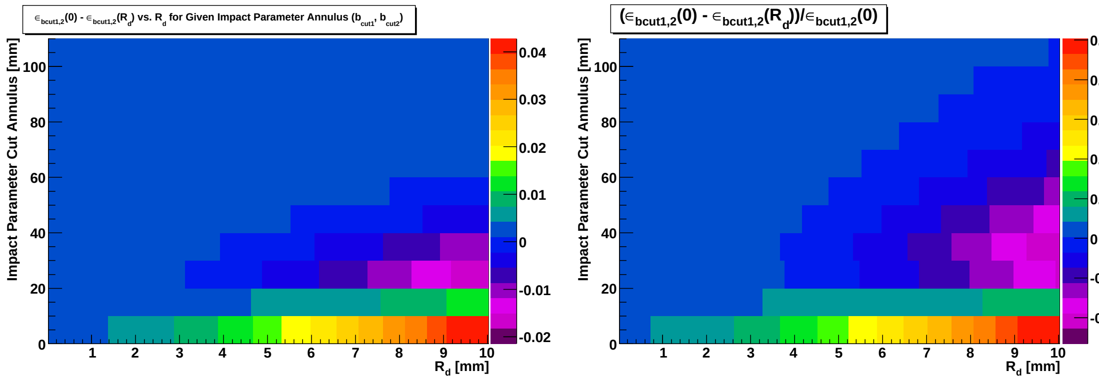

(a) (b)

Figure B.8: Change in acceptance of a given impact parameter cut annulus from a decay position displacement of R_d from the stop position. These are calculated by numerical integration of Eq. B.16 with the experimental impact parameter distribution (Fig. 6.20). The y-axis of the plots indicate the impact parameter cut annulus as follows: (a) Absolute change in acceptance: $\epsilon_{bcut1,2}(0) - \epsilon_{bcut1,2}(R_d)$. (b) Relative change in acceptance: $(\epsilon_{bcut1,2}(0) - \epsilon_{bcut1,2}(R_d))/\epsilon_{bcut1,2}(0)$. $\epsilon_{bcut1,2}(0)$ is the integral of $F_b(b)$ from b_{cut1} to b_{cut2}.

B.3.1 Model: Thermal Diffusion with Point Source

The two-dimensional distribution function with phase-space included is

$$F_{\mu p}(R_d) = \frac{R_d}{\sigma_t^2}\, e^{-\frac{R_d^2}{2\sigma_t^2}} \tag{B.25}$$

with $\sigma_t = k\sqrt{t}$. k is something like 0.7 mm/$\sqrt{\mu s}$ for μp under MuCap conditions; it will be the only parameter allowed to vary to match the c_d-independent rate deviation $y_p(b_{cut})$ calculated above. Performing the integrals of equations B.22 and B.23 with the distribution of equation B.25 gives

$$\mathcal{I}_t = \frac{-48\, D\, k^4 + -4\, \lambda_0^2\, B\, k^2 + \lambda_0^2}{\lambda_0^3} - \frac{3\, \pi\, k\, (15\, C\, k^2 + 2\, A\, \lambda_0)}{8\, \sqrt{2}\, \lambda_0^{5/2}} \tag{B.26}$$

$$\mathcal{I}_{norm} = 1 - \frac{128\, D\, k^4 + 16\, B\, k^2\, \lambda_0 + \pi \sqrt{2\, \lambda_0}\, (9\, C\, k^3 + 2\, A\, k\, \lambda_0)}{8\, \lambda_0^2} \tag{B.27}$$

where the values of the model-independent parameters A, B, C and D were found in section B.2 and are listed in table B.1.

B.3.2 $\Delta\lambda$ in terms of Moments of Arbitrary μp Distribution

Since $\Delta\epsilon_{bcut}(R_d)/\epsilon_{bcut}(0)$ is expressed in terms of a fourth order polynomial, the integrals over R_d in equations B.22 and B.23 can be expressed exactly in terms of the central moments μ_n of $F_{\mu p}(R_d)$, up to μ_4. [1] The n^{th} *central moment* of a distribution F is

$$\mu_n = \langle (x - \langle x \rangle)^n \rangle = \int (x-\mu)^n \, F(x) \, dx. \tag{B.28}$$

The n^{th} *raw moment* of a distribution F is

$$\mu'_n = \langle x^n \rangle = \int x^n \, F(x) \, dx. \tag{B.29}$$

The first four raw moments in terms of the central moments are

$$\begin{aligned} \mu'_1 &= \langle R_d \rangle \equiv \mu \\ \mu'_2 &= \mu_2 + \mu^2 \\ \mu'_3 &= \mu_3 + \mu^3 + 3\,\mu\,\mu_2 \\ \mu'_4 &= \mu_4 + \mu^4 + 6\,\mu^2\,\mu_2 + 4\,\mu\,\mu_3 \end{aligned} \tag{B.30}$$

In terms of these, the relative change in acceptance for an impact parameter cut is

$$\begin{aligned} -\Delta\epsilon(b_{cut})/\epsilon_{bcut}(0) &= \int_0^\infty dR_d\, F_{\mu p}(R_d)\,(A\,R_d + B\,R_d^2 + C\,R_d^3 + D\,R_d^4) \\ &= A\,\mu'_1 + B\,\mu'_2 + C\,\mu'_3 + D\,\mu'_4 \\ &= A\,\mu + B\,(\mu^2 + \,\mu_2) + C\,(\mu^3 + \mu\,\mu_2 + \mu_3) \\ &\quad + D\,(\mu^4 + 6\,\mu^2\,\mu_2 + 4\,\mu\,\mu_3 + \mu_4). \end{aligned} \tag{B.31}$$

For time-dependent acceptance, the moments must be time dependent. Writing equations B.22 and B.23 in terms of the moments μ_n (and putting in the eplicit expression for $n_{e0}(t)$) gives:

$$\begin{aligned} \mathcal{I}_t = &\ \lambda_0^{-1} - \int_0^\infty dt\,\lambda_0\,t\,e^{-\lambda_0 t} \\ &\times (A\,\mu + B\,(\mu^2 + \,\mu_2) + C\,(\mu^3 + 3\,\mu\,\mu_2 + \mu_3) + D\,(\mu^4 + 6\,\mu^2\,\mu_2 + 4\,\mu\,\mu_3 + \mu_4)) \end{aligned} \tag{B.32}$$

$$\begin{aligned} \mathcal{I}_{norm} = &\ 1 - \lambda_0 \int_0^\infty dt\,e^{-\lambda_0 t} \\ &\times (A\,\mu + B\,(\mu^2 + \,\mu_2) + C\,(\mu^3 + 3\,\mu\,\mu_2 + \mu_3) + D\,(\mu^4 + 6\,\mu^2\,\mu_2 + 4\,\mu\,\mu_3 + \mu_4)). \end{aligned} \tag{B.33}$$

---

[1] see, for example, http://mathworld.wolfram.com/CentralMoment.html for a primer on moments)

We can now choose a model distribution $F_{\mu p}(R_d)$, calculate its moments $\mu_n(t)$, and perform the integrals of equations B.32 and B.33.

Model: Thermal Diffusion with Point Source

As an example, the moments of the distribution $F_{\mu p}(R_d)$ for diffusion from a point source, equation B.25 with $\sigma = k\sqrt{t}$, are

$$\begin{aligned}
\mu &= \langle R_d \rangle = \sqrt{\tfrac{\pi}{2}}\, k\sqrt{t} \\
\mu_2 &= \langle (R_d - \langle R_d \rangle)^2 \rangle = \tfrac{1}{2}(4-\pi)\, k^2\, t \\
\mu_3 &= \langle (R_d - \langle R_d \rangle)^3 \rangle = (\pi - 3)\sqrt{\tfrac{\pi}{2}}\, k^3\, t^{3/2} \\
\mu_4 &= \langle (R_d - \langle R_d \rangle)^4 \rangle = (8 - \tfrac{3}{4}\pi^2)\, k^4\, t^2
\end{aligned} \tag{B.34}$$

We will need integrals of powers of t times an exponential:

$$\begin{aligned}
\textstyle\int_0^\infty dt\, \lambda_0\, t^{1/2}\, e^{-\lambda_0 t} &= \tfrac{\sqrt{\pi}}{2}\lambda_0^{-1/2} & \textstyle\int_0^\infty dt\, \lambda_0\, t\, e^{-\lambda_0 t} &= \lambda_0^{-1} \\
\textstyle\int_0^\infty dt\, \lambda_0\, t^{3/2}\, e^{-\lambda_0 t} &= \tfrac{3\sqrt{\pi}}{4}\lambda_0^{-3/2} & \textstyle\int_0^\infty dt\, \lambda_0\, t^2\, e^{-\lambda_0 t} &= 2\,\lambda_0^{-2} \\
\textstyle\int_0^\infty dt\, \lambda_0\, t^{5/2}\, e^{-\lambda_0 t} &= \tfrac{15\sqrt{\pi}}{8}\lambda_0^{-5/2} & \textstyle\int_0^\infty dt\, \lambda_0\, t^3\, e^{-\lambda_0 t} &= 6\,\lambda_0^{-3}.
\end{aligned} \tag{B.35}$$

With these integrals, $\mathcal{I}_t$ and $\mathcal{I}_{norm}$ can be expressed as polynomials in the model parameter k, and Equations B.26 and B.27 follow.

Prescription for Using Diffusion Monte Carlo Data

Monte Carlo data for μp diffusion will likely consist of an isotropic 3D spatial distribution of the μp atoms versus time. The above calculations are formulated in terms of a 2D spatial distribution function $F_{\mu p}(R)$ that is normalized at all times; muon decay is expressed by integrating over the decay-time distribution of Eq. B.18. Therefore, 1) the 3D Monte Carlo distribution with muon decay turned off should be projected onto a plane to get $F_{\mu p}(R)$ (don't forget to include the 2D phase-space factor in $F_{\mu p}$); 2) the moments $\mu_n(t)$ of the ensemble should be calculated at a series of time slices, so that the time-integral over the decay-time distribution can be done numerically.

Alternatively, if we are given a list of N decay positions and times, $(\vec{R}_i, t_i)$, where $\vec{R}_i$ is the displacement in 3D detector space of the i^{th} muon, then we could build up the integrals of Equations B.32 and B.33 muon-by-muon by replacing the integrand as follows:

$$\lambda_0 \, e^{-\lambda_0 \, t} \, F_{\mu p}(R) \rightarrow \frac{1}{N} \sum_{i=1}^{N} \delta(R - |\vec{R}_i - \hat{x} \cdot \vec{R}_i \, \hat{x}|) \delta(t - t_i), \tag{B.36}$$

where $\hat{x}$ is a unit vector aligned along some detector axis. The expression $|\vec{R}_i - \hat{x} \cdot \vec{R}_i \, \hat{x}| \equiv r_i$ gives the length of $\vec{R}_i$ projected onto the plane perpendicular to $\hat{x}$. This leads to the following expressions for $\mathcal{I}_t$ and $\mathcal{I}_{norm}$:

$$\mathcal{I}_t = \lambda_0^{-1} - \frac{1}{N} \sum_{i=1}^{N} t_i \, (A \, r_i + B \, r_i^2 + C \, r_i^3 + D \, r_i^4) \tag{B.37}$$

$$\mathcal{I}_{norm} = 1 - \frac{1}{N} \sum_{i=1}^{N} (A \, r_i + B \, r_i^2 + C \, r_i^3 + D \, r_i^4) \tag{B.38}$$

B.4 Generalization of the Derivation

It turns out that the completely reasonable assumption of isotropic μp diffusion is a powerful one. As will be argued in this section, this single premise means that the derivation of Section B.1, using the observed impact parameter distribution $F_b(b)$ which depends only on b, already contains such complications as TPC spatial resolution and asymmetric electron detector resolution function $g_b(\vec{b})$.

We start with a general, asymmetic detector resolution function, $g_b^{\Omega}(\vec{b})$, for a given *observed* electron decay direction. $\vec{\Omega}$ is defined in the absolute detector coordinate system S_{eDet}. (The superscript Ω on g_b is dropped for the remainder of this section.) Let Ω define z-axis of the the space S_Ω of g_b up to a rotation about Ω. The origin of S_Ω is fixed at the muon decay position. Since the variation of g_b is naturally fixed with respect to the orientaion of S_{eDet}, we take the projection of the z_{eDet}-axis onto the plane perpendicular to z_Ω to define the x_Ω-axis. To clarify, $g_b(r, \theta)$ is now allowed to vary with both r and θ, where θ is the angle in the S_Ω system.

Recall that in the derivations of this note, the relative coordinate system (call it S_{Rd}) for g_b is oriented such that the μp displacement $\vec{R}_d$ is along the $+x$-axis. Let γ denote the angle between $\vec{R}_d$ and the z_{eDet}-axis projected onto the plane perpendicular to Ω. Then S_{Rd} and S_Ω are related by a rotation γ about their common z-axis. Now that we are allowing g_b to vary with angle, we must account for the orientation of the S_{Rd} coordinate system. Let

$\vec{a} = (a, \theta_a)$ be a vector in the relative coordinate system. Then the substitution

$$g_b(a, \theta_a) \rightarrow g_b(a, \theta_a - \gamma) \tag{B.39}$$

maps g_b from S_Ω to S_{Rd}.

B.4.1 Asymmetric Resolution Function

That the general asymmetric $g_b(\vec{b})$ can be replaced with a symmetric $\overline{g}_b(b)$ in case of isotropic μp diffusion follows immediately from the mapping of S_Ω to S_{Rd}. We have a μp distribution function $F_{\mu p}(R_d) = \int_0^{2\pi} d\gamma\, F_{\mu p}(\vec{R}_d)$, where $\vec{R}_d$ is the vector displacement of the muon decay position from the muon stop position in the S_Ω coordinate system. The change in acceptance $\epsilon(b_{cut})$ for some impact parameter cut b_{cut} is given by the integral

$$\Delta\epsilon(b_{cut}) = \int_0^\infty dR_d \frac{1}{2\pi} \int_0^{2\pi} d\gamma\, F_{\mu p}(R_d)\, \Delta\epsilon_{bcut}(R_d, \gamma), \tag{B.40}$$

where the second argument of $\Delta\epsilon_{bcut}(R_d, \gamma)$ is necessary to keep track of the direction of $\vec{R}_d$. $\Delta\epsilon_{bcut}(R_d, \gamma)$ is given by Eq. B.7 written in terms of g_b:

$$\Delta\epsilon_{bcut}(R_d, \gamma) = \int_{C_2 - C_1} db\, b\, d\theta_b\, g_b(b, \theta_b - \gamma). \tag{B.41}$$

The integration areas C_2 and C_1 are those shown in Fig. B.2, defined in the S_{Rd} coordinate system, i.e., not explicitly dependent on γ. Substituting this into Eq. B.40 gives

$$\begin{aligned} \Delta\epsilon(b_{cut}) &= \textstyle\int_0^\infty dR_d \frac{1}{2\pi} \int_0^{2\pi} d\gamma\, F_{\mu p}(R_d)\, \int_{C_2 - C_1} db\, b\, d\theta_b\, g_b(b, \theta_b - \gamma) \\ &= \textstyle\int_{C_2 - C_1} db\, b\, d\theta_b\, \int_0^\infty dR_d\, F_{\mu p}(R_d)\, \frac{1}{2\pi} \int_0^{2\pi} d\gamma\, g_b(b, \theta_b - \gamma). \end{aligned} \tag{B.42}$$

Therefore, if the μp diffusion is isotropic, we can without approximation work with an averaged resolution function $\overline{g}_b$:

$$\overline{g}_b(b) \equiv \int_0^{2\pi} d\gamma\, g_b(b, \gamma) = \frac{F_b(b)}{2\pi b}. \tag{B.43}$$

B.4.2 TPC Spatial Resolution

The TPC indicates the muon stop position at discrete points with 4 mm spacing in x_{eDet} and z_{eDet}, and somewhat better (≈1 mm) in y_{eDet}. These discrete points will have quite different spacing in the S_Ω coordinate system. For a measured muon stop position $\vec{R}_{meas}$ in the S_Ω coordinates, let $\vec{R}$ be the vector to the actual stop position. We define a distribution function $g_{res}(\vec{R})$ to represent the actual stop position.

With these definitions, we can account for the TPC resolution simply by making the replacement

$$g_b(\vec{b}) \rightarrow \int d\vec{R}\, g_{res}(\vec{R})\, g_b(\vec{b} - \vec{R}). \tag{B.44}$$

Note that as with g_b, the orientation of the space of g_{res} is fixed with respect to the absolute detector coordinate system, and otherwise g_b and g_{res} could transform differently under rotation, invalidating the substitution.

The observed impact parameter resolution for short times after the muon stop, taking into account asymmetric g_b and the TPC spatial resolution, is

$$F_b^{obs}(b) = \int_0^{2\pi} d\theta_b\, b \int d\vec{R}\, g_{res}(\vec{R})\, g_b(\vec{b} - \vec{R}) \tag{B.45}$$

By using the *observed* impact parameter distribution function to define g_b, we were already taking into account both the TPC resolution and possible (likely) asymmetries in the e-Detector resolution function.

B.4.3 Translational Variance of the Resolution Function

The resolution function will certainly vary with muon stop location to some extent, particularly for large impact parameters for which the electron track is near the edge of the electron detector. The question is, have we already taken into account such variation of g_b by using the observed $t \approx 0$ impact parameter distribution? Within the bulk of the muon stopping distribution, that is away from its edges by at least the μp diffusion length scale $l_d \sim \langle R_d \rangle$, the answer seems to be affirmative. A second requirement, other than being away from the edges of the TPC, is that the muon stopping distribution does not vary too much over the distance l_d. In this case we can imagine that the *actual muon decay position* is approached symmetrically from the *actual muon stop position*; therefore, the arguments of the previous subsections are still valid.

By diffusing outward, muon stops near the edge of the TPC fiducial cut ($\sim 10^{-2}$ of all stops) can sample a slightly different detector resolution than the bulk of the stops. As long as the overall impact parameter distribution at $t > 0$ is well represented by the $t \approx 0$ distribution, the edges are probably not important.

Appendix C

Description of Analysis Software

C.1 Raw Data Parsing

The bulk of the raw data are from time-to-digital-conversion (TDC) data-aquisition (DAQ) modules, which record the times of hits in each input channel. The raw data from each DAQ module are sorted into time-ordered arrays of hits. Hits from all channels serving electron detector elements and muon entrance detectors are combined into a single, time-ordered array of hit times and corresponding channel identification numbers. TDC400 data are more conveniently arranged into a separate, time-ordered array of structures, with each structure comprising bit patterns representing the status of each wire of the TPC for each threshold (EL, EH, EVH). Low-level data-quality checks identify and remove the rare occurences of blocks that exhibit known, troublesome behavior. The procedures that handle these basic raw data parsing tasks are common to both the UIUC and UCB analyses.

C.2 Electron Definition

C.2.1 eSC Clustering

Clustering of singles (PMT) hits into 4-fold clusters, time-coincidences between all four PMT's the same eSC segment ("gondola"), is performed separately on each gondola. The algorithm is the following:

1. Loop over singles hits, and as each singles hit is encountered, apply a fixed 65-ns dead time to that PMT channel.

2. Adjust each singles hit time, by an amount specified in the parameters file, to account for slight variation in the timing with respect to the other PMT channels (from slightly different cable lengths, for example). In practice, the times are adjusted by up to ≈2 ns.

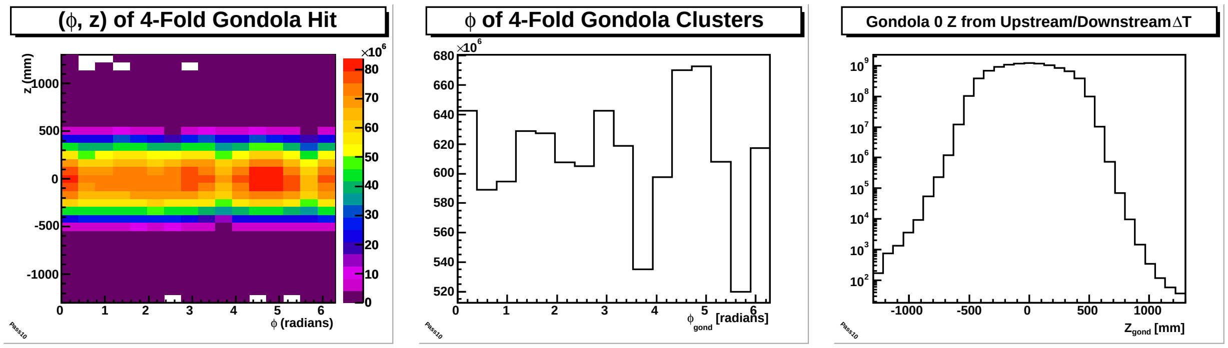

Figure C.1: Left: (ϕ, z) Distribution Based Only on eSC Information; Middle: ϕ-Projection of the leftmost histogram; Right: z-Projection of the leftmost histogram. ϕ is taken at the center line of each eSC segment, and z is based on the time difference between upstream and downstream detectors of a 4-fold cluster.

3. Find clusters of singles hits within 30 ns, the maximum coincidence window plus a few ns to account for the small relative timing offsets between the PMT channels. These clusters can be considered 4-fold candidates. Since the individual PMT channels have artificial dead times of 65 ns, there can never be more than four time-coincident PMT hits on a given gondola, up to one hit from each of its four PMT channels.

4. Check the candidates for good 4-fold hits. Each must contain exactly one hit from each of the four PMT's and have relative PMT timings within 15 ns for PMT's on the same end (upstream or downstream), and 25 ns for PMT's on opposite ends. The time is taken to be the average of the four PMT times. The z-position is the time difference between the average of the upstream PMT times, minus the average of the downstream PMT times, and multiplied by a velocity factor: $z = v_{\text{gond}}(t_{\text{upstream}} - t_{\text{downstream}})$, where $v_{\text{gond}} = 67$ mm/ns from a study in which a source was placed along the length of one of the gondolas. The angle ϕ of the cluster is simply the angle of the lengthwise centerline of the eSC segment.

The resulting (ϕ, z) distribution is shown in Fig. C.1. Each (t, ϕ, z) cluster itself is considered an electron object in the simplest definition considered. Temporal and spatial coincidence of these clusters with ePC clusters define complete e-detector tracks, as described below.

C.2.2 ePC Clustering

The analysis initially treats the ePC's separately, constructing for each an array of ePC objects corresponding to particle traversals. Each ePC object requires a hit in an anode and zero, one (inner or outer), or both (inner and outer) cathodes. Selection on whether or not the cathodes are present is done at a later stage, when ePC1 objects are paired with ePC2 objects to form "*e*-detector track candidates."

Since a particle traversing a multiwire proportional chamber plane can cause multiple wires to fire, the singles hits must be grouped together into clusters, each characterized by time, location in the plane, and size. The basic single-plane clustering algorithm is the following:

1. Project singles hits in the plane onto the time axis and find time-coincident hits.
2. Sort time-coincident hits by wire number.
3. Define clusters as groups of singles hits continuous in wire number, possibly allowing a small gap. The cluster time is taken to be the time of the first hit of each cluster. Cluster location is the average of the wires in the cluster, and cluster size is the number of singles hits.

Details of the clustering algorithm are set by a collection of parameters that are customized for each detector plane.

- `TimeWindow.` The clustering time width, its specific meaning depends on the value of the next setting. Its value is ≈ 300 ns for each ePC plane.
- `DiffClustering.` If non-zero (TRUE), the time difference between successive singles hits in step 1 of the clustering algorithm are compared to the clustering time width. If zero (FALSE), the time with respect to the earliest singles hit in the potential cluster is used instead. This parameter was set to TRUE in the final analysis pass; no significant differences were noticed in the past by varying this parameter, but more further studies could be envisioned.
- `DeadTime.` As the singles are encountered in chronological order, individual wires are "killed" for this number of ns. That is, if a subsequent hit occurs on the same wire within this time, it is ignored. In a special study, this value was varied around its nominal setting of around 1000 ns for each ePC plane, and no appreciable effect was observed.
- `UpdatingDeadtime.` If non-zero (TRUE), hits that fall within the deadtime of a previous hit on the same wire extend the deadtime. This is similar to how an updating

discriminator extends the output pulse if an additional input signal falls within the output pulse width. This value is nominally set to TRUE.

- `AllowedGap.` In step 3 of the clustering algorithm above, this is the maximum allowed wire number gap to be part of the same cluster. (1 means adjacent wires, 2 means one wire missing, etc.) This value is set to 2 for ePC anodes and 3 (two wires allowed to be missing) for ePC cathodes.

After the individual planes are clustered, an attempt is made to find coincident cathode clusters for each anode cluster. The procedure to fill information into an ePC hit object starts with an anode cluster, which gives the time t_{ePC} and cylindrical coordinate ϕ_{ePC}, and then goes on to fill in the cathodes-based data as follows:

1. Search for inner and outer cathode clusters each time-coincident with the anode cluster, and the z-position from the anode×inner coincidence ($Z_{\mathrm{anode}\times\mathrm{inner}}$) near that of the anode×outer coincidence ($Z_{\mathrm{anode}\times\mathrm{outer}}$). The z-position is taken to be the average of $Z_{\mathrm{anode}\times\mathrm{inner}}$ and $Z_{anode\times outer}$.

2. If no anode/innner/outer coincidence is found, search for an inner cathode cluster time-coincident with the anode cluster and with $Z_{\mathrm{anode}\times\mathrm{inner}}$ within the active length of the detector.

3. If no anode×inner cathode cluster is found, search for an outer cathode cluster time-coincident with the anode cluster, and $Z_{\mathrm{anode}\times\mathrm{outer}}$ within the active length of the detector.

C.2.3 ePC1×ePC2×eSC Coincidences

Coincident ePC1 and ePC2 hits are considered "electron track candidates," subject to later approval by the eSC. Different versions of the track candidates are considered separately:

- *Anodes Only.* Cathode information in the ePC objects are ignored.

- *Either Cathode.* At least one cathode is required to be coincident with the anode.

- *Both Cathodes.* Both inner and outer cathodes must be coincident with the anode.

All ePC1, ePC2 pairs that satisfy the cuts constitute the electron track candidates for a given cathodes requirement (none, either, or both).

Description of Constraint
$T_{eSC} - T_{ePC1} \geq -15$ ns
$T_{eSC} - T_{ePC1} \leq 166$ ns
$T_{eSC} - T_{ePC2} \geq -46$ ns
$T_{eSC} - T_{ePC2} \leq 131$ ns
$Z_{eSC} - Z_{ePC1\times ePC2@eSC} \geq -300$ mm
$Z_{eSC} - Z_{ePC1\times ePC2@eSC} \leq 300$ mm
$\phi_{eSC} - \phi_{ePC1\times ePC2@eSC} \geq -0.3$
$\phi_{eSC} - \phi_{ePC1\times ePC2@eSC} \leq 0.3$

Table C.1: eSC×ePC1×ePC2 Coincidence Cuts. The ϕ- and Z-cuts act on the ϕ and Z location of the ePC1×ePC2 track extrapolated to the radius of the eSC.

The electron track-finding procedure associates eSC 4-fold clusters with electron track candidates (ePC1×ePC2) to form complete electron detector track objects, which will be used directly in muon decay time spectra. Each eSC 4-fold hit and ePC1×ePC2 candidate is used at most once, though it should be noted that, in ePC1×ePC2, a hit in one of the ePC's can be used more than once if there is more than one hit in the other ePC.

An important design decision of the UIUC analysis was to keep the electrons and muons logically separate until the last step of formation into lifetime spectra. This has immediate consequences in how the electron tracks are formed in the case of ambiguities, that is, when there is a choice in any of the detectors of which hit to associate with the others. One option is to retain all possible combinations until a later stage of the analysis, when the electron tracks are associated with muons, and then do some kind of "redundancy reduction" to avoid overcounting; that is the approach of the Berkeley analysis. Another option is to make a choice earlier on, even if it's wrong, of which e-detector track candidates to use. As long as the choice is not somehow lifetime dependent or exaggerates deadtime effects, it should only amount to perhaps a difference in time-independent efficiency. The UIUC analysis indeed takes the latter option: eSC 4-fold hits are each paired with one and only one ePC1×ePC2 candidate.

If there is only one ePC1×ePC2 candidate that is T-, ϕ- and z-coincident with the eSC 4-fold hit, then the track is unambiguous and is considered a good e-detector track; table C.1 lists the coincidence parameters.

The situation is more interesting if there are more than one ePC1×ePC2 candidate for a given eSC 4-fold hit. The code tries to "optimize" the matching of eSC 4-fold hits to ePC1×ePC2 candidates based on some loose criteria explained below. First, lists of all eSC 4-fold hits and ePC1×ePC2 candidates linked by time and space coincidences are populated.

Then all ways of associating the eSC 4-fold hits with the ePC1×ePC2 candidates are tried, and the "best" combination is chosen. The algorithm is roughly the following:

1. The index of the eSC 4-fold hit being considered is entered as the first and only item in an eSC 4-fold indices list.
2. A list of indices of all ePC1×ePC2 candidates that are (T, ϕ, Z)-acceptable for the eSC 4-fold hit is populated.
3. A list of indices of additional eSC 4-fold hits that are (T, ϕ, Z)-acceptable, for at least one member of the ePC1×ePC2 indices list, is added to the eSC 4-fold indices list.
4. Steps 2 and 3 are repeated until no more hits are added.
5. If there are too many ways of associating the two lists, go to the next step. Otherwise, try each way, calculating a fitness function for each way. Basically, the fitness function favors a higher number of successful pairings of the eSC with the ePC's. The fitness of a way of pairing them is initially zero (best), and points are added for each pair:

    - Check for time-coincidence. If the eSC 4-fold hit and ePC1×ePC2 are not time-coincident, give a 10-point penalty.
    - Check for ϕ-coincidence. If not ϕ-coincident then add 10 points to the overall fitness; if it is ϕ-coincident but the ePC1×ePC2 does not point directly at the eSC segment, then add to the fitness an amount ≤ 1, increasing the further away from the eSC segment the candidate track points.
    - Check for z-coincidence. If not z-coincident then add 10 points; otherwise, add an amount ≤ 1, increasing the further away from Z_{eSC} the track candidate points.

    Once all ways of pairing are evaluated, choose the one with the lowest penalty and make complete e-detector track objects from the valid (T, ϕ, Z)-coincident pairs.

6. In the very rare case there are so many ways of associating the two lists that computation time would be prohibitive, then, rather than throwing out all or just picking the first one, the ϕ-coincidence cut is made more restrictive: the ePC1×ePC2 candidate must point directly at the eSC segment. The more restrictive cut applies only to this group. Then the whole procedure of associating eSC with the ePC track candidates is repeated. If there are still too many combinations, only then is the group thrown out.

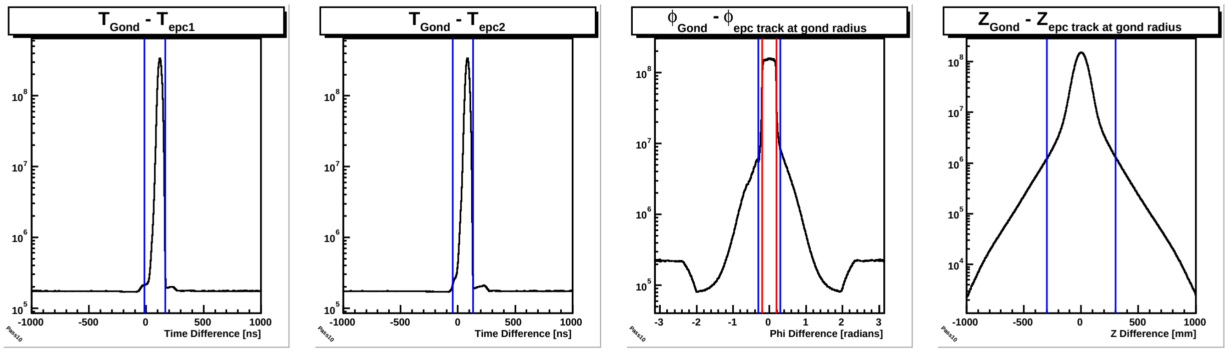

Figure C.2: e-Detector Track Cuts: eSC×ePC1×ePC2. The coincidence cuts are indicated by the vertical lines. In the ϕ-coincidence histogram (third panel from left), the red lines indicate the more restrictive cut optionally applied in Step 6 of the optimization algorithm. The histograms displayed are based on the ePC hits that have at least one cathode included ("Cathode OR" selection).

It is likely these are some kind of spark of weird shower event anyway, not something we want.

C.3 Spark and Noise Cuts

Sparks in a MWPC are characterized by high-multiplicity clusters. They are removed at various stages of the analysis by vetoing all muon entrances within a specified time interval $\sim 50\ \mu$s around the the spark time. Several methods identify spark intervals:

- An early analysis stage looks for 45-μs periods during which there are an unusually high number of singles hits in any MWPC plane except the TPC. This method only finds very large spark events, but removing these very-high-multiplicity events at an early stage prevents them from wasting computation time in later analysis stages.
- Signals on TPC anodes 1–4, which are non-amplifying, provide a simple means to identify sparks in the TPC.
- The most aggressive spark cut is on ePC and MuPC cluster sizes. In the most recent analysis pass, clusters that include more than 10 wires were flagged as sparks. No evidence of a lifetime shift was noted compared to earlier analysis passes with much less aggressive cuts ($\sim$ 100 wires), but more systematic studies should be considered in the future.

In a given ePC plane, some channels may show much higher count rates than any other in the same plane. These wires are identified in the first few data blocks of each data file and masked for the remainder of the analysis of that file.

Appendix D

World Average g_P Determination

In this chapter, previous measurements of muon capture in hydrogen are reinterpreted using modern values of the parameters in the kinetic equations (Section 3.3) and in the phenomenological calculation (Section 2.3). The goal is to produce a plot of g_P vs. λ_{op}, similar to those shown in Fig. 1.7, for each of the muon capture experiments. We start with the experimental conditions summarized in Table II of the review by Gorringe and Fearing [12]; relevant entries from the table are reproduced here in Table D.1.

For each experiment and given values of the molecular formation rate λ_{of} and the $p\mu p$ ortho-para molecular transition rate λ_{op}, the value of g_P that gives a theoretical prediction for the capture rate Λ_c^{Th} that matches the experimental result is found. The plot is produced by sweeping λ_{op}. The effect on the g_P determination from uncertainty in λ_{of} is studied by producing three different g_P solutions for each setting of λ_{op}: one with λ_{of} fixed to its central value, and two more with λ_{of} shifted larger and smaller by its 1-σ uncertainty. The (relatively small) uncertainty thus discovered is then added in quadrature to the experimental uncertainty in g_P. The uncertainty in g_P due to λ_{op} is read off the plot of g_P vs. λ_{op}. It is added in quadrature to finally produce a single number that is the experimental determination of g_P for the experiment considered — these are the g_P values shown in Fig. 7.2.

The procedure to calculate each of the plots in Fig. D.1 (except the radiative muon capture band and the averages in the lower right corner) is outlined:

1. The kinetics parameters λ_{of} and λ_{op} are fixed to some values. These will be used in the calculation of a theoretical prediction for the capture rate.

2. The results of the phenomenological calculation outlined in Section 2.3 are used here for Λ_S and Λ_T as a function of g_P (all other parameters of the phenomenological calculation are fixed). Capture rates from the molecular states, Λ_{om} and Λ_{pm}, are determined by Λ_S, Λ_T, and the well-known molecular overlap factors γ_{O} and γ_{P} (see Eqs. 2.48 and 2.49).

Reference	Density $n/n_0 \equiv \phi$	Start Time t_1 (μs)	Capture Rate Λ_c (s^{-1})
Hildebrand (1962)	1.0	0.0	420 ± 120
Hildebrand and Doede (1962)	1.0	0.0	428 ± 85
Bertolini *et al.* (1962)	1.0	0.0	450 ± 50
Bleser *et al.* (1962)	1.0	1.0	515 ± 85
Rothberg *et al.* (1963)	1.0	1.2	464 ± 42
Alberigi-Quaranta *et al.* (1969)	0.014	0.9	651 ± 57
Bystritskii *et al.* (1974)	0.072	1.4	686 ± 88
Bardin *et al.* (1981)	1.0	2.5	433 ± 15

Table D.1: (from Table II of Gorringe and Fearing [12]) Summary of experimental parameters and results from previous measurements of ordinary muon capture in hydrogen. The density ϕ of the hydrogen target is with respect to liquid hydrogen density. The start time t_1 is the (average) time delay from when the muon stops in the target to when observation begins. The Bardin *et al.* experiment, which used the lifetime technique, is updated with the most recent world average of the positive muon lifetime [8].

3. The theoretical prediction Λ_c^{Th} depends on the particular experimental conditions: hydrogen density ϕ, observation start time t_1, and whether neutrons (for the absolute capture yield) or electrons (for the lifetime technique) are detected.

   If the measurement is based on neutron detection, as in most prior ordinary muon capture (OMC) experiments, a neutron appearance time spectrum $y_n(t)$ is generated from the solution to the full kinetics equations (Appendix A): $y_n(t) = N(\Lambda_S n_1(t) + \Lambda_{\mathrm{om}} n_2(t) + \Lambda_{\mathrm{pm}} n_3(t))$. The predicted capture rate is

   $$\Lambda_c^{\mathrm{Th}} = \lambda_0 \frac{\int_{t_1}^{t_2} y_n(t)dt}{N(e^{-\lambda_0 t_1} - e^{-\lambda_0 t_2})}, \tag{D.1}$$

   where t_2, the stop time of the observation interval, is set to 20 μs in this study if it is unknown for the particular experiment (Λ_c^{Th} is not sensitive to t_2 as long as t_2 is sufficiently large).

   If the measurement is based on the lifetime technique, as in the Bardin *et al.* and MuCap experiments, the electron appearance time spectrum is generated according to Eq. A.16. The predicted capture rate is then $\Lambda_c^{\mathrm{Th}} = \lambda_\mu^- - \lambda_0$, where λ_μ^- is from a single exponential fit to the generated lifetime spectrum with the fit range $t_1 < t < t_2$. (Actually, the equivalent method described in Section A.2.1 of calculating the shift, in fit parameter space, of the χ^2 minimum is used to calculate directly $\Delta\lambda \equiv \lambda_\mu^- - \lambda_0 =$

Λ_c.)

4. The previous step gives a prediction $\Lambda_c^{\mathrm{Th}}(g_P)$, for a given value of g_P, that can be compared directly to the experimental capture rate Λ_c^{Ex}. A χ^2 function is defined:

$$\chi^2 = \left(\frac{\Lambda_c^{\mathrm{Ex}} - \Lambda_c^{\mathrm{Th}}(g_P)}{\sigma_\Lambda} \right)^2 , \tag{D.2}$$

   where σ_Λ is the reported uncertainty in Λ_c^{Ex}. The χ^2 function is minimized by calling standard MINUIT algorithms, with values of the model function $\Lambda_c^{\mathrm{Th}}(g_P)$ generated as describe above. The result of the minimization gives the experimental determination of g_P and its uncertainty.

5. New values of λ_{of} and λ_{op} are chosen, and the procedure repeats starting with Step 3.

The radiative muon capture (Wright *et al.*) band is not calculated in this study but is copied from Fig. 1.7. The "world average" bands in the lower right panel of Fig. D.1 are calculated by averaging together the g_P vs. λ_{op} bands of the individual experiments. Following Gorringe and Fearing [12], the g_P determinations from the bubble-chamber experiments (top row of Fig. D.1) are omitted from the world-average calculation.

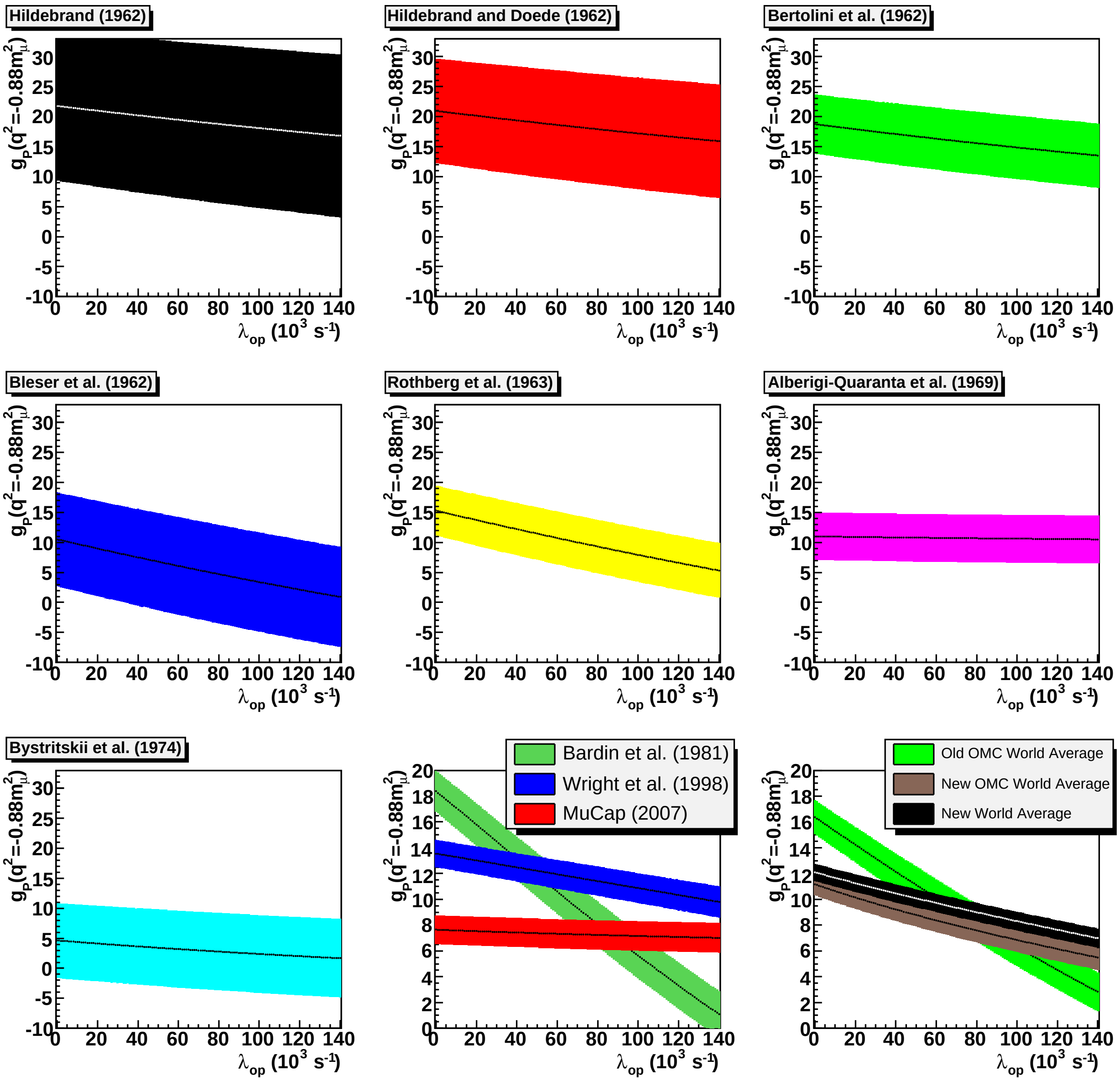

Figure D.1: Updated experimental determinations of g_P vs. the $p\mu p$ molecular transition rate $\lambda_{\rm op}$ ($\lambda_{\rm of} = (2.3\pm0.5)\times10^6\ {\rm s}^{-1}$). All determinations except that from the radiative muon capture (RMC) experiment (Wright *et al.*) are calculated by comparing the experimental capture rates to the theoretical prediction versus g_P. The band for g_P from the Wright *et al.* experiment is copied directly from Fig. 7.1. The vertical scale is changed in the last two plots, which show the three most precise measurements and averages computed from combinations of the experimental determinations. The "old OMC world average" includes Bleser *et al.* through Bardin *et al.* (five experiments). The "new OMC world average" additionally includes MuCap. The "new world average" further includes the Wright *et al.* radiative muon capture (RMC) experiment.

Bibliography

[1] Nimai C. Mukhopadhyay. Nuclear muon capture. *Physics Reports. Physics Letters Section C*, 30C(1):1–144, March 1977.

[2] R. H. Hildebrand. Observation of μ^- capture in liquid hydrogen. *Physical Review Letters*, 8(1):34–37, 1962.

[3] A. Alberigi-Quaranta et al. Muon capture in gaseous hydrogen. *Physical Review*, 177(5):2118–2132, January 1969.

[4] V. M. Bystritskiĭ et al. Measurement of the muon capture rate in gaseous hydrogen. *Sov. Phys. – JETP*, 39(1):19–26, July 1974.

[5] G. Bardin et al. A novel measurement of the muon capture rate in liquid hydrogen by the lifetime technique. *Nuclear Physics*, A352:365–378, 1981.

[6] M. Adam et al. An ultra-pure, deuterium-free liquid hydrogen target. *Nuclear Instruments and Methods*, 177:305–308, 1980.

[7] H. Überall. Decay of μ^- mesons bound in the k shell of light nuclei. *Physical Review*, 119(1):365–376, July 1960.

[8] D. B. Chitwood et al. Improved measurement of the positive muon lifetime and determination of the fermi constant. *submitted to PRL*, 2007.

[9] G. Bardin et al. Measurement of the ortho-para transition rate in the $p\mu p$ molecule and deduction of the pseudoscalar coupling constant g_p^μ. *Physics Letters*, 104B(4):320–324, September 1981.

[10] D. D. Bakalov, M. P. Faifman, L. I. Ponomarev, and S. I. Vinitsky. μ-capture and ortho-para transitions in the muonic molecule $pp\mu$. *Nuclear Physics A*, 384(3):302–322, August 1982.

[11] J. H. D. Clark et al. Ortho-para transition rate in mu-molecular hydrogen and the proton's induced pseudoscalar coupling g_{p}. *Physical Review Letters*, 96:073401, 2006.

[12] T. Gorringe and H. W. Fearing. Induced pseudoscalar coupling of the proton weak interaction. *Reviews of Modern Physics*, 76:31, 2004.

[13] G. Jonkmans et al. Radiative muon capture on hydrogen and the induced pseudoscalar coupling. *Physical Review Letters*, 77(22):4512–4515, November 1996.

[14] D. H. Wright et al. Measurement of the induced pseudoscalar coupling using radiative muon capture on hydrogen. *Physical Review C*, 57(1):373–390, January 1998.

[15] V. A. Andreev et al. Measurement of the rate of muon capture in hydrogen gas and determination of the proton's pseudoscalar coupling g_{p}. *submitted to PRL*, 2007.

[16] E. D. Commins and P. H. Bucksbaum. *Weak Interactions of Leptons and Quarks*. Cambridge University Press, Cambridge.

[17] V. Bernard, N. Kaiser, and Ulf-G. Meissner. Qcd accurately predicts the induced pseudoscalar coupling constant. *Physical Review D*, 50(11):6899–6901, 1994.

[18] S. L. Adler and Y. Dothan. Low-energy theorem for the weak axial vertex. *Physical Review*, 151:1267, 1966.

[19] N. Kaiser. Induced pseudoscalar form factor of the nucleon at two-loop order in chiral perturbation theory. *Physical Review C*, 67:027002, 2003.

[20] V. Bernard, L. Elouadrhiri, and U.-G. Meissner. Axial structure of the nucleon. *J. Phys. G: Nucl. Part. Phys.*, 28:R1–R35, 2002.

[21] W.-M. Yao et al. Review of particle properties. *J. Phys. G: Nucl. Part. Phys.*, 33:1, 2006.

[22] P. Mergell et al. Radii of the dirac and pauli form factors. *Nuclear Physics*, page 367, 1996.

[23] L. A. Ahrens et al. A study of the axial-vector form factor and second-class currents in antineutrino quasielastic scattering. *Physics Letters*, B202(2):284–288, March 1988.

[24] W. J. Marciano and A. Sirlin. Improved calculation of electroweak radiative corrections and the value of v_{ud}. *Physical Review Letters*, 96:032002, January 2006.

[25] E. D. Commins. *Weak Interactions*. McGraw-Hill.

[26] Jan Govaerts and Jose-Luis Lucio-Martinez. Nuclear muon capture on the proton and ^{3}He within the standard model and beyond. *Nuclear Physics A*, 678(1–2):110–146, September 2000.

[27] S. Ando, F. Myhrer, and K. Kubodera. Capture rate and neutron helicity asymmetry for ordinary muon capture on hydrogen. *Physical Review*, pages 015203–1–015203–7, 2000.

[28] V. Bernard, H. W. Fearing, T. R. Hemmert, and U.-G. Meissner. Ordinary and radiative muon capture on the proton and the pseudoscalar form factor of the nucleon. *Nuclear Physics*, pages 290–316, 2001.

[29] M. R. Goldman. Order α corrections to muon capture in hydrogen. *Nuclear Physics*, pages 621–632, 1972.

[30] A. Czarnecki, W. J. Marciano, and A. Sirlin. Electroweak radiative corrections to muon capture. *e-Print Archive*, arXiv:hep–ph/0704.3968v1, April 2007.

[31] Steven Weinberg. Muon absorption in liquid hydrogen. *Physical Review Letters*, 4(11):575–578, June 1960.

[32] T. Suzuki, D. F. Measday, and J. P. Roalsvig. Total nuclear capture rates for negative muons. *Physical Review C*, 35(6):2212–2224, June 1987.

[33] P. Kammel. Energy deposits and thresholds in the tpc. Technical report, MuCap Internal Note, 2005.

[34] S. S. Gershtein and L. I. Ponomarev. *Mesomolecular processes induced by μ^- and π^- mesons*, volume 3, pages 141–233. 1977.

[35] T. S. Jensen and V. E. Markushin. Collisional deexcitation of exotic hydrogen atoms in highly excited states. *Eur. Phys. J. D*, 21:271–283, October 2002.

[36] A. Adamczak and J. Gronowski. Diffusion radius of muonic hydrogenic atoms in h-d gas. *Eur. Phys. J. D*, 41(3):493–497, March 2007.

[37] M. P. Faifman. Nonresonant formation of hydrogen isotope mesic molecules. *Muon Catalyzed Fusion*, 4:341–364, 1989.

[38] E. J. Bleser, E. W. Anderson, L. M. Lederman, S. L. Meyer, J. L. Rosen, J. E. Rothberg, and I-T. Wang. Muonic molecules in liquid hydrogen. *Physical Review*, 132(6):2679–2691, December 1963.

[39] G. Conforto, C. Rubbia, E. Zavattini, and S. Focardi. Direct measurement of μ-mesonic molecule formation rates in liquid hydrogen. *Nuovo Cimento*, 33:1001, 1964.

[40] V. M. Bystricky et al. Direct measurement of the formation rate of $pp\mu$ and $pd\mu$ molecules in gaseous hydrogen. *Sov. Phys. JETP*, 43:606, 1976.

[41] F. Mulhauser et al. Measurement of muon transfer from proton to triton and $pp\mu$ molecular formation in solid hydrogen. *Physical Review A*, 53(5):3069–3080, 1996.

[42] T. I. Banks and P. Kammel. Revisions to the high-z impurity correction numbers. Technical report, MuCap Internal Note, 2006.

[43] L. Schellenberg et al. In *Muonic atoms and molecules*, pages 187–192, 1992.

[44] L. Schellenberg. Muon transfer in gas mixtures with hydrogen. *Muon Catalyzed Fusion*, 5/6:73–85, 1990/91.

[45] A. Werthmüller et al. *Hyperfine Interactions*, 116:1–4, 1998.

[46] H. Schneuwly. In *Muonic atoms and molecules*, pages 209–215, 1992.

[47] R. Jacot-Guillarmod et al. *Physical Review*, page 3447, 1997.

[48] N. I. Voropaev et al. μcf experiments in d_2 and hd gases — final results. *Hyperfine Interactions*, 138:331–341, June 2002.

[49] D. F. Measday. The nuclear physics of muon capture. *Physics Reports*, 354(4–5):243–409, November 2001.

[50] D. V. Balin et al. High precision measurement of singlet $p\mu$ capture in H_2 gas. Proposal R–97–05, Paul Scherrer Institute, 1996.

[51] H.-A. Synal, M. Stocker, and M. Suter. Micadas: A new compact radiocarbon ams system. *Nuclear Instruments and Methods*, B259:7–13, 2007.

[52] V. A. Ganzha et al. A ciculating hydrogen ultra-high purification system for the mucap experiment. *submitted to NIM*, 2007.

[53] T. I. Banks. Mucap run8 muon detector inefficiencies. Technical report, MuCap Internal Note, May 2006.

[54] J. F. Ziegler. `http://www.srim.org/`, 2006.

[55] P. Winter. private communication, 2007.

[56] P. Kammel and B. Kiburg. Practical impurity corrections. Technical report, MuCap Internal Note, 2007.

[57] Y.-A. Thalman et al. Muon transfer from excited states of hydrogen and deuterium to nitrogen, neon, and argon. *Physical Review A*, 57(3):1713–1720, March 1998.

[58] Y.-A. Thalman et al. Energy dependence of the charge exchange reaction from muonic hydrogen to oxygen. *Hyperfine Interactions*, 116:1, 1998.

[59] S. M. Clayton, P. Kammel, and B. Kiburg. Analysis of time distributions in the mucap experiment. Technical report, MuCap Internal Note, 2006.

[60] H. C. von Baeyer and D. Leiter. Nuclear recoil corrections to the lifetime of bound muons. *Physical Review A*, 19(4):1371–1374, April 1979.

[61] A. Czarnecki, G. P. Lepage, and W. J. Marciano. Muonium decay. *Physical Review D*, 61:073001, February 2000.

Author's Biography

Steven Michael Clayton was born in October, 1976, in Dallas, Texas. Steven graduated from the University of Minnesota in the Spring of 1997 with a degree in physics, and he moved to Urbana, Illinois later that year to pursue graduate study in physics at the University of Illinois. In the summer of 2001, Steven joined the Precision Muon Group of the University of Illinois Nuclear Physics Laboratory to work on the MuCap experiment.